Tip-enhanced near-field optical microscopy: from symmetry selectivity to single molecule sensitivity

D I S S E R T A T I O N

zur Erlangung des akademischen Grades

doctor rerum naturalium (Dr. rer. nat.)
im Fach Physik

eingereicht an der
Mathematisch-Naturwissenschaftlichen Fakultät I
Humboldt-Universität zu Berlin

von
Herr Dipl.-Phys. Corneliu Catalin Neacsu

Präsident der Humboldt-Universität zu Berlin:
Prof. Dr. Dr. h.c. Christoph Markschies

Dekan der Mathematisch-Naturwissenschaftlichen Fakultät I:
Prof. Dr. Lutz-Helmut Schön

Gutachter:
1. Prof. Dr. Thomas Elsässer
2. Prof. Dr. Markus B. Raschke
3. Prof. Dr. Oliver Benson

eingereicht am: 28. April 2008
Tag der mündlichen Prüfung: 18. July 2008

La steaua care-a răsărit
E-o cale-atât de lungă,
Că mii de ani i-au trebuit
Luminii să ne-ajungă.

La steaua, Mihai Eminescu (1886)

Abstract

This thesis describes the implementation of scattering-type near-field optical microscopy (s-SNOM) for linear and nonlinear optical imaging. The technique allows for optical spectroscopy with ultrahigh spatial resolution on the order of few nanometers. New results on the microscopic understanding of the imaging mechanism and the employment of s-SNOM for structure determination at solid surfaces are presented.

The method relies on the use of metallic probe tips with apex radii of only few nanometers. The local-field enhancement and its dependence on material properties are systematically investigated. The plasmonic character of Au tips is for the first time identified and its importance for the optical tip-sample coupling and subsequent near-field confinement are discussed. The experimental results offer valuable criteria in terms of tip-material and -structural parameters for the choice of suitable tips required in s-SNOM.

An apertureless near-field optical microscope is developed for tip-enhan-ced Raman spectroscopy (TERS) studies. The principles of TERS and the overwhelming role of the tip plasmonic behavior together with clear distinction of near-field Raman signature from far-field imaging artifacts are described. TERS results of monolayer and submonolayer molecular coverage on smooth Au surfaces are presented. Near-field Raman enhancement factors of up to 10^9, corresponding to field enhancements of up to 130 are obtained, allowing for Raman detection down to the single molecule level.

Second harmonic generation (SHG) from individual tips is investigated. As a partially asymmetric nanostructure, the tip allows for the clear distinction of local surface and nonlocal bulk contributions to the nonlinear polarization and the analysis of their polarization and emission selection rules. With SH response being generated only at the tip apex, the local-field enhancement factor is estimated for bare tips. Tip-enhanced SH microscopy and dielectric contrast imaging with high spatial resolution are demonstrated. With its symmetry selectivity, SHG couples directly to the ferroelectric ordering in materials, and in combination with scanning probe microscopy can give access to the morphology of mesoscopic ferroelectric domains. Using a phase-sensitive self-homodyne SHG s-SNOM imaging method, the surface topology of 180° intrinsic domains in hexagonal multiferroic $YMnO_3$ is resolved.

The present work demonstrates the s-SNOM versatility. Its combination with time-resolved optical spectroscopy is possible over a broad frequency range.

Zusammenfassung

Die vorliegende Arbeit beschreibt neue Entwicklungen im Verständnis und in der Umsetzung der aperturlosen, optischen Nahfeldmikroskopie (scattering - type scanning near-field optical microscopy, s-SNOM) für die lineare und nichtlineare optische Bildgebung mit ultrahoher Auslösung und Empfindlichkeit.

Die fundamentalen Mechanismen, die der Feldverstärkung am Ende von ultrascharfen metallischen Spitzen zugrunde liegen, werden systematisch behandelt. Die plasmonischen Eigenschaften der Spitze wurden erstmalig beobachtet, und ihre Bedeutung für die optische Kopplung zwischen Spitze und Probe sowie für die sich ergebende Einengung des Nahfeldes wird diskutiert. Aus den experimentellen Ergebnissen ergeben sich wertvolle, die Struktur und das Material betreffende Kriterien für die Wahl geeigneter Spitzen für die Nahfeldmikroskopie.

Ein aperturloses Nahfeldmikroskop für die spitzenverstärkte Ramanspektroskopie (tip-enhanced Raman spectroscopy, TERS) wurde entwickelt. Die Grundlagen der TERS und die wesentliche Rolle des plasmonischen Verhaltens der Spitze sowie die klare Unterscheidung von Nahfeld-Ramansignatur und Fernfeld-Abbildungsartefakten werden beschrieben. TERS-Ergebnisse, die bei einer molekularen Bedeckung von maximal einer Monolage auf glatten Gold-Oberflächen erzielt wurden, werden vorgestellt. Nahfeld Raman Verstärkungsfaktoren von bis zu 10^9 wurden erreicht, was einer Feldverstärkung von bis zu 130 entspricht und Raman-Messungen bis auf Einzel-Molekül-Niveau ermöglichte.

Die optische Frequenzverdopplung (second harmonic generation, SHG) an einzelnen Spitzen wurde untersucht. Aufgrund ihrer teilweise asymmetrischen Nanostruktur erlauben die Spitzen eine klare Unterscheidung von lokalen Oberflächen und nichtlokalen Volumenbeiträgen zur nichtlinearen Polarisation sowie die Analyse ihrer Polarisations- und Emissions-Auswahlregeln. Da die Frequenzverdopplung nur am Ende der Spitzen stattfindet, kann der Feldverstärkungsfaktor für einzelne Spitzen abgeschätzt werden. Die spitzenverstärkte Frequenzverdopplungs-Spektroskopie und die räumlich hoch aufgelöste Abbildung auf Basis des dielektrischen Kontrasts werden demonstriert. Aufgrund ihrer Symmetrieempfindlichkeit koppelt die Frequenzverdopplung direkt mit der ferroelektrischen Ordnung in der Probe und kann daher in Verbindung mit der Rastersondenmikroskopie die Morpholgie von mesoskopischen ferroelektrischen Domänen aufklären. Mit Hilfe einer phasen-sensitiven, Selbst-homodyn-Frequenzverdopplungs-s-SNOM-Abbildungsmethode kann die Oberflächen-Struktur der intrinsischen 180°-Domänen im hexagonal multiferroischen $YMnO_3$ aufgelöst werden. Prinzipiell ist die gleiche Technik auch für Materialien mit einer beliebigen Orientierung der Domänen anwendbar, und sie erlaubt sogar die Abbildung von gleichzeitig existierenden ferroelektrischen und magnetischen Domänen in Multiferroika.

Contents

1 Introduction

The optics on mesoscopic length scales is concerned with the study of phenomena occurring in structures with at least one dimension on roughly between 1 and 100 nm[i]. This nanoscale is unique because here the properties of bulk materials meet the properties of atoms and molecules. Furthermore, at the nanoscale the chemical and physical properties of materials change, evident when they (i) are dependent on the finite size of the structure, (ii) might be dominated by particular interfacial effects, and (iii) exhibit properties due to a limited number of constituents. For example, the electronic and optical properties of quantum dots, quantum wires and quantum wells are dictated by a quantum confinement effect. This manifests as a change in the energy spectrum from continuous to discrete when the diameter of the particle is on the same order of magnitude as the wavelength of the wave function of electrons [1].

The ability to resolve, image, identify and investigate samples down to the atomic/molecular level is of central importance in a wide variety of scientific disciplines and emerging technologies. The combination of optical microscopy and spectroscopy is highly desirable for spatially resolving spectral features, which would give new insights into the fundamental microscopic physics. Reaching the above goals is highly dependent on two vital parameters: sensitivity and spatial resolution.

1.1 Spatial resolution in far-field optics

Image formation in a classic (far-field) microscope is achieved by specimen illumination using a plane wave. The light scattered by the object is then collected by transmission or reflection and focused on a detector. The lens is situated more than several wavelengths away from the object, in the optical far-field. The highest achievable spatial resolution in such an optical system is determined by the wave nature of light, which manifests itself in diffraction. According to the Rayleigh criterion, two objects are just resolved if the two central diffraction peaks are separated by at least their half-width [2]. Abbe showed that the smallest distance between objects that can still be spatially resolved is given by [3]:

$$d_{min} \sim \frac{0.61\lambda}{n \sin\theta}, \tag{1.1}$$

where λ is the wavelength of the incident light, n is the refraction index of the embedding medium and θ is the half-angle subintended by the object and the lens [4]. The factor $n\sin\theta$ defines the numerical aperture (NA) of the imaging instrument. Hence, the resolution of

[i] The prefix *nano* is derived from the Greek $\nu\alpha\nu o\zeta$ and it means dwarf. It is used in the SI system of units denoting a factor of 10^{-9}, *e.g.*, one nanometer represents one billionth of a meter.

an optical microscope is fundamentally limited to about half of the wavelength of incident light.

Different far-field techniques were developed in order to further stretch the spatial resolution. In immersion-lens microscopy and 4π-microscopy the NA is extended by a large refraction index n and large acceptance angle θ, respectively [5]. Confocal microscopy has become an established tool for material characterization [6, 7], and in conjunction with Raman and fluorescence spectroscopy, this technique provides sensitivity down to the single molecule level. In dark-field microscopy individual objects much smaller than the wavelength of light can be imaged by making use of the scattered light (Mie scattering). The invention of pulsed laser radiation propelled the field of nonlinear optics: multiphoton microscopy, second-harmonic and third-harmonic generation, coherent anti-Stokes Raman scattering are extremely important for visualizing processes with high spatial resolution. Besides nonlinear interactions, it has also been demonstrated that saturation effects (*e.g.*, stimulated depletion) can be applied to achieve arbitrary spatial resolution [8]. However, for most applications the desired spatial resolution often exceeds the one attainable through far-field optical methods.

1.2 Near-field optical microscopy[ii]

In 1928, E. H. Synge introduced the concept of *ultra-microscopy* [14], based on the discovery of evanescent light by Sir Isaac Newton by frustrated total internal reflection in his "two prisms experiment" [15]. Synge's idea was to illuminate the sample through a subwavelength aperture brought close to the sample (Fig. 1.1 b). The light passing through the aperture illuminates only a sample area comparable with the aperture opening (and thus, smaller than the diffraction limit). By raster-scanning the aperture above the sample while the proximity is preserved, a point-by-point image can be recorded. The resolution is dictated by the aperture size and the distance between the aperture and the sample, rather than the diffraction limit.

The need for very small apertures ($<10^{-7}$ m) and controllable sample-aperture distance on the nanometer lengthscale was not possible at the time when the concept was introduced (see facsimile in Fig. 1.1 a). The first near-field experiments were performed by Ash and Nichols, with incident radiation in the microwave spectral range [16].

It was the invention of the scanning probe techniques (*e.g.*, STM, AFM) which allowed for the implementation of Synge's idea at optical frequencies [17]. In this modern version of Synge's microscope, the end of a tapered optical fiber forms the subwavelength aperture. A near-field optical image with spatial resolution beyond Abbe's limit can be recorded when scanning the fiber over the sample surface [18, 19, 20, 21]. The technique is called scanning near-field optical microscopy (SNOM).

There are several *modi operandorum* employed in SNOM, depending on the position of the

[ii] A detailed review of the theory and physics of near-field imaging is not the subject of the present work. For an in-depth analysis the reader is referred to several reviews [9, 10, 11, 12, 13] (and references therein). Specific aspects of relevance for the present study are offered in the subsequent chapters, together with the results.

a)

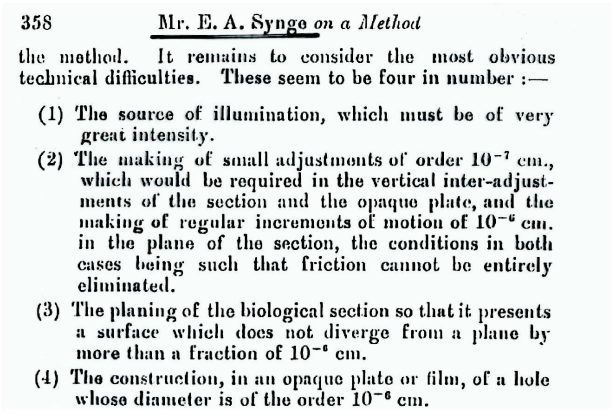

358 Mr. E. A. Synge *on a Method*

the method. It remains to consider the most obvious technical difficulties. These seem to be four in number :—

(1) The source of illumination, which must be of very great intensity.

(2) The making of small adjustments of order 10^{-7} cm., which would be required in the vertical inter-adjustments of the section and the opaque plate, and the making of regular increments of motion of 10^{-6} cm. in the plane of the section, the conditions in both cases being such that friction cannot be entirely eliminated.

(3) The planing of the biological section so that it presents a surface which does not diverge from a plane by more than a fraction of 10^{-6} cm.

(4) The construction, in an opaque plate or film, of a hole whose diameter is of the order 10^{-6} cm.

b)

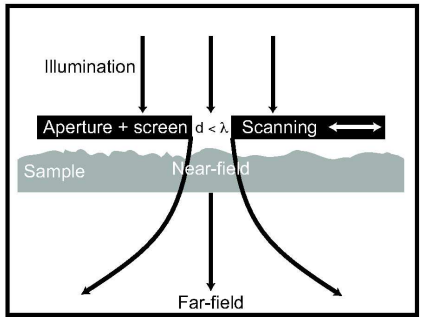

Figure 1.1: a) Facsimile from the original paper of E.H. Synge showing the difficulties he saw in realizing his idea. b) Conceptual illustration of Synge's idea.

probe with respect to the sample: (i) the collection mode, where the sample is illuminated in the far-field region and the near-field is collected through the aperture, (ii) the illumination mode where the incident light is through the fiber and the optical response is detected in the far-field, and (iii) the illumination-collection mode as a combination of the two previous modes.

Aperture-based near-field microscopes are confronted with a number of difficulties, such as the attenuation of the fields as the aperture opening diameter d is reduced below the wavelength dimensions. The light throughput falls off as $(d/\lambda)^4$ when $d << \lambda$, resulting in a rather low efficiency (10^{-3}-10^{-5}) [22]. Increasing the diameter d would result in a higher sensitivity, but at the expense of spatial resolution, and therefore a trade-off must be made between the two limiting factors.

1.2.1 Scattering-type near-field optical microscopy

An elegant way to surpass the above difficulties is offered by the scattering-type scanning near-field optical microscope (s-SNOM) where the aperture-tip is replaced by a nanoscopic, in general metallic tip[iii] [23, 24, 25, 26]. Here, the incident light is focused onto the tip-sample gap, and the tip acts primarily as a local scatterer which partially converts the evanescent waves into propagating radiation, which is then is detected (Fig. 1.2). The spatial resolution is independent of the incident light wavelength, and is given by the tip-apex radius alone. By raster scanning the sample, spatially resolved optical mapping with nanometer resolution can be obtained simultaneously with the topography in atomic force microscopy (AFM) or surface electronic properties in scanning tunneling microscopy (STM). The main experimental schemes employed for s-SNOM are (i) the axial illumination and/or detection which allows for higher NA but in general requires transparent samples or substrates [27, 28], and (ii) the epi-illumination and -detection geometry which allows for a greater flexibility in the selection of light polarization and k-vector as well as the use of non-transparent samples [29, 30].

[iii] As alternative denomination for s-SNOM, apertureless near-field optical microscopy is frequently used.

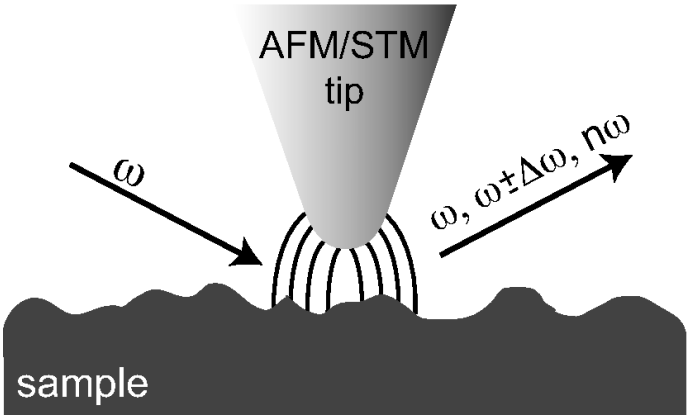

Figure 1.2: Conceptual schematics of the s-SNOM arrangement. The incident light is focused onto the tip-sample gap and the tip-scattered and -enhanced response is detected.

Under appropriate incident polarization conditions and the use of suitable tip materials and geometries, the localized electromagnetic field at the tip apex region[iv] can be strongly enhanced with respect to the incident field, and thus providing a nanoscopic light source. The origins of the field enhancement are attributed to the singular behavior of the electromagnetic field, akin to the lightning rod effect [33]. In addition, the spatial confinement allows for possible excitation of localized surface plasmon-polaritons (tip-plasmons) for certain tip materials, leading to a resonant enhancement of the local field at the driving laser frequency and thus for greater sensitivity and contrast [12]. Therefore, the tip is used as an active probe which concentrates and enhances the incident radiation into the tip-sample gap and simultaneously serves as efficient scatterer, in a similar way to electromagnetic antennas [34].

With its virtues of spatial resolution down to a few nm, ultrahigh sensitivity and access to a broad frequency range, s-SNOM represents a powerful technique for material characterization. In combination with optical spectroscopy, it provides chemical specificity on the nanoscale, with information on a single and *chosen* emitter, *spectroscopically* and *topographically* resolved. All-optical resolution down to just several nanometers has been achieved for linear scattering in the visible [26, 35, 36] and infrared (IR) spectral regions [37, 38, 39, 40]. Processes as two-photon fluorescence [36], second harmonic generation [41, 42, 43] and vibrational Raman spectroscopy [27, 44, 30] are also successfully employed.

Despite important progress in s-SNOM being routinely reported, there are still a number of challenges associated with the technique which require special attention and new directions of development are still open. The performance of s-SNOM critically depends on the degree of confinement and enhancement of the optical field at the tip apex. for probing electronic and dielectric properties of a medium by means of the aforementioned technique, the spectral response of the probe tip has to be known [45, 46]. At a fundamental level, a detailed knowledge of the microscopic mechanisms underlying the enhancement is desirable, including the role of the plasmonic character of the metallic tips, the nature of the tip-

[iv] These strong field-gradients have been previously proposed and used for whisker diodes or optical nanotweezers [31, 32].

sample optical coupling and the local field confinement.

From the experimental point of view, the differentiation of true optical contrast from topographic imaging artifacts is in general difficult due to the strong dependence of the scattering efficiency on the tip-sample distance. Furthermore, a clear distinction between the enhanced near-field response and various far-field artifacts requires the demonstration of the near-field localization on the lengthscale of the tip apex.

In addition to providing the field enhancement and confinement, and hence sensitivity and spatial resolution, the tip provides one with its unique spatial symmetry. This has yet received comparatively little attention. As a result of the mirror symmetry being broken along the main axis, tapered tips are partially asymmetric (∞mm) nanostructures, and thus allow for, *e.g.* the distinction of different sources for second-order polarizations [47]. By proper choice of polarization directions and k-vectors of the incident and detected light, selection of desired components of the second order susceptibility tensor can be implemented for nonlinear optical near-field imaging. Similarly, combined with the selection rules of Raman process, s-SNOM might allow for the determination of crystallographic orientation on the nanoscale.

The present work is organized as follows:

Chapter 2 is centered around the experimental concepts and techniques. The basic principles of the shear-force atomic force microscope (AFM) are discussed, and the setup of the apertureless near-field optical microscope (s-SNOM) is introduced. This is followed by the description of the electrochemical etching procedure of ultrasharp metallic tips. The various light sources and optical signal detection schemes used for the experiments are presented.

Chapter 3 is devoted to the characterization of the optical properties of metallic tips. Their plasmonic resonant behavior in the degree of local field enhancement at the tip apex is experimentally identified for the first time. The fundamental processes leading to local field enhancement, confinement and the tip-sample optical coupling are theoretically discussed. The experimental findings are found to agree with a theoretical model where the tip is modeled as a prolate hemispheroid and its relative polarizability is calculated.

Chapter 4 integrates these results in the context of scanning probe Raman spectroscopy on the nanoscale. Used in conjunction with optical microscopy, the Raman effect may give access to the intrinsic chemical specificity and spatial heterogeneity and composition of analytes. The basic principles of tip-enhanced Raman spectroscopy (TERS) are discussed together with its experimental implementation. After a clear distinction between near-field character and far-field imaging artifacts in the Raman response is made, tip-enhanced near-field spectra of monolayer and sub-monolayer of molecular adsorbates on smooth Au surfaces are presented. Near-field Raman enhancement factors of up to 10^9 are experimentally found and compared with theoretical simulations. This high sensitivity allowed for the detection of TERS response with single molecule sensitivity.

In chapter 5 the optical characterization of metallic tips is extended to nonlinear optics by means of second harmonic generation (SHG) from the tip apex region. As a partially asymmetric nanostructure the tip allows for the distinction of otherwise inseparable *local* surface and *nonlocal* bulk second-order polarizations. Selection rules for SH emission from tip apex are found and implemented for tip-enhanced second harmonic microscopy, allowing for nonlinear optical imaging with ultrahigh spatial resolution. Phase-sensitive SHG s-SNOM is employed for surface topology imaging of the intrinsic 180° ferroelectric domains in single crystalline $YMnO_3$.

Chapter 6 summarizes the work and identifies new and promising extensions of the tip-enhanced near-field optical microscopy and spectroscopy.

2 Experimental setup

The present chapter describes the experimental technique used, covering the general concepts common to all the experiments performed. Issues concerning experimental elements and arrangements specific to the experiments on linear spectroscopic characteristics of the metal tips, the scanning-probe Raman spectroscopy and the second-harmonic imaging of ferroelectric nano-domains will be described later in the respective chapters together with the results.

The room temperature scanning probe near-field optical microscope is based on a home-built atomic force microscope (AFM) [48, 17] using the shear-force distance control mechanism [49, 50, 51]. As scanning probes we use electrochemically etched metal tips [52].

The optical studies are performed by focusing a laser beam onto the tip-sample gap region, and detecting the scattered signal in an epi-illumination and detection geometry. The side-on illumination of the tip has the main advantages of also allowing for the study of nontransparent samples and flexibility in the selection of the polarization and k-vector. In order to maintain constant illumination conditions at the tip apex, the sample – rather than the tip – is scanned. A diagram of the experimental setup is shown in Fig. 2.1.

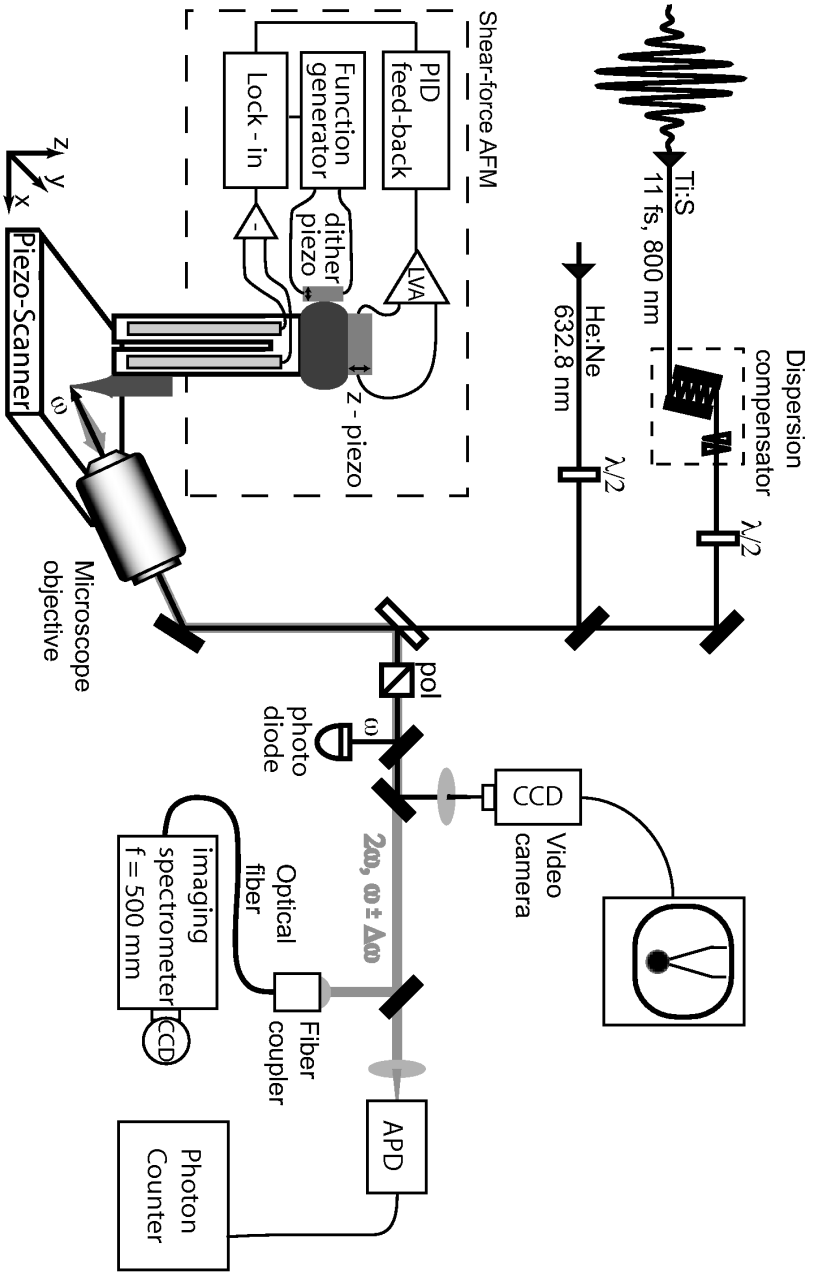

Figure 2.1: Experimental setup for the tip-enhanced near-field experiments. The incident light beam is focused onto the tip-sample gap using a long working distance microscope objective and the back-scattered signal is detected. A CCD camera is employed in order to better control the focusing conditions. The polarization direction of incoming and scattered light is varied by means of waveplates and polarizers, respectively.

2.1 The shear-force atomic-force microscope

For the purpose of the experiments described in the present work a shear-force AFM is used. This approach provides us with a number of advantages. Unlike the dynamic cantilever AFM methods, the distance between the tip and the sample is kept constant and small, and thus the sample surface is continuously subject to the strong optical near-field enhancement localized around the tip apex. The interaction forces between the tip and the sample are much smaller than in the case of contact AFMs. If for the latter the typical forces are on the order of 10 - 100 nN [53, 54], for shear-force based AFMs they are smaller than 100 pN [51, 55, 56]. Furthermore, the shear-forces are relatively long range (up to 25 nm) [57], and therefore tip-sample physical contact can be avoided, making it a non-destructive imaging technique for the scanning probe. This non-contact operation is also important in the context of the tip-enhanced Raman experiments described in Chapter 4, where the contact would lead to the contamination of the tip with the analyte adsorbed on the sample.

The shear-force damping and distance control mechanism were introduced by Betzig *et al.* [49] and Toledo-Crow *et al.* [50]. They found that the vibration of a tip in a direction parallel to the sample surface is damped at sub 25 nm tip-sample separation. This effect is the foundation of shear-force AFM. It found widespread applications especially in conventional near-field optical microscopy using tapered fiber tips (*e.g.*, [58]).

Despite that practical success, the details of the shear-force damping mechanism are still not fully understood [10]. Van-der-Waals forces [59] were discussed as possible explanations of the origin of the shear-force. Later, other models were proposed, *e.g.* the non-linear bending force model which considers the transfer of the energy of a vibrating probe to the sample due to elastic collision [60], or the dry contact friction model for vacuum or low temperature conditions when the tip is in mechanical contact with the sample surface [61]. For the latter conditions experiments showed that the force depends strongly on the sample properties [62, 63]. The role of Coulomb forces was also emphasized [64].

It was suggested [51, 65] that a tip oscillating along a parallel direction with respect to the sample surface behaves as a damped harmonic oscillator which experiences viscous damping from a thin water layer on the surface of the sample [65, 66, 67, 68, 69, 70, 71]. When the tip is close to the surface (10-20 nm) the liquid film becomes confined [72, 73] and new dynamic behavior emerges. This gives rise to a viscoelastic shear-force [74], which can be described as a force with an elastic and a dissipative component [75].

The equation describing the driven harmonic oscillation with damping of the lateral tip motion $x(t)$ is [76, 77]:

$$m\frac{\partial^2 x(t)}{\partial t^2} + m\gamma\frac{\partial x(t)}{\partial t} + m\omega_0^2 x = F sin(\omega t) \tag{2.1}$$

where m is the effective oscillator mass, γ is the damping coefficient and $\omega_0 = 2\pi f_0$ is the resonance frequency of the system. F is a driving force which is, for example, supplied by a dither piezo element attached to the tuning fork. The solution of equation 2.1 has the form:

$$x(t) = A(\omega, Q) sin(\omega t + \varphi) \tag{2.2}$$

with the amplitude $A(\omega)$ being a Lorentzian-shaped function of the frequency:

$$A(\omega) = \frac{F/m}{\sqrt{(\omega_0^2 - \omega^2)^2 + \gamma^2\omega^2}} \tag{2.3}$$

Here, we use quartz crystal tuning forks as mechanical resonators. They were originally developed for time-standards in quartz watches. The used tuning forks (part # 78D200, Bürklin OHG) have the resonance frequency at 32768 (*i.e.*, 2^{15}) Hz. The quality factor Q can be defined as $Q = f_0/\Delta f$, where Δf is the full frequency width at half maximum (FWHM) of the amplitude curve corresponding to γ [78]. Having a high quality factor translates into high sensitivity [51]. With Q-factors on the order of $10^3 - 10^4$ when used in ambient conditions, forces down to the pN range can be detected [79]. It has to be noted, however, that very high Q-values ($Q > 10^4$) would require slow scanning velocities due to the damping time constant $\tau = 2Q/\omega_0 \geq 1s$ [80].

For our purposes the metal case encapsulating the fork is removed. The tip is then glued along one prong of the fork, using a UV curing glue (Norland Optical Adhesive 81, Norland Products Inc.). The length of the tip protruding the fork-end is about 0.3 mm. It is important to keep this length as short as possible to avoid the oscillation of the tip itself at its resonance frequency.

Both prongs of the tuning fork are coupled through surface metallic electrodes (pads A and B in Figure 2.2, respectively) which serve as a pickup for the piezoelectric signal. The layout of the electrodes ensures that only movements of the prongs relative to each other can be detected. Two contact pins attached to the electrodes hold the fork onto a plastic socket.

In order to excite the mechanical resonance of the fork, the socket is attached to a ceramic piezoelectric element (PL055.20, Physik Instrumente GmbH, maximum displacement 2.2 μm at 100 V). This serves as a dithering element, giving rise to a tip-oscillation parallel to the surface. The tip-sample distance regulation detection scheme is based on the piezoelectric properties of the quartz crystal [57, 81]. The piezoelectric signal acquired from the tuning fork is on the order of 1μV to 1 mV. It is amplified using a home-made differential voltage preamplifier with an amplification factor of 1000 (two stages: LT1101 from Linear Technology, gain 100; OP27G from Texas Instruments Inc., gain 10). The preamplifier is connected to the tuning fork using short electrical wires in order to diminish capacitive load and leakage of long connection cables [82]. For finding the resonance frequency we use lock-in detection. Experimentally this is done by using the Easy PLL FM Detector and Sensor Controller (Nanosurf AG) operated in the "Self-Oscillating mode". The excitation frequency provided by an incorporated function generator is swept through a wide range (10 - 40 KHz, 5.5 mHz resolution) while the excitation amplitude is kept constant. The piezoelectric tuning fork signal is measured using a lock-in technique synchronous with the dither frequency.

With the gold tip attached, the resonance frequency ω_0 of the tuning fork shifts to lower frequencies (typically 29-32 kHz), due to the weight of the tip and corresponding to the asymmetric loading of the tuning fork. The quality factor decreases to typical values of less than 1000. A measured resonance curve (circles) with Q = 780 is shown in the inset

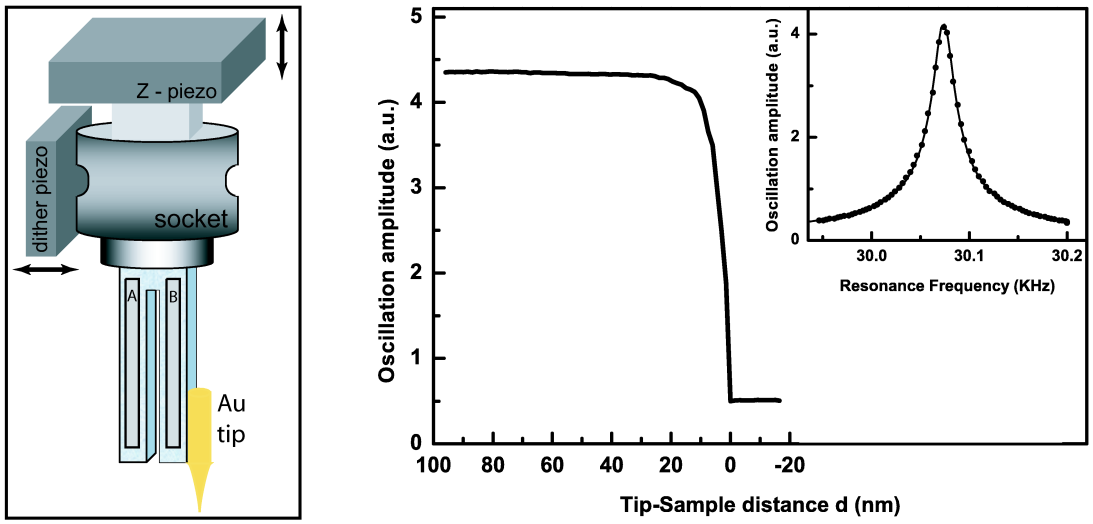

Figure 2.2: Left panel: Schematic of quartz tuning fork fixed rigidly inside a socket having the dither piezo and the z-piezo attached; on one of the tuning fork's prongs a Au tip is glued. Right panel: Typical force-distance curve for quartz tuning fork - metal tip system. The 0 distance is defined as being into the surface plane of the sample; inset: representative resonance curve for quartz tuning force with tip, with $\omega_0 = 30.074$ KHz and Q= 780. The experimental data (circles) are fitted with a lorentzian-shaped function (line).

of the right panel of Fig. 2.2, together with a lorentzian-shape fit (solid line), according to Eq. 2.3.

The damping of the oscillation increases with increasing force between the tip and the sample. This can be seen in Fig. 2.2 (right panel) where the amplitude of the oscillation is damped to almost 0 when the tip is in physical contact with the sample. Its monotonous behavior allows for the oscillation amplitude to be used as distance control parameter.

With apex radii of the tips as small as 10 nm and hence very sensitive to any mechanical contact, the tip-sample distance control is one of the main issues in the good functioning of a s-SNOM. As in other types of scanning-probe techniques, an active feed-back loop is required. It has to keep the tip close to the sample (within few nm) while avoiding any possible contact between tip and sample surface. It also needs to allow for smooth tip approaches and respond fast enough to enable the scanning of the tip above the surface topography. For this purpose a home-built PID (Proportional/Integral/Differential) electronic feedback loop acting on a z-piezo actuator (PL055.20, Physik Instrumente GmbH, maximum displacement 2.2 μm at 100 V) is implemented. A single-channel low-voltage piezoelectric amplifier (E-660, Physik Instrumente GmbH) controls the z-piezo element. The excitation frequency and amplitude are kept constant and the amplitude response of the sensor is measured. While in feed-back, the vertical stability of the tip with respect to the sample is within 1 nm.

The sample is positioned on a small magnetic holder (7 x 7 x 2 mm) glued onto the piezo scanner. The latter is a piezoelectrically driven multi-axis (100 x 100 x 20 μm) nano-

positioning linearized stage (Piezo Flexure Stage P-517.3CL, Physik Instrumente GmbH). Its linearized movements are realized in a closed loop operation modus. This is done via a Position Servo Controller (E-509.X3, Physik Instrumente GmbH), offering a resolution of less than 1 nm. The controller unit for the scanner is a Computer Interface and Display Module (E-516 PZT, Physik Instrumente GmbH), operated from the computer via the IEEE-488 GPIB interface. The voltage amplification necessary for the piezo stages is achieved through the low voltage (0-100 V) amplifier (E-503, Physik Instrumente GmbH).

The scanner performs line scans of the x axis, and after each line scan the y axis is moved incrementally. The measurements were always performed in both forward and backward scan directions (along x axis), hereafter referred to as *trace* and *retrace*, respectively. The two-way scanning is realized in an interleaved manner, *i.e.*, each *retrace* line is acquired immediately after the corresponding line of the *trace* direction. This allows for a better interpretation of the acquired data. It also enables the discrimination between real signal change and possible drifts, noise or other signal changes random in time during the scanning.

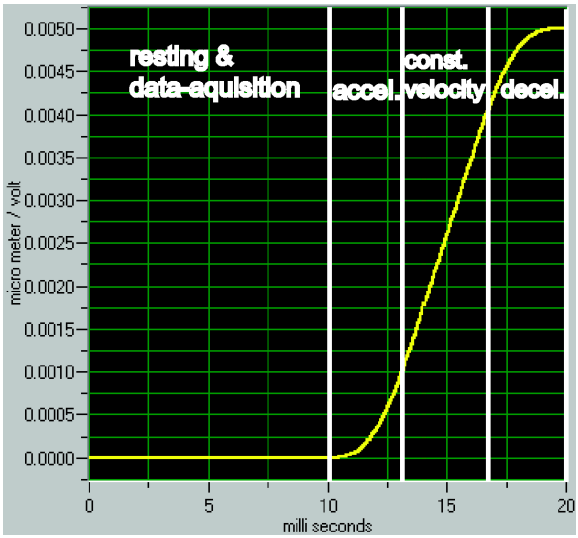

Figure 2.3: Screen-shot with the wave-like scanning step. The four regions of the motion for one step (see text) are indicated. The ordinate scale of the figure presents the scanning step in μm.

Abrupt lateral movements of the sample have to be avoided especially in the case of high topographic relief. The PID feed-back loop has to respond quickly to vertical sample variations in order to avoid physical contact between the AFM tip and the surface to allow the acquisition of an accurate topographic image. For that we implement a smooth displacement procedure of the piezo stage for each scan step. A *wave-like* movement was used for the line scans. This results in a gradual change of the sample position. In Fig. 2.3 one period – equivalent to one scan step– of the wave-like motion is displayed, for a *trace* case. The *retrace* direction motion is the reverse of the one shown here. Each step of the line scan comprises of 4 regions: the region where the stage is at rests while the optical data are acquired, the acceleration region where the stage accelerates from 0 to a constant velocity, the region with constant velocity and the deceleration region where the stage

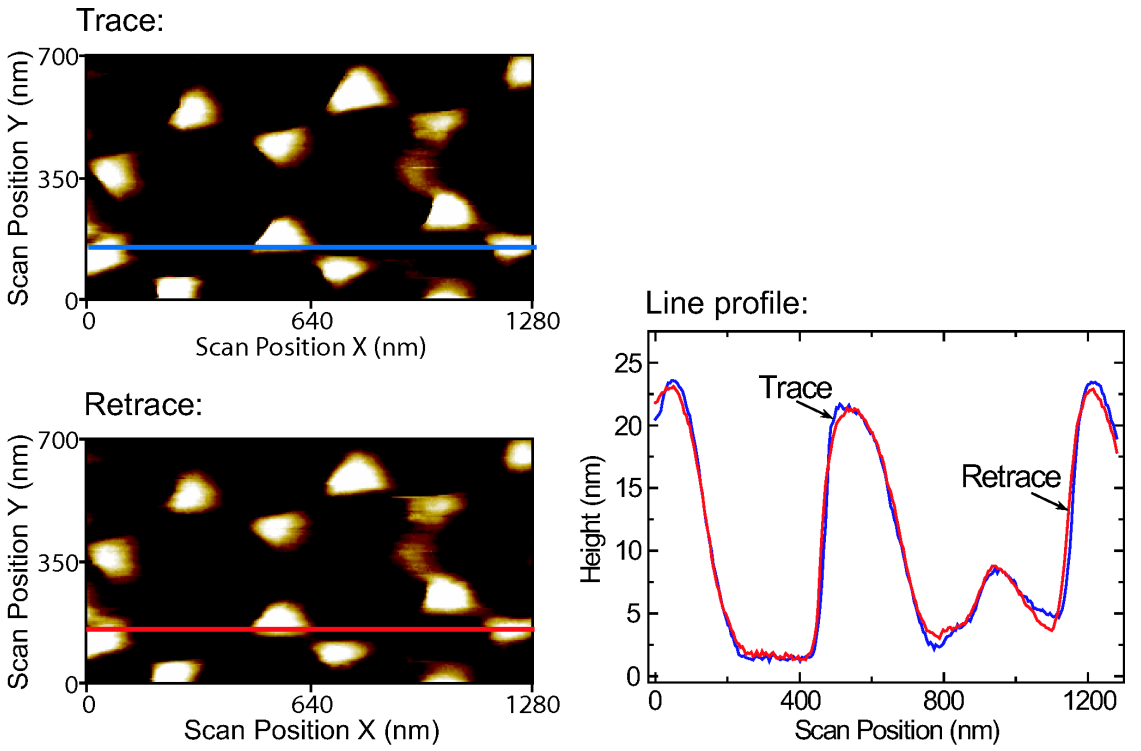

Figure 2.4: Topography scan of an Al Fischer pattern. Both *trace* and *retrace* images are shown. Line (blue and red for trace and retrace, respectively) profiles along the scanning direction (x), averaged over 5 consecutive pixels along y, are shown on the right hand side.

comes back to rest. The determining factor in choosing the scan velocity is the strength of the optical signal detected. Typically, the experiments were performed on a time-scale of 10-100 ms/step.

Due to the high sensitivity of the system with respect to the tip-sample distance, damping the low frequency vibrations coupled to the AFM from the surrounding environment (*e.g.* building vibrations) is extremely important. The AFM is situated on a optics board (Newport) which is placed on three vertical stacks composed of alternating Viton rings and aluminum plates. This suppresses the coupling of vibrations from the environment to the system. To minimize the influence of air currents the AFM is enclosed inside a plastic box. The acoustic range vibrations are damped by using an insulating foam on the inner walls of the box.

Fig. 2.4 shows a typical topographic scan obtained with our shear-force AFM. The sample is a so-called Fischer pattern, with triangular Al island on glass substrate. A gold tip with apex radius r $\sim$ 15 nm is used. Both trace and retrace images are shown. The sample is scanned with a step of 5 nm in both x and y directions, and the total area is 1280 nm x 700 nm. Thus the image comprises of 256 x 141 pixels. The images presented here are only corrected for the small tilt of the sample surface with respect to the scanning direction. The synchronized scan profiles (blue and red for trace and retrace directions, respectively)

on the right hand side of the figure correspond to the marked lines inside the images. They are averaged over five consecutive pixels on a direction perpendicular to the scanning lines. The lateral differences between the two profiles are on the order of one scan step. Vertical differences of about (1 - 2) nm are visible for a maximum height of $\sim$ 23 nm. All these together with the only minor lateral drifts of the sample with time observed, enable us to use the home-built shear-force AFM for sensitive optical near-field studies.

2.2 Electrochemical etching of metallic tips

The single most important element of the setup is the metallic tip used as scanning probe. Both the geometrical shape and the material of the tip prove to be of crucial importance for the near-field optical experiments [83], as will be discussed in Chapter 3.

Since the development of the scanning probe microscopy, many ways of obtaining sharp metal tips were developed: angle-cutting the metal wire was used in the beginning [84], then DC or AC voltage electrochemical and milling procedures were considered [52, 85, 86, 87]. For the experiments presented here, we chose a DC voltage electrochemical etching method for both tungsten and gold tips. It involves the anodic dissolution of the metal wire used as electrode [88].

In the case of the gold tips, a Au wire with a diameter of $\phi = 125$ μm (purity 99.99% , temper as drawn, Advent Research Materials Ltd.) was etched into sharp tips. As etching solution a 1:1 mixture of hydrochloric acid (HCl, aq. 37%) and ethanol (CH_3CH_2OH) was used. The main chemical reactions driving the etching process are:

$$\begin{array}{rll} Anode: & Au + 4Cl^- \longrightarrow & AuCl_4^- + 3e^- \\ Chatode: & H_3O^+ + e^- \longrightarrow & 1/2H_2 + H_2O \\ \hline & 3H_3O^+ + Au + 4Cl^- \longrightarrow & 3/2H_2 + AuCl_4^- + 3H_2O \end{array} \qquad (2.4)$$

A schematic of the electrochemical cell used is depicted in Fig. 2.5 panel a). After careful cleaning in acetone the Au wire is partially immersed ($\sim$ 2-3 mm) into the etching solution. It serves as anode for the electrical circuit. As the cathode, a platinum wire ($\phi = 0.3$ mm) circular ring with a diameter of $\sim$ 1 cm is used. It is disposed around the anode, on the surface of the solution. The etching occurs when a DC voltage difference is applied between the Au wire and the Pt ring. The voltage is provided by a DC power supply (Laboratory Power Supply, Voltcraft) and is set to a value of 2.2V, which was found to give the best tips. Under these conditions, the etching process takes a few minutes for each tip.

The surface tension of the solution causes a meniscus to form around the wire once it is placed into the electrolyte. This is shown schematically in Fig. 2.5 panel b). It is primarily the shape of the meniscus which determines the aspect ratio and overall shape of the tip [89]. The etching proceeds as a continuous necking of the Au wire, until the lower immersed wire portion falls off. The remaining upper part of the wire is used as the AFM tip. Since it still remains in the solution (under the meniscus) after the detaching of the lower part, it is

of important to break the electrical circuit as fast as possible. Further etching would result in blunt tips. A home-built fast cut-off electronic circuit can be used for that purpose. It is based on a fast 10 ns comparator (LT1016, Linear Technology) followed by a high speed MOSFET driver (EL7104, Intersil Corporation).

The vertical alignment of the Au wire with respect to the solution surface and the centering inside the cathode are of major importance. Any deviation gives odd shapes of the tip-apex. This, together with fresh electrolyte, low vibration and air-draft free environment, are prerequisites for obtaining good tips.

A telescope (2 bi-convex achromatic lenses, f = 99.6 mm, Astromedia) with a CCD video-camera are used for a good visualization of the etching process and precise alignment of the setup. The total magnification (optical + digital) of the system is 40X.

After etching the tips are cleaned in distilled water and stored in isopropanol prior to usage, to avoid possible contamination from air.

Tips having apex radii as low as 10 nm are obtained with this procedure, as characterized by electron microscopy (JSM-6400 F Scanning Microscope, JEOL). Only those tips with a smooth surface and apex radii lower than 30 nm are used for the optical experiments.

The same etching procedure is used for the tungsten tips. A W wire (ϕ = 200 μm) is immersed for 2-3 mm in 2M KOH as electrolyte. The counter electrode is a stainless-steal cylinder centered around the W wire and a 3V DC bias voltage is used.

Representative micrographs of obtained Au and W tips are displayed in Fig. 2.6. The left hand side panels show the apex area of the tips where the smooth surface and the small radius can be seen. The right hand side shows a larger region of the tip-shaft. Panels a) and b) show Au tips with radii r $\sim$ 10 - 15 nm. The W tip in panel c) of the figure has a

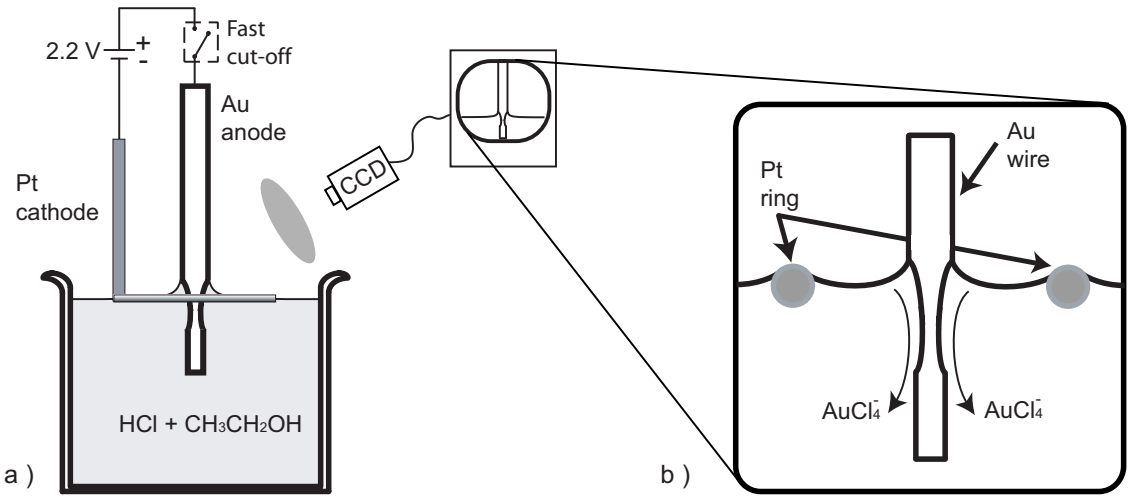

Figure 2.5: Schematics of the electrochemical etching cell. a) The Au wire (anode) is immersed partially into the solution. It is surrounded by the Pt cathode-ring. The etching process is monitored using a video-camera. b) The etching take place just underneath the meniscus formed around the Au-wire. The downward flow of $AuCl_4^-$ is showed. For W-tips a similar procedure is used (see text).

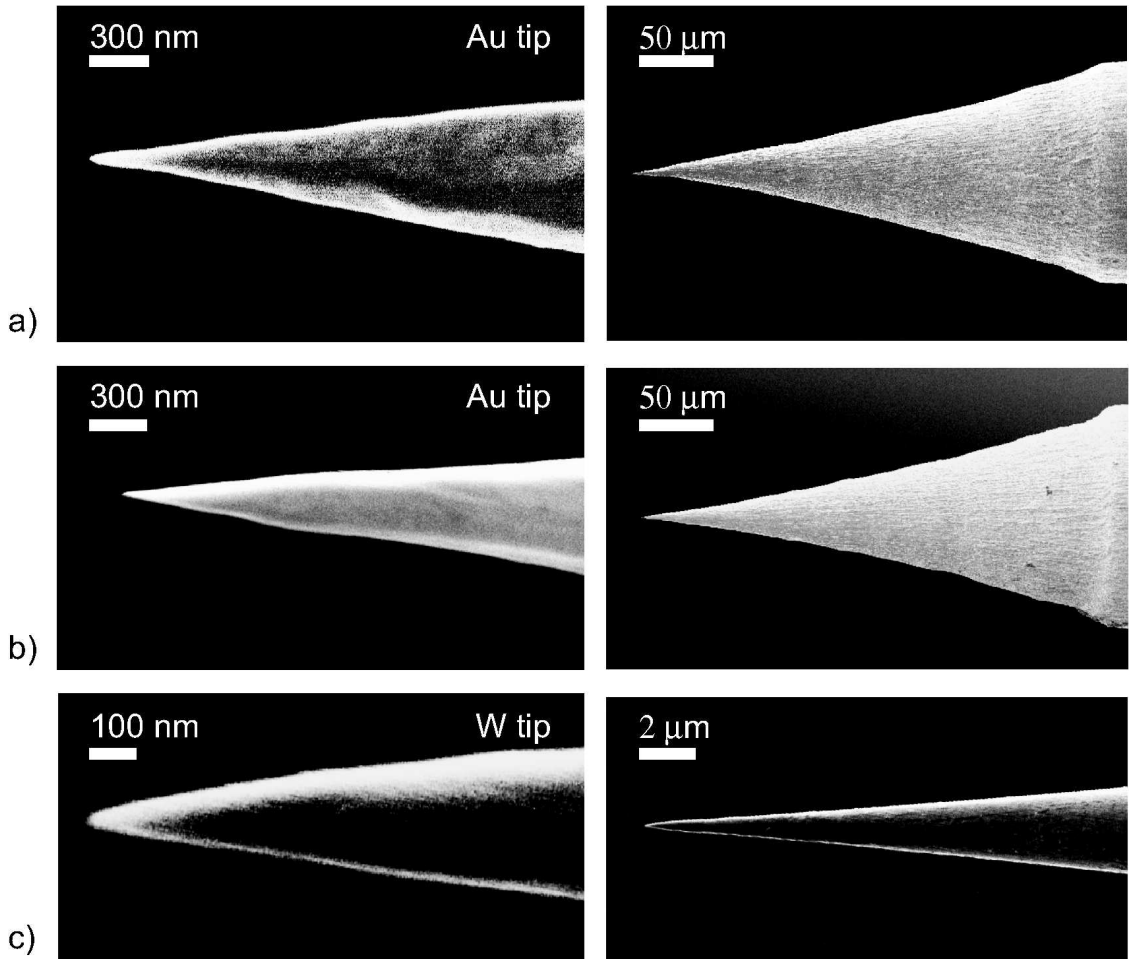

Figure 2.6: Electron-microscope micrographs of electrochemically etched tips. Left panel displays the tip apex zoom-in region, of the tips shown on the right. a) and b) Au tips, c) W tip.

radius r $\sim$ 15 nm.

2.3 Illumination sources and optical signal detection

The apertureless scanning near-field optical experiments were performed in a back-scattering geometry. The incident laser light is focused onto the tip-sample gap by means of a long working distance microscope objective with the optical axis at an angle $\theta \cong 70^\circ$ with respect to the tip axis direction as shown in Fig. 2.1. The back-scattered optical signal is acquired by the same objective and then spectrally filtered and detected.

The nonlinear optical studies were realized using a passively Kerr-lens mode-locked (ML) Titanium Sapphire Oscillator (Femtosource, Femtolasers Produktion GmbH) [90, 91]. It is pumped by a an intra-cavity doubled Nd^{3+}:YVO_4 laser (Millennia Vs, Spectra Physics). The pulse duration was measured using interferometric autocorrelation and found to be

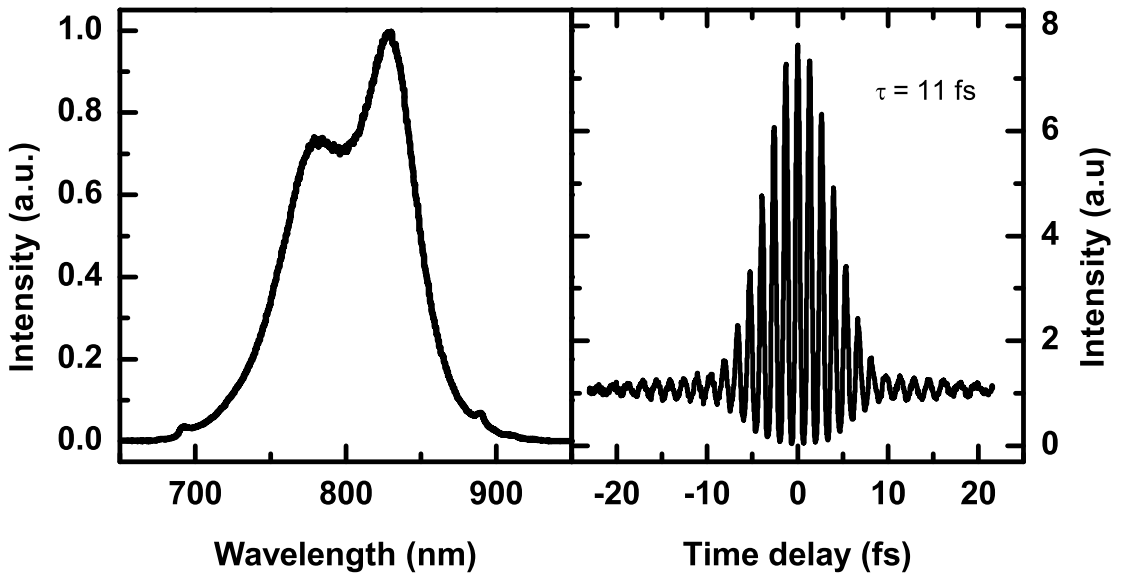

Figure 2.7: Left panel: Spectrum of the Titanium-Sapphire laser working in mode-locked regime. The center wavelength is $\lambda \approx 805$ nm and the full width at half maximum is FWHM=105 nm. Right panel: Interferometric autocorrelation of the laser pulse after the oscillator.

τ=11 fs. The pulses have a repetition rate of 78 MHz. The spectrum is centered around λ = 805 nm with the full width at half maximum FWHM = 105 nm (Fig. 2.7). The maximum power in the mode-locked regime was P_{ML} = 405 mW (corresponding to a pulse energy of 5.2 nJ) at a pump power of P_{pump}= 4.04 W. In continuous wave (CW) operation, the maximum output power for the same pump power was P_{CW}=760 mW.

Studies using ultrafast laser sources require dispersion control because of the large bandwidth of the short pulses [92]. In order to keep the pulse short, mainly reflective optics was employed, except for the thin air-spaced half-lambda waveplate (B. Halle Nachfl. GmbH). After being steered by the reflective elements the beam was focused onto the tip-sample gap using a microscope objective (Nikon CF Plan 20x, ∞/0 Epi SLWD, N.A=0.35, W.D.=20.5 mm).

To account for the severe group delay dispersion (GDD > 2000 fs^2) introduced by the microscope objective, a specially designed (Femtolasers Produktion GmbH) dispersion precompensator was used (shown in Fig. 2.1). It consists of a pair of dispersive "chirped" mirrors and a pair of thin fused-silica optical wedges (minimum thickness 200 μm, opening angle 2°48′). The laser beam is reflected five times onto the surface of each mirror before passing through the two wedges. Each reflex introduces a negative dispersion of -225 fs^2. The wedges account for fine adjustments of the dispersion [93, 94].

Without the precompensator, the pulse duration in the focus of the microscope objective is few hundred femtoseconds. With compensation, the pulse duration was τ = 13 fs. For this measurement a dispersion-balanced Michelson interferometer was inserted into the beam path, as shown in Fig. 2.8. The second order interferometric autocorrelation was recorded with a two-photon photodiode (GaAsP) placed in the focal plane of the microscope objective

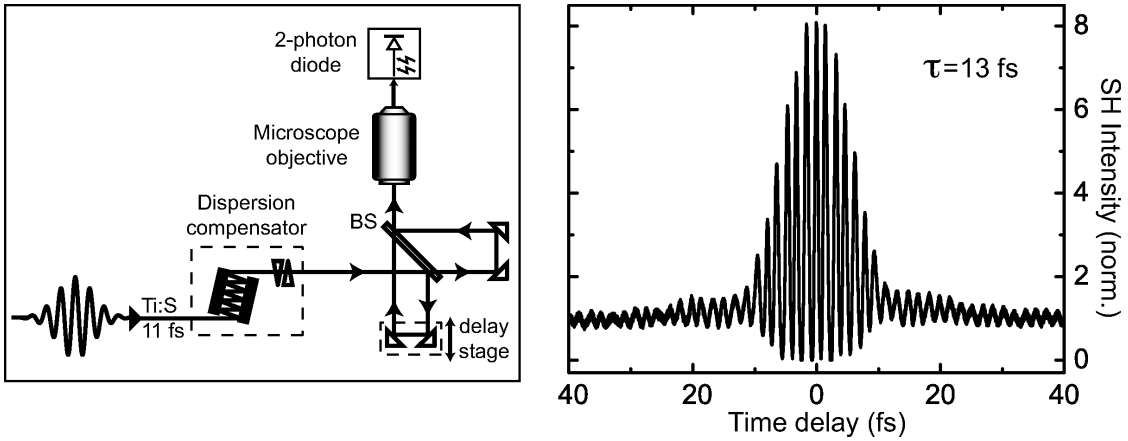

Figure 2.8: Interferometric autocorrelation measurement of the laser pulse into the focal plane of the microscope objective after passing through the specially designed dispersion pre-compensator. Left panel: scheme of the experimental setup. Right panel: measured second order interferometric autocorrelation of the laser pulse in the focus of the microscope objective.

(2-Photon Femtometer, Femtolasers Produktion GmbH). The photodiode has the cut-off wavelength $\lambda = 550$ nm and is sensitive within the range (600 - 1100) nm.

For detecting the optical signal originating from the tip-sample near-field region, two schemes are employed. One is making use of an avalanche photodiode (APD) (SPCM-200, EG&G) followed by a single photon counter (SR400 Two Channel Gated Photon Counter, Stanford Research Systems). After being appropriately filtered, the back-scattered optical response is focused onto the surface of the APD. The photon counter can be operated both in gated and non-gated modes and the two acquisition modes are discussed in detail with the experiments in the corresponding chapters.

For spectroscopic studies, the optical signal is filtered and then focused into multimode optical fiber (BFH22-200-CUSTOM, Thorlabs GmbH) with a numerical aperture NA=0.22, and a transmission T $\geq$ 99% throughout the used spectral range. The fiber directs the signal onto the entrance slit of an imaging spectrometer (Spectra Pro 500i, Ropers Scientific), (see Fig. 2.1). The latter has a focal length of f=500 mm with three interchanging diffracting gratings: 150, 1200 and 1800 groves/mm, respectively. An important point into choosing the appropriate grating for each experiment is the intensity level of the detected signal. Most of the described experiments were performed using the 150 groves/mm grating. The dispersed light is then imaged onto a deep depletion N_2 cooled charge coupled device (CCD) camera connected to the exit slit of the spectrometer.

To better control the focusing conditions on the tip apex, a video camera is employed after the microscope objective. The collimated beam formed by the microscope objective is focused onto the CCD chip of the camera by means of a tube lens (convex lens, f=100 mm) and then displayed on a TV monitor. In the case of the infinity corrected objective used in our experiments the magnifications specified by the manufacturers are for a nominal tube length of 200 mm. With a tube lens focal length of only 100 mm and an infinity "afocal" space (defined by parallel light beams in every azimuth between the objective and

the tube lens) of ~ 600 mm, the optical magnification[i] of the system is ~ 30X. The digital magnification is 40X, and the total magnification is then $\sim$1200X. This is also used to visualize the coarse approach of the tip to the sample surface.

With the microscope objective at a $\sim 70^\circ$ angle with respect to the sample surface-normal, it is difficult to distinguish certain regions of interest onto the sample. For that purpose, an additional color video camera (Sony XC-555, Edmund Optics) was employed. It was positioned near the sample at an angle of $\sim 30^\circ$ with respect to the surface-normal. It is used in combination with a small optical microscope (Video Lens VZM-1000, Edmund Optics) which offers an optical magnification M=8X at a working distance WD=32 mm.

[i] The calculation holds for angles between the axial and off-axial light flux which obey the small angle approximation ($\sin\alpha \simeq \alpha$), as is the case here.

3 Plasmonic light scattering from nanoscopic metal tips

The concept of apertureless near-field optical microscopy is based on a number of physical phenomena such as optical field enhancement and spatial confinement at the tip-apex, which provide the sensitivity needed for studies on the nano-scale. The optical characteristics of dielectric tips (*e.g.*, tapered glass fiber) have intensely been investigated because of their importance as probes for scanning near-field microscopy (SNOM) [13]. In contrast, the optical properties of metallic tips have received comparatively little attention.

In the present chapter, the spectral characteristics of elastic light scattering from individual sharp metal tips are investigated. Their details are correlated with the tip structural and material properties and the results are discussed in the context of the local plasmonic resonant behavior.

3.1 Metallic tips as optical nano-antennas

It is known from microwave engineering that far-field radiation couples effectively to a receiver if the latter is attached across the feed-gap terminals of an antenna [34]. When the two are impedance-matched, all of the incident power will couple to the receiver. Therefore, the design of an optical near-field probe can be viewed a classical antenna problem.

Antennas are structures designed for radiating or receiving electromagnetic waves and concomitant energy transfer to or from a confined volume [95]. The radio-wave antenna converts radiation into a local oscillation in its so called *feed-gap*, the space between the antenna arms. This *near-field* region comprises of two zones: the reactive zone is the closest to the antenna and up to one wavelength λ away from it. Here, the field is highly concentrated and spatially bound to medium, strongly enhanced over the radiated far-field intensity. The near-field radiating zone extends from the reactive boundary to a distance defined as $2D^2/\lambda$, where D is the antenna dimension. Here, the average energy density remains fairly constant at different distances from the antenna [96].

From a theoretical point of view, the simplest antenna is the *dipole antenna* [97]. Practically, it is realized as a half-wave ($\lambda/2$) dipole antenna formed by two conductors whose total length is half the wavelength as schematically depicted in Fig. 3.1 a). For a sinusoidal electrical current traversing the antenna arms, the maximal amplitude of the current I(z) is at the antenna center.

The size of half-wave dipole can be reduced by replacing the lower half by conducting ground (Figure 3.1 b), resulting in a quarter wave ($\lambda/4$) antenna (first introduced by Guglielmo Marconi [98]). The conducting ground acts as a mirror and the system radiates only in

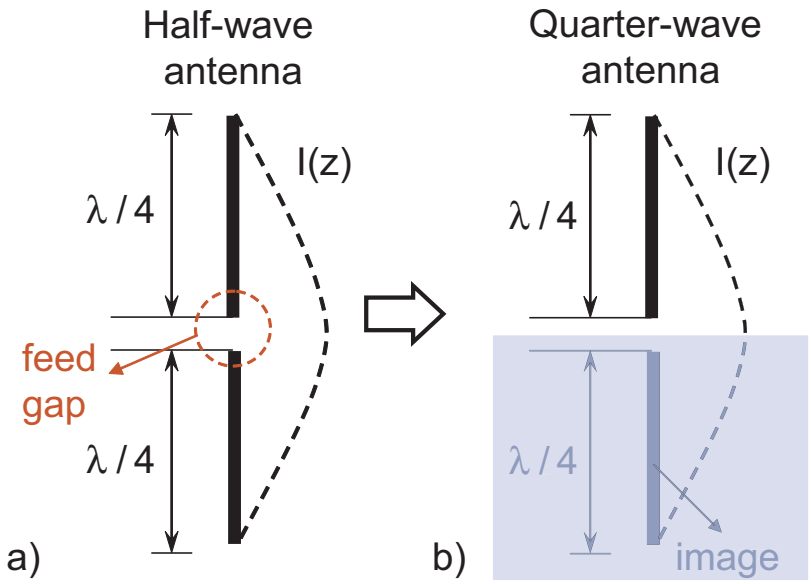

Figure 3.1: a) Schematics of a half-wavelength dipole antenna. b) Schematics of a quarter wave dipole antenna. One antenna arm is replaced by a ground plane. The current distribution for both antennae has a maximum at the center.

the upper half-space. In this region the emitted field has the same amplitude of the field radiated by a half-wave dipole fed with the same current.

Currently, much effort is devoted to scaling dimensions down to the optical regime. A molecule emitting a photon in the optical spectral range corresponds to a point dipole or, in the antenna theory language, a strongly mismatched antenna with the optical wavelength of several hundred nm and the sub-nanometer-size molecule. This situation corresponds to the bare radio wave coaxial cable [99]. In contrast, large efficiency can be obtained coupling the radiation into a matched, typically half-wave antenna structure. For example, the excitation rate of a single molecule close to an optical antenna can be strongly increased due to the local field enhancement [100]. Note that here nonradiative energy transfer to the metal could impose loss channels [101, 102].

However, whereas for radio waves, a metal can be modeled by a perfect conductor, at optical frequencies the field can penetrate the material and can be absorbed [103], with the absorption depending on the frequency of light [104]. Related interests range from an understanding of the fundamental differences compared to the radio frequency range [105, 106] to the design and manufacturing of sophisticated device structures [107, 108, 109, 110, 111, 112, 113] for guiding and switching light, optical computing and chemical and biological sensor applications [114, 115].

Resonant optical antennas combine (i) field line concentration at a local shape singularity, that is, a gap [38, 27], (ii) optimum impedance matching to freely propagating waves, and (iii) resonant collective oscillations (plasmons) of the free electron gas in the antenna arms [116, 117]. One of the most widely used structures in this respect is the tapered tip used as sensor in scanning probe microscopy.

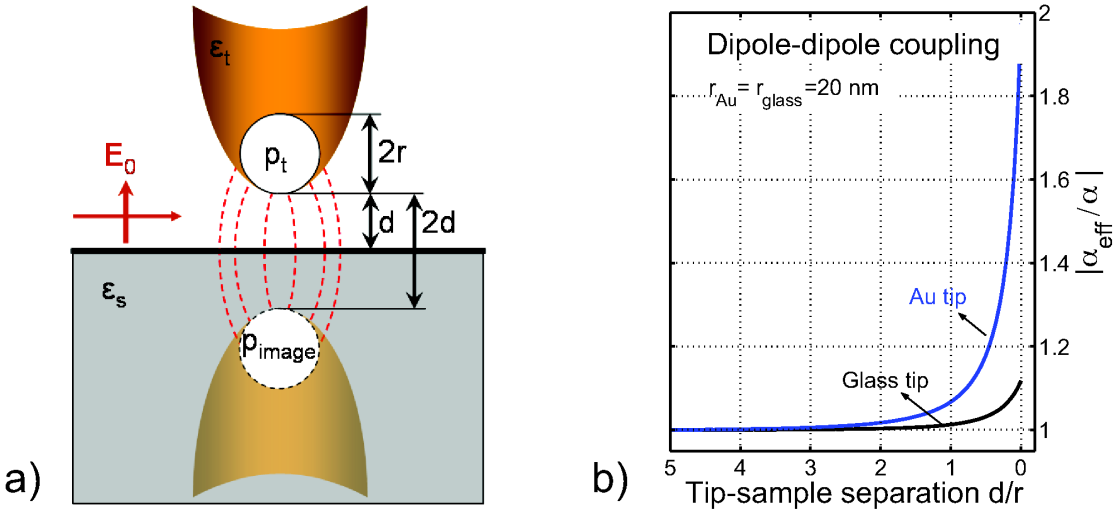

Figure 3.2: a) Schematics of the dipole-dipole model to describe the tip-sample coupling. b) $|\alpha_{eff}/\alpha|$ versus tip-sample separation d/r for Au tip (blue) and glass tip (black). Both have the apex radius $r = 20$ nm and approach a gold sample.

3.1.1 The dipole-dipole model

Using a simplified model, the tip apex can be treated as a homogeneous sphere of radius r and dielectric function $\epsilon_t(\omega)$ illuminated by a plane wave $\mathbf{E}_0(\omega)$ (wave vector $\mathbf{k}$) polarized along the tip axis [118]. Since the apex has a small size compared with the wavelength of the incident field, the local field distribution can be considered in the quasi-static approximation. Thus retardation effects are ignored and all the fields in the region of the sphere oscillate in phase. Note that the optical wavelength dependance is explicitly taken into account considering the frequency dependence of the dielectric function of the tip material. The external field $\mathbf{E}_0(\omega)$ induces a dipole $\mathbf{p}_t$ in the tip according to [39]:

$$\mathbf{p}_{sphere}(\omega) = \alpha(\omega)\ \mathbf{E}_0(\omega) \tag{3.1}$$

where α is the quasi-static polarizability. For a small polarizable sphere,

$$\alpha(\omega) = 4\pi r^3 \frac{\epsilon_t(\omega) - \epsilon_m}{\epsilon_t(\omega) + 2\epsilon_m} \tag{3.2}$$

with ϵ_m the dielectric constant of the surrounding medium. The field created by the sphere is the same as the one of a point-dipole situated in its center.

If the sphere is brought near a ground plane - the surface of the sample used in s-SNOM experiments (schematics shown in Figure 3.2 a), it experiences a primary field $\mathbf{E}_p$ which is the sum of the incident field $\mathbf{E}_0$ and the Fresnel field reflected by the surface [119]. The dipole in the tip is now $\mathbf{p}_t(\omega) = \alpha(\omega)\mathbf{E}_p(\omega)$.

The tip-sample distance is d, and the sample is characterized by the dielectric function $\epsilon_s(\omega)$. The dipole model for the tip can be extended to account for the presence of the sample by considering the image dipole [120]. This is located at a distance $(d + r)$ inside

the sample. In the electrostatic limit we only need to solve Laplace's equation to describe the system [33].

The field above the surface can be written as a superposition of the fields of two dipoles: the one of the tip dipole $\mathbf{p}_t$, and the one of an image dipole $\mathbf{p}_{image}$. The image dipole moment writes:

$$\mathbf{p}_{image} = \frac{\epsilon_s(\omega) - 1}{\epsilon_s(\omega) + 1}\mathbf{p}_t \tag{3.3}$$

with

$$\frac{\epsilon_s(\omega) - 1}{\epsilon_s(\omega) + 1} = \beta \tag{3.4}$$

being the quasi-static Fresnel reflection coefficient. The total induced dipole moment in the tip takes the form:

$$\mathbf{p} = \alpha[\mathbf{E}_p + \mathbf{E}_{image}(2r + 2d)] = \alpha_{eff}\mathbf{E}_p \tag{3.5}$$

with α_{eff} the effective polarizability of the coupled tip-sample system:

$$\alpha_{eff} = \alpha\left(1 - \frac{\alpha\beta}{16\pi(r + d)^3}\right)^{-1} \tag{3.6}$$

The mutual polarization of the tip and the sample thus enhances the optical near-field $E_{nf} \propto \alpha_{eff}E_p$ which is subsequently scattered by the tip [121, 122].

If the incident light field is polarized perpendicular to the tip axis, the dipole $\mathbf{p}_t$ is oriented parallel to the sample surface. Correspondingly, the image dipole $\mathbf{p}_{image}$ points in the opposite direction, leading to a partial cancellation of the two [10].

The distance dependence of the tip-sample optical coupling for an incident field polarized along the tip axis is shown in Fig.3.2 b) for two selected cases: Au tip (blue) and glass tip (black). Both tips considered have the apex radii $r = 20$ nm and approach a gold sample. The calculated absolute value of $|\alpha_{eff}/\alpha|$ is displayed versus tip-sample separation d/r. The incoming field is polarized parallel with the tip axis and its wavelength is selected as $\lambda = 530$ nm; the dielectric constants for Au and glass are (-5.8106 + 2.1397i) and 2.37, respectively [123]. At this spectral position, the glass presents no loss. The effective polarizability α_{eff} decays rapidly with increasing tip-sample distance, at separations of $3r$ being already comparable with the polarizability α of the free sphere subject to the same incident electric field. The tip is only sensitive to the presence of the sample when the separation is on the order of the apex radius r or shorter. With the near-field at the apex decaying on the same length scale in lateral directions [120], this allows for spatial resolution in the s-SNOM experiments scaling with the apex radius. With tips as sharp as 10 nm already available, this exceeds the diffraction limit by more than one order of magnitude in the visible optical range.

As it can be seen, the magnitude of the effective polarizability is highly dependent on the tip material. For the Au tip it almost doubles due to strong coupling to the Au sample, while for the glass tip the increase is only on the order of 10% under the same conditions. In addition, as a nearly free electron metal, Au also allows for plasmonic resonant behavior, as discussed below.

Likewise, the coupling is dependent on the sample optical properties ($\epsilon_t(\omega)$, and $\epsilon_s(\omega)$, respectively). The scattering optical response resulting from the tip-sample coupling would this way allow for *e.g.*, high resolution dielectric contrast. This was already realized in a number of experiments, both for visible and infrared wavelengths [25, 118, 121, 124, 40, 125].

It has to be said that the dipole-dipole model describe only qualitatively tip-sample coupling. For a quantitative analysis more realistic models would have to be employed, to take into account effects neglected in the model presented here (*e.g.*, more realistic tip shape, quadrupole or higher-order dipole contributions, retardation effects) [119, 31, 126, 127]. In Chapter 4 of the present work the field enhancement at the apex of a hyperbolic tip is calculated in the context of the tip-enhanced Raman spectroscopic experiments. Both experimental and theoretical results of field enhancement of the metallic tip in the vicinity of a sample are published in ref. [126]. There the spatial distribution and spectral characteristics of the field generated between a Au tip and Au sample when illuminated at an angle with respect to the tip apex are calculated using a fully-3D finite-difference time-domain (FDTD) method. The length of the tip is considered, and retardation effects are included.

3.1.2 Field enhancement at the tip apex

Much experimental [27] and theoretical effort (see, *e.g.*, [105, 31, 128, 129] and references therein) has been devoted to the understanding of the local-field enhancement at sharp tips or related model structures. When we speak about field enhancement, we intrinsically refer to the interaction of electromagnetic fields with matter. This interaction is described by the electrodynamical theory based on the developments of Maxwell's theory [130, 131].

Calculation of the enhancement factor and the field distribution requires in principle an exact solution of the Maxwell equations. For particles of nanometric size – much smaller than the light wavelength – the wave character of the governing equation (the Helmholtz wave equation for the electric field vector) can be ignored and the field distribution can be derived through the solution of the Laplace equation for the electric potential with appropriate boundary conditions [132].

The field enhancement at the apex of a metal tip is due to a twofold effect. The small curvature of the structure leads to a concentration of the field lines, and thus to a nonresonant field enhancement, purely geometric in origin. This phenomenon is known in electrostatics as *the lightning rod effect*. In addition, the interaction of the electromagnetic field with the metal leads to a periodic displacement of the free electrons on the surface of the metal along the direction of the oscillating electric field. Depending on both geometrical and material properties of the tip, resonances can occur for certain frequencies. These so-called *surface plasmon resonances* are associated with strong field enhancements.

The frequency dependent complex dielectric function $\epsilon(\omega)$ of a material is defined as:

$$\epsilon(\omega) = \epsilon_0(1 + \chi) + i\sigma/\omega \tag{3.7}$$

with ϵ_0 the dielectric permittivity of the vacuum and the phenomenological coefficients χ and σ being the electric susceptibility and conductivity, respectively [103].

For metals, a simple and efficient phenomenological model was developed by Drude and completed by Somerfeld with corrections based on the Pauli exclusion principle. According to this so-called free electron model, many properties of metallic materials can be described referring to a gas (plasma) of independent, point-like electrons which move freely in between uncorrelated/random collisions (with other electrons, phonons, etc.). The average collision rate is $\gamma_0 = \tau^{-1}$, with τ the electron relaxation time. According to the Pauli exclusion principle, only the electrons near the Fermi level move independently. Band structure corrections have to be taken into account, and they are incorporated into an effective electron mass m^*, in general different from the free-electron mass m_e.

In an external electric field the electrons are accelerated in between collisions resulting in a drift motion. The frequency-dependent dielectric function $\epsilon(\omega)$ of the metal can be described as:

$$\epsilon(\omega) = 1 - \frac{\omega_p^2}{\omega(\omega + i\gamma_0)} = 1 - \frac{\omega_p^2}{\omega^2 + \gamma_0^2} + i\frac{\omega_p^2\gamma_0}{\omega(\omega^2 + \gamma_0^2)} \tag{3.8}$$

where ω is the frequency of the applied electric field. ω_p is the (bulk) plasma frequency for the metal:

$$\omega_p = \sqrt{\frac{ne^2}{\epsilon_0 m^*}} \tag{3.9}$$

with e, n and m^* the electron charge, density and effective mass, respectively.

For Au, the plasma frequency is $\omega_p = 13.8 \times 10^{15} s^{-1}$ and the average collision rate $\gamma_0 = 1.075 \times 10^{14} s^{-1}$ [10], which results in a negative real part of the dielectric function over the visible optical wavelength range (Fig. 3.14). One consequence of this is the small penetration depth - skin depth - of the light inside Au since the negative dielectric constant leads to a strong imaginary part of the refraction index $n = \sqrt{\epsilon}$. The imaginary part of ϵ describes the energy dissipation associated with the electron motion in the metal.

It has to be noted that for a correct description of the optical properties in metals in the UV-Vis range of the frequency range, the Drude-Somerfeld model has to be supplemented with the response of bound electrons. This is because higher-energy photons can also promote electrons of lower-lying bands into the conduction band. In Au - and noble metals in general - the electrons responsible for these interband transitions originate in completely filled d-bands situated close to the Fermi level.

Longitudinal density fluctuations (plasma oscillations) can be excited and propagate through the volume of the metal [133]. The eigenmodes of collective oscillations of the electrons in metal are described in terms of quasiparticles called *plasmon polaritons*, a hybrid of the electron density oscillations in the metal (plasmons) coupled with the electromagnetic field (polaritons), in the following abbreviated as *plasmons*. The boundary conditions for electromagnetic fields lead to different appearance conditions for plasmons in bulk material, on the metal-dielectric interface and for small metal particles.

By definition, surface plasmons are the quanta of surface-charge-density oscillations. They are electromagnetic modes bound to a metal-dielectric interface, involving charges in the metal and electromagnetic fields in both media. The surface plasmons behave as waves propagating along the surface and the field intensity falls off exponentially in both metallic

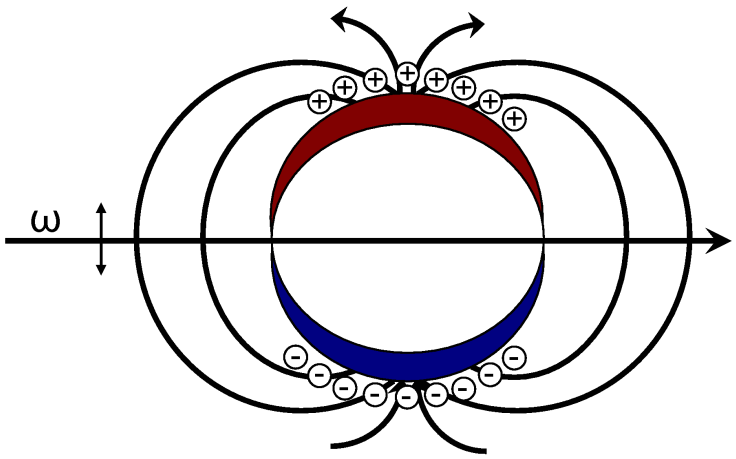

Figure 3.3: Particle plasmon excited by an external field of angular frequency ω

and dielectric media.

One of the important results obtained for plasmons at a flat metal-dielectric interface is the dispersion relation between the wave vector along the propagation direction along the interface $k_{||}$ and the frequency ω:

$$k_{||}^2 = \frac{\epsilon_m \epsilon_d}{\epsilon_m + \epsilon_d} \frac{\omega^2}{c^2} \tag{3.10}$$

where ϵ_m and ϵ_d are the dielectric functions of the metal and dielectric, respectively, and c is the speed of light in vacuum [133]. The ratio $\omega/c = k_{ph}$ gives the momentum of the incident photon.

As long as the dielectric function of the metal is negative, the momentum of surface plasmons is larger than the one of plane waves propagating in vacuum (Eq. 3.10). Therefore, in order to excite surface plasmons, additional momentum is required. This is achieved in practice using nanostructured metals such as 1D and 2D gratings [134], rough metal films [135], arrays of subwavelength sized holes [136, 137], or letting the incident light pass through a high refractive index medium (*e.g.*, prism) [133].

In the case of metallic nanoparticles, we can speak about *particle plasmons*. Upon interaction with the incident light field, the conduction electrons are shifted collectively with respect to the fixed positive charge of the lattice ions (Fig. 3.3). Consequently, a charge separation is built which leads to the appearance of a restoring force.

The latter in turn can rise to specific particle plasmon resonances depending on the geometry of the particle and the frequency of the incident field. In particles of suitable shape, extreme local charge accumulations can occur which are accompanied by strongly enhanced optical fields [10].

The scattering and absorption of light by small - relative to the light wavelength - particles was first described by Lord Rayleigh. His approach is based on a quasi-static model, where the retardation effects due to field propagation are neglected. For a small metallic

sphere and with dielectric constant relative to the embedding medium $\epsilon_r = \epsilon_r' + i\epsilon_r''$, the polarizability α can be written according to the Clausius-Mossotti relation (see also Eq. 3.1):

$$\alpha = 3\epsilon_0 V \frac{\epsilon_r - 1}{\epsilon_r + 2} \tag{3.11}$$

with ϵ_0 the permittivity of the free space and V the volume of the sphere. The scattering and absorption cross-sections write [103]:

$$C_s = \frac{k^4}{6\pi}\left|\frac{\alpha}{\epsilon_0}\right|^2 = \frac{k^4}{6\pi}(3V)^2\frac{(\epsilon_r' - 1)^2 + \epsilon_r''^2}{(\epsilon_r' + 2)^2 + \epsilon_r''^2} \tag{3.12}$$

$$C_a = kIm\left(\frac{\alpha}{\epsilon_0}\right) = 3kV\frac{3\epsilon_r''}{(\epsilon_r' + 2)^2 + \epsilon_r''^2} \tag{3.13}$$

with $k = 2\pi/\lambda$ the wavenumber of the external light field. The condition for a plasmon resonance is fulfilled for the frequency where $\epsilon_r' = -2$.

The Rayleigh model is limited to particles much smaller than the wavelength of the incident light field. For an exact electrodynamical treatment of the general case of a sphere of arbitrary radius r subject to an external homogeneous field one has to resort to the Mie treatment [103]. Defining the scattering efficiency (Q_s) as the ratio between the scattering cross-section (C_s) and the geometrical cross-section of the sphere (πr^2), the Mie theory gives:

$$Q_s^{(n)} = \frac{2}{x^2}(2n+1)\left(|a_n|^2 + |b_n|^2\right) \tag{3.14}$$

with n the multipole number in the multipole extension. $x = kr$ and a_n and b_n are the Mie coefficients:

$$a_n = \frac{m\Psi_n(mx)\Psi'(x) - \Psi_n(x)\Psi'(mx)}{m\Psi_n(mx)\xi'(x) - \xi_n(x)\Psi'(mx)} \tag{3.15}$$

$$b_n = \frac{\Psi_n(mx)\Psi'(x) - m\Psi_n(x)\Psi'(mx)}{\Psi_n(mx)\xi'(x) - m\xi_n(x)\Psi'(mx)} \tag{3.16}$$

where $m = \sqrt{\epsilon_r}$ and Ψ_n, ξ_n are the Riccati-Bessel functions [103].

For non-spherical particles, the spectral position of the plasmon resonance depends mainly on the structure size and shape, the dielectric properties of the material and the surrounding medium, and the polarization state of the incident light [138]. These elementary electronic excitations have been the subject of extensive research, both fundamental and with view to applications [139]. The particle plasmon excitation is accompanied by a strongly localized field enhancement around the nanostructure.

Fig. 3.4 shows the spectral profile of the scattering intensity observed from a spherical Au nanoparticle of ∼80 nm diameter. A very pronounced plasmon resonance is present, with the peak at λ=565 nm (2.19 eV). Together with the experimental values (squares) the calculation for the scattering using the Rayleigh (dashed line) and Mie (solid line) formalisms is presented. The bulk values for the dielectric functions given in in Ref. [123] are used throughout this work and for all considered materials. Fig. 3.14 left panel displays both real and imaginary parts of the dielectric function for Au in the (400 - 1000) nm spectral region. With Rayleigh calculation not taking into account the diameter of the

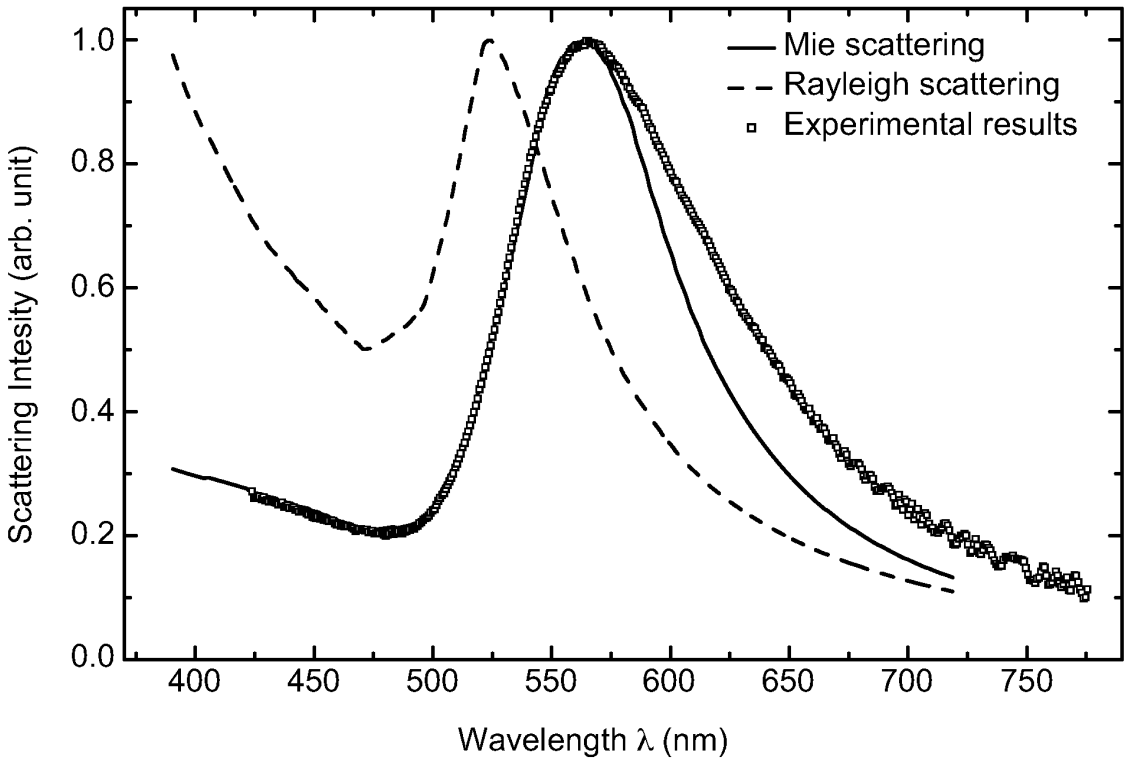

Figure 3.4: Scattering intensity of spherical Au nanoparticle with ∼80 nm diameter, showing plasmon resonance at λ=565 nm (2.19 eV). Experimental values (squares) together with the calculations using the Rayleigh (dashed line) and Mie (solid line) formalisms are displayed.

particles, the resonance peak (λ=524 nm) is blue shifted with respect to the experimental value. The Mie formalism accounts for the real dimensions of the particle, and the peak overlaps with the experimental one. The resonance broadening observed in the experimental data with respect to the theoretical prediction is due to radiation damping [140, 141].

3.2 Experimental

The spectral and polarization characteristics of the light scattering from individual sharp metal tips is investigated. In our experiment we use dark-field scattering spectroscopy. The evanescent wave based on frustrated total internal reflection at a dielectric interface serves as light source to selectively illuminate the tip-end only.

3.2.1 Frustrated total internal reflection (FTIR)

At the end of the 17^{th} century Sir Isaac Newton used a prism to "bend" the incident light by means of total internal reflection (TIR) [15]. During the experiment, he brought a convex lens in contact with the prism surface. To his surprise, light came through the prism base on an area much larger than the physical contact area between the two glass pieces. He

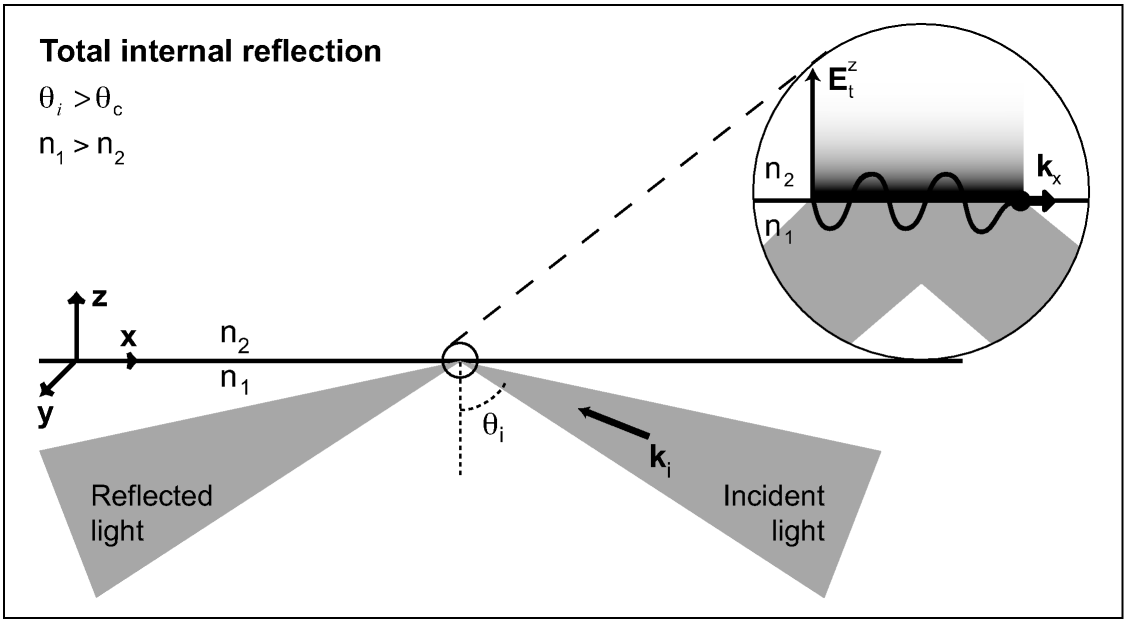

Figure 3.5: Total internal reflection at the interface between two media with formation of evanescent waves. The light is incident from the optically denser medium n_1 at an angle $\theta_i > \theta_c$.

discovered the *evanescent electromagnetic fields* [i], fields that decay exponentially on a lengthscale given by a few wavelengths.

When light impinges on the interface between two media (with refraction indexes n_1 and n_2, respectively), it is partly transmitted into the second medium and partly reflected back into the first. The angle of incidence θ_i is defined as the angle between the propagation vector $\mathbf{k}_i$ of the incoming light and the surface normal $\mathbf{n}$, and analogous the angle of transmittance θ_t is the angle between the propagation vector $\mathbf{k}_t$ of the transmitted beam and the surface normal. If the first medium is optically denser than the second one (*i.e.*, $n_1 > n_2$) and the angle of incidence (θ_i) exceeds a critical angle (θ_c), total internal reflection occurs. The critical angle is deduced from the Snell-Descartes relation:

$$n_1 \cdot \sin(\theta_i) = n_2 \cdot \sin(\theta_t), \tag{3.17}$$

when $\theta_t = 90°$:

$$\theta_c = \arcsin\left(\frac{n_2}{n_1}\right) \tag{3.18}$$

33 If the incident angle is larger than θ_c, we get:

$$\cos\theta_t = \pm i\sqrt{\sin^2\theta_i \frac{n_1^2}{n_2^2} - 1} \tag{3.19}$$

As depicted in Fig. 3.5 the interface between the two media lies into the (xy) plane, with

[i] The etymology of the word *evanescent* originates from the Latin verb *evanescere*, meaning "tending to vanish like vapor".

the z direction pointing away from the optically denser medium (n_1). According to the boundary conditions imposed by Maxwell's equations, the tangential component of the electric field has to be continuous across the interface [4].

Considering an infinite plane wave as incident light

$$\vec{E}_i = \vec{E}_i^0 \cdot e^{i(\vec{k}\cdot\vec{r}-\omega t)}, \tag{3.20}$$

with ω the angular frequency, $\vec{E}_i^0$ the amplitude of the electric field and $\vec{k}$ the propagation vector. We then obtain for the total transmitted electric field:

$$\vec{E}_t = \vec{E}_t^0 \cdot \exp(i\omega t) \exp\left(i\frac{x\sin(\theta_i)}{v_1}\right) \exp\left(\mp\frac{\omega z}{v_2}\sqrt{\sin^2\theta_i \frac{n_1^2}{n_2^2} - 1}\right) \tag{3.21}$$

with $\vec{E}_t^0$ the amplitude of the transmitted field. $v_1 = c/n_1$ and $v_2 = c/n_2$ are the velocities of light into the first (n_1) and the second (n_2) media, respectively. Eq. 3.21 describes the evanescent field, a transmitted wave propagating along the x direction, varying exponentially on the z direction and having the same frequency as the incident one [142, 143].

A penetration depth d_p of the evanescent field can be defined as being the distance along the z axis inside the rarer medium on which the electric field intensity decreases by a factor of e^{-1} [144, 145]:

$$d_p = \frac{c}{\omega\sqrt{n_1^2 \sin^2\theta_i - n_2^2}} \tag{3.22}$$

If the total internal reflection takes place at a glass-air interface, and the incident light is in the visible spectral range, the penetration depth is on the order of few hundred nanometers [146]. For the case of an infinitely large second medium (n_2), only the minus sign in the argument of the second exponential term of Eq. 3.21 can be considered, since otherwise the amplitude would increase exponentially with z.

If the rarer medium is limited by a third denser medium ($n_3 > n_2$), both two terms must be taken into account. In this case, the total internal reflection is *frustrated* (FTIR), a term coined by Leurgans and Turner [147]. Under these conditions, the decay of the frustrated evanescent field does not follow an exponential behavior (see inset of Fig. 3.6). Close to the $n_1 - n_2$ interface, the curve bends, so that when meeting the interface its slope is 0 [148]. For a more in depth mathematical analysis, the reader is referred to [145, 149] and references therein. In analogy with the the quantum mechanical concept of tunneling - energy barrier penetration [150, 151, 152] - FTIR is often referred to as *optical tunneling* [153, 154].

The frustration of the evanescent field depends on both the optical properties and shape of the third medium [148]. A nanoscopic tip used as third medium both frustrates the evanescent field and it scatters the frustrated distribution. For gold as tip material, a plasmon resonant behavior of the scattered light is to be expected in the visible range [83], and its measurement is described in Sect. 3.3.

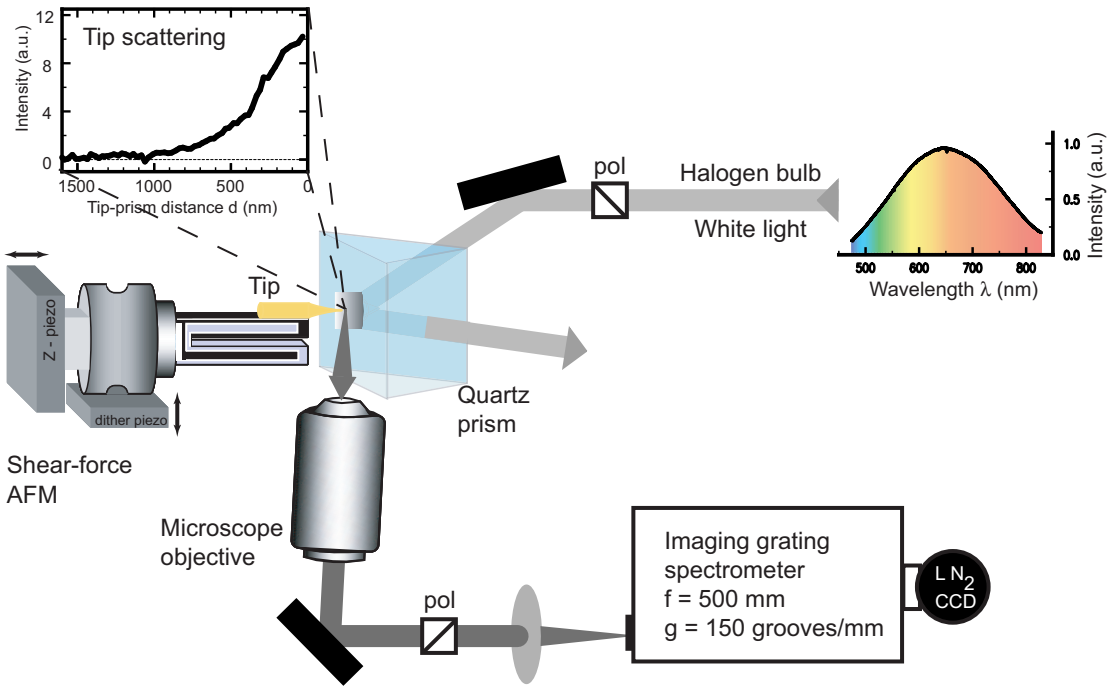

Figure 3.6: Schematics of the experimental setup. The parallel white light beam is directed onto the base of a quartz prism in a total internal reflection geometry. The scattered light is collected via a microscope objective and spectrally analyzed by a spectrometer. Inset: characteristic tip-prism distance dependence of the spectrally integrated response for a W tip.

3.2.2 Experimental arrangement

The plasmonic light tip-scattering experiments are realized in a Kretschmann configuration [155]. Here, a halogen-bulb light source (U-LH100-3, Olympus) is used for the studies concerning the spectral and spatial characteristics of the light scattered by the metallic tips.

Fig. 3.7 shows the broad white-light spectrum of the source employed. The near parallel white light beam (see Section 2.3) is directed onto the base of a quartz prism in total internal reflection conditions ($\theta_i = 45°$), as depicted in Fig. 3.6. The evanescent field of the prism-base surface is frustrated and scattered with metallic (gold and tungsten) tips and the scattered light is collected through an long working distance microscope objective (Nikon CF PLan 20x, $\infty/0$ Epi SLWD, $N.A = 0.35$, $W.D. = 20.5$ mm) and then imaged onto the entrance slit of a grating spectrometer (described in Chapter 2). The collection is perpendicular with respect to the incident plane defined by the incoming ($\mathbf{k}_i$) light beam and the normal direction on the interface ($\mathbf{n}$).

Thin film and glass polarizers with spectrally flat response function in the (480 - 830) nm range were used to control of polarization directions for both the incident and the scattered beams. The metallic nanoscopic tips used are attached to a quarts tuning fork as part of a shear force atomic force microscope (see Sect. 2.1).

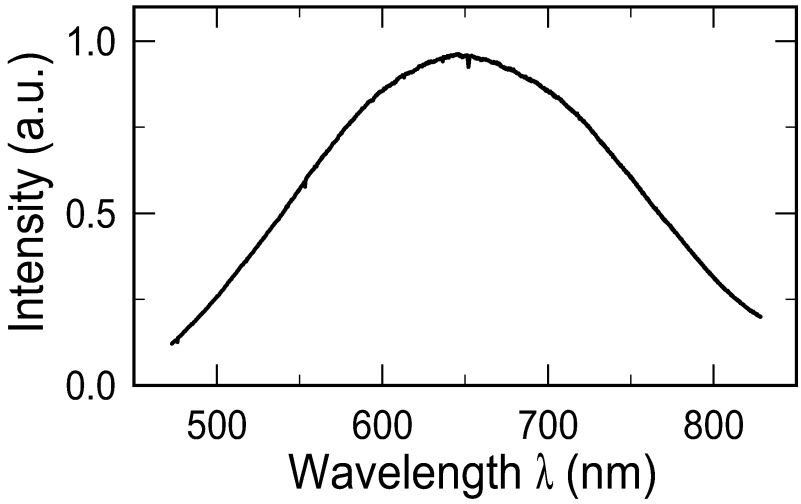

Figure 3.7: Spectrum of halogen-bulb source used as white-light for the determination of spectral and spatial characteristics of scattering from metallic tips.

3.3 Results

The light scattered by individual Au and W metal tips is measured. The excitation is limited to the near apex region of the tip, leading to a greatly reduced background compared to, *e.g.*, dark-field scattering based on far-field illumination. Both spectral and polarization dependence of the emission are measured. The results provide selection criteria for tips to be used in scattering-type near-field microscopy.

The data presented are acquired within the spectral range (480 – 830) nm. They are background corrected and normalized with respect to the excitation lamp spectrum, the spectral instrument response function and if needed different integration time periods (10 - 30 s). realized Fig. 3.8 shows the spectrally integrated scattered linear optical signal for two Au tips as a function of the tip-prism distance. The signal has its highest value on the prism base, where the evanescent field is maximum (eq. 3.21). The two tips presented display different scattering efficiencies. Although they have roughly the same apex radius (r$\sim$15 nm), the overall geometry in terms of aspect ratio is rather different, with tip I somewhat more slender than II. The higher scattering signal observed for tip II is consistent with its larger volume frustrating the evanescent field region

The decay length of the two curves is almost the same, with 428 nm and 435 nm for the I and II cases, respectively. For the tips investigated, the penetration depth measured is larger than the one for the pure evanescent field. This is in accordance with the theoretical treatment, which states that the penetration depth of the frustrated evanescent field increases with the lateral dimensions of the third medium (in our case, the metal tip) [145]. The case of an unfrustrated "pure" evanescent field can be treated in the limit of infinitely small third medium.

Similar data are obtained in the case of tungsten tips, albeit smaller scattering intensities are observed. One distance dependence of the scattering signal for a W tip is shown as

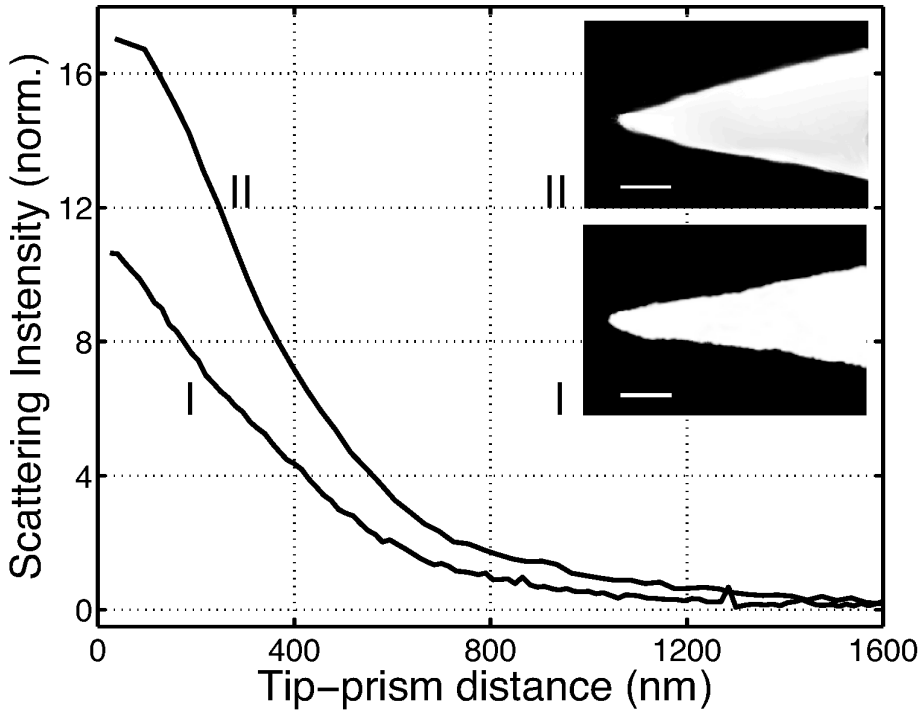

Figure 3.8: Distance dependence of the spectrally integrated response for two Au tips approaching the prism surface. The characteristic penetration-depth for a frustrated evanescent field is 428 nm and 435 nm, respectively. Inset: electron micrographs of the two tips. The scale bar represents 100 nm.

inset in Fig. 3.6.

3.3.1 Spectral dependence

Fig. 3.9 shows representative scattering spectra for different Au (a, b) and W (c, d) tips. Both the excitation and detected light fields are unpolarized. All spectra are acquired with the tips within few nanometers above the prism surface, as controlled by shear force AFM. The intensity scale is the same for all four cases, and the spectra presented are vertically displaced for a better visualization. Their zero intensity value is indicated by small horizontal lines on the left hand side of the figure, underneath each spectrum, respectively. Electron micrographs for the tip structures investigated are presented (right).

For W tips, in general, a spectrally flat optical response is observed with weak overall scattering intensities (Fig. 3.9 c). The spectral behavior is found to show little variation with tip radius and tip cone angle. This is except for the case of very slender tips where a modulation is observed, as shown in Fig. 3.9 d). The results are in agreement with the theoretical model developed, as discussed in Sect. 3.4.

In contrast, for the Au tips, the scattering intensity is strongly wavelength dependent, characteristic for a plasmon resonant behavior. Also off-resonant higher overall emission intensities are observed compared to tungsten. Both scattering intensity and spectral po-

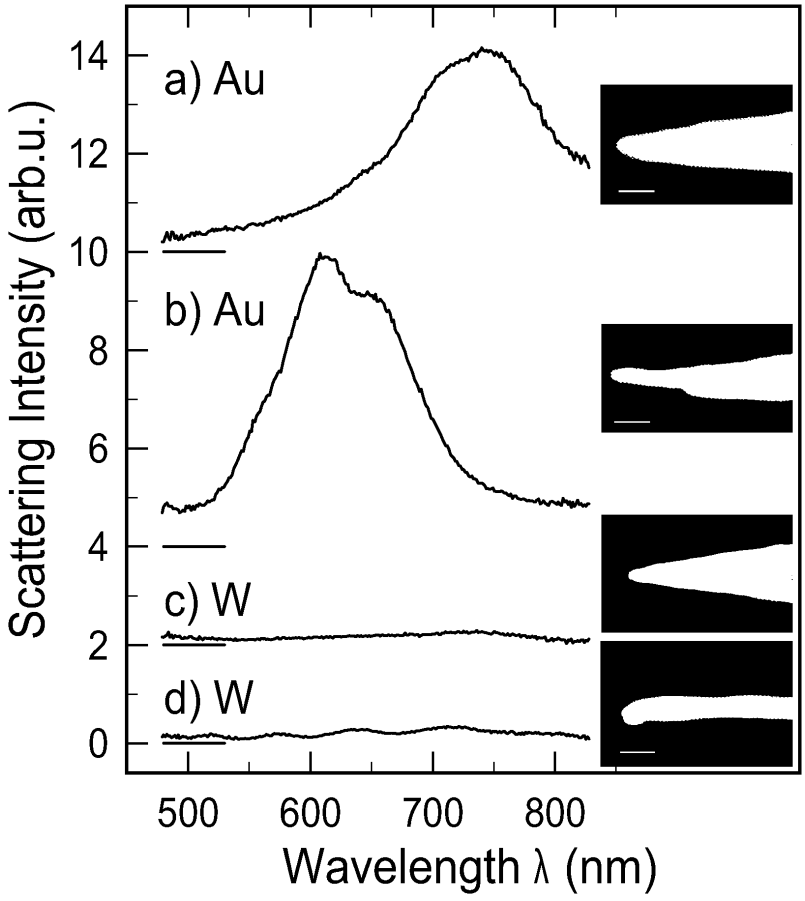

Figure 3.9: Scattering spectra for different Au and W tips. a), b) A plasmon-resonant behavior is observed for Au tips. c), d) Weaker and in general spectrally flat signal is observed in the case of W tips The spectral data are juxtaposed with the electron microscope image (inset) from the corresponding tip. The scale bar corresponds to 100 nm.

sition of the resonance are found to be very sensitive to structural details of the tips.

For regular tip shapes the resonance is characterized by one (Fig. 3.9 a) (or two, as will be discussed below) distinct spectral features. The spectral position and shape of the plasmon resonance depend sensitively on the aspect ratio of the tip.. Inhomogeneities in the geometric shape result in irregular peaks (Fig. 3.9 b). It should be noted, however, that in several instances, despite a regular tip shape the spectral response defied the characteristic signature of a plasmon resonance (not shown here). Here, throughout the spectral range accessible experimentally the scattering intensities were found to be of order of the typical off-resonant signal levels comparable to the data shown in Fig. 3.9 a) and b).

A spectrally resolved tip-prism distance dependence of the scattering intensity for a Au tip with apex radius of r$\sim$ 15 nm is shown in Fig. 3.10. Clear plasmonic resonant behavior is present, with the resonance peak centered around λ=692 nm. An increase in scattered intensity with decreasing the tip-prism distance is seen as the tip frustrates rising evanescent field intensities. The absence of a change in the spectral scattering characteristics demonstrates that the signal intensity observed at the strong resonance is dominated by

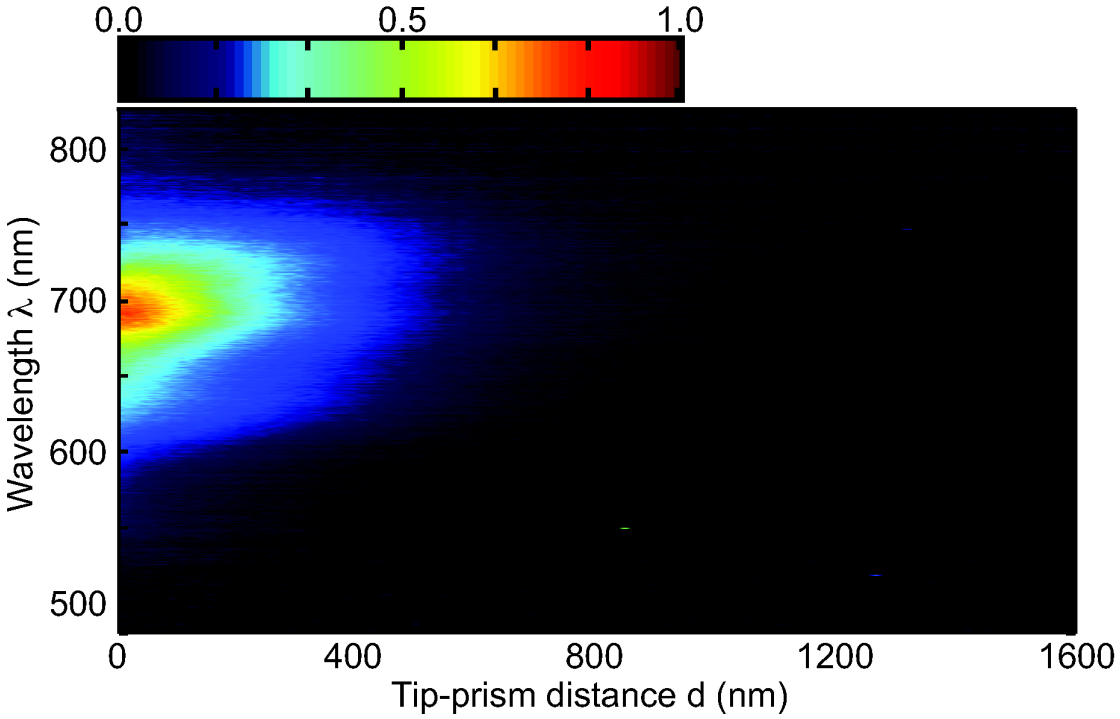

Figure 3.10: Spectrally resolved signal as Au tip approaches prism surface. Clear surface plasmon resonance centered around $\lambda = 690$ nm is present. The absence of a spectral shift associated with the tip approaching the prism surface demonstrates the tip-apex region as the origin of the resonance peak.

the tip-apex region, with the shaft contributing to a spectrally unspecific background.

3.3.2 Polarization dependence

An interesting behavior is observed by studying the polarization dependence of the tip scattering process. Here, the polarization directions are defined as parallel (p) and perpendicular (s) with respect to the plane of incidence formed by the incoming wave vector $\mathbf{k}(\omega)$ and the surface normal $\mathbf{n}$ of the prism base.

In general, stronger emission is observed for the electric field detected parallel to the tip axis (p-polarized emission) for both Au and W tips. The intensity ratio of p to s is typically found to range between 2 to 5 with a maximum value of ~ 10.

Fig. 3.11 a) displays the polarization dependence of the scattering intensity in the case of a gold tip with slightly irregular shape in the axial direction [ii]. This gives rise to featured plasmon resonance which nearly vanishes detecting polarized perpendicular to the tip axis (*i.e.*, s-polarized). For gold tips in general, the difference in scattering intensity between the two polarization states is most pronounced at the plasmon resonance with only small to

[ii] All data presented here are normalized with respect to the difference in pump field intensities for the evanescent electric field components oriented $\perp$ and $\parallel$ to prism surface.

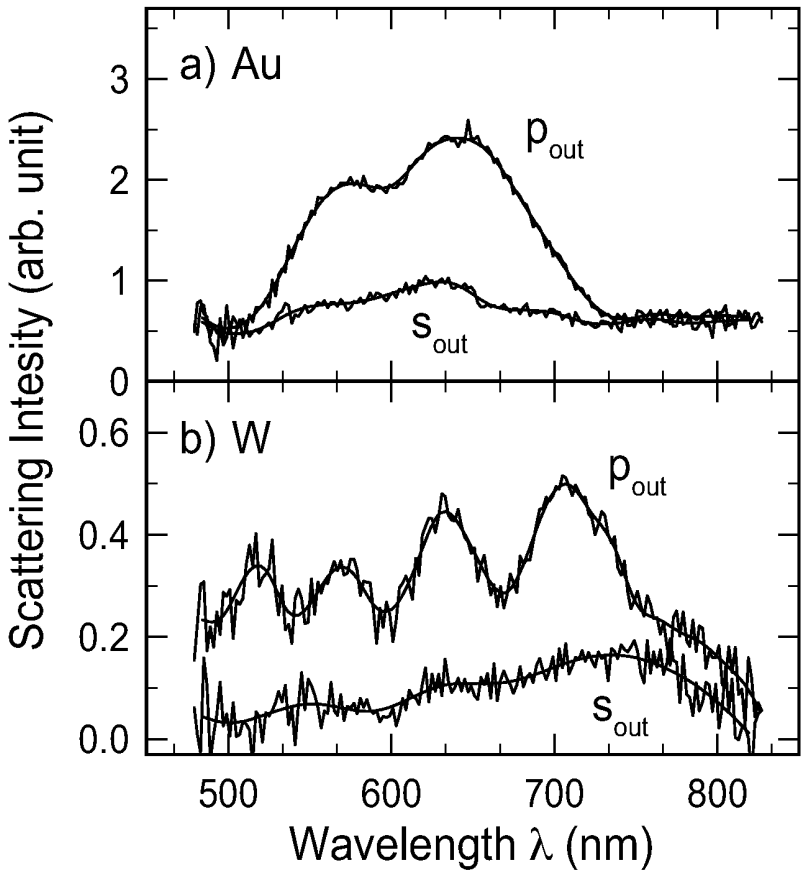

Figure 3.11: Polarization dependence of scattering spectra: (a) Au tip with slightly irregular shape in the axial direction. (b) Example for W tip with very large aspect ratio. Note: the smooth lines are only guides for the eye.

near-negligible off-resonance contrast. Studying the polarization dependence can provide further information on the nature of the plasmon resonance.

The data shown in Fig. 3.11 b) represent the limiting case of the W tip with the exceptionally large aspect ratio shown in Fig. 3.9 d). Except for the spectral variations in p polarized detection the behavior is typical for most W tips investigated, with the ratio of s to p emission only weakly wavelength dependent. The variations are discussed below within the context of the theoretical model used.

As discussed above, the occurrence of a spectrally structured plasmon response can be the result of irregularities of the kind shown in the electron micrograph of Fig. 3.9 b). These geometric features effectively lead to a spatial variation of the confinement of the correlated electron motion in the axial direction at the tip apex and can thus give rise to in general different oscillation frequencies. In that case in s-polarized emission both resonant features would diminish simultaneously as seen in Fig. 3.11.

However, favorable conditions for the formation of a radiating plasmon resonance can also occur for excitation with the electric field aligned perpendicular to the tip axis. Thus, in

unpolarized detection this would give rise to two distinct resonance features as shown in Fig. 3.12 a). Depending on polarization, these different contributions from the longitudinal and transversal plasmon resonance can then be separated as shown in the lower panel. The position of the resonance peak for the *s*-polarized output is blueshifted with respect to the main peak of the *p*-polarized case. This could indicate the excitation of surface plasmons in a geometrical structure much closer to the spherical shape [156]. In this situation the *s*-polarized emission intensity can exceed *p*-polarized emission within certain wavelength regions – in contrast to those tips which only allow for an axial plasmon excitation.

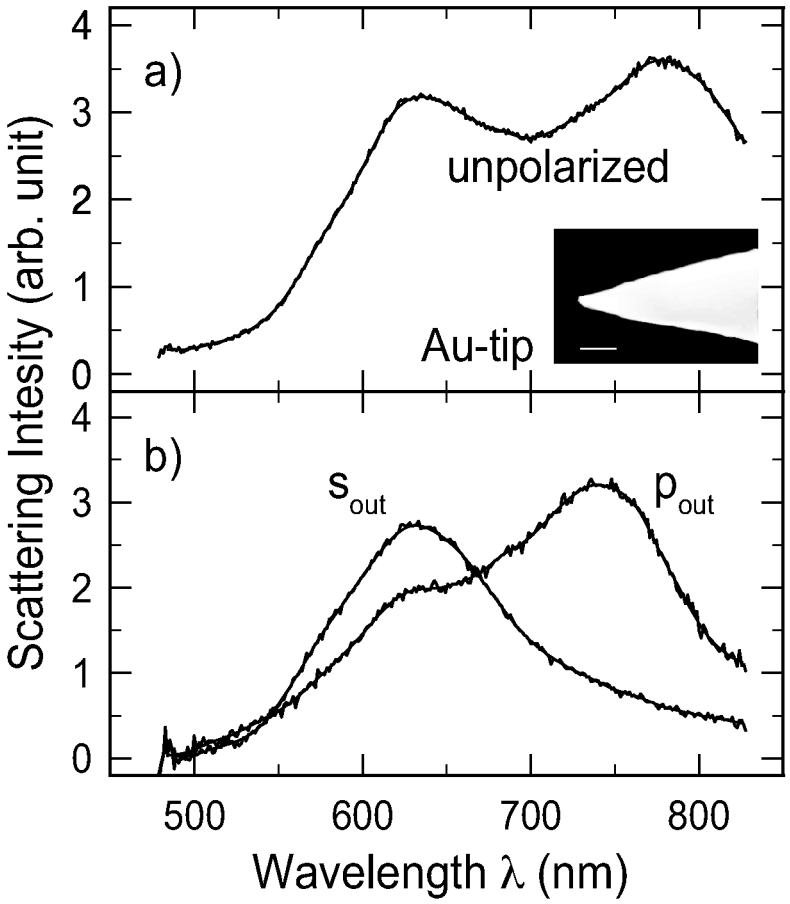

Figure 3.12: Resonant light scattering from a Au tip where the two distinct resonances (a) can be attributed to the excitation of the plasmon oscillation perpendicular (*p*) and parallel (*s*) with respect to the tip axis, respectively, as evident from the polarization resolved study (b).

Yet, comparing the topologies of the tips shown and other data for different tips investigated, we were not able to identify the relevant structural parameter responsible for whether a tip supports just one or both, longitudinal and transversal, plasmon excitations. This behavior in particular, and the in general small polarization ratios seem to contrast expectations based on theoretical modeling of the electric field near the tip apex region. There, from the calculated large enhancement when the electric field is oriented parallel to the tip axis compared to the perpendicular direction [105, 27], strongly enhanced scattering for

p-polarization should result. From the experimental point of view, a possible reason for the reduced polarization contrast even for an ideal tip is the fact that the induced surface current density is very sensitive to the exact orientation of the applied electric field. Thus, for realistic structures small deviations from the rotational symmetry, surface inhomogeneities or other structural imperfections, which are difficult to control given the preparation procedure, would give rise to a possibly complex form of the induced polarization [103, 157].

In the experimental geometry used, the excitation is limited to the outermost several 100 nm of the tip end, given by the spatial extent of the evanescent field. Yet, the general characteristic spectroscopic response of the tips is solely determined by this near-apex region of the tip. This is concluded from far-field spectroscopy carried out for comparison using direct illumination exciting a tip region of several μm. Here, essentially the same spectral dependence is observed, only offset in scattering intensity by a large spectrally unspecific background.

3.4 Model calculation and discussion

From the experiments shown and series of other spectra taken for different tips we conclude that the details of the optical response in terms of scattering intensity, shape and spectral position of the resonance depend sensitively on structural details of the tip apex region. Despite this rich behavior observed the experimental results can be rationalized with a simple model based on the solution of the Maxwell's equations.

Here, as an approximation of the tip apex we treat it as a small hemispheroid with semi-major and semiminor axis a (length) and b (width), respectively. A cartoon for the case of a prolate hemispheroid is shown in Fig. 3.13. Considering the tip to be radially symmetric, its model-shape is reduced from an ellipsoid with a $\neq$ b $\neq$ c to a spheroid having a $\neq$ b = c. This model qualitatively describes the experimentally observed trends in the optical response of the tips with regard to: a) dependence on tip material, b) tip apex shape, c) scattering intensity, d) spectral, and e) polarization characteristics (*vide infra*). This model has been applied previously to describe the electromagnetic mechanism of surface-enhancement of Raman scattering [158, 159] and second-harmonic generation from rough surfaces [160].

The incident field across the hemispheroid is considered to be uniform (*i.e.*, $kr \ll 1$). In this quasi-static limit and Laplace's equation and its boundary conditions completely describes the system. In the natural ellipsoidal coordinates (ξ, η, ζ), Laplace's equations can be written as [33]:

$$\begin{aligned}\nabla^2\Phi(\eta,\xi,\zeta) &= (\eta-\zeta)R(\xi)\frac{\partial}{\partial(\xi)}\left(R(\xi)\frac{\partial\Phi}{\partial(\xi)}\right) + (\zeta-\xi)R(\eta)\frac{\partial}{\partial(\eta)}\left(R(\eta)\frac{\partial\Phi}{\partial(\eta)}\right) \\ &\quad + (\xi-\eta)R(\zeta)\frac{\partial}{\partial(\zeta)}\left(R(\zeta)\frac{\partial\Phi}{\partial(\zeta)}\right) \\ &= 0, \end{aligned} \tag{3.23}$$

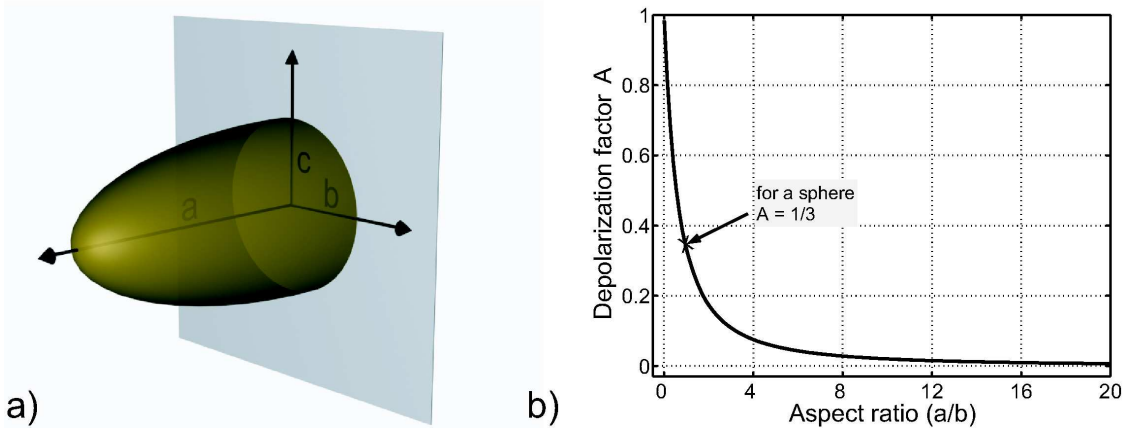

Figure 3.13: a) Schematics of the prolate hemispheroid (a ≥ b = c) assumed to model the tip; b) The depolarization factor A as a function of aspect ratio. A= 1.3 value for the sphere case is indicated.

where

$$R(s) = \sqrt{(s+a^2)(s+a^2)(s+c^2)}; \quad s = (\xi, \eta, \zeta) \tag{3.24}$$

The potential Φ must satisfy the boundary conditions which state that $\Phi(\eta, \xi, \zeta)$ and $\partial\Phi(\eta, \xi, \zeta)/\partial\xi$ have to be continuous across the spheroidal boundary $\xi = \xi_0$ (*i.e.*, the tip surface), that Φ is finite everywhere, and that the total field at infinity is equal to the incident field.

The field outside the hemispheroid corresponds to a superposition of the uniform incident field and the field of an ideal dipole situated at the origin of the coordinates system, with an equivalent dipole moment [103]:

$$\vec{p} = 4\pi\epsilon_m(\omega)ab^2 \frac{\epsilon_t(\omega) - \epsilon_m(\omega)}{\epsilon_m(\omega) + A_i[\epsilon_t(\omega) - \epsilon_m(\omega)]} \vec{E}_0 \tag{3.25}$$

with ϵ_t and ϵ_m the permittivities of the tip and the surrounding medium (here, $\epsilon_m = 1$ for air), respectively. A_i is the depolarization factor along one axis and a function of the structural parameters a and b only [33]:

$$A_i = ab^2 \int_0^\infty \frac{ds}{(s+a^2)^{3/2}(s+b^2)}, \quad i = (x, y, z) \tag{3.26}$$

.

The depolarization factor is plotted in Fig. 3.13 b) as a function of the aspect ratio a/b of the hemispheroid. It describes the lightning rod effect and takes on the value of 1/3 for a sphere (indicated by arrow in figure) and approaches 0 for a very slender prolate spheroid, when ($a/b \cong a$). Note that the lightning rod effect strongly increases the fields at the end of a prolate spheroid, at the sides the fields are greatly reduced [161].

The polarizability α_i of this hemispheroidal protrusion in a uniform field parallel to one of

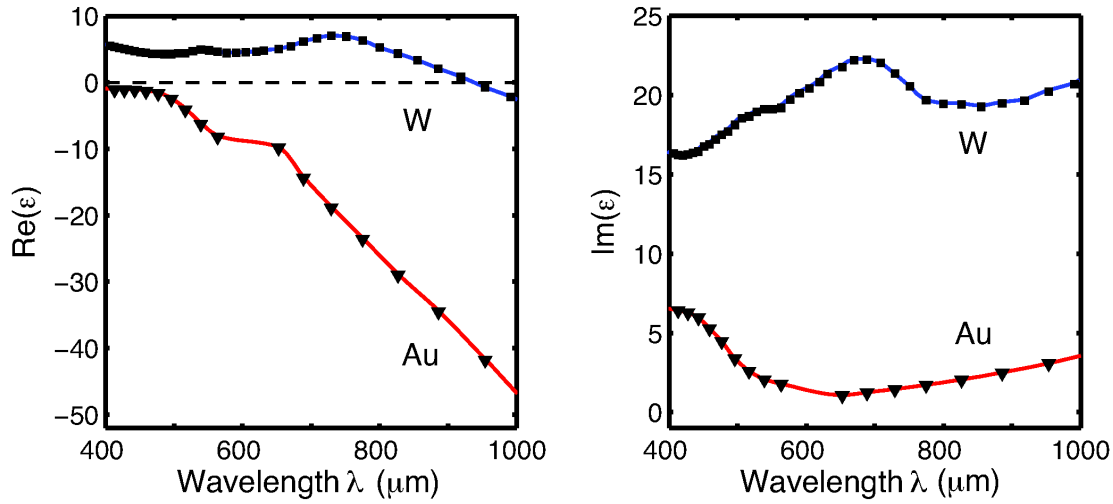

Figure 3.14: Real and imaginary parts of the dielectric function values for Au (triangles) and W (squares) in the range of visible frequencies. The values correspond to the experimental data from Ref. [123]. The solid lines represent interpolations and are added as guide for the eye.

its principal axes is then given by

$$\alpha_i(\omega) = \frac{4\pi ab^2}{3} \frac{\epsilon_t(\omega) - \epsilon_m(\omega)}{\epsilon_m(\omega) + A_i[\epsilon_t(\omega) - \epsilon_m(\omega)]} \tag{3.27}$$

This model allows for the direct visualization of the dependence of the polarizability and thus the scattering efficiency on tip material and structural parameter. The hemispheroid exhibits a resonant response to the applied field when

$$Re[\epsilon_m + A_i(\epsilon_t - \epsilon_m)] = 0 \tag{3.28}$$

This in general requires a negative real part of the dielectric function $\mathrm{Re}(\epsilon_t) < 0$ (*e.g.*, for the tip in air with $\epsilon_m \simeq 1$). The real and imaginary part for both materials are plotted in Fig. 3.14. With $\epsilon(\omega)$ ranging from $(-1.3 + 5.7i)$ to $(-31 + 2.2i)$ for Au and $(4.6 + 17i)$ to $(3.3 + 19i)$ for W in the spectral range of 450 to 850 nm, it is seen that only Au as a nearly free electron metal would allow for a strong plasmon resonant polarizability. A primary effect of the depolarization factor is to shift the plasmon resonance.

Using this model the dependence of the polarizability along the major axis is plotted in Fig. 3.15 as a function of both wavelength λ and aspect ratio a/b for a Au (panel a) and W (panel b) hemispheroid. In agreement with the experiment the optical response for Au is dominated by a strong plasmon resonance in this wavelength range, contrasting the spectrally flat and weak response for W.

As can be seen, the spectral position of the Au plasmon resonance is sensitive with respect to the aspect ratio of the hemispheroid. This is in accordance with the experimental observation where the tip plasmon for Au is found to depend critically on the shape of the

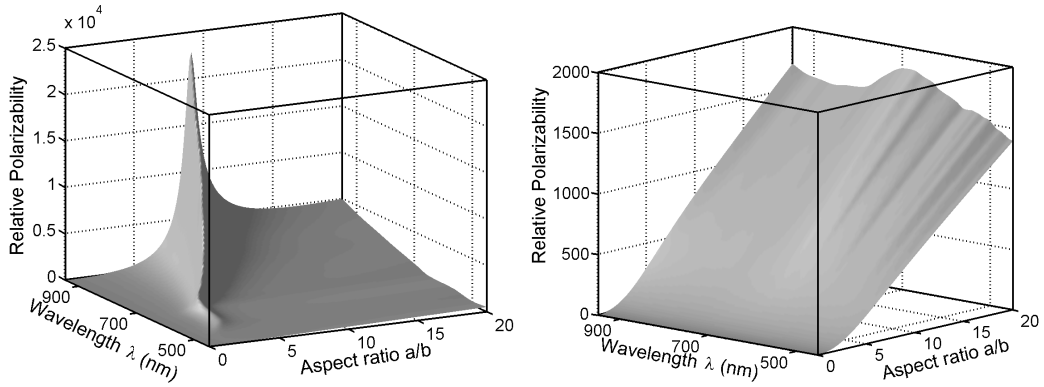

Figure 3.15: Relative polarizability of Au (a) and W (b) hemispheroids as function of aspect ratio and excitation wavelength calculated using the electrostatic model described in the text.

tip apex. Comparing the peak positions of the spectra for the Au tips investigated with the results of this model one can attribute aspect ratios in the range from 2 – 6 to describe the actual tip geometries. This is approximately consistent with the tip shapes in the apex region, as observed in scanning electron microscopy (Fig. 3.9 and Fig. 2.6).

The appearance of multiple resonances for inhomogeneous tips is readily explained considering different confined regions at the apex which correspond to different resonant conditions. Likewise, observing the scattering response polarized parallel or perpendicular to the tip axis, in the model this corresponds to the excitation either parallel or perpendicular to the major axis of the hemispheroid, respectively, which results in two distinct resonance positions.

For tungsten as tip material, the model shows spectral modulations in the case of tips with large aspect ratios. That is the polarizability becomes increasingly wavelength dependent with increasing aspect ratio. This reproduces the experimentally observed behavior of the W tip in Fig. 3.9 d, which is very slender.

The polarizability α would translate into values for the local-field enhancement L at the tip apex defined by $\mathbf{E}_{loc}(\omega) = L\mathbf{E}(\omega)$ with $L \simeq 3\alpha_i/4\pi b^2 a$ [157, 103]. Its spectral characteristics would thus follow that of the polarizability within this approximation. Values for the local-field enhancement, however, can not be derived in this experiment due to a lack of an absolute reference. They have been determined for both Au and W tips for certain wavelengths by means of second-harmonic generation [47] or tip-enhanced Raman scattering [27, 30] with corresponding values found to range from 8 to 25 for Au tips and 3 – 6 for both W and Pt(Ir) at $\lambda \sim 800$ nm.

The experimental findings described here indicate that the optical response of the tip is also sensitive to the shape of the tip rather than the apex radius alone. Yet, the latter plays an important role when scanning experiments are performed, since the degree of near-field

localization scales with the tip radius [122]. The model discussed here thus provides a qualitative understanding of the tip scattering response. Concerning quantitative values, the electrostatic approximation should be viewed as an upper limit for local-field enhancement and tip polarization. Because of the finite size of the tip, both polarizability and degree of local-field enhancement would be diminished [162]. They rapidly decrease when the structure size increases beyond $\sim \lambda/10$ because of dephasing or phase retardation effects [163]. Here, the fields scattered from different parts of the structure are partially out of phase and destructively interfere [163]. The model could be generalized to the exact Mie theory, to include retardation and radiation damping [158, 141] and for other model geometries. While this may provide a more quantitative agreement with the experimental findings, the qualitative behavior is not expected to change, and the conclusions drawn above would not be altered.

With respect to the notion of tips as optical antennas, a behavior close to the dipole-antenna is expected only for very slender highly conductive rods with diameter small compared with the length l. In that case, the electric field reaches its maximal values when $\mathrm{l} = n\lambda/2$ (n is positive integer) with the global maximum at $\mathrm{n} = 1$ [95]. This describes the lightning rod effect, when the electric field lines crowd at the narrow ends of the tip. For ellipsoids, the antenna resonance is shifted towards smaller lengths than $\lambda/2$ due to the finite width b [156]. Since the real metals are not perfectly conducting at optical frequencies (see Figure 3.14), the degree of enhancement is reduced [162].

3.5 Conclusion

The characteristics of light scattering from individual sharp metallic tips were investigated experimentally and modeled theoretically. Whereas for tungsten as tip material, the optical response is found to be only weakly wavelength selective, for gold the scattering process is characterized by a plasmon resonant behavior.

The details of the spectral response are found to depend sensitively on morphology and size of the tips as well as surrounding medium and field polarization. The results presented here can be generalized for other tip materials comparing the dielectric functions for different metals. This implies that for other nearly free-electron metals such as Al or Ag plasmonic behavior with large polarizability and local field enhancement is expected. In contrast, similar to the case of W, *e.g.*, Pt(Ir) alloy tips which are frequently applied in AFM related studies have poor optical properties due to the strong absorption in the UV-vis spectral range.

In this study the optical coupling of the tip to the quartz prism substrate could be neglected. This optical near-field interaction of the tip in close proximity to the substrate is the essence of scattering-type scanning near-field optical microscopy and spectroscopy (*s*-SNOM). In the case of a weak coupling as it is the case for optically dissimilar tip and sample materials the tip-scattered light in general would then be a spectral superposition of the optical response of the tip and the spectral properties of the polarization driven by the localized near-field in the substrate. In addition, for metallic substrates, strong tip-sample

coupling results in a large field built-up in the tip-sample gap region [129] accompanied by characteristic changes of the spectral response of the tip-scattered light [164].

Achieving good performance in *s*-SNOM is reportedly sensitive to structural details of the tip which are found to be hard to reproduce, resulting in a low yield of suitable tips for these experiments. This could be explained by the large variability of the spectral response observed in our study which would translate into a large variation of the efficacy of near-field enhancement in particular for excitation at fixed laser frequency.

The results presented here thus provide the necessary criteria for the selection of suitable tips. One way for obtaining tips with well defined plasmon response, although at the expense of a large field enhancement, has been demonstrated by attaching gold metal clusters to the apex of glass-fiber-based tips [138, 165]. It can be envisioned, however, that ongoing improvements in the preparation techniques will allow for an optimization of the geometric parameter of the tips by means of ion beam milling [134] or lithographic techniques and thus tailoring of the optical response for the performance needed in respective applications.

4 Scanning probe Raman spectroscopy

Optical spectroscopy provides nondestructive techniques for obtaining both structural and real time dynamic information of molecules and solids. Vibrational spectroscopy in particular, by directly coupling to the nuclear motion, offers insight into chemical composition, molecular bonds and their relative orientation, intermolecular coupling and zone-center phonons in crystalline solids [166, 167]. In that respect ir and Raman spectroscopy provide complementary information, with the feature of Raman spectroscopy of fewer constraints in terms of selection rules, readily providing access to low frequencies vibrations [168, 169, 170, 171], and being carried out in the vis-near ir spectral range in a comparably simple experimental design.

It is highly desirable to combine the intrinsic chemical specificity of Raman spectroscopy with optical microscopy for the investigation of the spatial heterogeneity and composition of the analyte. In that regard the optical far-field Raman microscope has become an established tool for material characterization on the micrometer scale and in a confocal implementation with spatial resolution down to just several hundred nanometers[172]. However, for most applications the desired spatial resolution needed often exceeds the resolution imposed by far-field diffraction [3, 173]. Near-field optical microscopy provides access to higher spatial resolution [18, 20, 19, 13, 174, 11, 175, 10], and when employed for nano-Raman spectroscopy is a powerful tool for identifying and analyzing molecular composition, offering spatially resolved spectral maps with nanometer resolution [27].

The detection and chemical identification of single molecules constitutes one of the main goals of chemical analysis, as it can reveal the full distribution of a certain molecular property, instead of statistical average as in the case of ensemble measurements. Both static and dynamic heterogeneity in a population of molecules in a complex condensed system can be identified and related to the molecular environment. Therefore, a single molecule can be viewed as a local reporter of its nano-environment.

Here, the results on near-field tip-enhanced Raman spectroscopy (TERS) on Malachite Green molecules adsorbed on planar Au surfaces are discussed. The high degree of Raman enhancement observed allows for sensitivity down to the single molecule level.

4.1 Raman fundamentals

When an atom or molecule is illuminated with a beam of monochromatic light of wavenumber $\tilde{\nu}_0$, most photons are elastically scattered (Rayleigh scattering). In addition, inelastic emission at $\tilde{\nu}' = \tilde{\nu}_0 \pm \tilde{\nu}_{vib}$ occurs, where the wavenumbers $\tilde{\nu}_{vib}$ correspond to transitions between rotational or vibrational (rarely electronic) energy levels of that molecule. The appearance of this spectrally shifted emission is called *Raman effect* [176].

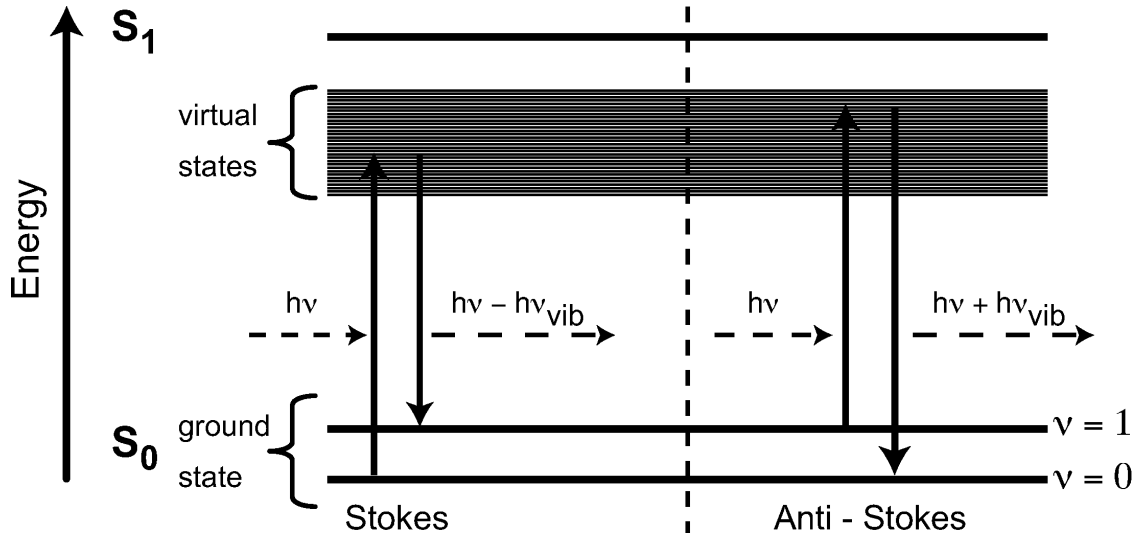

Figure 4.1: Raman process for both Stokes (left) and anti-Stokes (right) frequency shifts of molecule with the ground state S_0 and vibrational levels ν_1 and ν_1.

The possibility of light scattering with a change of frequency was first predicted theoretically by Smekal in 1923 [177]. The first observations of the phenomenon were made in 1928 in liquids by Raman and Krishnan [178], and independently in crystals by Landsberg and Mandelstam [179]. The first comprehensive treatise of the underlying theory was offered by Planczek [180] in 1934. As a practical tool, Raman spectroscopy proved difficult initially, due to its rather low scattering cross-section ($\sigma_R \sim 10^{-27} - 10^{-30}$ cm^2/molecule) [i]. It was the invention of laser that rescued Raman spectroscopy from oblivion [182].

The interaction of an incident electric field $\mathbf{E} = E_o \cos 2\pi\nu t$ with a molecule can be classically described by the induced electrical dipole $\mathbf{p}$:

$$\mathbf{p} = \alpha\mathbf{E} \tag{4.1}$$

where α is referred to as the molecular polarizability. For a vibrating molecule, the polarizability of the bond is a time-varying term that can be expressed as a time series expansion about the equilibrium geometry:

$$\alpha = \alpha_0 + \left(\frac{\partial\alpha}{\partial Q}\right)_0 Q + \ldots, \tag{4.2}$$

with α_0 the permanent polarizability of the molecule, Q represents the normal coordinate associated with the vibrational frequency ν_{vib} and the subscript 0 refers to derivatives taken at the equilibrium configuration. Q has the form [181]:

$$Q = Q_0 cos 2\pi\nu_{vib} t, \tag{4.3}$$

[i] The Raman cross-section σ_R is defined as the ratio between the total Stokes scattered light I_R (photons s^{-1}) and the incident flux of photons I_0 (photons s^{-1} cm^{-2}): $I_r = \sigma_R I_0$ [181].

and the modulus of the induced electric dipole is then written:

$$p = \alpha_0 E_0 \cos 2\pi\nu t + \frac{1}{2}\left(\frac{\partial\alpha}{\partial Q}\right)_0 Q_0 E_0[\cos 2\pi t(\nu - \nu_{vib}) + \cos 2\pi t(\nu + \nu_{vib})] \tag{4.4}$$

The first term on the right side of Eq. 4.4 accounts for the Rayleigh scattering. The second and the third stand for the Stokes and Anti-Stokes Raman scattering, respectively.

The ratio of the intensity of the Raman anti-Stokes and Stokes lines is given by [183]:

$$\frac{I_A}{I_S} = \left(\frac{\nu + \nu_{vib}}{\nu - \nu_{vib}}\right)^4 e^{\frac{-h\nu_{vib}}{kT}} \tag{4.5}$$

with the Boltzmann factor expressing the probability for thermally induced occupation of the first excited state.

The Raman selection rules will be determined by the properties of the Raman tensor $(\partial\alpha/\partial Q)$. Following Eq.4.4 and taking only the dipole radiation into account, a given normal vibration of a molecule may appear in the Raman spectrum if at least one component of the polarizability tensor α changes during this vibration:

$$\left(\frac{\partial\alpha_{ij}}{\partial Q_k}\right)_0 \neq 0, \tag{4.6}$$

where Q_k is the k^{th} normal coordinate associated with the vibration of wavenumber $\tilde{\nu}_k$. According to quantum theory, for a harmonic oscillator transitions are allowed only when the quantum number n changes by one ($\Delta n = \pm 1$). For radiation to be emitted or absorbed, a transition should therefore occur between different neighboring vibrational levels of the molecule. This may be concomitant with the loss or gain of energy in the form of electromagnetic radiation [176]. In Fig. 4.1 a cartoon describing the Raman process is shown. The incident field excites the system from its ground state S_0 to one virtual state [ii]. The Raman emission is indicated for both Stokes ($h\nu - h\nu_{vib}$) and anti-Stokes ($h\nu + h\nu_{vib}$) shifts.

It has to be noted that for certain experimental arrangements (*e.g.*, strong field gradients on the molecular lengthscale) contributions from higher order multipolar radiation may have a non-negligible contribution to the total Raman response [185]. This will be discussed later on in the present chapter in conjunction with the experimental results obtained.

When the frequency of the incident radiation falls within the electronic absorption band, an enhancement of the Raman intensities can be observed (by as much as a factor of 10^6) [186, 187, 188, 189]. This is referred to as *resonance Raman effect* (RRE) [190, 191, 192]. The technique is appealing for a number of reasons: (i). the enhanced signal allows the investigation of more dilute samples [193]; (ii). offers new information on the interaction between electronic and nuclear motions of molecules, *i.e.* the intensity of the Raman bands as a function of the frequency of light (vibronic coupling); (iii). brings additional symmetry information [186].

[ii] Virtual levels are not energy eigenlevels of the free molecule, but rather the energy combination of energy eigenstates of the molecule and the radiation field photons [184].

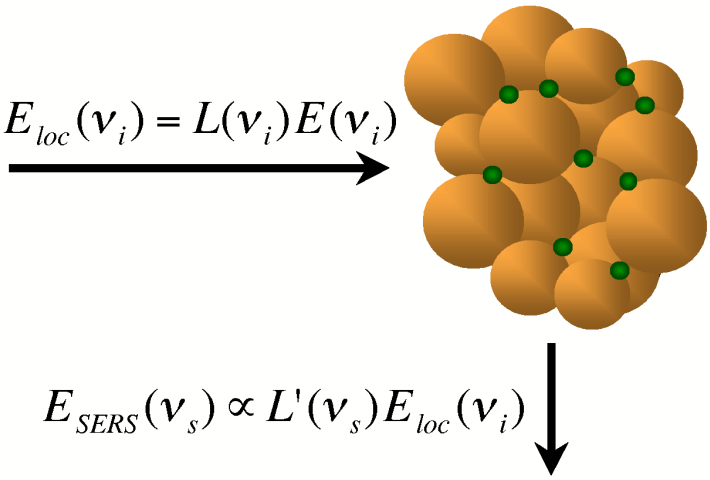

Figure 4.2: Schematics of SERS concept.

Concomitant, fluorescence emission is a challenging problem in many applications of Raman spectroscopy. This is more prevalent under resonance conditions, as the radiation used to excite the Raman spectrum may also excite the fluorescence emission. With smaller Stokes shift and typical quantum yields several orders of magnitude larger than that for Raman scattering ($\sigma_F \sim 10^{-16}$ cm^2/molecule), the fluorescence makes measuring the resonant Raman spectrum very difficult.

4.1.1 Surface-enhanced Raman Spectroscopy (SERS)

Surface enhanced Raman spectroscopy (SERS) was observed in 1974, when Fleischmann *et al.* noticed enhanced Raman response from pyridine adsorbed from aqueous solution onto a silver roughened electrode [194]. They attributed the signal strength to an increase in the electrode surface area and therefore in the larger number of molecules sampled. Van Duyne and Jeanmaire [195] and independently Albert and Creighton [196] were the first to recognize that the intensification of the effective Raman cross-section could not be accounted for by the increased number of molecules as a result of surface's roughness factor alone.

It was early recognized that the excitation of surface plasmons on rough metallic surfaces is mostly responsible for the increase of the Raman response observed in SERS [197]. This so-called *electromagnetic enhancement* is based on the fact that the dipole moment induced in an adsorbed molecule will be due both to the directly incident field and the field elastically scattered by the metallic protrusion underneath the molecule [158, 198, 199, 200, 201, 202].

Furthermore, for small particles compared with the wavelength of light ($kr \ll 1$), the scattered field may be enhanced when the frequency is resonant with that of the surface plasmon polariton [103] as detailed in Sect. 3.4 for nanoscopic metallic tips. A conceptual sketch of a SERS experimental arrangement is presented in Fig. 4.2. The molecules (green) are adsorbed at the interstices of metallic nanoparticles shown here as colloidal spheres (golden).

Following the discussion in Chapter 3 of the present work, the local-field enhancement $L(\nu_i)$ just outside a metallic particle is defined by $E_{loc}(\nu_i) = LE(\nu_i)$, with $E_{loc}(\nu_i)$ and $E(\nu_i)$ the magnitudes of the local near-field at the particle surface and the incident field, respectively. The molecule adsorbed at the surface will therefore experience the field $E_{loc}(\nu_i)$ and the Raman-scattered light will have a field strength $E_R(\nu_s) \propto \alpha_R E_{loc}(\nu_i)$. Furthermore, the Raman-scattered field can be further enhanced in the same manner as the incident field: the metallic protrusion will scatter light due to induced polarization at the Raman-shifted frequency with an enhancement factor $L'(\nu_s)$. The amplitude of the SERS-scattered field field will therefore be given by [203]:

$$E_{SERS}(\nu_s) \propto \alpha_R L(\nu_i) L'(\nu_s) E(\nu_i) \tag{4.7}$$

With the SERS intensity $I_{SERS}(\nu_s)$ proportional to the square modulus of $E_{SERS}(\nu_s)$, this gives:

$$I_{SERS}(\nu_s) \propto |\alpha_R|^2 |L(\nu_i) L'(\nu_s)|^2 |E|^4(\nu_i) \tag{4.8}$$

For small frequency shifts, the Raman scattered field will be itself resonant with the surface plasmon of the metallic particle, in which case it will encounter the same enhancement factor $L'(\nu_s) \cong L(\nu_i)$. According to Moskovits [204], the "SERS enhancement" G can be defined as the ratio of the Raman-scattered intensity in the presence of the metal particle to its value in the absence of the latter:

$$G = \left| \frac{\alpha_R}{\alpha_{R0}} \right|^2 |L(\nu_i)|^4 \tag{4.9}$$

where α_{R0} is the polarizability of an isolated molecule. α_R is the polarizability of the molecule in the presence of both the metallic scatterer and it may result in altered magnitude, symmetry and resonant properties from the Raman polarizability of the isolated molecule due to the adsorption geometry [205]. This is important in systems where metal-to-molecule and/or molecule-to-metal charge transfer occurs, leading to the so-called *chemical enhancement*. Here an electron can be transferred from the molecule into the empty levels of the metal surface or from the occupied surface levels to the molecule. The process resembles an electronic excitation of the molecule-surface system and may lead to the appearance of a new band in the electronic spectrum of the molecule. The chemical enhancement is restricted by its nature to the molecules directly adsorbed onto the surface, in contrast with the electromagnetic mechanism which extends for a larger distance beyond the surface [206]. Calculations showed that the electromagnetic enhancement factor can be as high as 10^{11} - 10^{12} for properly chosen corrugated surfaces or colloidal solutions [119, 198, 207, 208]. The contributions from the chemical enhancement are much lower, on the order of only 10^2 [209, 210].

Note however, that the above determination of the total enhancement factor needs further corrections if retardation effects are included [211, 212]. In the later case, it is not anymore enough to write G as in Eq. 4.9, since the enhancement contributions of the excitation and emission channels are different. It was demonstrated both experimentally and theoretically that radiation damping becomes important with increasing the particle size (r > 25 nm), and it acts as to limit the degree of enhancement [140, 141]. With yet a lack in a perfect grip on the microscopic experimental conditions, the above description offers a satisfactory basic understanding of the process.

With SERS a near-field phenomenon, this leads to a relaxation in the selection rules when compared with the normal Raman process. Hence, normally forbidden vibrational modes could be observed in the SERS spectrum [213, 205, 214].

SERS is seldom reported from single isolated particles, almost all effective SERS-active systems consist of assemblies of interacting nanostructures referred to as *hot spots* [215, 216, 207]. It was shown that higher enhancements are obtained when the molecules are adsorbed on small colloidal aggregates or interstices between multiple nanostructures [217], in accordance with the theoretical predictions that gaps between closely spaced metal features concentrate the electromagnetic energy even further than the isolated structures [204, 208]. In a SERS experiment on crystal violet molecules adsorbed on Ag nanoparticles in a colloidal solution, Kneipp *et al.* estimate that less than 1% of the total metallic aggregates show sufficient enhancement [218] so that only a very small fraction of the adsorbed molecules contribute to SERS.

With SERS enhancements of $\sim 10^{14}$ already experimentally observed [210], this translates into Raman cross-sections on the order of 10^{-16} cm^2 / molecule, comparable with the fluorescence cross-section. This allowed for single-molecule Raman spectroscopy, akin to the studies of fluorescence from single emitters [219]. For the latter case, one of the hallmarks in the observation of fluorescence emission from single molecules is the temporal fluctuation of both intensity and spectral profile [220, 221, 222, 223, 224, 225, 206]. Similar evidence emerged also from single molecule SERS (smSERS) studies. Nie *et al.* reported intensity and spectral changes in time of single Rhodamine 6G molecules spectra [226]. In experiments on the same molecular species, Weiss *et al.* obtained resonant SERS cross-sections of $\sim 10^{-13}$ cm^2/molecule and showed that the spectra display dramatic fluctuations in relative intensity of particular vibrational modes, while their spectral positions remain constant [206]. Xu *et al.* found Raman enhancements of 10^{10} in single hemoglobin protein molecules attached on immobilized Ag particles together and observed spectral jumps [227]. In smSERS studies of tyrosine on Ag particles, Bjerneld *et al.* estimate an enhancement factor of 10^{12} and found similar spectral jumps, attributed to changes in the adsorption of the molecule on the surface [228]. Using insertion of 60 nm diameter Au colloids inside living cells, Kneipp *et al.* achieved spatially resolved SERS spectra and infer a minimum Raman enhancement of 10^3 - 10^4 [229].

In the context of the experiments presented here, it has to be noted that enhanced molecular absorption and fluorescence might also be seen for molecules placed near SERS-active surfaces, provided the molecular absorption bands are close to the surface-plasmon frequency of the metal particle [230]. However, in competition with that, one has non-radiative damping processes that reduce the lifetime of the excited molecule by exciting surface polariton resonances and electron-hole excitations, often so efficiently that the overall effect is a reduction in fluorescence quantum yield (fluorescence quenching) [231, 212]. Thus, in the presence of the metal substrate the fluorescence is reduced [232, 233], and the Raman scattering process is enhanced.

Despite its potential for chemically specific detection of minute amounts of analytes, it has remained challenging to develop SERS into a a routine analytic spectroscopic tool, mostly due to difficulties associated with the reproducible fabrication of SERS-active substrates [217, 208, 218, 234].

At a more fundamental level, the physical understanding of the underlying enhancement mechanisms (electromagnetic and chemical) and their interplay is still far from complete. Large electromagnetic enhancement without interfering chemical (electronic) effects is the aim of analytical chemistry, where molecules must be recognized and their concentration measured irrespective of the chemical nature of the adsorbed molecule [234]. These, together with the difficulty to select specific target molecules has thus far prevented the application of SERS as a routine analytic tool.

For an in depth and thorough summary of the main theoretical and experimental works in the field of SERS the reader is referred to [203] chapters 1 - 10.

4.2 Tip enhanced Raman-spectroscopy (TERS)

In general, better control over the SERS active sites and their field enhancement can be achieved by what may be viewed as resorting to an inverse geometry with respect to SERS: suspension of the metal nanostructure providing the field enhancement at a small distance above the analyte [235]. This is the basis of tip-enhanced Raman scattering (TERS) making use of a single plasmon-resonant metallic nanostructure provided in the form of a scanning probe tip of suitable material and geometry.

Fundamentally, TERS is a variant of apertureless near-field optical microscopy (*s*-SNOM) [24, 25, 236, 237, 23]. *s*-SNOM and special aspects of TERS have been addressed in recent reviews [238, 175, 10, 239, 240, 241] (and references therein). A conceptual sketch of the TERS arrangement is shown in Fig. 4.3. The apex of the metallic tip is brought close to the molecules adsorbed on the surface in a controllable way offered by the scanning-probe techniques (AFM, STM). The incident radiation (ν_i) is focused onto the tip-sample gap and the scattered Raman shifted response (ν_s) is detected. As stated in Chapter 2, under ambient conditions a thin water layer (blue region in figure) is adsorbed onto the sample surface. This layer, present on most hydrophilic samples, may play an important role in possible surface diffusion of the analyte molecules and possibly transition of molecules to adsorb onto the tip (*vide infra*).

The single nanoscopic tip apex provides the local field enhancement at a desired sample location without requiring any special sample preparation [128, 242]. This way, the interaction of adsorbates with a substrate and the enhancement provided by the tip are completely decoupled and the Raman enhancement is purely electromagnetic in nature. In addition, the local nature of the tip enhancement adds scanning/imaging capabilities. By raster scanning the sample, spatially resolved spectral Raman maps with nanometer resolution can be obtained simultaneously with the topography in atomic force microscopy (AFM) or surface electronic properties in scanning tunneling microscopy (STM).

Ultra-high sensitivity and nanometer spatial resolution imaging using TERS were obtained on various materials and molecular systems adsorbed on both flat and corrugated surfaces [243, 244, 245, 246, 247, 248, 249, 27, 250, 44, 251, 252, 253, 254, 255, 30, 256, 257, 258, 259].

The possibility of decoupling the "hot spot" from the substrate for the purpose of SERS was early recognized by Aravind *et al.* [235]. They developed a model where a sphere was suspended above a planar surface and the electromagnetic enhancement factor was

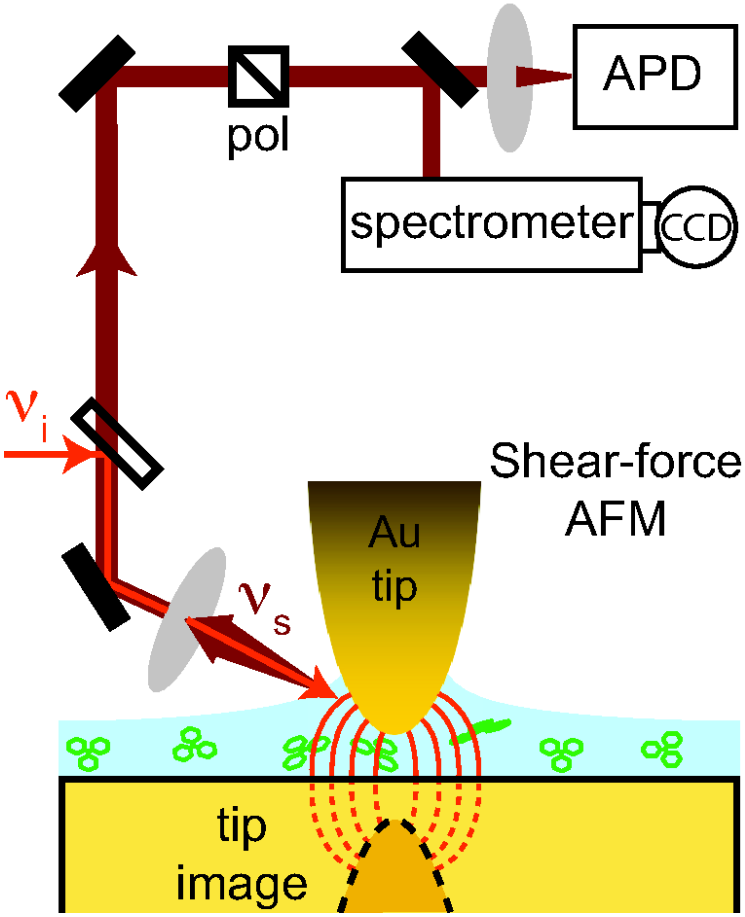

Figure 4.3: Conceptual schematics of the TERS arrangement. The incident light is focused onto the tip-sample gap and the tip-backscattered and -enhanced Raman response is detected. The blue layer indicates a thin surface water layer on the sample.

calculated for different materials. This can be viewed as a precursor of the actual TERS techniques.

The first approach to apertureless near-field Raman spectroscopy was designed by Stöckle *et al.* in 2000 [243] who reported that "a fine metal tip brought to within a few nanometers of a molecular film is found to give strong enhancement of Raman scattered light from the sample". They observed the near-field enhancement while the tip approached the sample, and also realized a spectral mapping of Raman scattering with a resolution of 50 nm. Having large Raman cross-sections, several dye molecules (*e.g.*, malachite green, rhodamine 6G, brilliant cresyl blue) were used and near-field Raman enhancement factors up to $\sim 10^9$ were achieved [248, 245, 252, 30, 256]. Using Ag coated AFM tips, spatial resolution below 50 nm was obtained on surface layers of Rhodamine 6G dye molecules [248, 245]. In later experiments, they proved the possibility of TERS to reveal new molecular vibrations and they showed Raman images with high spatial resolution . TERS and SERS were experimentally combined by positioning the tip above a grainy Ag surface covered with dye molecules. Here, near-field Raman spectra enhanced both electromagnetically and chemically were observed and The possibility of TERS to reveal new molecular vibration was shown [246, 247].

By raster scanning the sharp tip over the sample surface, Hartschuh *et al.* imaged vibrational modes of bundles and isolated single-walled carbon nanotubes [249, 27] and achieved a spatial resolution as high as 14 nm and estimated a Raman enhancement factor of $\sim 10^4$. This allowed for the study of local variations in the Raman spectra of single nanotubes.

In studies of adenine as well as C_{60} molecules, the tip-induced mechanical force was shown to lead to mechanical strain induced frequency shifts of the normal Raman modes [250, 255]. Furthermore, it was observed that when interacting with individual metal atoms of the tip apex, adenine molecules form different isomers, demonstrating the potential TERS for atomic site selective sensitivity [257].

Extension of TERS implementation for coherent spectroscopy was shown for Coherent Anti-Stokes Raman scattering (CARS) of adenine molecules included in a DNA network [44]. Owing to the third order nonlinearity of the CARS process, the induced polarization at the tip apex is further confined, and higher lateral resolution is in principle possible [251].

Concomitant, theoretical studies on TERS report field enhancements up to three orders of magnitude in particular frequency regions [260, 132, 261, 262, 263, 264]. However, the expected resulting TERS enhancement of 12 orders of magnitude has not yet been observed experimentally.

The aperture-based SNOM using tapered glass fiber tips has been also employed for nano-Raman spectroscopy [265, 266, 267, 268]. However, the low optical throughput of the aperture probes - 10^{-3} - 10^{-5} - restricts the sensitivity and results in a long imaging time (60s/point). Additionally, the spatial resolution is severely limited by the aperture size to 100-200 nm parasitic Raman signal from the glass tip that could be an impediment [267].

Similar to the case of SERS where the enhancement is given by the ratio of Raman intensities in the presence and absence of the metallic protrusion - Eq. 4.9, for TERS experiments G is estimated by the increase in Raman intensity with the tip close to the surface with

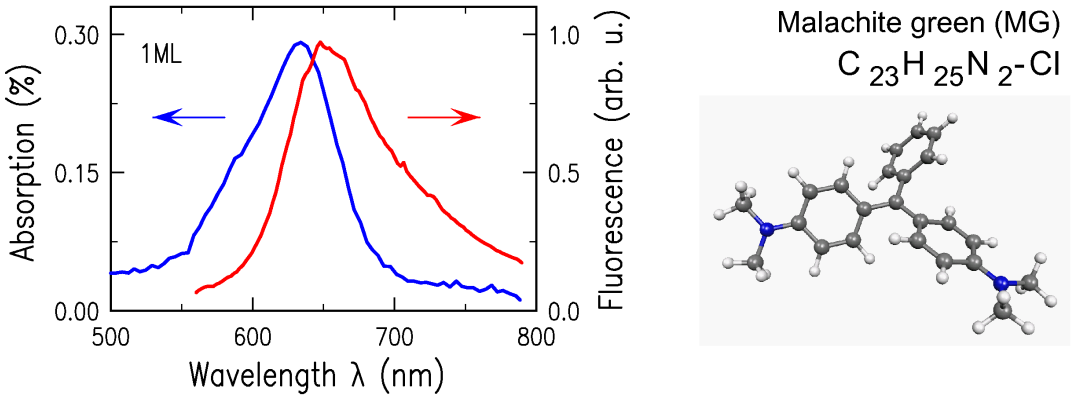

Figure 4.4: Absorption (blue) and fluorescence (red) of one monolayer of Malachite Green (MG) dye molecules adsorbed on a glass plate. Molecular structure of MG shown in right panel.

respect to the one when the tip is retracted. As detailed later in this chapter, although this is an indication that near-field enhancement can be responsible for the increase in intensity, without studying the lateral resolution and/or vertical tip-sample distance dependence of the increase in signal it is in principle not possible to discriminate near- from far-field contributions in inelastic light scattering from metal tips.

4.3 Malachite green molecule

For our experiments, we chose Malachite Green ($C_{23}H_{25}N_2 - Cl$, hereafter named MG). It is an organic tryphenylmethane laser dye, with an extended delocalized π-electrons system, and a molecular weight of 364.92. Using the inter-atomic distances the molecule is estimated to occupy a surface area of ~ 0.87 nm^2 (actual 3D spatial filling: 1.18 nm $\times$ 1.39 nm $\times$ 0.98 nm).

Fig. 4.4 presents the typical [269] absorption (blue) and fluorescence (red) spectra of one monolayer of MG molecules deposited on a glass substrate. The absorption peak is centered around $\lambda = 635$ nm. For the measurement of the fluorescence profile a micro-Raman spectroscopic technique [270] was employed. The excitation wavelength is $\lambda = 543$ nm, and the fluorescence peak is centered around $\lambda = 650$ nm.

4.4 Experimental

Various experimental schemes have been employed for TERS experiments. A tip axial illumination and detection geometry has been used, allowing for high NA, but requiring transparent samples or substrates [27, 28]. Similarly, but allowing to probe non-transparent samples, a high-NA parabolic mirror can be used [271, 272]. In both schemes, the tip is illuminated along the axial direction, with the tip apex positioned in the laser focus. For these geometries, polarization conditions require either a Hermite-Gaussian beam [273] or

radial incident polarization [274, 271]. While allowing for efficient excitation and detection with the tip, independent polarization and k-vector control is limited, but desirable for symmetry selective Raman probing. In contrast, side-on illumination and detection allows for greater flexibility in the selection of polarization and k-vector as well as the use of nontransparent samples.

A brief illustration of the experimental principle used for the back-scattering near-field tip-enhanced Raman studies on MG molecules is shown in Fig. 4.3. With most of the setup described in Chapter 2, only elements specific to the TERS experiments are mentioned here.

As incident light source, a continuous wave Helium-Neon laser was used, with $\lambda_i = 632.8$ nm (1.96 eV) very close to the molecular absorption peak (Fig. 4.5). This leads to a resonant Raman excitation via the S_0-S_1 electronic transition of the conjugated π-electron system. Maximum fluence in the focus of the microscope objective of $5 \times 10^3 \ - \ 3 \times 10^4$ W/cm^2 was used.

After passing through a laser-line filter, the incident light is focused onto the tip-sample gap and the tip-scattered light is spectrally selected using a notch filter (Kaisers Holographic Notch-Plus-Filter) and an imaging spectrograph, and detected with a N_2(l)-cooled CCD detector. Even for large enhancements the signal intensities are weak and noise is significant in part due to the strong nonlinear dependence of the enhancement with tip-sample distance. We therefore limited the spectral resolution to 25 cm^{-1} for the tip-enhanced experiments.

The Au nanoscopic tip used here present strong plasmon resonances in the spectral region of interest, leading to enhanced pump (ν_i) and Stokes Raman fields (ν_S) at the apex. A representative linear light scattering spectrum showing the plasmonic behavior of a Au tip is plotted in Fig. 4.5 (Tip plasmon spectrum).

It is important to note that the use of a shear-force and not cantilever AFM is most suitable for the tip-enhanced Raman studies. Due to the short range tip-sample distance dependence of the field enhancement, dynamic non-contact AFM is less suitable. The time-averaged signal is greatly reduced due to the oscillating tip action. Contact AFM, maintaining constant and small tip-sample distance, experiences strong forces, making it unfavorable for probing molecular or soft matter samples. In contrast, in the shear-force arrangement the tip is kept at a constant height of several nanometers above the surface without actual physical contact.

The far-field spectroscopic studies of MG molecules were conducted using a micro-Raman confocal setup, based on an inverted microscope (Zeiss Axiovert 135). The pump light was focused onto the sample using a microscope objective with N.A. = 0.9 and the emitted Raman response was spectrally analyzed using the same spectrometer as for the near-field experiments. With a higher numerical aperture, this setup allows the use of a 1 cm^{-1} spectral resolution, higher than in the near-field case.

Experimental quantification of the near-field Raman enhancement

In contrast to SERS where the quantification of the enhancement is a difficult task in

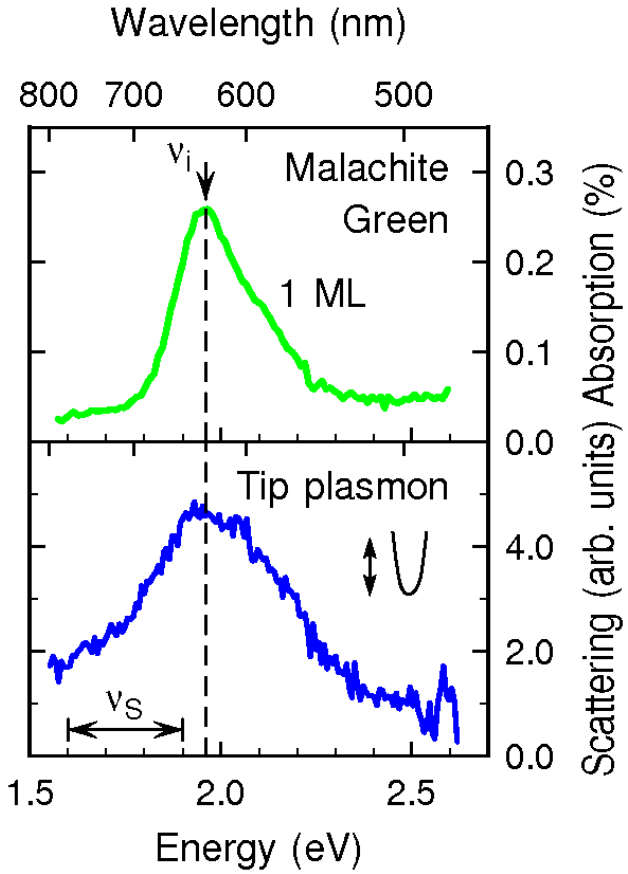

Figure 4.5: Absorption spectrum from 1ML of MG (top). Linear light scattering showing the plasmon resonance of the Au tip (bottom).

general, for the tip-scattering experiment, the enhancement factor can be derived from comparison of tip-enhanced versus far-field response of the same surface monolayer. For the experiments presented here, the integrated Raman signal over the 1150 - 1650 cm^{-1} spectral region is used after background subtraction, as described in Sect. 4.5.

The electromagnetic near-field enhancement originates form a surface area approximated by the area of the tip apex [27], representing the tip-averaged near-field region at the sample surface [275]. For the evaluation of the enhancement factor, the different areas probed in the near-field (TERS) and far-field (FF) cases are then taken into account. For the TERS setup, under orthogonal illumination the focus has a diameter $d = (\lambda/NA)\times 1.5 = 1.7\ \mu m$[iii]. Considering the $\sim 70^\circ$ angle of incidence made by the propagation direction of the pump light with the surface-normal in our setup, the actual surface region illuminated is elliptical and larger, with a total area of about 27 μm^2. In the case of the micro - Raman setup (FF), the laser illuminated area is 870 nm^2. Using the estimation of the MG molecular area, we find that for 1ML surface coverage, approximately 10^6 molecules are in the focus of the far-field setup and only < 200 are responsible for the tip-enhanced signal for a tip with 10 nm apex radius.

Besides the illuminated areas in the laser focus, we must also consider the detection efficiencies for the two different experimental arrangements. The two microscope objectives used cover distinct solid angles, and thus the amount of detected Raman signal is different. Considering the far-field response to be emitted only in half space (solid angle $\Omega = 2\pi$) following an isotropic dipolar intensity pattern, up to 27% of the total Raman signal is detected in the FF case. In contrast, for the TERS experiments only 2% of the total signal is detected by the microscope objective, if we take the emission pattern to follow a $cos^2(\theta + \frac{\pi}{2})$ law ($\theta \in [0, \pi]$). Taking all the above into consideration, the final Raman enhancement factor can be estimated, and was found to vary in the range of 10^6 - 10^9, with the variation mostly depending on the tip used.

Sample preparation

Smooth gold surfaces were produced by vacuum evaporation (Auto 306, Edwards), resulting in films with thicknesses of ~ 100 nm, as characterized by the quartz crystal micro-balance. Carefully cleaned microscope cover glass was used as substrate.

Figure 4.6 displays shear-force topographic images of one of the Au films for both *trace* and *retrace* scanning directions. The 100 x 100 nm^2 area is scanned with 1 nm scanning step (100 x 100 pixels). The surface is found to be flat within the $\sim$2 nm noise level. No topographic structures are present on the sample, which could account for SERS activity. This was verified by both near- and far-field scanning.

Monolayer (ML) and submonolayer coverages of the malachite green (MG) molecules were prepared by spin coating (SCS|G3-8 Spincoat, Cookson Electronics Equipment) from dilute (0.03 and 0.3 mM) ethanolic solutions. The molecular coverage of the prepared samples was estimated comparing the absorption spectra for a known number of molecules with that of the spin coated sample used in the experiments. Absorption spectra of a solution with known concentration (*i.e.*, known number of MG molecules) was taken, and normalized to

[iii] the 1.5 factor is added to account for deviation of the laser beam from a perfect gaussian profile.

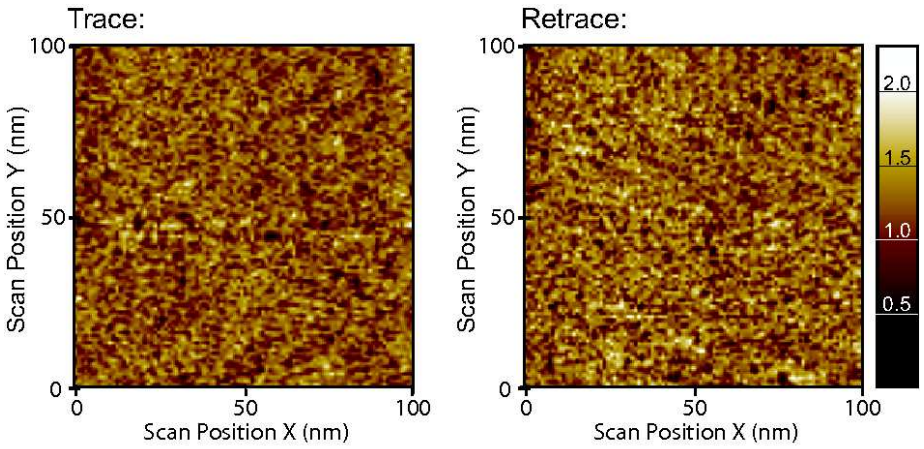

Figure 4.6: Shear-force topographic image of flat Au substrate. Area of 100 x 100 nm is scanned with a 1 nm step (*trace* and *retrace*). The colorbar on the right hand side reads nanometers and holds for both images.

the absorption spectrum of ethanol alone. Part of the solution was spin coated onto a bare cover-glass slide under the same parameters as the real samples: same amount, surface area and spinning parameters.

The spin coated layer was then dissolved in a known amount of ethanol and absorption spectrum was acquired. The direct comparison of the two absorption spectra allows the deduction of the total number of MG molecules present onto the cover glass sample. Note that the outer region of the glass slide was cleaned carefully, since in that region the spin coated molecules clustered, and all the experiments were done within the central region of the samples. In separate test experiments it was verified that the molecular coverage of the bare cover-glass is similar with the one of a Au-covered sample.

Considering the known surface area of a molecule and with the sample total surface measured to be 108 nm^2, this gives a number of N = 1.24 x 10^{14} MG molecules spread into one homogeneous monolayer. It was found that in the case of the 0.3 mM solution the sample is covered with $\leq$2 monolayers of MG molecules, while for the 0.03 mM concentration, the sample is covered with only < 0.5 monolayers.

Note that the above estimation represents an upper limit of the actual molecular coverage, since it was considered that the molecules lay flat and are closely packed onto the surface, with no empty spaces in between. Raman spectra were acquired on different randomly chosen regions of the sample and resulted in similar intensity levels within experimental uncertainty, indicating a rather homogeneous distribution of molecules on the surface.

4.5 Results

Near-field character and far-field artifacts in TERS

TERS manifests itself in an enhancement of the Raman response, with the increase confined to the region underneath the tip-apex. However, with the illumination extended on a larger

surface region determined by the far-field focus, the discrimination of the variation of far-field response due to the presence of the tip inside the focus is difficult in general [27].

Without any lateral scanning or systematic vertical tip-sample distance variations this in general does not allow for the unambiguous assignment of the observed optical effect to a near-field process. The apparent Raman signal rise may be due to far-field effects occurring when the tip is scanned inside the tight laser focus that can influence both signal generation and detection. With the tip penetrating into the focus region it would allow to scatter additional, otherwise forward-scattered (non-enhanced) far-field Raman light back into the detector. Furthermore, the interference of tip-scattered, surface reflected and incoming pump light results in locally enhanced pump intensities. With both processes affecting a surface region not confined by the apex area, they can dominate over the near-field effects.

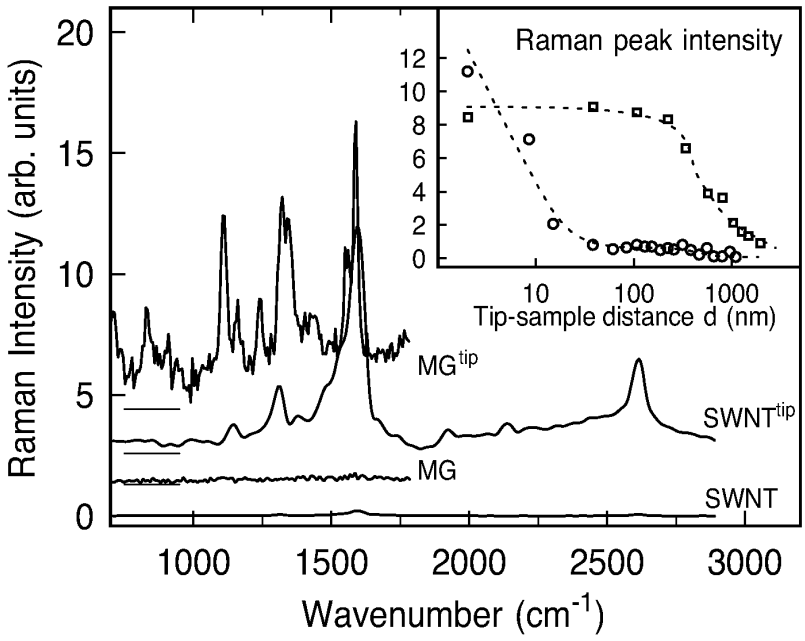

Figure 4.7: Near-field signature vs. far-field artifact: Raman spectra of single-walled carbon nanotubes and MG molecules with tip retracted (SWNT, MG) and tip engaged (SWNT^{tip}, MG^{tip}). Inset: tip-sample distance dependence of the Raman signal obtained under similar conditions but displaying very different behaviors: the ∼20 nm length scale increase is characteristic for the near-field signal origin (circles); the few hundred nanometer decay length (squares) shows a far-field artifact - leading to similar signal increase as the near-field response. Dashed lines added as guide for the eye.

In Fig. 4.7 tip-scattered Raman results are shown for single-wall carbon nanotubes (SWCN) and and monolayers (ML) of malachite green (MG) molecules with the tip in force feedback at $d = 0$ nm, versus tip retracted by several 100 nm. Note that here and in the following, d=0 is defined as corresponding to a 20-30% decrease in the shear-force amplitude. When the tip is within several nanometers above the sample surface, a strong increase in Raman intensity is observed for both adsorbates (spectra denoted SWNT^{tip} and MG^{tip}). Note that the difference in noise level from the SWNT to the MG spectra is due to different spectral

resolution settings of the spectrometer. Despite being frequently applied to assign the observed signal to TERS [276] simply comparing surface vs. tip scattered Raman intensities near- and far-field processes are *a priori* indistinguishable. The inset of Fig. 4.7 shows the Raman peak intensity as a function of the tip-sample distance obtained in two similar experiments for monolayers of MG molecules adsorbed on flat Au surface. The overall increase in signal is comparable in both cases, and an estimate of the Raman enhancement factor gives G $> 10^6$ (*vide supra*). However, with the distance variation occurring on a length scale correlated with pump wavelength or focus dimensions, in one case the enhancement can solely be attributed to far-field effect (squares). A true near-field effect manifests itself in a correlation of the spatial signal variation with the tip radius ($\sim$ 20 nm). Here, with high quality tip (sharp apex, smooth tip shaft), the near-field contribution can dominate the overall signal (circles).

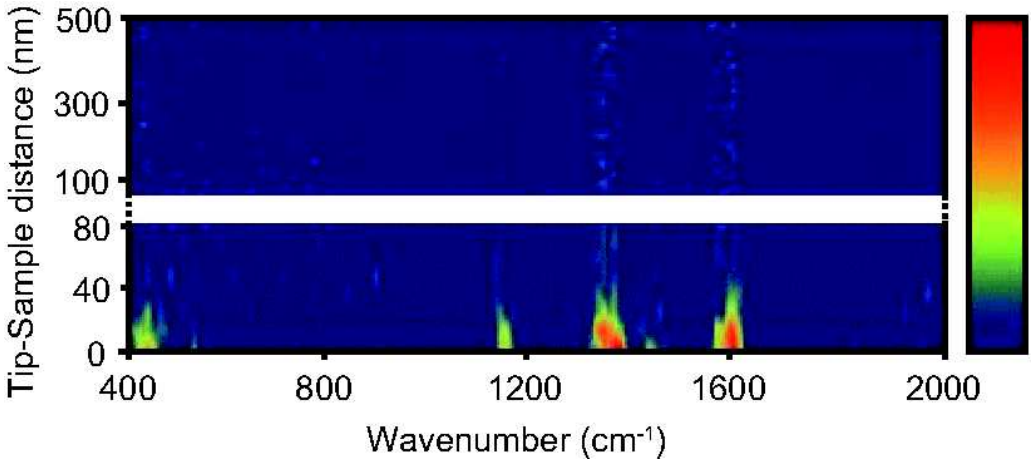

Figure 4.8: Tip-sample distance dependence of spectrally resolved Raman signal during approach of $\sim$ 1 ML of MG on gold. Each spectrum is acquired for 1 s and the approach is realized with 2 nm increments. Near-field tip-enhanced signal is observed with the tip within $\sim$ 20 nm above the sample, displaying typical Raman modes for MG molecules (see text).

Fig. 4.8 shows the spectrally resolved tip-scattered Raman signal during approach of $\sim$ 1 ML of MG on gold (2 nm/step, 1 s/spectrum acquisition time). The pump light is polarized along the tip axis (p^{in}) and the Raman signal is detected unpolarized. Although a faint Raman signature of the molecules is observed with the tip far away, a clear molecular fingerprint is obtained only when the tip is within $\sim$20 nm from the sample. The prominent bands around 1615 cm^{-1} and 1365 cm^{-1} are assigned to combinations of the C=C stretching vibrations of the phenyl ring and the mode at 1170 cm^{-1} is due to a methyl group rocking mode or an in-plane C-H bending mode of the phenyl ring [277]. The details of mode assignment are discussed below, in Sect. 4.6.

The enhancement is confined to a tip-sample spacing of just several nanometers and correlated with the apex radius of the tip, as expected for the near-field signature. The increase in Raman response is accompanied by a weak rise in a spectrally broad fluorescence background which has been subtracted in Fig. 4.8. With the molecular fluorescence being

quenched due to the electronic coupling to the metal substrate, this emission can largely be attributed to the enhancement of the intrinsic tip fluorescence [278] as evident from the control experiment shown in Fig. 4.9. Here, the spectra are acquired from the tip alone (Au tip) and from the sample alone (Au surface), respectively.

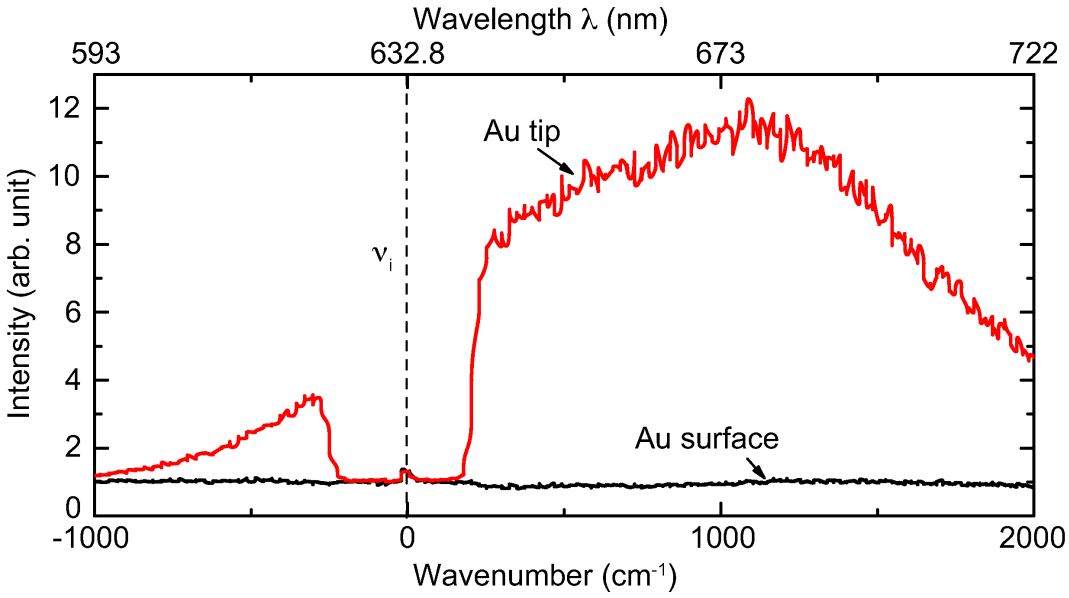

Figure 4.9: Spectra of clean Au tip and surface showing intrinsic fluorescence from the tip alone (red) as opposed to the very weak response of the Au-surface (black). The spectral discontinuity visible around the pump frequency ν_i is due to the presence of the notch filter.

Fig. 4.10 shows the field enhancement factors (E/E_0) for the integrated Raman signal from $\sim$ 1 ML of MG on gold as a function of tip-sample distance for two different Au tips (r < 15 nm). The signal is integrated over the 1150 - 1650 cm^{-1} spectral region after background subtraction. Maximum enhancements of 93 and 65 (black and blue curves, respectively) are obtained considering variation of the tip-scattered Raman response with the forth power of the electrical field, as indicated above.

The study of the polarization dependence of the Raman response offers additional insight into the electromagnetic enhancement of TERS. Fig. 4.11 shows near-field Raman spectra from $\sim$ 1 ML of MG on gold for the different polarization combinations of both pump and Raman light. Incident laser power and acquisition times are identical for all spectra. The polarization directions are defined as parallel (p) and perpendicular (s) with respect to the plane of incidence formed by the incoming wave vector k(ω_i) and the tip axis. No background has been subtracted and the data are normalized with respect to the intensity of the 1615 cm^{-1} mode measured in p^{in}/p^{out} configuration (upper left panel).

With the incident field polarized perpendicular on the tip axis (s^{in}), almost no Raman signal is observed, irrespective of the polarization of the scattered light. In contrast, with the pump polarized along the tip axis (p^{in}), clear Raman fingerprints of MG molecules are observed with the Raman response being predominantly polarized parallel to the tip

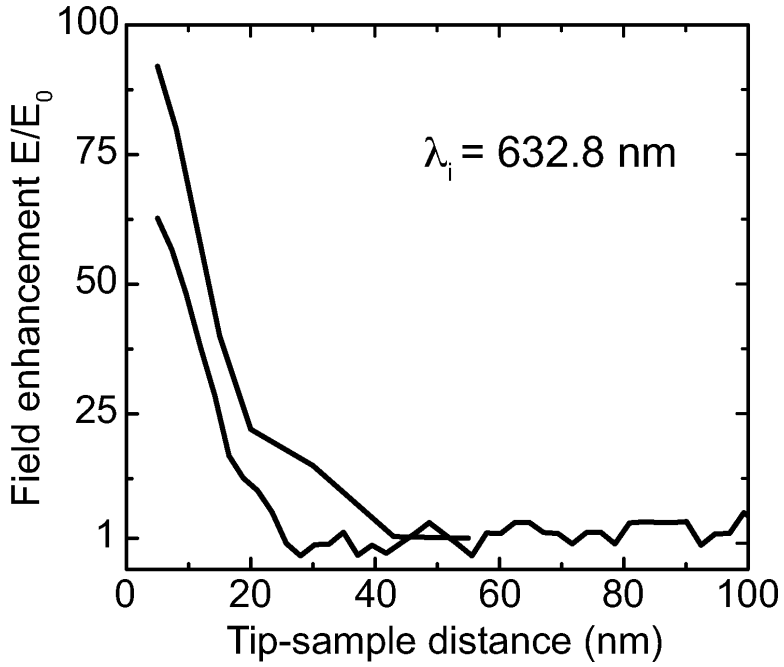

Figure 4.10: Field enhancement (E/E_0) for two different Au tips approaching ~ 1 ML of MG on gold. The Raman response is integrated over the 1150 - 1650 cm^{-1} spectral region after background subtraction and the enhancement factors are calculated according to $I_{TERS} \propto E^4$.

(p^{in}/p^{out}) as expected for near-field TERS from isotropically distributed molecules with diagonal Raman tensor components as the case of MG. For both s^{in}/p^{out} p^{in}/s^{out} configuration, weak overall signal is observed due to the absence of the tip-sample optical coupling. For s^{in}/s^{out} a larger background is observed, albeit with no Raman enhancement, as expected.

TERS of molecular adsorbates

One of the most important observations is the change in the Raman signature of MG molecules with the degree of near-field enhancement. In Fig. 4.12 several tip-scattered near-field enhanced Raman spectra are shown. They are taken for the same surface coverage of $\sim$ 1ML of MG, but using different tips exhibiting enhancements of 3×10^8 (a), 7×10^7 (b), 1×10^7 (c), and 1×10^6 (d), respectively. The experimental uncertainty is estimated at a factor of 3 – 5 for each value. Note that the tip-enhanced Raman spectra are reproducible for a given tip, but as seen from the data, their spectral details vary from tip to tip.

With the lateral confinement of the tip-enhancement within a $\sim$ 10 nm diameter surface region and a molecular density of $\sim 1/nm^2$ we estimate that the signal observed in Fig. 4.12 a) - d) originates from of order 100 molecules. In the lower panel of the figure the far-field Raman spectrum from the same sample is shown for comparison (black line). The spectrum closely resembles that in aqueous solution [277] indicating that the molecules are physisorbed in isotropic orientation at the surface. The blue bars represent normal

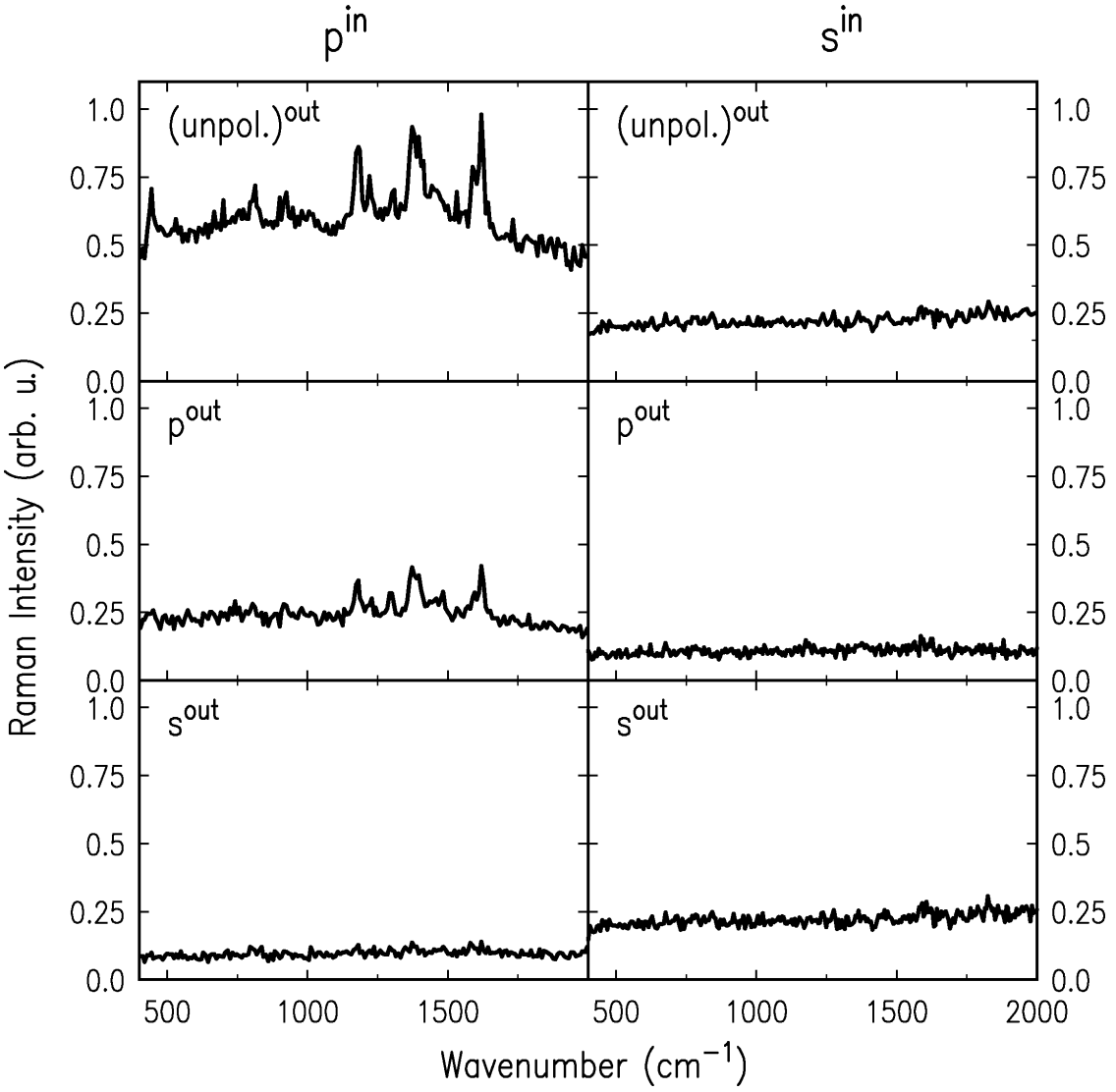

Figure 4.11: Polarization dependence of the near-field tip-enhanced Raman response originating from $\sim$ 1 ML of MG on gold. All spectra are acquired for the same time and normalized to the maximum intensity value of the 1615 cm^{-1} mode in p^{in} - (unpol.)^{out} geometry. Very weak Raman response is observed with the pump polarized perpendicular on the tip axis (s^{in}), in contrast with the (p^{in}) case where the MG Raman modes are present.

Raman modes of the MG anion calculated using density functional theory as implemented in Gaussian03 [279] and discussed below.

The tip-enhanced Raman response is notably different in terms of the relative peak amplitudes compared to the far-field Raman spectrum. This characteristic difference is the result of the strong optical field localization, and may be related to different selection rules for the tip-scattered Raman response - akin to SERS [280] - as discussed later on. For weak enhancement (Fig. 4.12 c and d) the tip-scattered spectra closely resemble the far-field response. However, with increasing enhancement of 7×10^7 (b), and most pronounced for

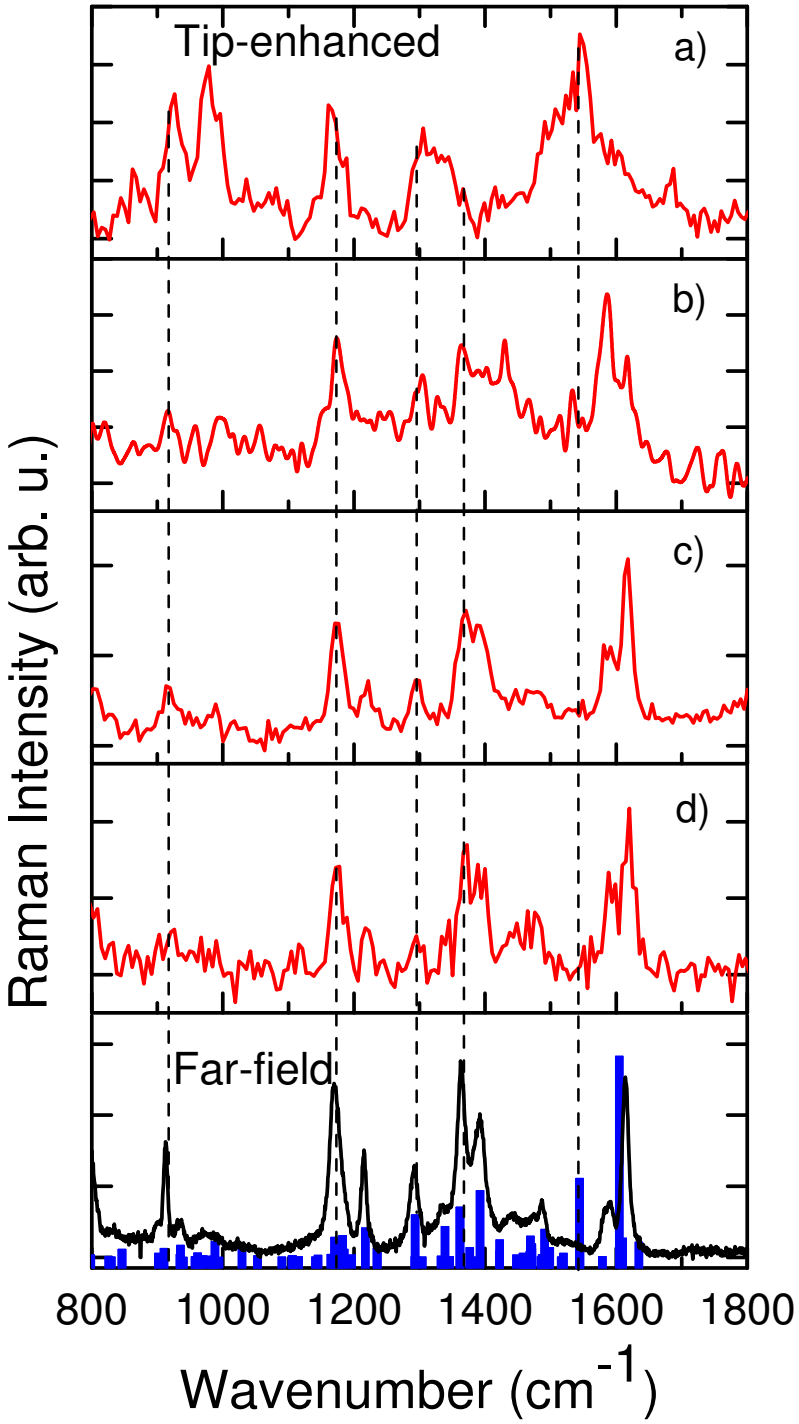

Figure 4.12: Tip-enhanced Raman spectra for $\sim$ 1 ML of MG for different degrees of enhancement (a,b,c,d) in comparison with the corresponding far-field Raman spectrum (bottom graph) and DFT calculation for the mode assignment (blue bars). The Raman enhancement factors derived are 3×10^8 (a), 7×10^7 (b), 1×10^7 (c), and 1×10^6 (d), respectively. Data are acquired for 1 s (a), 100 s (b,c), and 30 s (d), respectively. Spectral resolution is 25 cm^{-1} for the near-field and 1 cm^{-1} for the far-field spectra.

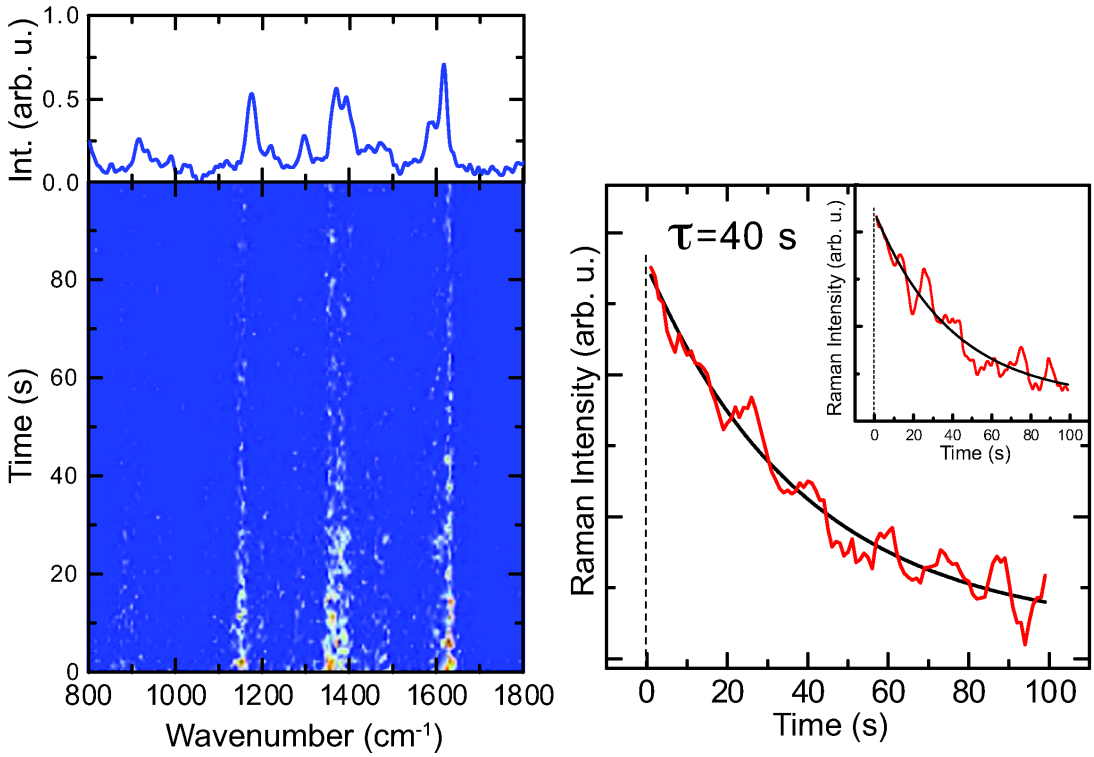

Figure 4.13: a) Time series of 100 consecutive near-field Raman spectra (acquired for 1 s each) for ~ 1 ML MG on Au (Raman enhancement 1.3×10^7). The sum Raman spectrum clearly resembles the far-field spectrum.
b) Bleaching kinetics derived for the spectrally integrated Raman time series and the region from 1550 to 1650 cm^{-1} (inset). An exponential decay constant of $\tau = 40 \pm 5$ s is derived.

3×10^8 (a), the vibrational modes start to look markedly different. While some of modes are present in both far-field and near-field spectra (*e.g.*, 920 cm^{-1} , 1170 cm^{-1} , 1305 cm^{-1}), some other are characteristic for the highly enhanced near-field results (*e.g.*, 1365 cm^{-1} , 1544 cm^{-1}). Vertical dashed lines in Fig. 4.12 are shown at these representative vibrational modes.

The spectral variations of the Raman features observed for high enhancements when compared with the far-field spectrum call for the question, whether they are due to structural changes and the signature of decomposition products of the molecules or whether they are indeed intrinsic to MG and a result of, *e.g.*, the large field gradient in the tip-sample gap as suggested in [214]. In the following results of control experiments are discussed which support that the effect is intrinsic and decomposition products and/or carbon contamination do not affect the Raman response in our experiments.

Molecular bleaching

Resonant Raman excitation offers additional enhancement, but is more susceptible to

photo-chemical degradation of the molecules [281]. To probe for the possible appearance of photoreaction products and their signature in the Raman spectra, the evolution of the Raman emission is monitored in time-series experiments. Fig. 4.13 a) shows consecutive near-field Raman spectra acquired for 1 s each for an enhancement of 1.3×10^7 with an incident laser fluence of 3×10^4 W/cm^2. The molecules bleach on a time scale of ~ 100 s and the signal decays to zero. During the bleaching no new spectral features appear from possible photoreaction products. Also, the signal decays with the relative peak amplitudes remaining constant. After complete bleaching no discernible Raman response can be observed.

The fluctuation observed in the time series is expected given the small number of ~ 100 molecules probed in the near-field enhanced region under the tip apex and the likely surface diffusion of the molecules. The sum over all spectra (top graph) or the sum of any large enough subset even at later times, *i.e.*, after substantial bleaching has already occurred, closely resembles the far-field response of MG and thus allows to attribute the Raman response to MG molecules.

The same behavior of a gradual and homogeneous disappearance of the Raman response without a relative change in peak intensity is also observed for larger enhancements, *i.e.*, the case where a different mode structure is observed. However, the larger local field experienced by the molecules leads in general to decreasing decay time constants.

Fig. 4.13 b) shows the decay kinetics of the spectrally integrated intensity for the Raman time series shown in panel a). This is shown in comparison to the integral intensity of the region from 1550 to 1650 cm^{-1} encompassing only the two prominent modes (inset). Assuming an exponential decay behavior of $I/I_0 = \exp(-t/\tau)$ for the Raman intensity a decay time $\tau = 40 \pm 5$ s is derived from the fit in both cases (solid lines). From the applied laser fluence of 3×10^4 W/cm^2 and the enhancement of the pump intensity of $\sim \sqrt{1.3 \times 10^7}$ the bleaching would be induced by a local pump fluence of 4.7×10^7 W/cm^2.

An extreme case of molecular bleaching is shown in Fig. 4.14. A time series of 100 consecutive Raman spectra from a sample with submonolayer molecular coverage, with each spectrum acquired for 1s is recorded. The estimated Raman enhancement factor is 9x10^7 and, as clearly seen, the spectral features deviate from the far-field Raman spectrum presented in Fig. 4.12 d, akin to the ones shown in the same figure panels a) and b) for high enhancement level (*e.g.*, the mode at 1544 cm^{-1}). After an illumination time of about 50 s, the overall Raman intensity drops suddenly over the whole spectral region, and most visible for the peak at 1306 cm^{-1}. With this being a clear indication that the probed molecules undergo a bleaching process, it is interesting to note that no new features are discernible in the subsequent spectra recorded, nor does the relative Raman intensity change. A physical degradation of the tip and thus a decrease in Raman enhancement can be out-ruled here, since this would lead to an overall change in spectral signature, not seen in the data. Thus even for extreme cases as the one presented here, the molecular decomposition products do not contribute at all to the observed Raman signal.

Carbon Raman response

With the experiments carried out under ambient conditions, special care must be taken to use clean samples and tips. It is well known [282] that contaminating carboniferous species

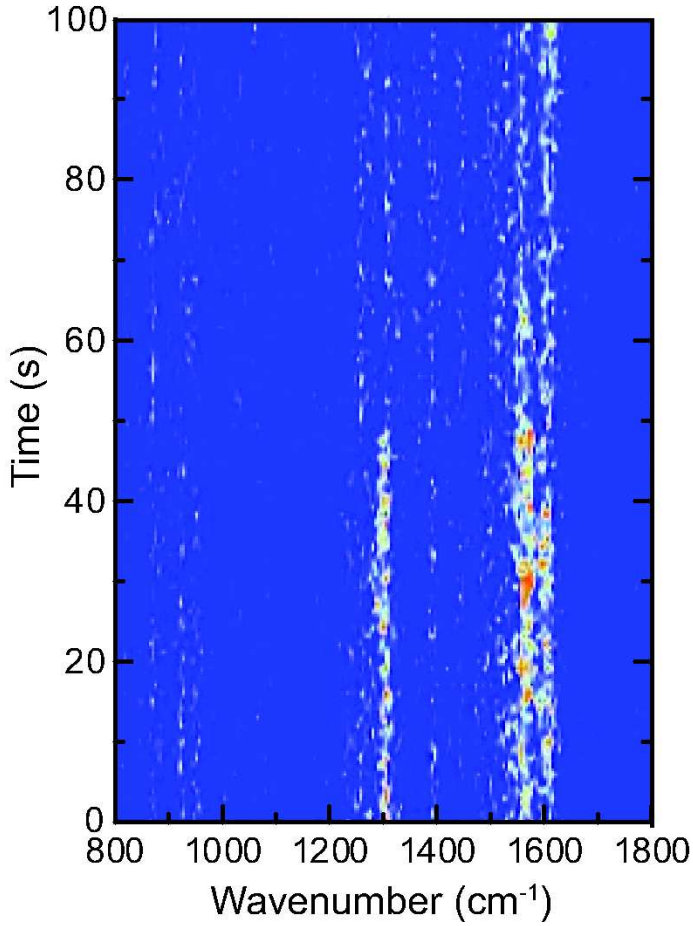

Figure 4.14: Time series of 100 NF Raman spectra acquired for 1s each. After ∼50 s the Raman intensity reduces due to bleaching, but no signature of secondary products is visible.

and/or carbon clusters can adhere to either tip or sample and reveal their Raman signature in the tip-enhanced spectra, *e.g.*, Raman bands of appreciable intensity at frequencies above 1750 cm^{-1} [283].

Carbon clusters and carboniferous decomposition products exhibit Raman bands of appreciable intensity at frequencies above 1750 cm^{-1} [283]. Fig. 4.15 shows experimental Raman spectra for the energy range beyond 2000 cm^{-1}. The tip-scattered spectrum (red) is obtained for ∼1 ML MG molecules and the enhancement is estimated to $\sim 10^8$. The spectrum displays the characteristic near-field enhanced Raman modes of MG for high enhancement, different from the far-field ones (blue spectrum). Even for this high enhancement our near-field spectra do not show significant features above 1700 cm^{-1} , which are expected for a carbon response. Note that C–H stretching modes below 3000 cm^{-1} are not resonantly enhanced and their absence in the spectra is in accordance with corresponding spectra in solution.

For comparison, in the following we analyze a carboniferous Raman response. Fig. 4.16 shows a time series of consecutive tip-enhanced Raman spectra acquired for 1 s each from a multilayer of photodecomposed MG. The observed behavior is characteristic for Raman

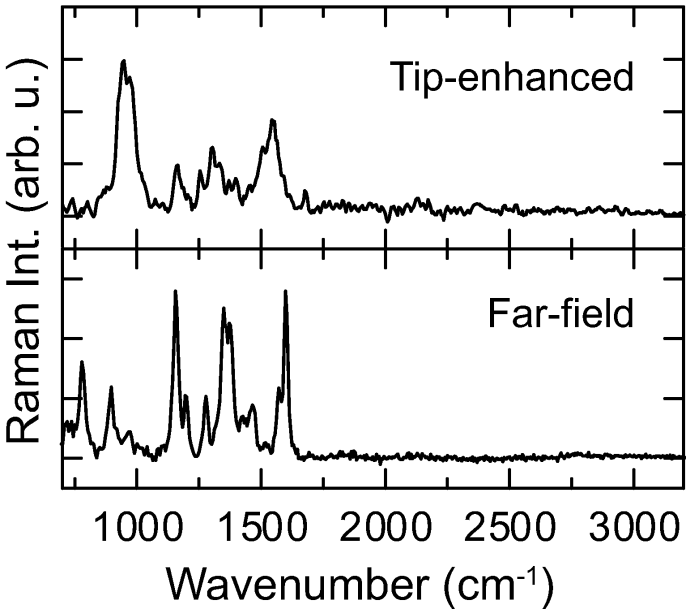

Figure 4.15: Tip-enhanced (enhancement $\sim 10^8$) and far-field MG Raman spectrum for ~ 1 ML of MG including the higher energy spectral range. Although spectrally different from the far-field response the absence of any spectral signature above 1700 cm^{-1} for the tip-enhanced response contrasts the observation for carbonaceous species.

scattering from carbon clusters and very distinct from the spectral response discussed above for monolayer or submonolayer MG in several ways: First, in accordance with previous observations [283, 284, 282], the Raman response is comparatively large and fluctuates rapidly and in an uncorrelated way. This behavior is very different compared to all our observations for MG. Second, by contrast to the data in Fig.4.15, a distinct spectral feature emerges around 2000 cm^{-1} which has been assigned to, for instance, modes within the segments of carbon chains [283].

Third, this carbon Raman response is due to extended carbon chains and aggregates which can readily form by multilayer MG decomposition. In contrast, at ambient temperatures, one would expect that the bleaching of monolayer and submonolayer coverages (< 0.01 ML for the single molecule experiment presented below) leads to smaller molecular fragments and subsequently to a dilute surface carbon distribution. Fourth, large Raman cross sections are reported for carbon clusters and carbonaceous species in SERS consistent with the strong signals observed in Fig. 4.16. Should they have formed in our experiments, they would have manifested themselves in an appreciable Raman response in the time series experiments.

Besides the degradation of the analyte, another potential source of carbon contamination is the near-field probe itself. At room temperature and in a non-controlled atmosphere, contamination molecules from the environment could stick to the tip surface and reveal highly enhanced Raman signals. In order to discriminate this unwanted signature from the MG one, two kinds of control experiments were performed: (i) for a contaminated tip, the observed signal should persist upon retracting the surface for several tens of nanometers - out of the enhancement region of the tip - and maintaining the tip in focus. (ii) the

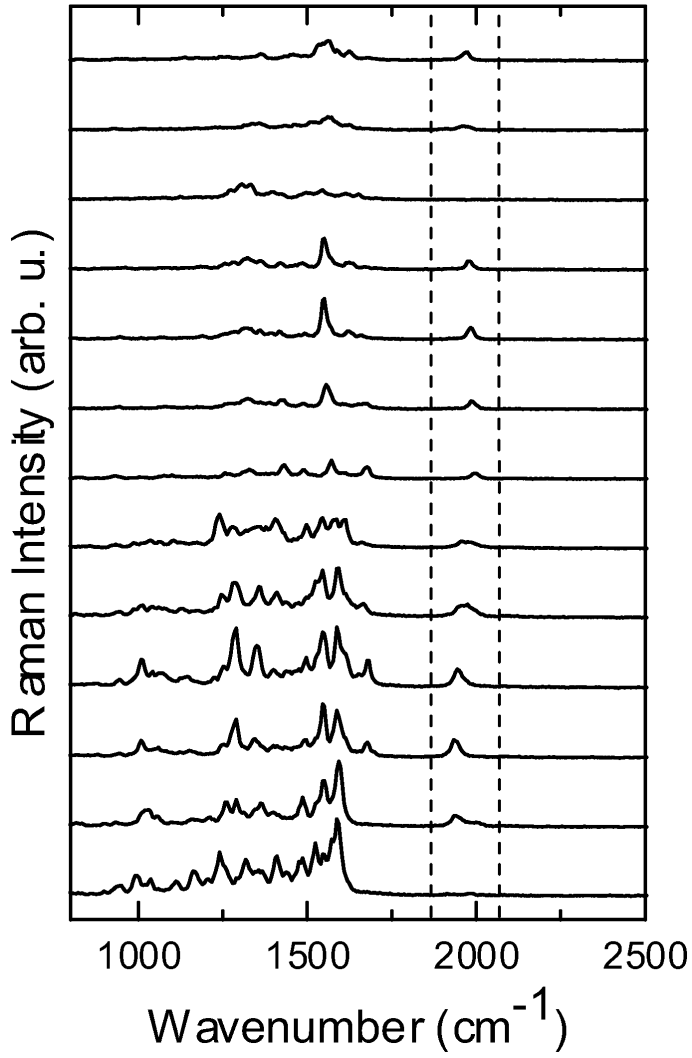

Figure 4.16: Time series of consecutive near-field Raman spectra acquired for a photodecomposed MG multilayer. The large and uncorrelated spectral fluctuations and the band at 1870 - 2100 cm^{-1} are characteristic for carbon clusters.

MG covered substrates were exchanged with clean Au surfaces, and TERS spectra were recorded with the same tips. In conclusion, the lack of any Raman signal in both cases is a strong indication of the absence of a response from either decomposition products or carbon impurities.

4.6 Discussion

The results presented in Fig. 4.7 reveal that only the demonstration of a clear correlation of the lateral or vertical tip-molecule distance dependence with tip radius allows for an unambiguous near-field assignment of the optical response [27], as is true for all near-field microscopies including *s*-SNOM and the special case of TERS [10, 238, 12, 174].

The highly polarized TER response observed in our experiments indicates the absence of significant near-field depolarization, for the homogeneous and slender tip geometries used. This is required for symmetry selective probing in TERS and other nonlinear tip-enhanced processes that rely on polarization-selective and -conserving light scattering [43, 285, 286, 287]. In contrast, for a Ag particle-topped quartz AFM probe as used for probing the 520 cm $^{-1}$ Raman band of Si [288] the observed Raman depolarization has been attributed to the wide cone angle of the tip [289].

In our experiments we expect the enhancement to be purely electromagnetic in origin. As discussed above and similar to SERS, the total Raman enhancement factor G is given by [204, 27]:

$$G = L^2(\nu_i)L'^2(\nu_s) \tag{4.10}$$

Although different, the field enhancement factors for pump and Raman-shifted frequencies ($L(\nu_i)$ and $L'(\nu_s)$, respectively), can be assumed to be similar for the purpose of the present study [290, 291]. This is motivated by both the spectrally broad plasmonic resonance of the tip - described in Chapter 3 - and its red-shift upon approaching the sample surface [119, 129, 275]. Accordingly, the observed enhancement of $2\times10^7-3\times10^8$ would correspond to average local field factors of 70 – 130.

In addition, the molecules adsorbed onto the planar Au surface experience further enhancement given by the Fresnel factor [292]. Therefore, the total enhancement observed here must be defined with respect to the free molecule response. This translates into a Raman enhancement of up to 5×10^9.

From comparison of different tip materials as well as pump and Raman polarizations we find that the source of this strong amplification of the local optical field for the Au tips is the excitation of the axial plasmon resonance of the tip [83]. That plasmon mode is evident from the spectral tip Rayleigh scattering response [83], as shown in Fig. 4.4, and it gives rise to a local field enhancement in the range of 10 to 25 for free standing tips [47].

In the presence of the metal surface, strong optical coupling between the metallic tip and substrate is effective. This coupling is a manifestation of the boundary conditions for the optical field in the gap imposed by the substrate plane (mirror image) [212] as covered in Chapter 3.

The effect is seen in Fig. 4.17 where the field distribution is calculated for a Au hyperbolic tip of apex radius $r = 10$ nm with (b) and without (a) sample. Taking advantage of the small dimensions of the tip apex compared to the optical wavelength ($kr \ll 1$, with k the wave vector), the problem is treated in the quasistatic approximation which allows solving the Laplace equation analytically for certain geometries [162, 33, 105, 132, 129, 293, 294, 295, 275] and retardation effects can be neglected [296, 103].

The calculation is performed for a tip-sample distance of 10 nm. The presence of the surface leads to a further increase in the lateral field confinement and to a local field enhancement an order of magnitude larger compared to corresponding values for the bare tip. With values for the local field enhancement of order 10 at the apex of the bare tip and 70 at the substrate surface in the presence of the tip, this model calculation is in good accordance with these and other experimental results and more accurate theoretical descriptions [297, 126]. The detailed description of the model is given in [275].

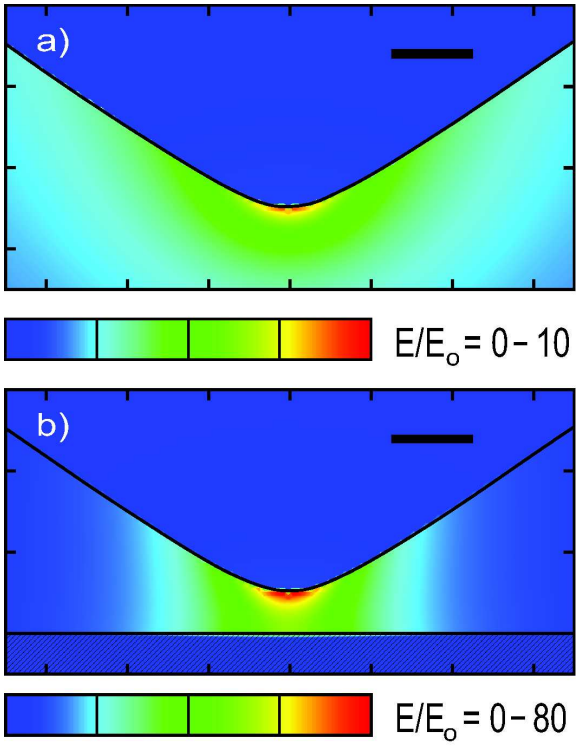

Figure 4.17: Calculated local field distribution and enhancement E/E_0 for a Au hyperbolic model tip with $r = 10$ nm, free standing (a) vs. near Au sample at $d = 10$ nm distance (b). Scale bar = 10 nm.

To facilitate the identification of the underlying Raman selection rules we performed a computation of the normal modes and polarization derivative tensor elements $\partial\alpha/\partial Q$ for the MG anion using density functional theory (B3LYP/6-31G(d,p)) as implemented in Gaussian03 [279]. The vibrational Raman frequencies obtained, scaled by a factor of 0.975 are shown in Fig. 4.12 lower panel (blue bars). The assignment and spectral position of the calculated modes agree well with the values published in the literature [277, 298].

The DFT calculations allow the identification of the spectral features in the far-field spectrum of Fig. 4.12. The majority of the intense Raman modes can be attributed to modes either localized at the phenyl ring or delocalized over the two dimethylamino phenyl rings. Cartoons for two of these Raman modes are presented in Fig. 4.18 : the peak at 1170 cm^{-1} is attributed to the rocking methyl group bending mode. At 1615 cm^{-1} another intense mode is present and is due to a combination of C=C stretching motions of the aromatic ring.

Furthermore, the calculations show that the new spectral features seen in the highly enhanced near-field spectra Fig. 4.12 may correspond to vibrational modes of MG, as discussed here. Several Raman features are present in both the far-field and the strongly enhanced near-field spectra. Prominent Raman modes at 920 cm^{-1}, 1170 cm^{-1}, 1305 cm^{-1} appear for all enhancements. In the spectral region of 910 cm^{-1} to 980 cm^{-1} several vibrational

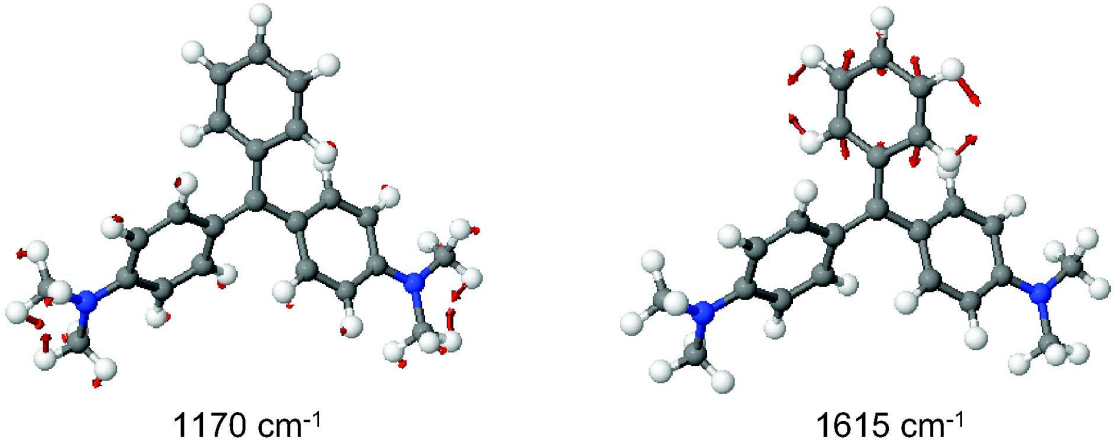

Figure 4.18: Cartoons of normal Raman modes of the MG anion at 1170 cm^{-1} and 1615 cm^{-1} . According to DFT calculation performed, they are assigned to the rocking methyl group bending mode and to a combination of C=C stretching motions of the aromatic ring, respectively.

modes, typically characterized by in-plane skeletal bending and/or out-of-plane C−H motions, are found. The 1170 cm^{-1} mode may be assigned to a methyl group rocking mode or an in-plane C−H bending mode of the phenyl ring. Around 1300 cm^{-1}, in-plane C−H deformation modes and C−C stretching modes of the methane group are located (Fig. 4.19 a).

Among the characteristic near-field enhanced modes, the peak at 1365 cm^{-1}, which is very strong in the far field spectrum, but decreases with increasing enhancement, can be assigned to combination of C=C stretching motions of the aromatic ring. In contrast, the prominent peak at 1544 cm^{-1} which dominates for the highest enhancement is very weak for small enhancements or in the far-field spectra. Here, the calculation shows a mode characterized by stretching motions combined with in-plane C−H bending motions of the conjugated di-methyl-amino-phenyl rings (Fig.4.19 b). The two modes at 1585 and 1615 cm^{-1}, which can be assigned to C=C stretching vibrations of the phenyl ring, decrease with enhancement.

This change in both intensity and spectral signature with increasing near-field enhancement together with the vibrational analysis shows that the peaks observed may well correspond to vibrational modes of MG, whereby different selection rules must apply for the Raman spectra obtained under condition of high enhancements [204].

The pronounced spectral difference between the tip-enhanced and far-field Raman response resembles the observation made in SERS, where vibrational modes which are normally not Raman allowed are found [299, 300]. In an experiment by Moskovits *et al.* [301] involving benzene adsorbed on Ag, it was found that the modes of the metal-adsorbed molecules were shifted and additional Raman modes appeared with intensities about the same with those active in the case of free molecule. Aside from orientational effects, these spectral variations are typically interpreted to arise from conformational changes and/or transient

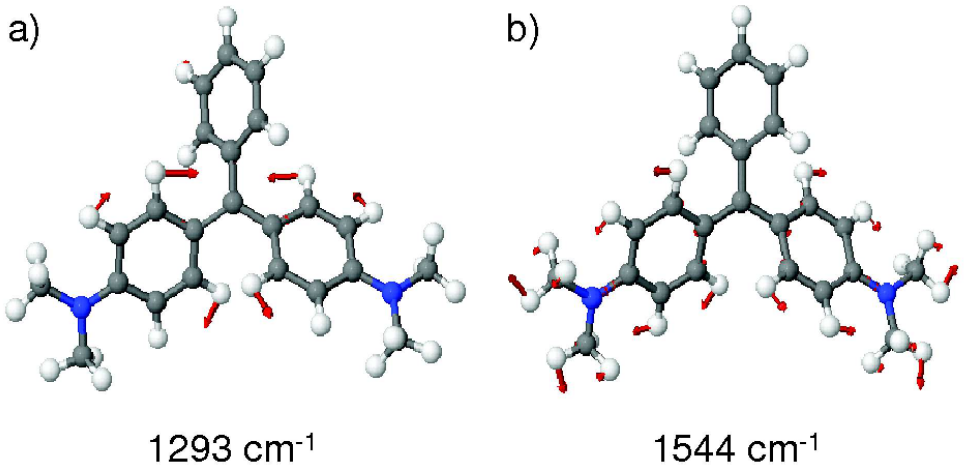

Figure 4.19: Illustration of calculated Raman active normal modes of the MG molecule at 1293 cm^{-1} (a) and 1544 cm^{-1} (b). a) In-plane C−H deformation mode together with C-C stretching of the methane group. This mode is observed in all near-field spectra irrespective of the enhancement level. b) skeletal stretching motions combined with in-plane C−H bending motions of the conjugated di-methyl-amino-phenyl rings. This mode is not present in the FF spectrum, but its intensity grows with the near-field enhancement (see Fig. 4.12).

covalent binding of the molecule at "active sites" [205]. With that being unlikely in the tip-enhanced Raman geometry discussed here, this indicates that purely electromagnetic mechanisms can already induce the kind of spectral selectivity observed in this experiment.

Due to the high localization of the optical near-field, the molecules in the tip-sample gap experience a large field gradient. In that case, different Raman symmetry selection rules can come into play, in general [302, 213, 280]. A description of the mechanism by which strong field gradients can influence the molecular Raman spectra by altering the selection rules is realized by Ayars *et al.* [214]. They find that the relevant terms of the dipole moment μ_a of a molecule situated in the presence of a high field-gradient are:

$$\mu_a = \Big\{ \underbrace{\left(\frac{d\mu_a^p}{dQ}\right)_0 E}_{ir} + \underbrace{\left(\frac{d\alpha_{ab}}{dQ}\right)_0 E}_{Raman} + \underbrace{\alpha_{ab}\left(\frac{dE}{dQ}\right)_0}_{GFR} + \underbrace{\frac{1}{3}\frac{\partial E}{\partial c}\left(\frac{dA_{abc}}{dQ}\right)_0}_{QuadrupoleRaman} \Big\} Q \tag{4.11}$$

with E the amplitude of the applied electric field, μ_a^p the permanent molecular dipole moment, α_{ab} the polarizability tensor at vibrational frequency and A_{abc} the quadrupole polarizability. Q represents the coordinate of vibration and $\{a, b, c\}$ are a permutation of the coordinates $\{x, y, z\}$.

The first term on the right hand side of Eq. 4.11 results in ir absorption. For an ir mode to be active, a variation in the dipole moment along the vibration coordinate is necessary [303]. The presence of the field gradient fulfills this requirement and thus allow for ir modes to become Raman active.

Fig. 4.20 shows the experimental ir spectrum of the MG as measured in KBr (black line) together with the near-field Raman spectrum (dotted blue line) obtained for the highest

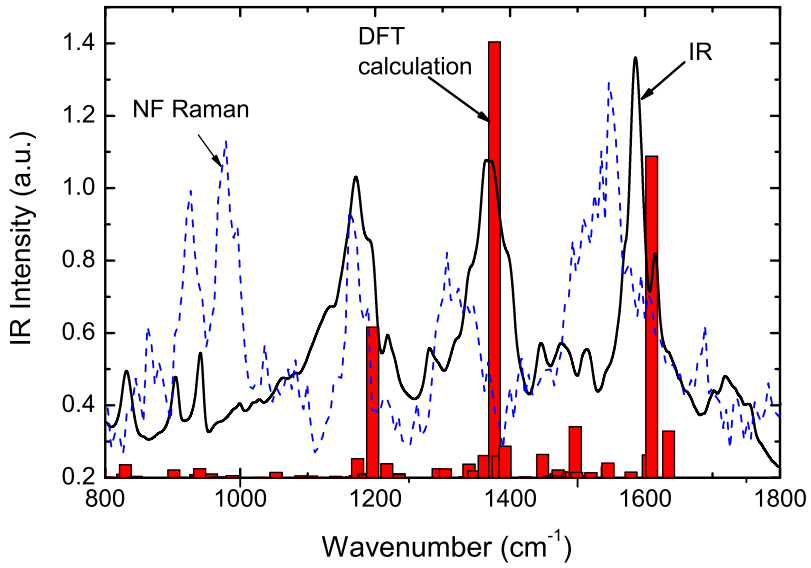

Figure 4.20: ir experimental spectrum as measured in KBr (black solid line) and DFT calculation of ir normal modes (red bars) for MG molecule. Highly enhanced near-field Raman spectrum (shown previously in Fig. 4.12 panel a) is shown for comparison (blue dashed line).

enhancement (previously shown in Fig. 4.12 upper panel). The tip-enhanced Raman spectrum, however, shows no resemblance to the few ir-active modes of MG and identified with the help of the DFT calculation (red bars). The conclusion holds for all the other experimental spectra.

The second term in Eq. 4.11 describe the normal Raman emission, where only a change in polarizability ($d\alpha_{ab}/dQ$) leads to active modes. The next term denotes the Gradient Field Raman (GFR) effect. It requires that the electric field belongs to the same symmetry species as the vibration ($dE/dQ \neq 0$) and the polarizability (α_{ab}) must simultaneously be nonzero. The resulting selection rules resemble the surface selection rules [205], and result in GFR lines which complement the Raman spectra. According to [214] the presence of GFR modes cannot be proven but strong circumstantial evidence comes from normally forbidden modes, akin with the experimental result presented in this work. Similar differences between far- and near-field Raman spectra were reported previously in the literature [265, 266].

In addition, the field gradient can also couple to vibrations via the derivative of the quadrupole polarizability A_{ijk} of a mode ($\propto \partial A_{\mathrm{ijk}}/\partial Q\, \nabla \mathbf{E}$) [280]. With α_{ab} and A_{ijk} transforming differently in terms of symmetry and their ratio being highly mode dependent this could account for the mode selectivity observed in tip-enhanced Raman scattering. Although the calculation of A_{ijk} is still deemed challenging for large molecules it might contribute to a unified description of the underlying processes, given the well characterized structural environment in tip-enhanced Raman in contrast to most SERS experiments. It might also help to resolve the striking observation that the strength of the calculated four modes at 846, 988, 1029, and 1544 cm^{-1} are overestimated by DFT calculation as compared to the far-field spectra, but are modes found to be strongly enhanced in the tip-enhanced Raman spectra.

The near-field enhanced Raman spectra start to deviate significantly only for enhancements $G > 10^7$. In the case of moderate enhancements, both spectral positions and relative intensities of the modes resemble the far-field signature, as seen in Fig.4.12 c) and d). This is in accordance with the results of Domke *et al.* [254] who obtained maximum enhancement comparable with our low enhancement values and did not observe any change in the molecular spectral signature.

With the molecules under investigation exposed to the strongly localized and enhanced near-field, this leads to a sometimes rapid photo-decomposition process. An important question regarding the appearance of different spectral features in the near-field tip-enhanced Raman spectra is the influence of the molecular bleaching decomposition products [281, 304].

The tip-enhanced Raman results of the present study show that the decay and subsequent disappearance of the spectral response due to the eventual bleaching on time scales of 100's of seconds (Fig .4.13 b) depending on enhancement is uniform, *i.e.*, maintaining the relative peak amplitudes. This, together with the qualitative analysis of the decays in Fig. 4.13 a) and Fig. 4.14 for enhancements of 1.3×10^7 and 9×10^7, respectively, rules out that the spectra for large enhancement shown in Fig. 4.12 a) and b) are due to carbon clusters or other decomposition products and instead have to be assigned to malachite green.

In addition, transfer or binding of molecules to the tip is unimportant as evident from the absence of any Raman response approaching a clean surface region with a tip which has previously been exposed to a MG covered region (data not shown). These results show that at least for monolayer coverages or below the decomposition products of MG during bleaching do not contribute to the Raman response – irrespective of the level of enhancement considered here. If bleaching would lead to photoreaction products with appreciable Raman activity, one would expect to see the appearance of new spectral features in the time series experiments.

It was suggested that the molecular bleaching rate could be used for the derivation of the enhancement factor [276]. It should be noted that the bleaching rate is not a characteristic physical quantity universal for a given molecule. For example, malachite green isothiocyanate - a sister dye of MG - was found to bleach with a rate constant more than two orders of magnitude higher than the MG studied here [276], if renormalized to the same experimental conditions. Bleaching mechanisms can be quite diverse [305]. They may include irreversible photoinduced or even multi-photon induced reactions such as rearrangements, dissociation and fragmentation, elimination or hydrogen abstraction or perhaps photooxidation with ambient oxygen via triplet states. It can depend on, e.g, humidity or cleanliness of tip and sample, and is hence not a useful measure to compare experiments performed under different conditions in different laboratories.

Therefore, we can conclude that the different Raman active modes observed for the cases of high near-field enhancement originate from MG molecules and not intermediate products due to molecular decomposition.

4.7 TERS with single molecule sensitivity

With the measured tip-enhanced Raman spectra presenting a signal-to-noise ratio of more than 40:1 when probing ∼100 molecules for 1 s accumulation time, this demonstrates the potential for even single molecule sensitivity. For the subsequent experiment we resort to a sample prepared with sub-monolayer surface coverage, adjusted to expect on average < 1 molecule under the tip-confined area of ~ 100 nm^2.

Corresponding near-field tip-enhanced Raman spectra measured in a time series with 1 s acquisition time for each spectrum are shown in Fig. 4.21 (left panel). Here the tip has been held at a constant distance $d = 0$ nm above the sample and the total Raman enhancement is estimated at 5×10^9. The observed Raman signal exhibits temporal variations of relative peak amplitudes and fluctuations in spectral position. These are characteristic signatures of probing a single emitter in terms of an individual molecule. Similar observations have been made before in SERS [226, 227, 228, 306] with the fluctuations in the spectroscopic signature of a single emitter typically attributed to changes in its local environment, its structure, molecular diffusion [210, 307], and changes in molecular orientation [304].

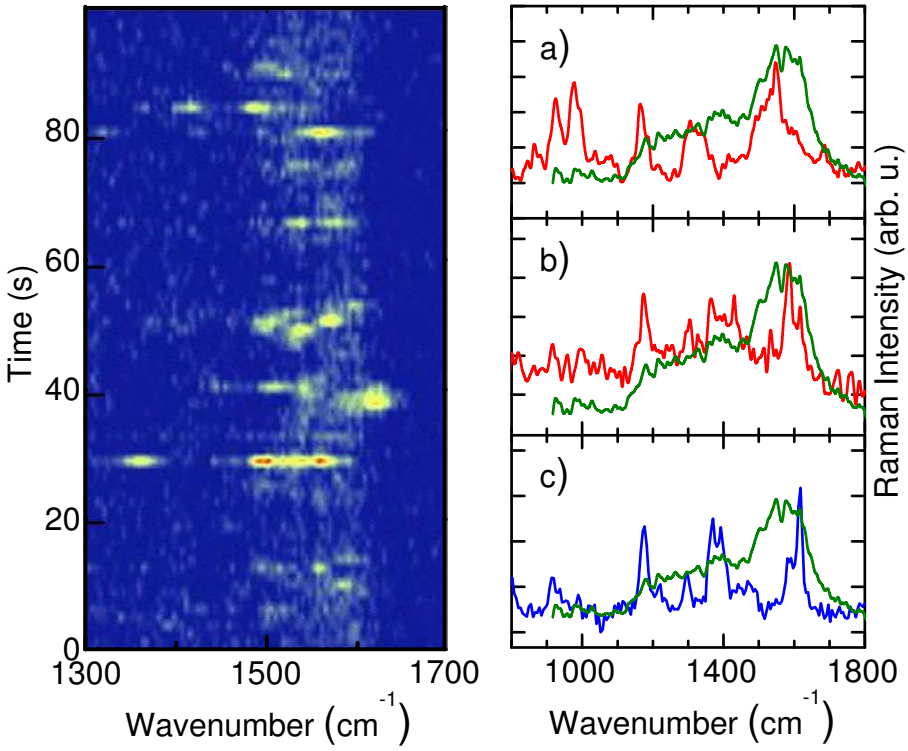

Figure 4.21: Left: Time series of tip-scattered Raman spectra for a sub-monolayer MG surface coverage. The spectral diffusion observed together with the analysis of the spectral intensity are highly indicative for probing single MG molecules. Right: Comparison between sum spectrum of data shown in left panel (olive) and tip-enhanced Raman spectra for different degrees of enhancement (red, a) and b)) and sum spectrum of data shown in Fig. 4.13 (blue).

With MG only physisorbed, it has to be considered in particular that the molecules can

diffuse in and out of the apex-confined probe region and they experience different degrees of enhancement. The diffusion dynamics can be facilitated by the thin water layer existent onto the sample surface at room temperature, as discussed above.

In the time series in Fig. 4.21 the apparent bleaching rate seems reduced compared to what is expected from the analysis of the ensemble bleaching discussed above. This is a result of the low surface coverage where new molecules directly neighboring the tip-sample gap can diffuse into the near-field enhanced region. However, the signal vanishes rapidly after 100 s due to the eventual depletion area after the molecules surrounding the tip have bleached.

Akin to the results presented above for strong enhancements, a different Raman mode structure of MG is observed compared to the far-field response. A strong evidence of probing single MG emitters and not decomposition products is offered by the comparison of the Raman spectrum of a molecular ensemble with the sum spectrum over the entire time series [206]. The resemblance of the two ensure that the signal observed in the strongly fluctuating case originates from the same molecular species. Note that the sum over the times series shall therefore resemble an ensemble spectrum for large enhancement, rather than the far-field Raman spectrum or TERS spectra for weaker enhancements.

Fig. 4.21 displays the sum spectrum (olive) for the single molecule response for the 100 s time series (left) in comparison with ensemble spectra of ~ 100 molecules probed for 1 s (red) showing different degrees of enhancement: 3×10^8 in a) and $7{\times}10^7$ in b). Panel c) presents the sum spectrum (blue) of data shown above in Fig. 4.13. In assessing the resemblance of the spectral characteristics is has to be considered that at low coverage the molecules have more degrees of freedom to dynamically change orientation and they can diffuse. Given the rather weak response, the signal detected can only be expected to emerge from the region of largest enhancement. Sampling over this region with its lateral variation in enhancement would give rise to further broadening of the strongly enhanced near-field response compared to the far-field case. Therefore, while individual spectral features at positions in accordance with the strongly tip-enhanced near-field response are observed in the time series, it is not surprising that the sum spectrum no longer exhibits clearly resolved lines. With the diffusing molecules probing the spatial variation of the enhancement under the tip this corresponds to an extreme case of inhomogeneous broadening. This interpretation is further sustained considering, e.g, the improved resemblance of the peak in the 1550 – 1600 cm^{-1} region of the single molecule sum spectrum with the sum of the two near-field spectra (in a and b) of different enhancement.

Further insight is obtained by studying the statistical behavior of the single molecule Raman response [210]. Fig. 4.22 top panel displays the integrated 1430 cm^{-1} to 1650 cm^{-1} spectral intensity for the data in Fig. 4.22 a). The signal intensities cluster with intervals of 170-230 counts$\cdot\mathrm{s}^{-1}$, as already evident from visually inspecting the time-series of integrated intensities (dashed lines), and this manifests itself in the corresponding histogram in an asymmetric distribution with discrete peaks (inset). Note that the details of the histogram, however, depend on the binning procedure especially for such a small data set. This behavior is qualitatively reproducible for experiments with the same surface coverage and it can be interpreted as the Raman emission from $n = 0$ (noise peak), 1, 2, and 3 molecules being probed under the tip. This assignments is corroborated from experiments

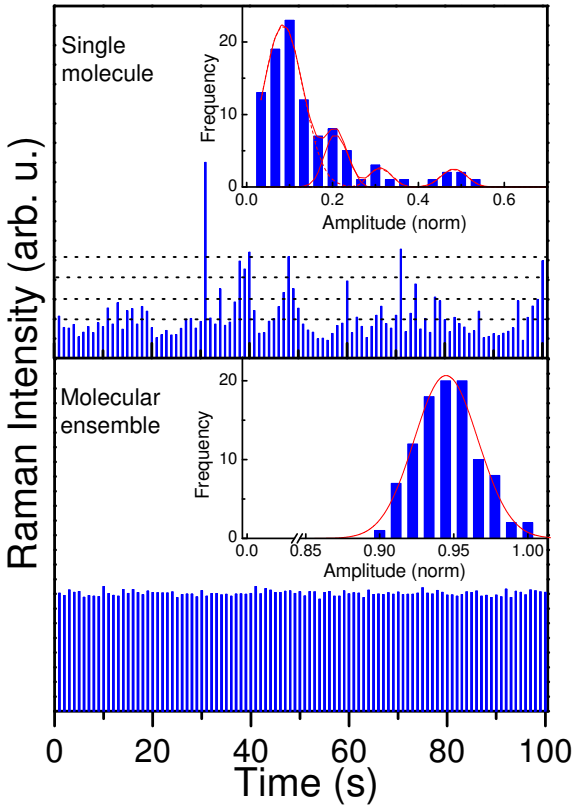

Figure 4.22: Top: Temporal variation of the Raman intensity of the integrated 1480 - 1630 cm^{-1} of time series shown in Fig. 4.21. From the corresponding histogram (inset) a discretization of Raman intensities can be seen. with 170-230 counts·molecule$^{-1} \cdot s^{-1}$ (dashed line increment). Bottom: Temporal variation of the Raman intensity of the integrated 1480 - 1630 cm^{-1} of big molecular ensemble (far-field) and corresponding histogram (inset).

with different surface coverages: for lower coverages only the $n = 0$ and 1 peaks remain and with increasing coverage the distribution converges to a narrow random Gaussian distribution which is observed for monolayer coverages as seen in the lower panel, where 100 consecutive far-field spectra were acquired for 100 s each and the signal is integrated over the same spectral range as in the case of the single molecule experiment. The details of the histogram, however, depend on the binning procedure especially for a small data set as has been shown to be insufficient as the sole argument for single molecule observation [308].

The optical trapping and alignment of MG under the tip has to be considered as possible source of the observed surface diffusion and intensity fluctuations [309]. With the local pump intensity of 7×10^7 W/cm^{-2} estimated inside the tip-sample gap and the anisotropic molecular polarizability calculated as $\alpha_{xx} \simeq 150$ Å^3, $\alpha_{yy} \simeq 63$ Å^3, and $\alpha_{zz} \simeq 22$ Å^3 a trapping potential energy of order 10^{-4} eV results [309] with four distinct local minima corresponding to different relative molecular orientations with respect to the tip axis. However, with this energy being much smaller compared to the thermal energy of kT $= 2.6 \times 10^{-2}$ eV, this can not explain the discretization of Raman peak intensities in the single molecule

response.

The experimental findings presented here and published in [30] were put under scrutiny in a Comment by Domke *et al.* [310]. There, the authors question whether the Raman response observed originates from MG molecules or wether the spectral features have to be assigned to carbon clusters and molecular decomposition products. The near-field character of the Raman response and the large enhancements are not debated. Their concerns are based on the pronounced spectral differences visible in the case of high near-field enhancement as compared tot the FF response. With the results shown above and published as a Reply to the Comment [311] we have refuted the proposed alternative interpretation based on "carbonaceous species" of our tip-enhanced and single molecule Raman signature.

Furthermore, in a recently reported TERS experiment, Zhang *et al.* [259] observed single molecule Raman response from brilliant cresyl blue molecules adsorbed on planar Au. The experiments were performed in a similar manner with the one presented here, and the results reproduced TERS with single molecule sensitivity. For an analogous enhancement level, they observed temporal fluctuations in both intensity and mode frequency, albeit with no remarkable differences between far-field and near-field spectra.

Corroborating all these observations with the series of experimental data presented above and the lack of contamination or decomposition products lead us to the conclusion that we observe the Raman response of a single MG molecule.

4.8 Conclusion

Single molecule vibrational Raman spectroscopy of Malachite Green adsorbed on *planar* metal surfaces is achieved by means of optical local-field enhancement provided by a scanning nanoscopic metallic tip. The optical tip-sample coupling gives rise to a more than 10^9 Raman enhancement when compared with the free standing molecule response and a localization of the response down to a sub-10 nm length scale. This proved sufficient to allow for *single molecule* Raman spectroscopy.

Prominent spectral differences were observed between the tip-enhanced near-field and the far-field Raman response. With the help of careful control experiments it was ruled out that photo-decomposition or carboniferous products contribute at the observed signal. Furthermore, theoretical calculation revealed that the near-field characteristic features are part of the normal Raman modes of the MG molecule. Following related theoretical and experimental observations [214] we attribute the differences to the gradient field Raman effect. However, given the inherent experimental challenges involved, the data lack the precision to arrive at a definite conclusion about the physical mechanisms at this stage.

The evidence for single molecule signature is based on a number of experimental conditions and observations: (i) the use of a dilute sample where in average only one molecule is expected under the tip apex; (ii) temporal fluctuations of intensity and spectral position of the Raman bands; (iii) resemblance of the single molecule sum-spectrum with the ensemble spectrum in the near-field regime; (iv) statistical analysis of the discrete intensity levels in the measured time-series.

With the enhanced sensitivity demonstrated here using metallic substrates, these experiments parallels the vibrational imaging of single molecules in inelastic electron tunneling at low temperatures [312, 313]. Given the additional virtues of being an optical technique and applicable under ambient conditions this opens new possibilities for ultrasensitive *in situ* vibrational nanospectroscopy of individual chemical and biological structures.

5 Nonlinear near-field microscopy

5.1 Nonlinear microscopy and spectroscopy

Nonlinear optics is the study of phenomena that occur as a consequence of the modification of the optical properties of a material system by the presence of light. The beginning of the field of nonlinear optics is considered to be the discovery of second-harmonic generation (SHG) by Franken et al. in 1961 [314], shortly after the demonstration of the first working laser by Maiman in 1960 [315]. One of the first theoretical treatments of the SHG process was realized by Amstrong *et al.* and dates back to 1962 [316].

The response of a material upon applying an incident electric field $\mathbf{E}(\omega)$ is given by the induced polarization $\mathbf{P}(\omega)$, which in the case of linear optics writes:

$$\mathbf{P}(\omega) = \epsilon_0 \chi^{(1)} \mathbf{E}(\omega) \tag{5.1}$$

where $\chi^{(1)}$ is the linear susceptibility. For the nonlinear response of the material subject to an incident electric field expressed as a group of m monochromatic plane waves

$$\mathbf{E}(t) = \sum_m E(\omega_m) e^{-i\omega_m t} + c.c.\,, \tag{5.2}$$

the total induced polarization $\mathbf{P}(\omega)$ in the frequency domain can be expanded in a power series of $\mathbf{E}$:

$$\mathbf{P}(\omega) = \epsilon_0 [\chi^{(1)} \mathbf{E}(\omega_{m1}) + \chi^{(2)} \mathbf{E}(\omega_{m2}) \mathbf{E}(\omega_{m3}) + \ldots] \tag{5.3}$$

with $\mathbf{E}(\omega_{m1})$, $\mathbf{E}(\omega_{m2})$, and $\mathbf{E}(\omega_{m3})$ the electric fields at frequency ω_{m1}, ω_{m2} , and ω_{m3}, respectively (m1, m2, m3, ... = (1,...,m)). $\chi^{(n)}$ is the n^{th} order dielectric susceptibility tensor [184].

The second-order response due to the second-order nonlinear susceptibility $\chi^{(2)}$ describes sum-frequency generation ($\omega = \omega_j + \omega_k$), difference-frequency generation ($\omega = \omega_j - \omega_k$), with the degenerate cases of second-harmonic generation (SHG) ($2\omega = \omega + \omega$), or optical rectification (DC $= \omega - \omega$).

In the case of (SHG), $\mathbf{E}(\omega)$ induces a second order nonlinear polarization in the medium, which can be expressed as:

$$\mathbf{P}_i^{(2)}(2\omega) = \epsilon_0 \chi_{ijk}^{(2)} \mathbf{E}^j(\omega) \mathbf{E}^k(\omega) \tag{5.4}$$

$\chi^{(2)}$ is a third rank tensor with - in the most general case - 27 elements $\chi_{ijk}^{(2)}$ (i, j, and k describe the Cartesian coordinates x, y, z).

However, in most cases the number of independent non-vanishing elements is greatly re-

duced as dictated by the symmetry of the medium [317]. Any additional symmetry property of a nonlinear optical medium can impose additional restrictions on the form of the nonlinear susceptibility tensor. By explicit considerations of the symmetries of each of the 32 crystal classes, one can determine the allowed form of the susceptibility tensor for crystals in that class. Results of such calculation [184] for the second-order nonlinear response - performed originally by Butcher [318] - are presented in Table 5.1 for the $6mm$ point group symmetry class which includes the hexagonal $YMnO_3$ - of interest for the following nonlinear optical studies presented here.

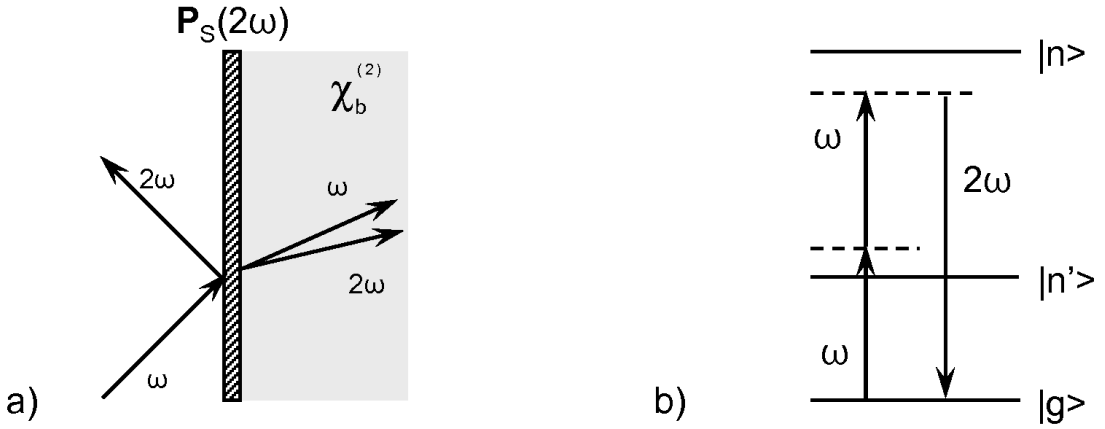

Figure 5.1: a) Geometry of second-harmonic generation. Reflection from interface $\left(\mathbf{P}_s^{(2)}\right)$ and transmission through the bulk - no inversion symmetry $\left(\chi_b^{(2)}\right)$ - cases are shown. b) Energy level diagram describing second-harmonic generation.

Due to its higher symmetry selectivity, the nonlinear optical response of a material gives access to properties difficult to access by linear optical techniques [317].

According to Eq. 5.1, if the medium has inversion symmetry, that is to say that the fields $\mathbf{E}(\omega)$ and $-\mathbf{E}(\omega)$ induce dipoles $\mathbf{P}^{(2)}(2\omega)$ and $-\mathbf{P}^{(2)}(2\omega)$ respectively, this implies that $\chi^{(2)} \equiv 0$ in the dipole approximation. At the surface or interface the inversion symmetry is broken and the nonlinear polarization induced in the interfacial sheet is given by:

$$\mathbf{P}(\mathbf{r},t) = \mathbf{P}_s \delta(z) e^{i(\mathbf{k}_{||}(2\omega)\mathbf{r} - 2\omega t)} \tag{5.5}$$

System	Symmetry class	nonvanishing elements of $\chi^{(2)}$
Hexagonal $YMnO_3$ [184]	$6mm = C_{6v}$	xzx=yzy xxz=yyz zxx=zyy zzz

Table 5.1: Non-zero elements of the second-order susceptibility tensor $\chi^{(2)}$ for $6mm$ symmetry class. Each element is denoted by its Cartesian indices.

Thus, for media with bulk inversion symmetry SHG is an intrinsically surface specific process [319]. Since 11 of the 32 crystallographic symmetry classes possess inversion symmetry, the rule is very powerful, as it immediately eliminates all crystals belonging to the respective classes from consideration for bulk second-order nonlinear optical interactions.

Microscopically, SHG corresponds to a sequence of electronic transitions from an initially occupied state $|g\rangle$, via two intermediate states $|n'\rangle$ and $|n\rangle$ induced by the two incident photons $\hbar\omega$ followed by the emission of one SH photon $\hbar(2\omega)$ when returning from $|n\rangle$ to the initial state $|g\rangle$ (see Fig. 5.1). The expression for $\chi^{(2)}$ in the dipole approximation consists of eight terms of the form [317, 184]:

$$\chi^{(2)}(2\omega) = -N\frac{e^3}{\hbar^2}\sum_{g,n,n'}\left[\frac{< g|r_i|n >< n|r_j|n' >< n'|r_k|g >}{(2\omega - \omega_{ng} + i\Gamma_{ng})(2\omega - \omega_{n'g} + i\Gamma_{n'g})} + \cdots\right]\rho_g^{(0)} \tag{5.6}$$

The quantities $\omega_{n'g}$ and $\Gamma_{n'g}$ are the energy difference and the line widths for the transitions between different quantum states, and $\rho_g^{(0)}$ describes the population of the ground state $|g\rangle$. Resonant enhancement thus occurs whenever the frequency of the transition matches that of the pump beam or the SH frequency.

Shrinking the dimensions of matter towards and beyond the length scale of the optical wavelength, distinctive phenomena such as *optical field confinement* and *structural resonances* occur [133], and light scattering starts to dominate over conventional geometric optics [103]. In contrast to the bulk, the lack of macroscopic translational invariance on the nanoscale makes *both* crystallographic symmetry and overall geometry in terms of size and shape crucially important [320, 321, 322, 323, 47]. Here, the problem of SHG becomes particularly intriguing as can be illustrated for small centrosymmetric particles.

The locally excited dipole term - the correspondent of the source for linear Rayleigh scattering - is absent for the nonlinear case because of the overall symmetry of the system [321, 324, 322, 325].

Even with the inversion symmetry being broken at the surface of the particle, the overall signal cancels out owing to the destructive interference of the different local surface contributions (schematically shown in Fig. 5.2). For large particles where the retardation effects cannot be neglected - the electromagnetic fields are not constant over a distance of the order of the particle diameter - higher order multipolar contributions to the nonlinear polarization have to be taken into consideration [326]. Emission from the sphere arises from both induced electric dipole and electric quadrupole moments at the SH frequency. The former requires a nonlocal excitation mechanism - propagation-induced phase-lags of the pump beam arise between spatially separated points of the particle -, while the later is present for a local-excitation mechanism [327].

Thus, the total nonlinear optical response of the system is described by a total induced polarization $\mathbf{P}^{2\omega}(r)$ that can be written as a sum of a dipole-allowed surface term $\mathbf{P}^{2\omega}_{surface}$

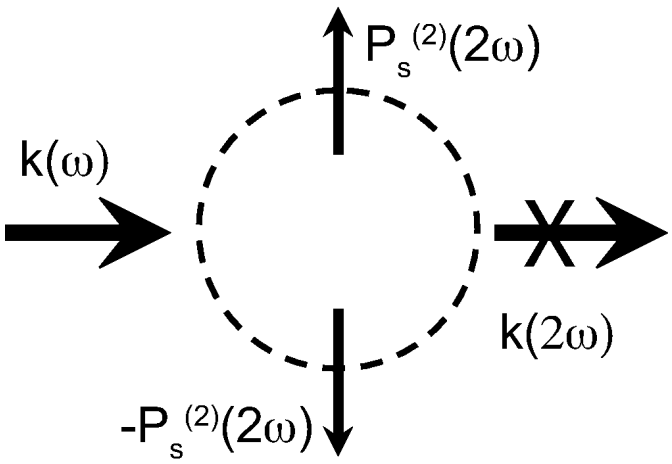

Figure 5.2: SHG from centrosymmetric particle. The surface SHG from centrosymmetric particles is forbidden for collinear detection.

and a nonlocal term $\mathbf{P}^{2\omega}_{nonlocal}$ [328]:

$$\begin{aligned}\mathbf{P}^{2\omega}(r) &= \mathbf{P}^{2\omega}_{surface} + \mathbf{P}^{2\omega}_{nonlocal} \\ &= \chi^{(2)}_s : \mathbf{E}^{(\omega)}(r)\mathbf{E}^{(\omega)}(r)\delta(r-a) + \chi^{(2)}_b : \mathbf{E}^{(\omega)}(r)\nabla\mathbf{E}^{(\omega)}(r)\end{aligned} \tag{5.7}$$

where (r-a) is the thickness of the spherical sheet contributing to the surface response, $\chi^{(2)}_s$ and $\chi^{(2)}_b$ are the corresponding second-order surface and bulk susceptibilities. Because of the lack of an in-plane translational invariance for a single nanoscopic system and with the nonlocal dipolar contribution oriented longitudinal, *i.e.*, parallel to the quadrupolar bulk polarization, both these polarization sources can emit only in noncollinear directions [321, 324]. In order to clarify the role of the different contributions to the nonlinear source polarization, the symmetry of the medium together with the experimental configuration represented by the wave - vectors $\mathbf{k}(\omega)$ and $\mathbf{k}(2\omega)$ have to be considered.

5.2 SHG from nanoscopic metal tips

Metallic tapered tips are partially asymmetric (∞mm) nanostructures with the mirror symmetry being broken along the tip axis. They provide a model geometry for addressing the different contributions to the nonlinear polarization and their directional and polarization selection rules. With the total nonlinear response of an interfacial system being a coherent superposition of local surface and longitudinal bulk polarizations, these contributions are in general inseparable without, *e.g.*, surface modifications [329, 330, 331]. The special geometry of the tip with its new selection rules, however, provides the additional degree of freedom which allows for their distinct observation. Here, metal wire tips (Au and W) with a nanometer size apex are investigated.

For experimental configurations sensitive only to the rotational symmetry, SHG from the tip is limited to the *nonlocal* longitudinal excitations and vanishes in the collinear direc-

tions, akin to the centrosymmetric particle case (see Sect. 5.1). In addition, the lack of mirror symmetry along the tip-axis gives rise to a fully local surface dipole-allowed SH contributions:

$$\mathbf{P}^{(2)}(2\omega) = \epsilon_0 \chi_s^{(2)} L(2\omega) L(\omega) L(\omega) : \mathbf{E}(\omega)\mathbf{E}(\omega) \tag{5.8}$$

Here, $\chi_s^{(2)}$ denotes the surface nonlinear susceptibility tensor with the components $\chi_{s,\perp\perp\perp}^{(2)}$, $\chi_{s,\perp\parallel\parallel}^{(2)}$, $\chi_{s,\parallel\perp\parallel}^{(2)}$, where $\perp$ and $\parallel$ refer to the local spatial components perpendicular and parallel to the surface, respectively. $L(\omega)$ and $L(2\omega)$ are the local-field correction factors for the pump and generated optical fields $\mathbf{E}(\omega)$ and $\mathbf{E}(2\omega)$, respectively [317].

By proper selection of observation direction and SH polarization these different contributions can be studied independently, providing information about the surface as well as bulk properties of the nanostructure.

5.2.1 Experimental

In our experiments, a mode-locked Ti:sapphire oscillator was used (pulse duration < 15 fs, center wavelength $\lambda = 805$ nm, repetition rate 72 MHz). The linearly polarized light is directed onto the sharp end of a free standing tip by means of achromatic reflective optics. With a focus diameter of about 12 μm exceeding the tip apex dimensions, plane wave excitation has been insured -necessary in order to avoid SH contributions due to intensity gradients.

The scattered second-harmonic light was collected using a long-working-distance microscope objective (20×, numerical aperture = 0.35), spectrally selected with a dichroic filter and monochromator, and detected using a photomultiplier tube and photon counting electronics. It was verified both from the spectral signature as well as from the square power dependence that the signal was of second-harmonic in origin up to a maximum pump flu-

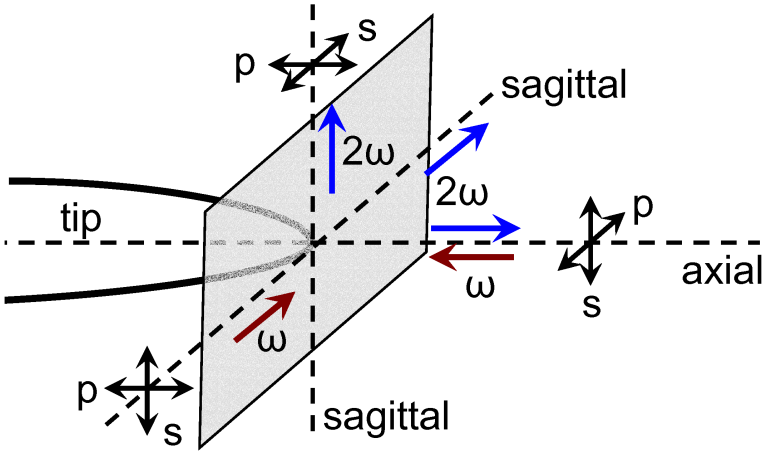

Figure 5.3: Schematic of experimental geometry: Pump light $\mathbf{k}(\omega)$ is directed onto the metallic tip in the axial or sagittal directions. The scattered second-harmonic light $\mathbf{k}(2\omega)$ is detected for all symmetrically distinct $\mathbf{k}(\omega) \rightarrow \mathbf{k}(2\omega)$ combinations.

ence of 40 GW cm^{-2}. To control tip orientation and illumination conditions the microscope objective was simultaneously used in combination with a CCD camera. Half-wave plates and polarizers served to control pump input and detected SH-output polarizations.

A scheme of the experimental geometry is shown in Fig. 5.3. Electrochemically etched (see sect. 2.2) radially symmetric gold (Au) and tungsten (W) tips were used for the experiments. Tip radii ranged from ≤ 10 nm to 50 nm as characterized by electron microscopy. The tips are illuminated in the axial - $\mathbf{k}(\omega)$ parallel with tip axis - or sagittal - $\mathbf{k}(\omega)$ perpendicular on tip axis - directions and selected combinations of pump wave vector $\mathbf{k}(\omega)$ and observation directions $\mathbf{k}(2\omega)$ are investigated. Note that the definitions of s and p polarization refers to the plane spanned by the respective wave vectors and the tip axis, and may differ from common conventions.

5.2.2 Results and discussion

Distinct symmetries result when the tip is illuminated in the axial or sagittal direction with the SH-light being emitted with characteristic spatial and polarization anisotropy. In the context of the near-field SH imaging experiments described later on in this chapter, only the data obtained for the crossed sagittal$_{in}$ - sagittal$_{out}$ experimental arrangement are shown, which are unique for the tip as a partially asymmetric nanostructure, as discussed below.

A characteristic SHG signature of the tip apex can be detected under sagittal configuration. Fig. 5.4 shows a schematics of the crossed sagittal$_{in}$ - sagittal$_{out}$ experimental arrangement.

In Fig. 5.5 the results for this experimental geometry are shown for the case of a Au tip. The SH polarization is set to be either p (trace a) or s (trace b), and the polarization dependence for the pump beam is monitored. Here, both the interfacial local dipole allowed $p_{\mathrm{in}}p_{\mathrm{out}}$ (trace a) as well as the longitudinal nonlocal $p_{\mathrm{in}}s_{\mathrm{out}}$ and $s_{\mathrm{in}}s_{\mathrm{out}}$ polarization combinations (trace b) are observed. In contrast, with the dipole $\mathbf{P}^{(2)}_{local}$ excited along the tip

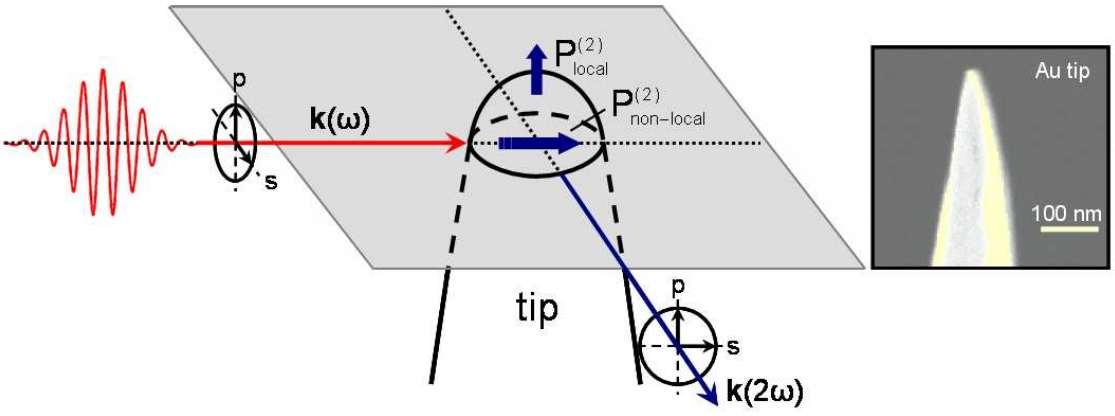

Figure 5.4: Experimental geometry for the SHG in sagittal$_{in}$-sagittal$_{out}$ configuration. p polarization direction is defined as spanned by the wave vector and the tip axis for both pump and SH beams. Right panel: electron micrograph of representative Au tip (r $\sim$ 20 nm).

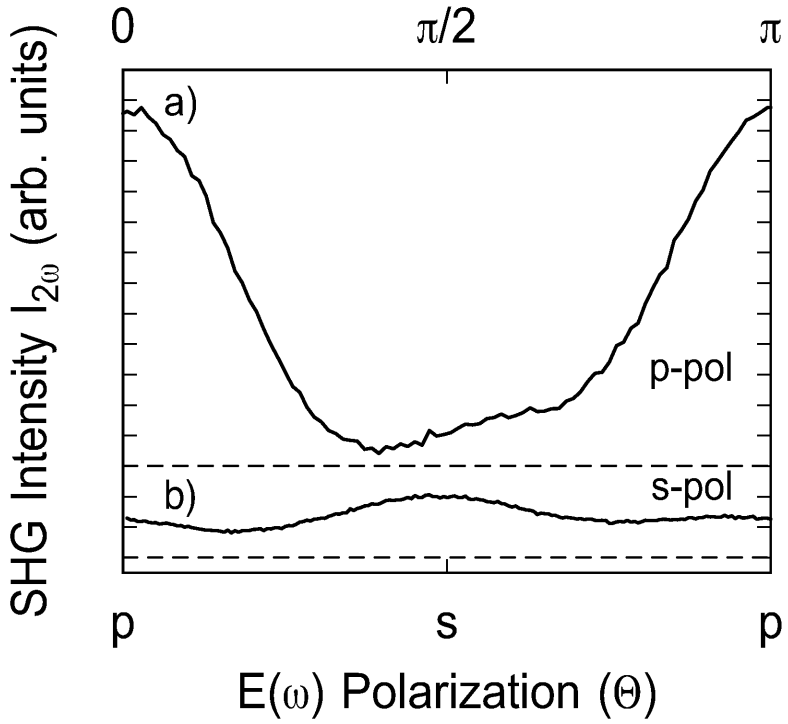

Figure 5.5: Pump polarization dependence for orthogonal sagittal illumination and sagittal $p-$ (a) and $s-$polarized (b) SH detection. In contrast to spherical particles both local $p-$ (a) and longitudinal nonlocal $s-$polarized (b) contributions can be observed in this configuration

axis (Fig 5.4) - due to the dominating $\chi^{(2)}_{s,\perp\perp\perp}$ tensor element [328] - no local SH response is expected for $p_{\mathrm{in}}s_{\mathrm{out}}$ geometry. The polarization dependence for the local contribution exhibits thus a twofold symmetry (Fig. 5.5 a). With the nonlocal component being longitudinal, the corresponding SH signal should be insensitive to the direction of the pump polarization. The modulation observed in Fig. 5.5 b and the small asymmetry in Fig. 5.5 a are attributed to deviations of the tip shape from a rotational symmetry along its axis and to small angle deviations of the experimental arrangement from the ideal sagittal$_{in}$ - sagittal$_{out}$ configuration. For other tips investigated, this small modulation was observed to change pattern, and even invert with respect to the input polarization. The SH intensity observed for the local polarization source is more than 10 times higher than the response for the non-local excitation. In a recent study [332], the higher multipole contribution to SHG from a regular array of particles was estimate to contribute up to 20% of the total SH field amplitude.

The results are found to be qualitatively reproducible for different tips of nominally similar radii. For tungsten tips, the same behavior has been observed albeit lower signal levels are found.

Depending on the experimental configuration, SHG relies on (i) a fully local dipolar response, (ii) a nonlocal source polarization and/or (iii) on the nonlocal coupling of a local SH-source to the emitted SH-wave. The longitudinal nature of the nonlocal source terms

implies not only the absence of collinear SH-emission in the axial direction but also the absence of *s*-polarized SH-light for coplanar pump/detection geometries, i.e, $\mathbf{k}(2\omega)$ in plane with tip axis and $\mathbf{k}(\omega)$. Thus, the SHG selection rules can be equivalent to that of a planar surface or resemble those of spherical or ellipsoidal particles. Unique for the tip structure are configurations without any mirror plane such as the crossed sagittal$_{in}$ - sagittal$_{out}$ configuration, where all polarization combinations can contribute to the SH-response. It should be noted that in sum-frequency generation (SFG) with two independent input beams, additional degrees of freedom exist to built asymmetric configurations [333].

Therefore, despite the shared symmetry properties of isotropic planar interface, spherical cluster and the axially symmetric tip, their SHG response differs profoundly.

Our experiments show that the SHG efficiency depends on structural details of the nanoscopic tip. An investigation of the influence of these geometric parameters would be highly desirable; however, the limitations due to the preparation procedure render this difficult. Yet, the contribution of the local field-enhancement on SHG from the metal tips can be derived comparing the signal strength obtained with that of a planar surface of the same material. With the SH-enhancement expected to be dominated by the tip apex, a hemisphere with tip radius r is used to approximate the effective tip area. For the local dipole allowed emission, assuming a dipolar radiation distribution, this translates into an SH-enhancement of $\sim 5 \times 10^3 - 4 \times 10^4$ for Au tips with $r \simeq 20\,\mathrm{nm}$. With the SH-power $\propto E^4$ [184] this corresponds to an amplification of $8 - 25$ for the average electric field near the apex. For W tips significantly lower values for the SH enhancement are found corresponding to local field factors between 3 and 6. These values derived for the local field enhancement are consistent with those estimated using the model described in Sect. 3.5, where the tip is treated as a hemispheroid.

It has to be noted that with the length of the incoming light pulse shorter than the illuminated tip, a deviation form the slowly varying amplitude approximation is possible. This gives rise to a varying nonlinear polarization along the length at a given time [317, 334], which must be taken into account when a precise quantitative analysis is performed, but should not alter the symmetry selection rules.

The results presented here have to be considered in the application of, *e.g.*, SHG from metallic tips for the purpose of scattering-type near-field microscopy (s-SNOM) [42, 335, 336], where the control of both direction and polarization dependence of the generated SH signal is of crucial importance, as detailed later on in this chapter. They have also fundamental implications for the use of second-order nonlinear optics in surface characterization of nanoparticles, *e.g.*, percolated metal island films [337, 338, 41, 339] or in SH-scattering from colloidal particles [340].

5.3 Second-harmonic near-field imaging

Far-field SH microscopy has already demonstrated its great potential for investigation of various materials [341, 342, 343, 344, 345]. However, for many applications, spatial resolution below the diffraction limit is necessary. The combination of scanning near-field optical microscopy (SNOM) and SHG spectroscopy enables the examination of nonlinear

optical phenomena at the nanoscale and constitutes a highly sensitive optical technique for material characterization [346, 347, 348, 349].

Apertureless SNOM makes use of the effect of the local field enhancement at a metallic tip, which is significantly larger than in the case of fiber tips used in traditional SNOM experimental setups. This leads to much stronger light confinement and better spatial resolution [339]. The near-field SHG response has a complex dependence on the polarization of the incident light and the properties of both tip and sample. Due to the field enhancement at the apex of the tip, the main source of SH light is situated either at the surface area just underneath the tip if the nonlinearity of the sample is dominant ($\chi^{(2)}_{sample} \gg \chi^{(2)}_{tip}$), or at the apex of the tip if the nonlinearity of the tip is larger than that of the surface ($\chi^{(2)}_{tip} \gg \chi^{(2)}_{sample}$). The electromagnetic coupling between the tip and the sample and possible surface plasmon resonances at both fundamental (ω) and SH (2ω) frequencies may lead to additional local field enhancement. The signal is localized on a lengthscale comparable with the tip apex radius, as discussed above.

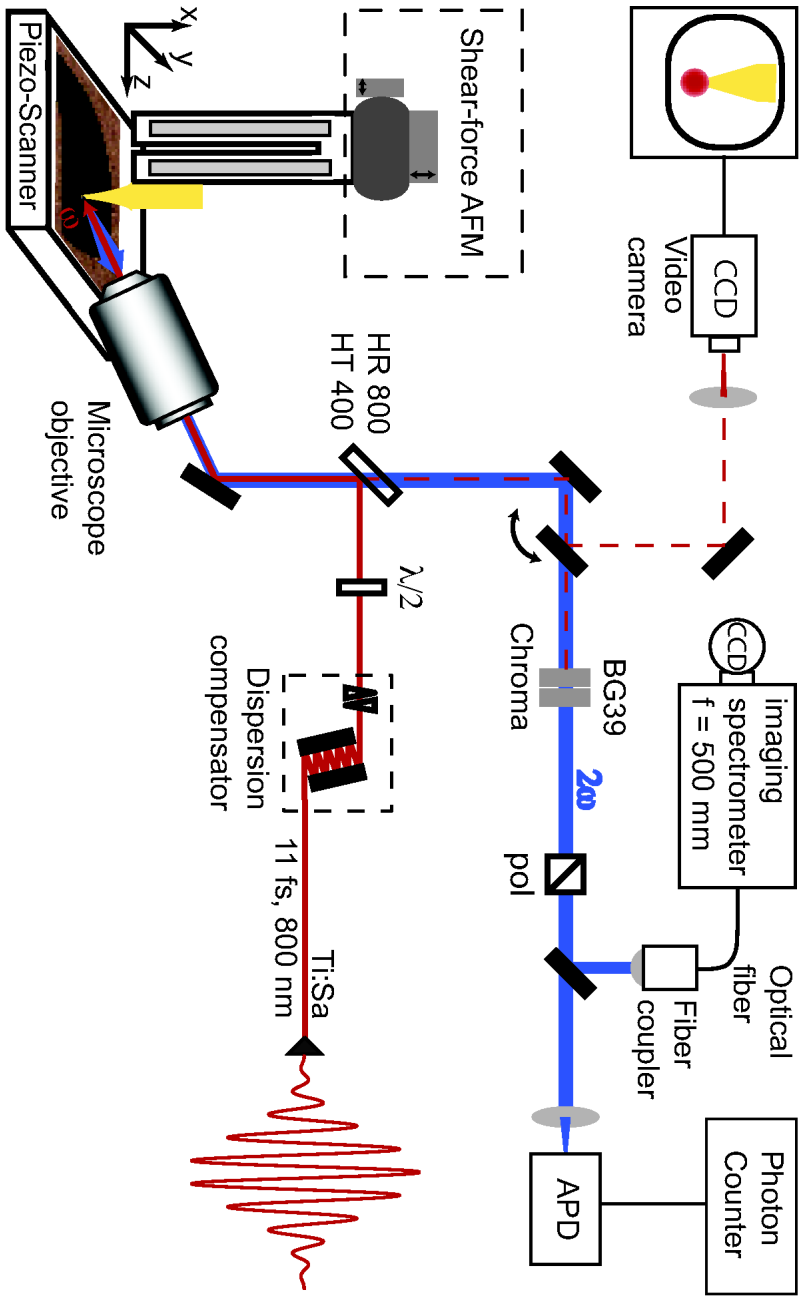

Figure 5.6: Experimental setup used for the SH near-field imaging. The fundamental incident light is focused onto the tip-sample gap, and the backscattered SHG is filtered and spectrally analyzed using an imaging spectrometer or integrated by means of an avalanche photodiode and detected with a single photon counter.

5.3.1 Experimental

The schematics of the experimental arrangement used for the near-field SHG studies is shown in Fig. 5.6. With most of the setup components already described in Ch. 2, only the elements specific for the near-field SHG experiments are discussed here.

With maximum 20 mW incident average power (0.13 nJ pulse energy), this corresponds to a 0.2 MW/cm^2 illumination power density in the focus, lower than the threshold for thermal damage of the tip [350]. The incident light is guided into the focusing microscope objective after dispersion precompensation as discussed in Sect. 2.3 by means of a highly reflecting mirror for the 700 - 900 nm spectral range (Layertec GmbH). Simultaneously, with a high transmission in the 350 - 600 nm spectral range, the mirror is used to separate the back-scattered SH from the fundamental light.

The mirror is also designed for minimum GVD to avoid temporal elongation of the ultrashort light pulses. Transmission spectra for this mirror are shown in Fig. 5.7 upper panel for both polarization directions of the fundamental light. For a better visualization, spectra of the incident (red) as well as SH (blue) light are super-imposed in the same figure.

For a complete spectral separation of the SHG from the fundamental light two filters are used in conjunction: a glass filter (BG39, Schott) and a band-pass filter (#4202, Chroma Technologies). Transmission spectra of the two filters are shown in Fig. 5.7 lower panel.

For the near-field SH imaging experiments, the response is detected using a single photon-counting scheme (see Sect. 2.3 and Fig. 5.6). Nonlinear optical contrast measurements are performed in both gated and non-gated configurations. With high signal to noise ratio, no signal gating was necessary in the case of the ferroelectric domain imaging experiments (Sect. 5.4).

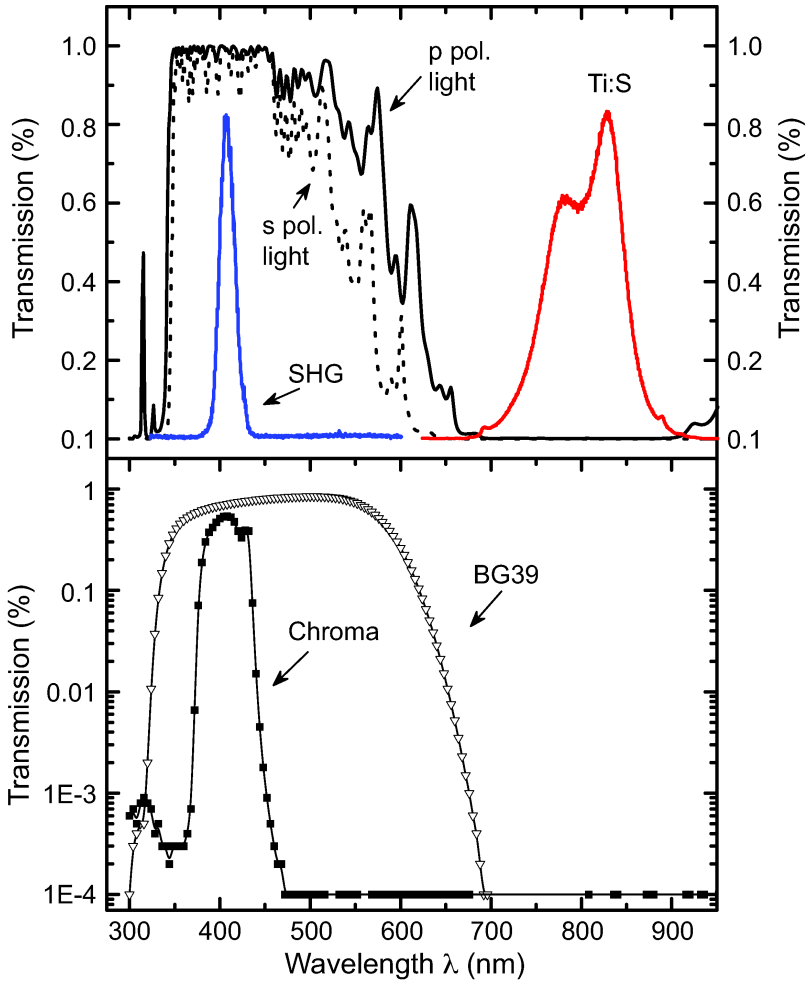

Figure 5.7: Upper panel shows the transmission characteristics of the mirror used as high reflector for SHG and high transmitter for fundamental light (HT 400, HR 800). Curves for both p (black dotted line) and s (black solid line) polarization directions are shown (left axis). Spectra of SHG (blue) and fundamental light (red) are displayed (right axis). Lower panel shows the transmission of the BG39 (hollow triangles) and Chroma (full squares) filters used to separate the SHG and the fundamental lights. Note the logarithmic vertical axis.

The separation of the near-field response from the far-field background is not always trivial [351], even in the case of SHG when the detected light is not at the frequency of the incident light. One of the schemes employed to help differentiate between the two components of the back-scattered signal is the dithering of the tip perpendicularly on the sample surface on a lengthscale comparable with the apex radius [122]. With the tip-sample coupling (and the near-field enhancement, correspondingly) decreasing rapidly with increasing the separation, the near-field signature is significant only for separations comparable with the apex radius. On the other hand, a large part - but not all - of the far-field background is independent on the tip-sample distance. Thus, dithering the tip and taking the difference

between the optical signal close and far from the sample a much better filtering of the near-field SHG is achieved.

A cartoon of this detection scheme is shown in Fig. 5.8 left panel. The tip is dithered (frequency f = 1190 Hz and amplitude Δ ∼30 nm) above the sample surface (function generator TG1010, Thurlby Thandar Instruments (TTi)). The optical signal recording by the photon counter is realized in a gated fashion, with one gate (A) corresponding to the position of the tip far from the surface, and the other (B) to the position of the tip in close proximity of the surface ("tip in" and "tip out" in Fig. 5.8). Each gate spans equal time durations ($\tau_A = \tau_B = \tau$), smaller than the half-period of the dithering waveform. The acquisition sequence is triggered using a TTL signal in phase with the dithering waveform. With the response of the z-piezo possibly delayed with respect to the TTL trigger, this would translate into shifted gate periods with respect to the peaks of the dithering function. To avoid that, the phase difference between the driving signal and the TTL trigger is swept until the optical signal (SH_B - SH_A = max) is maximized.

Figure 5.8 right panel shows the vertical spatial localization of the near-field SHG response for the Au tip (r ∼ 15 nm) approaching a smooth Au sample. Both fundamental and SH waves are polarized along the tip axis (p-pol), in the most favorable configuration for near-field enhancement (see Sect. 3.1.2) [337, 47]. The backscattered SH intensity increases on a tip-sample distance d of less than 20 nm, comparable with the radius of the tip apex, as expected for a strong coupling resulting in near-field enhancement (see Sect. 3.2) [352, 336, 42, 335, 10]. The signal reaches its maximum value (∼3.5 times larger than with the tip far from the sample) for the smallest tip-sample separation ($d \approx 0$). Here, the tip-sample distance $d \approx 0$ nm is defined by a ∼ 30 % decrease in the tuning-fork shear-force signal. With the corresponding signal trace, characterized by a width of 12 to 14 nm (5 to 95 % damping), the physical tip-sample contact is expected at $d \sim -9$ nm [57].

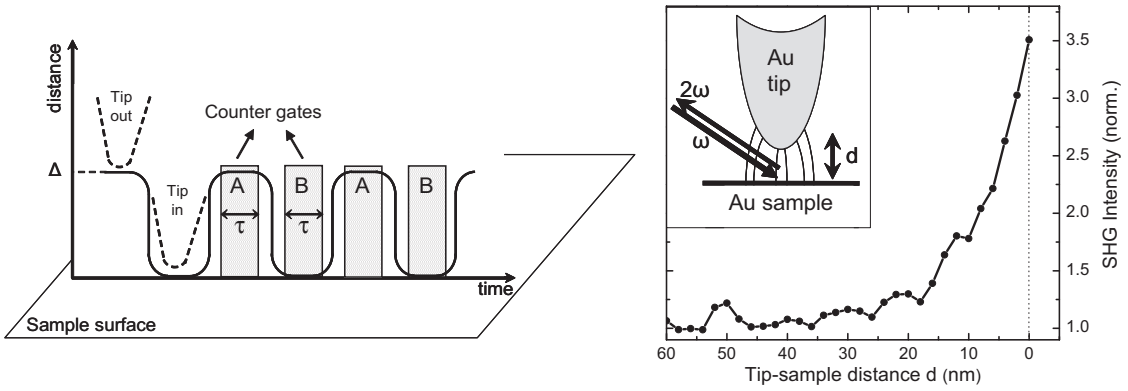

Figure 5.8: Left panel: conceptual cartoon of the gated near-field SH detection scheme. The tip is dithered perpendicularly on the sample surface with an amplitude Δ. The detected SH response represents the difference in signal between the "tip in" and "tip out" position, (gates B and A, respectively).
Right panel: near-field SHG scattering intensity as a function of the tip-sample distance d. Vertical localization of the near-field enhancement on a lengthscale comparable with the tip apex radius (r ∼ 15 nm) is visible.

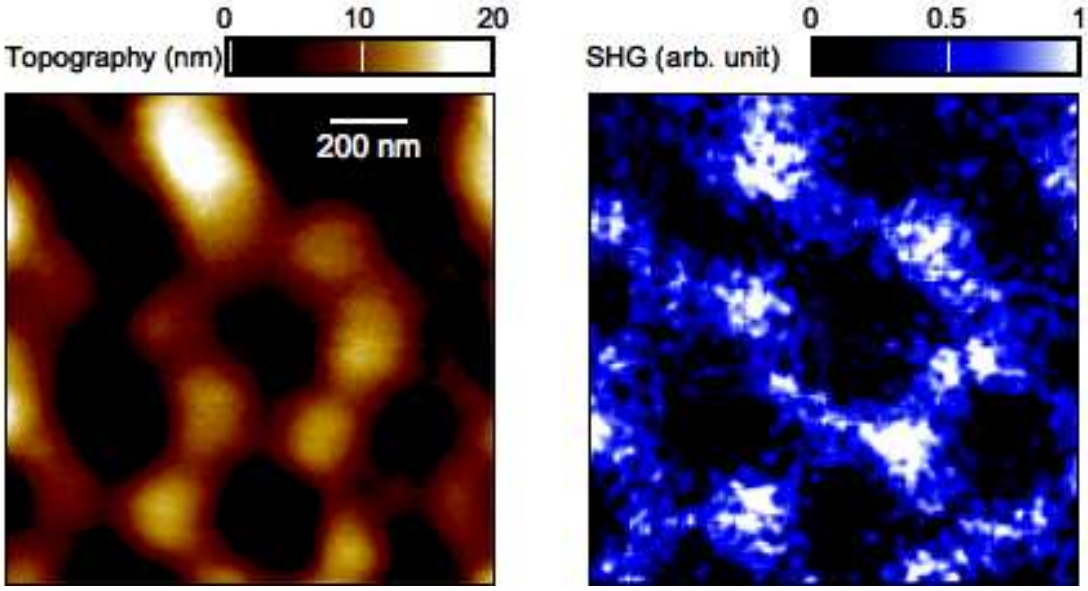

Figure 5.9: Near-field SHG from Al nano-islands on glass substrate. Left panel: shear-force topography of a 1.28 x 1.28 μm^2 surface area. Right panel: near-field SH intensity as a function of the position on the sample, showing strongly enhanced and localized signal above the metallic particles. The fundamental beam is p - polarized and the SH response is detected unpolarized.

5.3.2 Near-field SH optical contrast

To test the capabilities of the experimental apparatus, a glass sample covered with an Al projection pattern from 230 nm latex spheres was was imaged using a Au tip. Near-field SH contrast with spatial resolution higher than the diffraction limit was obtained.

Figure 5.9 presents the topography (left panel) and the simultaneously acquired near-field SH signal (right panel). A 1.28 x 1.28 μm^2 surface area is shown, and the images comprise of 128 x 128 pixels. The average height of the metallic nano-islands is $\sim$15 nm. The fundamental light is p-polarized - parallel with the tip axis - and the SH response is acquired unpolarized. Here, a non-gated detection scheme is employed.

A fairly small SH signal is observed with the tip above glass regions. The low nonlinear response of the glass ($\chi^{(2)}_{glass} \ll \chi^{(2)}_{tip}$) ensures negligible response of the sample compared with the one from the tip [336]. Furthermore, as discussed in Sect. 3.1.1 the tip-sample near-field coupling is weak, and thus most of the observed signal originates from the tip apex region. In contrast, strong and well-resolved near-field SH response is obtained when the tip is located above the metallic nano-islands. The strong Au-tip - Al-sample electromagnetic coupling could lead to field enhancement at both fundamental and SH frequencies. It is interesting to note that although all the Al particles identified in the topographic image show a strong SH signature, the signal varies from one particle to the other. The fine structure (corrugation) of the Al islands, not resolved in our topographic image, determine the local conditions for SHG, leading to different degrees of field enhancement in the tip-sample gap region. In addition, this could also explain the spatial variation of the enhanced SH

response.

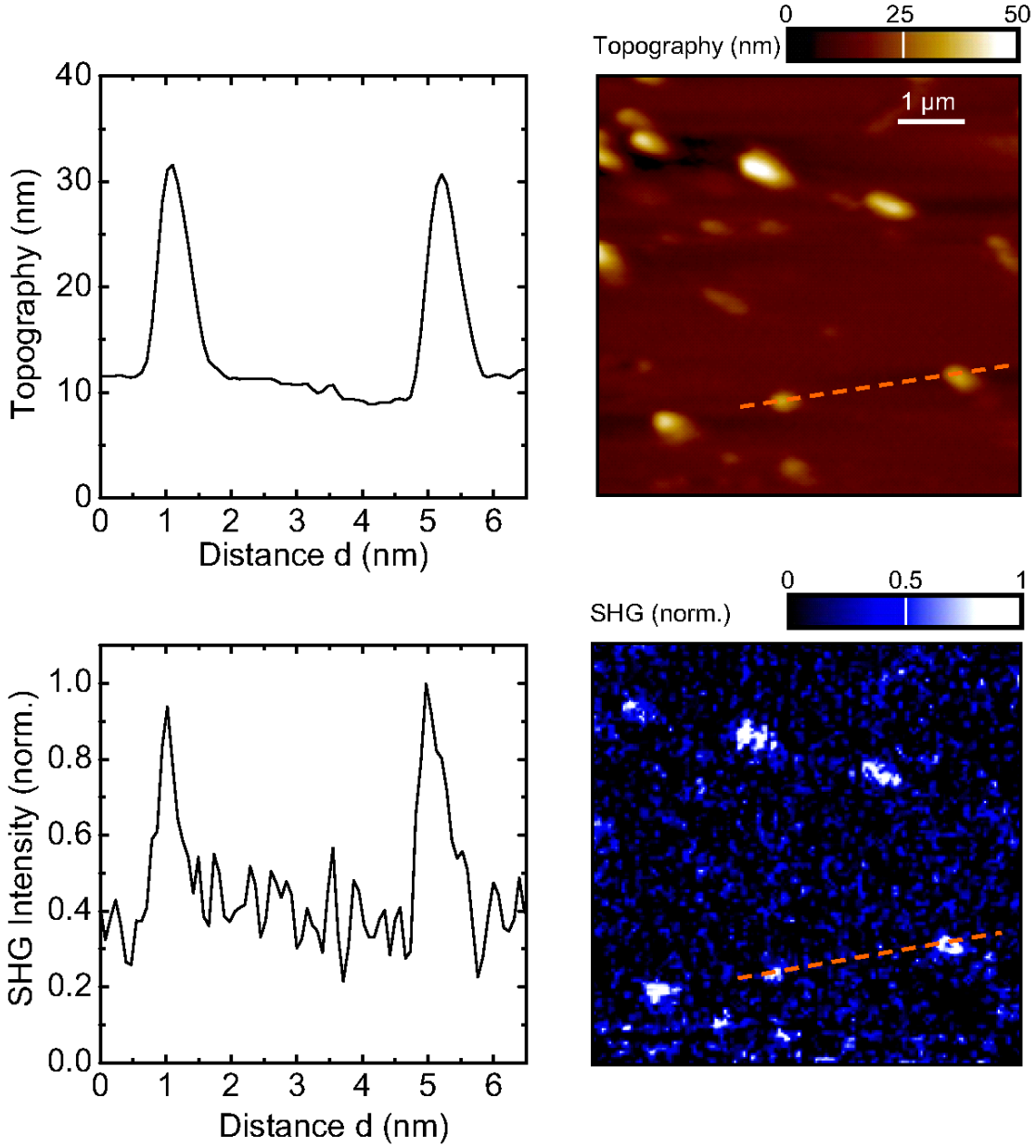

Figure 5.10: Near-field SH imaging of Au nanoparticles on Si substrate, obtained in a gated detection configuration. Upper panel: Topography of a 6.4 x 6.4 μm^2 sample region, with cross-section profile along the indicated dashed line. Lower panel: near-field SH response of the sample, with very low signal above Si regions, and high SH response localized only above Au particles. The cross-section shown is realized along the same line as for the topographic image.

Figure 5.10 shows one example of near-field SH imaging of metallic nanoparticles realized using the gated detection scheme described above. The upper panel displays the topography

of a 6.4 x 6.4 μm^2 area on the Si sample where Au nanoparticles (average height ∼20 nm, as seen in the line cross-section) are visible. The scanning step is 50 nm and the acquisition time for the optical signal is 70 ms/pixel. Note that the small elongation of the surface elements after the same direction (down-right to up-left) seems to indicate a drift of the sample during the scanning process. With a total data acquisition time of almost one hour for both *trace* and *retrace* scanning directions, this is not surprising. In the lower panel, the detected near-field SH response is shown. A clear enhancement in optical signal is observed with the tip above the Au particles, when compared with the rest of the sample. The observation is similar with the one described above for the case of the Al nano-islands, and is due to both the strong Au-tip - Au-sample electromagnetic coupling and to a higher second order susceptibility of the Au with respect to the Si substrate. Although on the scanned sample region are topographical elements other than Au particles, these do not present any individual SH signature. Being most probably surface defects or other contamination (*e.g.*, dust particles), the optical coupling to the tip is weak and no enhancement is expected. A cross section encompassing two Au particles (along the dashed line in the 2D images) is shown on the left hand side of Fig. 5.10 for both topography (upper panel) and near-field SH response (lower panel). The signal shown is the average over 3 consecutive pixels orthogonal to the cross-sectional direction. A SH signal more than 2 times greater is visible on top of the Au particles. Furthermore, the lateral spatial confinement of the SH response is higher than the corresponding topographic feature. This is due to the nonlinear dependence of the signal on the local field, as described by Eq. 5.1. The residual optical signal observed in the regions were no Au particles are present is attributed mostly to the SH generated at the apex of the tip (see Sect. 5.2.2).

5.4 Near-field SH imaging of ferroelectric domains

As modern portable electronic devices become more and more popular, there is an increase in the demand for nonvolatile memories [353]. The ferroelectric random access memory (FeRAM) is one of the most promising candidates for satisfying this demand, for its power consumption is the lowest among various semiconductor memories, and also possesses non-volatile and random access characteristics [354]. On the other hand, ferroelectric crystals are versatile candidates for optical frequency conversion since conversion rates in the order of 50% can be achieved by quasi phase-matching in artificially created domain structures [355, 356]. Thus, the study of the fundamental microscopic behavior of ferroelectric materials is of high interest for the understanding of the fundamental phenomena and applications. The electric domains in a ferroelectric crystal determine its crucial performances, such as hysteresis, optical linearity, creep, etc.

Since the first direct observation of ferroelectric domains in bulk $BaTiO_3$ and KDP crystals [357, 358], various techniques providing access to the topology of ferroelectric domains have been developed [359, 360]. Scanning probe microscopy (SPM) offers several possibilities to reveal nanoscale information on the domain configurations of ferroelectric crystals [361, 362]. Piezoresponse force microscopy (PFM), based on monitoring piezoelectric surface displacements induced by the electrically biased probing tip [363, 364, 365], allows for imaging domain structure of ferroelectric surfaces [366, 367, 368].

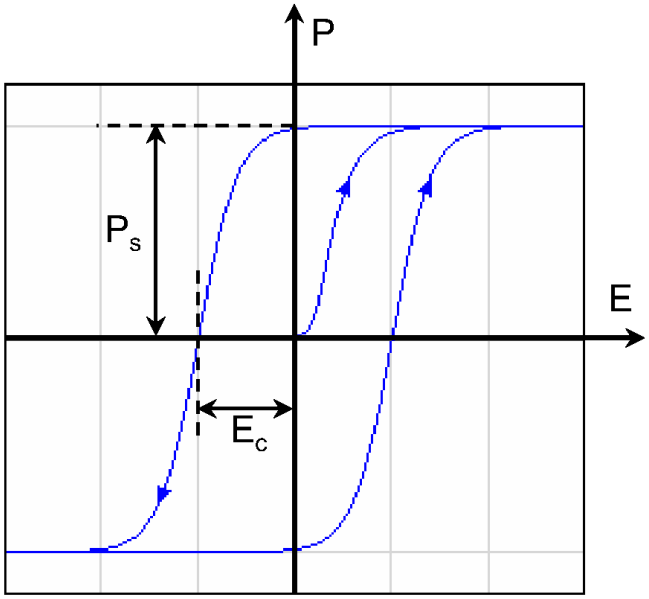

Figure 5.11: Typical hysteresis loop of a ferroelectric [360].

Among optical methods second harmonic generation (SHG) is particularly sensitive to the ferroelectric state since the loss of inversion symmetry in the long-range electric ordering is the origin of the SH response. It therefore couples directly to the FE ordering parameter, as discussed below. This was used to study the poling, growth and topology of domains in bulk crystals and Langmuir-Blodgett films [369, 370, 344, 371].

All these studies are devoted to cases where SHG in large or periodically poled domains is considered. Imaging of the intrinsic domain structures (*i.e.*, no poling) in multiple domain samples is highly desirable, for it can provide much finer information and insight into the microscopic mechanisms governing the ferroelectric behavior. The combination of the scanning near-field microscopy with SHG for mesoscopic ferroelectric domain imaging offers an ideal way to study the properties of a ferroelectric material [352, 372].

5.4.1 Ferroelectrics: fundamental concepts

A ferroelectric material is a material that exhibits, over some range of temperature, a spontaneous electric polarization $\vec{P}_s$ that can be reversed or reoriented by application of an electric field $\vec{E}$ (poling). A necessary criterion is the ever-present spontaneous polarization, with the requirement of reversibility or reorientation of that spontaneous polarization being a sufficient criterion for a ferroelectric phase [373]. That is to say that there exist directions $\vec{u}$ within the material such that, when a field is applied along them, the relation between $\vec{P} \cdot \vec{u}$ and $\vec{E}$ is not linear, but given by a hysteresis loop.

A cartoon describing a typical hysteresis loop is given in Fig. 5.11, where P stands for $\vec{P} \cdot \vec{u}$ and E for $\vec{E} \cdot \vec{u}$. As the hysteresis loop intersects the P-axis at a non-zero value, can be concluded that in absence of a field, the polarization maintains a finite value $\vec{P}_s$. The

direction of $\vec{P}_s$ is called the *ferroelectric axis*, and its magnitude P_s *spontaneous polarization* [359].

The ferroelectric phase transition is a second order structural phase transition, as a result of which the spontaneous polarization $\vec{P}_s$ occurs in the crystal due to the relative displacement of the ion inside the unit cell [360]: $\vec{P}_s = e_i \Delta\vec{r}_i / v_{uc}$ with: $\Delta\vec{r}_i$- the displacement of atom from the equilibrium position and v_{uc} the volume of the unit cell. The magnitude η of the displacement is called *order parameter*. The transition occurs at the Curie temperature T_C, above which the material loses its spontaneous polarization. The ferroelectric phase is then noncentrosymmetric. Ferroelectrics are commonly divided into two groups, the *displacive ferroelectrics* and *order-disorder ferroelectrics*. For the displacive type, the atomic displacement in the paraelectric phase is zero. In the order-disorder case, the displacements have a multiwell configuration of sites, with the disordered state being the paraelectric one.

The force from the local electric fields due to the ions in the crystal increases faster than the elastic restoring forces. This leads to an asymmetrical shift in the equilibrium ion positions and hence to a permanent dipole moment [373]. Usually, the net macroscopic polarization - and equivalently, dipole moment - is zero, due to domain formation in opposite polar directions [374, 375]. Domains are formed so that the the total free energy of the crystal is reduced. Formation of domain walls is a result of competition between several energies: electric field energy, elastic energy, and domain wall energy. Having domains with different uniform polarizations reduces the energy of the electric field in the expense of domain wall energy. The equilibrium configuration is obtained by minimizing the total energy [376]. The crystal energy is the sum overall the region-energies (i.e. domains) and interaction-energies (i.e. domain walls). It must be noted that at equilibrium the minimum energy in the absence of any defects would correspond to a single domain configuration [360]. However, such an equilibrium state is rarely achieved in a crystal in the absence of applied fields and it was observed in highly conducting ferroelectrics [377].

A *ferroelectric domain* is a region in a ferroelectric crystal exhibiting the same ion displacement (η = const.), resulting in a locally homogeneous and uniform spontaneous polarization. The boundary region between two ferroelectric domains is called a *domain wall*. The direction of the spontaneous polarization in each unique domain is constrained by the symmetry of the unit cell to a small number of equivalent directions. For example, $BaTiO_3$ is characterized by a cubic-to-tetragonal structural phase transition at the Curie temperature [360]. This is associated with a small axial displacement of the central Ti atom at temperatures below T_C which induces a spontaneous polarization in each unit cell, and hence the ferroelectric behavior. When undergoing the phase transition, each unit cell has a six-fold choice of P_s direction, resulting in two different types of domain walls: those separating antiparallel spontaneous polarizations (180° domains) and those separating spontaneous polarizations oriented orthogonal to each other (90° domains) [359].

The following description of fundamental concepts in ferroelectrics will be concerned only with 180° ferroelectric domains, in line with the studies presented in this chapter. In this case, the spontaneous polarization has the same direction throughout the material, and only changes sign in neighboring domains (hereafter denoted as 'up' and 'down' domains, respectively).

Thermodynamically, the domain formation is described by the behavior of the thermody-

namic potential Φ, e.g. the free energy. The displacement of atoms in crystalline regions remote from each other occurs independently and the crystal will develop such a combination of domains and domain walls, to get a relative minimum of the thermodynamic potential.

A displacement in the direction 'up' or 'down' of the crystal sublattice is energetically equivalent [373]. That means that the thermodynamic potential is invariant with respect to the sign of the displacement:

$$\Phi(\eta) = \Phi(-\eta) \tag{5.9}$$

The solutions resulting from the minimization of Φ are interconverted by symmetry transformations that disappears upon phase transition. In the non - symmetrical (ferroelectric) phase only those symmetry elements are retained which do not change η. That is to say that there is no symmetry element left that could exchange 'up' and 'down' domains with each other.

The appearance (nucleation) and growth of domains is intimately associated with the structure and the prehistory of the specimen [378, 379]. In remote crystal regions the phase transition occurs independently, so there is the possibility of having either $+\eta$ or $-\eta$.

Restricting the discussion to the case of 180° domains, is equivalent with considering a one component order parameter $\vec{\eta} = (0, 0, \eta_z)$, with z the ferroelectric (polar) axis. If the thermodynamic potential has the form: $\Phi = \Phi(\eta, T)$ with T being the temperature (equivalent to the Gibbs free energy when no stress is present), in the limit of small lattice distortions it can be developed in a power series with respect to η as:

$$\Phi = \Phi_0 + \frac{\partial \Phi}{\partial \eta}\eta + \frac{1}{2}\frac{\partial^2 \Phi}{\partial \eta^2}\eta^2 + ... \tag{5.10}$$

From symmetry considerations, we cannot have terms linear in η (see Eq. 5.9). That means:

$$\Phi(\eta, T) = \Phi_0(T) + A(T)\eta^2 + B(T)\eta^4 + ... \tag{5.11}$$

with the coefficients A and B depending only on the temperature.

In addition, for neighboring domains the approximate expression for the interaction energy per unit volume writes [373]:

$$\frac{c}{2d^3}\left[\eta(z_1) - \eta(z_2)\right] \approx \frac{1}{2}\delta\left(\frac{\partial \eta}{\partial z}\right)^2 = \frac{1}{2}\delta(\bigtriangledown\eta)^2 \tag{5.12}$$

where z is a certain direction in the crystal, and c and δ relate to the piezoelectric and electrostrictive coefficients [360]. d has dimensions of length and is determined by the interactions of atoms which are displaced during the phase transition of the sublattices, its magnitude being on the order of the domain size.

The thermodynamic potential can also be expressed as an volume integral of the density of the thermodynamic potential φ:

$$\Phi = \int_v \varphi(\eta(\vec{r}))\, dv \tag{5.13}$$

The density of the thermodynamic potential can be written as:

$$\varphi(\eta) = \frac{\partial \Phi}{\partial v} = \varphi_0 + A\eta^2(\vec{r}) + B\eta^4(\vec{r}) + \frac{1}{2}\delta(\bigtriangledown\eta)^2 \tag{5.14}$$

with A and B coefficients depending on the temperature and pressure.

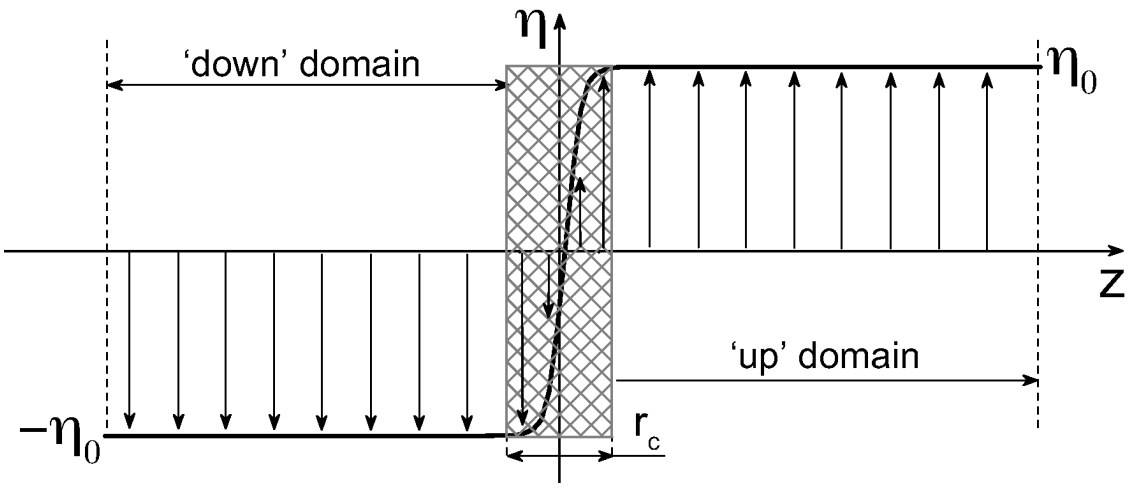

Figure 5.12: Schematics of idealized domain wall in a one component order parameter ferroelectric. The (z > 0) half space represents the 'up' domain. The domain wall (grey rectangle) contains the (xy) plane and has a structure following eq. 5.15. The arrows symbolize the spontaneous polarization.

For the idealized case of a crystal with only two domains each extending in one half space, *e.g.*, $\eta > 0$ for (z > 0) and $\eta < 0$ for (z < 0), the domain wall coincides with the (xy) plane. Far from the wall, the order parameter has to be finite, and its magnitude equal for the two domains: $\eta \to +|\eta_0|$ for $z \to \infty$ and $\eta \to -|\eta_0|$ for $z \to -\infty$. The structure of the domain wall is dictated by the dependence η=η(z) and at equilibrium must minimize the thermodynamic potential (eq. 5.13 and thus eq. 5.14). The solution writes:

$$\eta = \pm\sqrt{-\frac{A}{B}}\tanh\frac{xz}{r_c} \tag{5.15}$$

where $(A/B)^{1/2} = \eta_0$ is the displacement at the domain center and r_c is the *correlation radius*. The latter plays the role of effective wall thickness:

$$r_c = \left(\frac{\delta}{A}\right)^{\frac{1}{2}} \tag{5.16}$$

The wall energy can be evaluated, and for a periodic domain structure it writes [380]:

$$W_{wall} = \frac{4\sqrt{2}}{3} r_c A \eta_0^2 \tag{5.17}$$

From electromagnetic considerations the shape of the domain wall should be such as to

minimize the surface charge $\Delta\vec{P} \cdot \vec{n}$. $\Delta\vec{P}$ is the change of polarization vector across the domain wall, $\vec{n}$ is the normal to the domain wall. One effect of an electric field of bound charges is the predominant orientation of domain walls such that $\Delta\vec{P}$ between adjacent domains contains no component perpendicular to the wall. On such walls there is no charge, *i.e.*, they do not produce an electric field [373]. This tendency manifest itself in the appearance of domains extended along the polar axis [381].

The domain wall with is not a characteristic of the material *per se*, but varies greatly with location in the sample due to nearby impurities [378].

According to first principle theoretical studies on 180° domains $BaTiO_3$, the domain wall is expected to entail an abrupt reversal rather than a rotation, of the ferroelectric order parameter [382]. An estimated value for the wall thickness for that particular material is 5.6 Å. Experimental investigations on the same and other materials gave an upper limit of 50 Å [380, 383]. It is noticeable that the domain-wall thickness is only a few unit cells wide, in sharp contrast with the ferromagnetic domain walls. This difference is due to the fact that magnetic exchange energy is much larger than the elastic energy and slow rotation of the magnetization vector occurs over hundreds of unit cells. While the vector magnetization of a ferromagnet has a constant magnitude, the ferroelectric polarization decreases to zero at the centre of a domain wall [360, 384, 385, 386].

The origin of the off-centre displacement of the small cation in the common perovskite ferroelectrics such as $BaTiO_3$ is the ligand-field hybridization of a transition metal cation by its surrounding anions. This mechanism requires that the *d* orbitals of the small cation are formally unoccupied, and so in general precludes the coexistence of ferroelectricity and magnetism [387].

5.4.2 Hexagonal manganites

Due to the possibility to control magnetization by means of an electric field the class of hexagonal manganites has attracted much recent interest for nonvolatile data storage and nanoelectronic devices [388, 366]. This makes a detailed comprehension of their microscopic phase behavior and in particular of the ferroelectric domain structure very desirable.

Manganites, with the composition $RMnO_3$ (R = large lanthanide and/or alkaline earth ions such as La^{3+} or Sr^{2+}) are one family of the larger group of transition metal oxides. They are ferromagnetic materials and one of their important properties is the influence of the magnetic transition on the electronic conduction. In 1950 it was discovered that the resistance below the magnetic ordering temperature (Curie temperature T_C) exhibits a positive thermal coefficient, indicating metallic-like behavior and a negative gradient above T_c [389]. The implications of this discovery were explored in 1993, when *Giant/Colossal Magnetoresistance* (CMR) concept was observed [390, 391].

Some of the manganites, (R = La, Ce, Pr, Nd, Sm, Eu, Gd, Tb, Dy) have a orthorhombic crystal structure of the perovskite type, with *Pnma* space group symmetry [392]. They show ferromagnetic ordering and have been studied extensively for interesting physical properties such as high T_c superconductivity [393] and the colossal magnetoresistance [394].

If the lanthanide R has a radius smaller than that of holmium (R = Ho, Er, Tm, Yb, Lu or

Y), the corresponding manganites present a noncentrosymmetric hexagonal crystal structure ($P6_3cm$ space symmetry) as the thermodynamically stable state [395]. They undergo a ferroelectric distortion along the hexagonal axis in the temperature range T_C=570 -990 K [395, 396].

The non-perovskite (hexagonal) $RMnO_3$ attracted interest, initially due to their ferroelectric properties [397] and later due to the possibility of coexistence of combined ferroelectric and ferromagnetic behavior [398]. Such *multiferroics* are in general rare materials, since the usual atomic-level mechanisms driving ferromagnetism and ferroelectricity are mutually exclusive, for they require empty and partially filled transition metal d orbitals, respectively [399]. Therefore, for ferroelectricity and magnetism to coexist in a single phase, the atoms that move off-center to form the electric dipole moment should be different from those that carry the magnetic moment [400], as in hexagonal manganites [401]. The origin of the hexagonal structure and consequently the origin of the ferroelectric behavior in this class of materials was for a long time a matter of debate.

5.4.3 Origin of ferroelectricity in $YMnO_3$

Early work in 1960s established $YMnO_3$ to be ferroelectric with space group $P6_3cm$ [374]. It was also revealed that the material presents antiferromagnetic ordering with non-collinear Mn spins oriented in a triangular arrangement [397] (the relevant data are to be found in [402]). Recently, the coupling between the magnetic and the ferroelectric ordering in $YMnO_3$ was reported [403].

The early structure determinations concluded that the ferroelectric polarization arises from an off-centre distortion of the Mn ion towards one of the apical oxygen ions. It was only recently shown however [387], that the Mn is only slightly shifted and a small polarization appears, but from symmetry considerations, the next Mn atom would move in such a way that the total polarization would be zero.

Figure 5.13 shows the calculated atomic positions for $YMnO_3$ in the centrosymmetric (a) and ferroelectric (b) structures. The numbers give bond lengths in Å. The arrows in (b) indicate the atomic displacements with respect to the centrosymmetric structure.

Ferroelectricity in $YMnO_3$ arises from a buckling of the MnO_5 polyhedra and an unusual Y coordination as shown in Fig. 5.13 b). The Y-O displacement accompanied by MnO_5 rotation breaks the inversion symmetry and lowers the symmetry to that of the ferroelectric phase. These, together with the triangular and layered MnO_5 network give rise to a permanent dipole moment. The details of the origin of ferroelectricity in $YMnO_3$ are discussed in [395].

Above the Curie temperature $T_C = 913°$ (paraelectric phase) the $YMnO_3$ crystal structure is centrosymmetric (Fig. 5.13 a) with the point group $6/mmm$ [404]. At temperatures lower than the Curie temperature it orders ferroelectrically and presents a $6mm$ noncentrosymmetric point group symmetry. $YMnO_3$ has a single spontaneous polarization direction (that is to say: one component order parameter η) along the hexagonal c-axis $\vec{P}_s = (0, 0, P_z)$. This leads to the formation of 180° ferroelectric domains, distinguished by the opposite orientation of $\vec{P}_s$. The value of the polarization was experimentally found to be 5.5 μC/cm^2

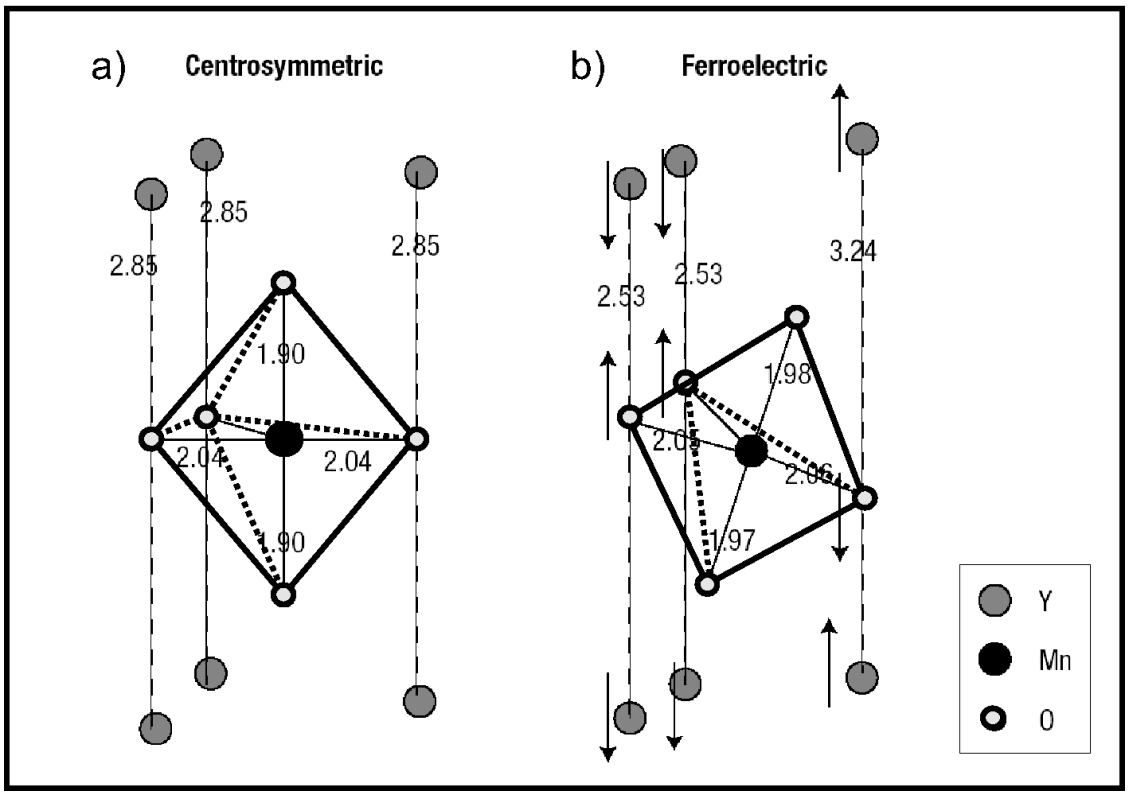

Figure 5.13: Schematics of the MnO_5 with Y layers above and below. a,b. The calculated atomic positions of the centrosymmetric (a) and ferroelectric (b) structures. LInes connecting the atoms of the MnO_5 polyhedra are added here as guides for the eye. (Figure taken from [387]).

[405] for an epitaxially grown film and a value of 6.2 μC/cm^2 is calculated in [387]. This is lower than in typical perovskite ferroelectrics, such as 25 μC/cm^2 in $BaTiO_3$.

5.4.4 SHG from $YMnO_3$

The SHG process in $YMnO_3$ is described here using a phenomenological theory, based on the existence of an order parameter and on symmetry considerations [406]. Due to the noncentrosymmetric ferroelectric ordering of charges, SHG is allowed in $YMnO_3$ in the electric-dipole approximation below T_C. Being due to the ordering of charges, the second order nonlinear susceptibility $\chi^{(2)}$ is of time-invariant type and a linear function of the ferroelectric order parameter and spontaneous polarization $\vec{P}_s$ [406, 407]. If we restrict the discussion to the $YMnO_3$ case as an uniaxial crystal, P_s is non-zero only along the ferroelectric axis z. The two 180° ferroelectric domains lead to a 180° phase difference of the corresponding SH fields. With the absolute value of the spontaneous polarization being the same for the two domains types, the magnitude of the SH fields will thus be the same, and phase sensitive nonlinear optical techniques are necessary for imaging of the domain structure [409]. Using the nonvanishing elements of the second order susceptibility tensor $\chi^{(2)}$ for the $6mm$ symmetry class (see Table 5.1), the induced second order polarization

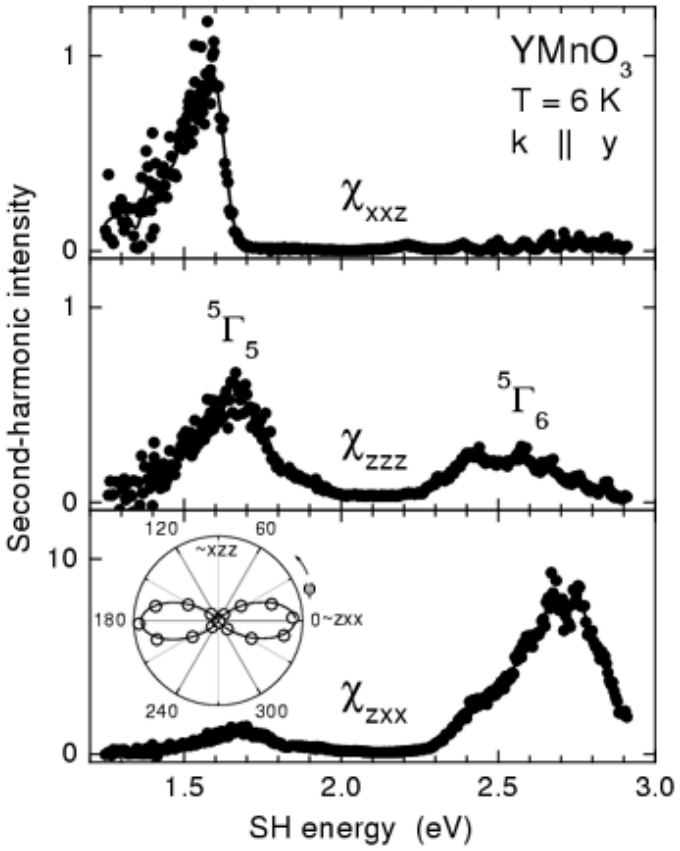

Figure 5.14: Crystalline SHG in $YMnO_3$. SH spectra of the χ_{xxz}, χ_{zzz} and χ_{zxx} tensor components of ferroelectric $YMnO_3$ measured at T = 6 K with light incident along the y axis. The magnitude of the SH response in the case of the χ_{zxx} tensor component (bottom panel) is $\sim$ 10 times larger than for the other two components. (Figure taken from [408]).

takes the form:

$$\begin{aligned} P_x^{(2)}(2\omega) &= 2\epsilon_0 \chi_{xxz} E^x(\omega) E^z(\omega) \\ P_y^{(2)}(2\omega) &= 2\epsilon_0 \chi_{xxz} E^y(\omega) E^z(\omega) \\ P_z^{(2)}(2\omega) &= 2\epsilon_0 \chi_{zxx} [(E^x(\omega))^2 + (E^y(\omega))^2] + \chi_{zzz} (E^z(\omega))^2, \end{aligned} \tag{5.18}$$

where $E^i(\omega)$ (i=x,y,z) are the components of the electric field of the fundamental light.

Figure 5.14 shows SH spectra of ferroelectric $YMnO_3$ at 6K, for a fundamental beam incident on the sample along the y direction. The SH response originating from the χ_{xxz} (upper panel), χ_{zzz} (middle panel) and χ_{zxx} (lower panel) components of the second order nonlinear susceptibility tensor are displayed. The SH intensity originating from the χ_{zxx} component is around 10 times higher than for the other components and will be selected for the imaging experiments.

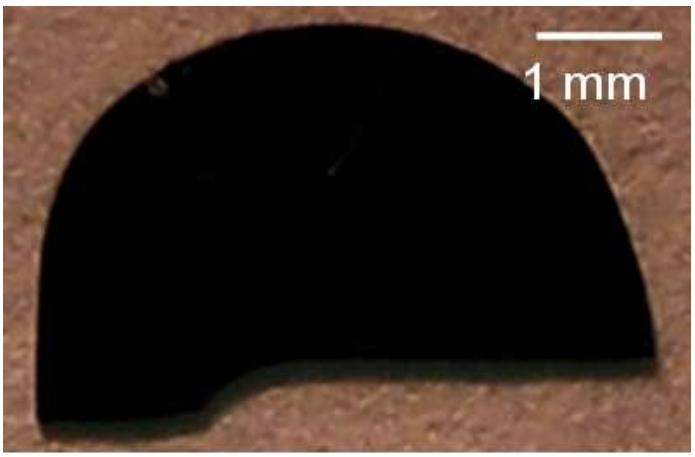

Figure 5.15: Photo of the $YMnO_3$ sample used.

5.4.5 $YMnO_3$ sample

The experiments presented here were performed on a single crystalline $YMnO_3$ sample shown in Fig 5.15. The sample is x-cut, *i.e.* the crystallographic x axis oriented along the surface normal direction.

To chose χ_{zxx} as the desired tensor component for the imaging experiments demands the determination of the crystallographic axes directions x, y, z For that purpose, SHG optical anisotropy measurements were employed. The experimental setup is described schematically in Fig. 5.16. The incident light (linearly polarized Ti:S laser, λ=800 nm) is focused inside the $YMnO_3$ crystal after a direction parallel with the x axis and the emitted SH light is detected in transmission. The polarization direction of fundamental electric field ($\mathbf{E}(\omega)$) is rotated in the (yz) plane as described in Fig. 5.16 b) by means of a half-waveplate (denoted as polarizer in Fig. 5.16 a). The SH light is spectrally filtered from the fundamental light and its integral intensity is detected. A polarizing film (analyzer) inserted in the beam path is used to select the desired polarization direction of the nonlinear response ($\mathbf{E}(2\omega)$).

Panel a in Fig 5.17 shows the dependence of the SH intensity on the output polarization direction for the parallel configuration ($\mathbf{E}(\omega) \parallel \mathbf{E}(2\omega)$). Both polarizer and analyzer are rotated simultaneously along the azimuthal angle α and for each increment in angle the generated SHG in the crystal is monitored. The data show a fourfold symmetry. In this configuration the only non-zero terms of the second order susceptibility tensor for $YMnO_3$ are: $\chi^{(2)}_{zzz}$, $\chi^{(2)}_{zyy}$ and $\chi^{(2)}_{yzy}$ (see Table 5.1). At λ=400 nm ($\sim$ 3 eV) the intensity of the light originating from the χ_{yzy} component is almost zero, and thus can be neglected (see spectrally resolved SHG data in Fig. 5.14 upper panel). Accordingly, the second order polarization $\vec{P}^{(2)}_{\parallel}$ can be written as:

$$\mathbf{P}^{(2)}_{\parallel} \propto \chi^{(2)}_{zzz}\mathbf{E}^z\mathbf{E}^z + \chi^{(2)}_{zyy}\mathbf{E}^y\mathbf{E}^y, \tag{5.19}$$

where $E^z = E\cos\alpha$ and $E^y = E\sin\alpha$. The intensity of the detected SHG ($I^{SH}_{\parallel}$) is

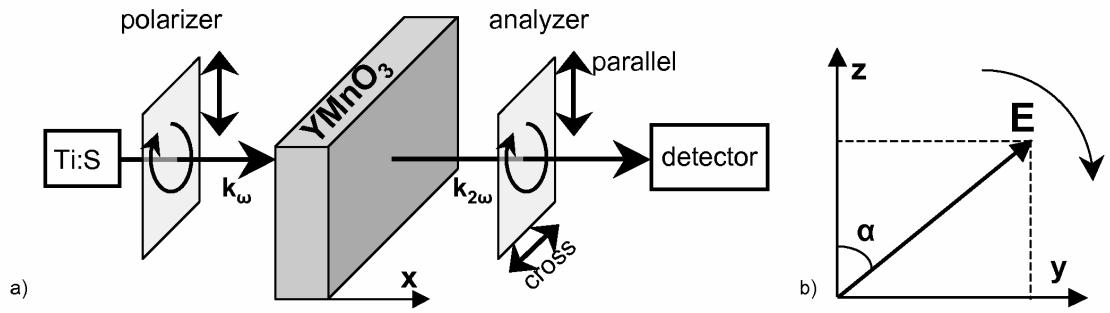

Figure 5.16: a) Experimental setup used for SHG optical anisotropy measurements. The fundamental light ($\mathbf{k}(\omega) \parallel x$) is focused within the volume of the $YMnO_3$ sample and the SHG is detected in transmission ($\mathbf{k}(2\omega) \parallel x$). The polarizer and analyzer are are simultaneously rotated, and their polarization axes are aligned parallel or perpendicular with respect to each other, according to the experimental configuration needed. b) Rotation of the incident field along the azimuthal angle α in the (yz) plane.

proportional with the second power of the nonlinear polarizability:

$$\begin{aligned} I_{\parallel}^{SH} &\propto |\mathbf{P}^{(2)}|^2 \\ &\propto \chi_{zzz}^{(2)} E^4 \cos^6\alpha + \chi_{zyy}^{(2)} E^4 \cos^2\alpha \sin^4\alpha \end{aligned} \tag{5.20}$$

A theoretical fit of the experimental data according to Eq. 5.20 is shown as solid line in Fig 5.17 a). With both polarizer and analyzer aligned following the y direction of the crystal, no SH is generated, since $\chi_{yyy}^{(2)} = 0$. This direction corresponds to $\alpha = 90°$ in our case. When the two polarizers are aligned along z, $\chi_{zzz}^{(2)}$ allows SH generation and detection. With $\chi_{zzz}^{(2)} \ll \chi_{zyy}^{(2)}$ (Fig. 5.14 middle and lower panels), the SH intensity is rather small in that case. Probably due to a slight misalignment of the sample from the plane normal on the wave vector $\mathbf{k}$ of the incident light, the four lobes observed have slightly different intensities.

Fig. 5.17 b) shows the results of the rotational anisotropy for the crossed configuration ($\vec{E}_{inc}(\omega) \perp \vec{E}(2\omega)$). For this geometry, the only SH source is the $\chi_{zyy}^{(2)}$ component of the second order susceptibility tensor. The data show a twofold symmetry with respect to the azimuthal angle α.

Using a similar argument as in the parallel configuration case, the intensity of the SH response I_{cross}^{SHG} is:

$$\begin{aligned} I_{cross}^{SHG} &\propto |\vec{P}^{(2)}|^2 \\ &\propto \chi_{zyy}^2 E^4 cos^6\alpha \end{aligned} \tag{5.21}$$

A fit to the experimental data performed according by Eq. 5.21 is shown as a solid line in the polar plot. These results permit the determination of the sixfold symmetry axis of the crystal z along the $\alpha = (0 - 180)°$ direction. Accordingly, the y axis is oriented along the $\alpha = (90 - 270)°$ direction. This allows for confident selection of specific components of the $\chi^{(2)}$ tensor for the near-field SH imaging experiments described below.

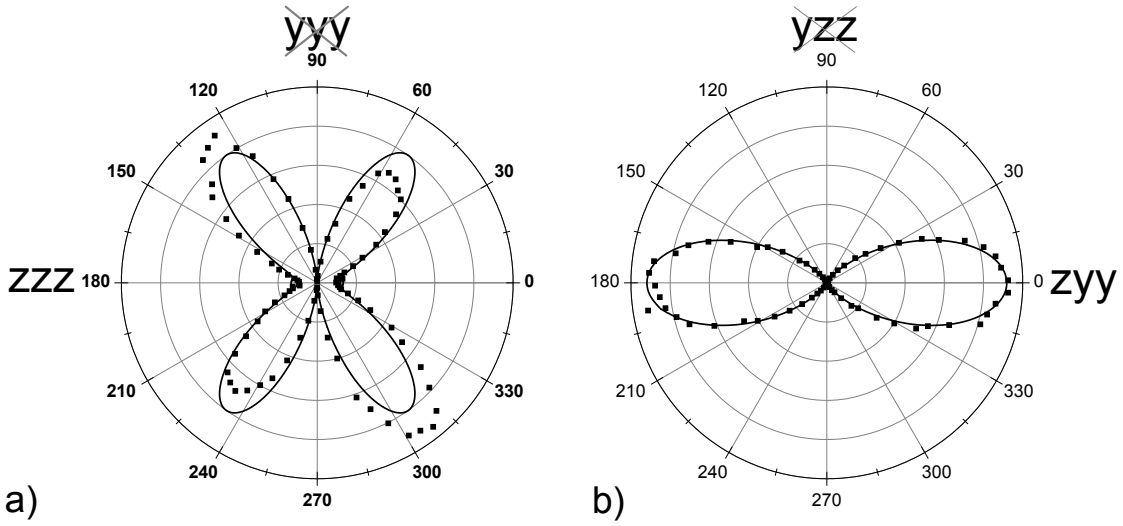

Figure 5.17: Polar plots of the SHG response in optical anisotropy measurements. Symbols represent the experimental data and solid lines are theoretical fits (see text). a) For parallel configuration the SHG intensity presents a fourfold periodicity. b) In crossed configuration only two lobes are observed, with the maximum intensity along the $\alpha = (90 - 270)^\circ$ direction.

5.4.6 Results

Au tips were used to probe and enhance the near-field ferroelectric SH intensity originating from the single crystalline $YMnO_3$. Imaging experiments revealed the ferroelectric domain structure of the sample surface with subwavelength resolution.

With the s-SNOM experiments presented here done in a back-scattering geometry, a plane of incidence cannot be defined [4]. Therefore, the polarization directions of both fundamental and detected SH beams are defined with respect to the plane spanned by the tip axis (or x axis of the $YMnO_3$ sample) and the corresponding propagation vector: p-polarized when contained in the plane (p^{in} and p^{out}, respectively) and s-polarized when orthogonal on the plane (s^{in} and s^{out}, respectively). The sample is aligned with the hexagonal z axis perpendicular with respect to the same plane, configuration in which the strongest ferroelectric SH response is expected, as detailed above.

Near-field signature and polarization dependence

Fig. 5.18 (left panel) shows the spectrally resolved SH response with the tip in close proximity to the surface ("tip in", d = 0 nm) and the tip far from the sample ("tip out", d = 2.2 μm). The fundamental light beam is p - polarized (p^{in}) and the SH response is detected unpolarized. For the "tip out" situation, the back-scattered SH signal is still larger than zero, since the $\chi^{(2)}_{zxx}$ component of the second - order susceptibility tensor is responsible for the generation of SH light from the total focus area (hereafter referred to as far-field SH signal). With the tip close to the sample, the SH signal increases ~ 4 times with respect to the one detected from the sample alone ("tip out"). The near-field response seen in this

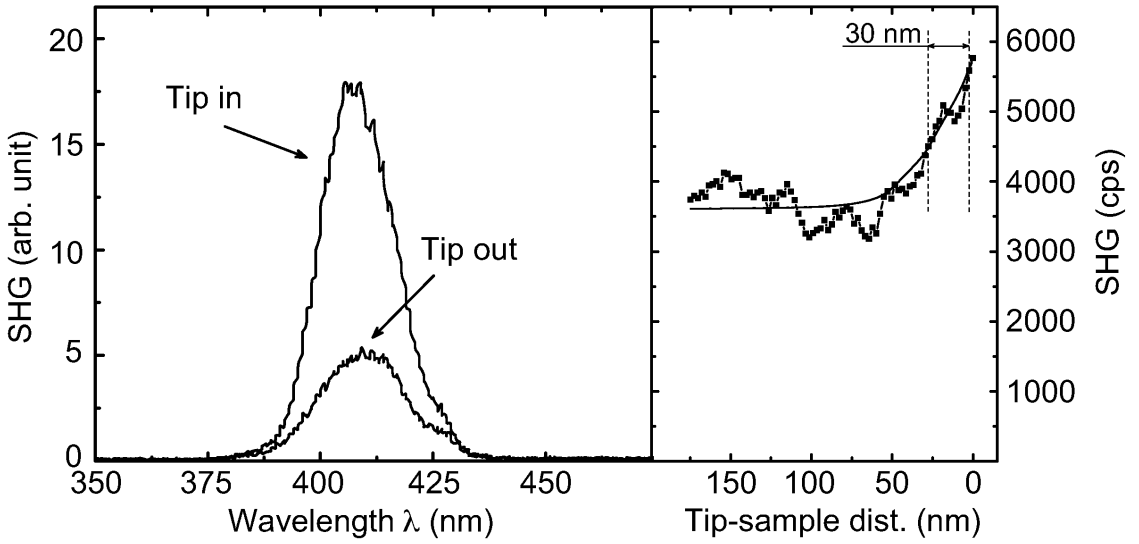

Figure 5.18: Near-field localization and enhancement of SHG from $YMnO_3$. Left: Significant increase in SH response is observed with the tip in close proximity of the sample (tip in) as compared to the situation when the tip is far away (tip out). The fundamental light beam is p - polarized (p^{in}) and the SH response is detected unpolarized. Right: Tip-sample distance dependence of the SH response reveals the near-field enhancement on a ∼30 nm lengthscale; solid line added as guide for the eye .

configuration can originate from both tip-generated SH (see Sect. 5.2) and the ferroelectric SH from the sample.

It has to be noted that with the angle between propagation direction of the pump light and the tip axis of about 70°, the p-polarized incident field has two components along the x and y axes of the sample: $\mathbf{E} = (E_x, E_y, 0)$.

$$\begin{aligned} E_x &= E\ \sin(70^\circ) = 0.94E \\ E_y &= E\ \cos(70^\circ) = 0.34E \end{aligned} \tag{5.22}$$

Therefore, SHG from the $\chi^{(2)}_{zyy}$ tensor component is also selected. Although the two tensor components have the same magnitude(*vide supra*), for the 70° angle the fundamental field component along the y direction - perpendicular on the tip axis - is much smaller than along the x axis (Eq. 5.22). Furthermore, as an optical antenna, the tip predominantly enhances the field component oriented along its axis. This results in a rather small SH-signal originating from the $\chi^{(2)}_{zyy}$ component when compared to the one from $\chi^{(2)}_{zxx}$.

To ensure the near-field character of the observed enhancement (see Sect. 3.1.1), the vertical localization of the increase is verified. A tip-sample distance dependence of the integrated SH signal is presented in Fig. 5.18 right panel. The steep increase in the signal is confined on a lengthscale of d ∼ 30 nm, close to the radial dimension of the tip apex r ∼ 20 nm, as given by the interference between the tip-scattered near-field SH response and the far-field SHG of $YMnO_3$, in addition to small contributions generated by the tip itself (*vide infra*). The signal is maximum for d = 0 nm (for a definition of d = 0 nm, see Sect. 5.3.2) where it reaches ∼1.5 times higher value than for d ∼ 100 nm. The increase is

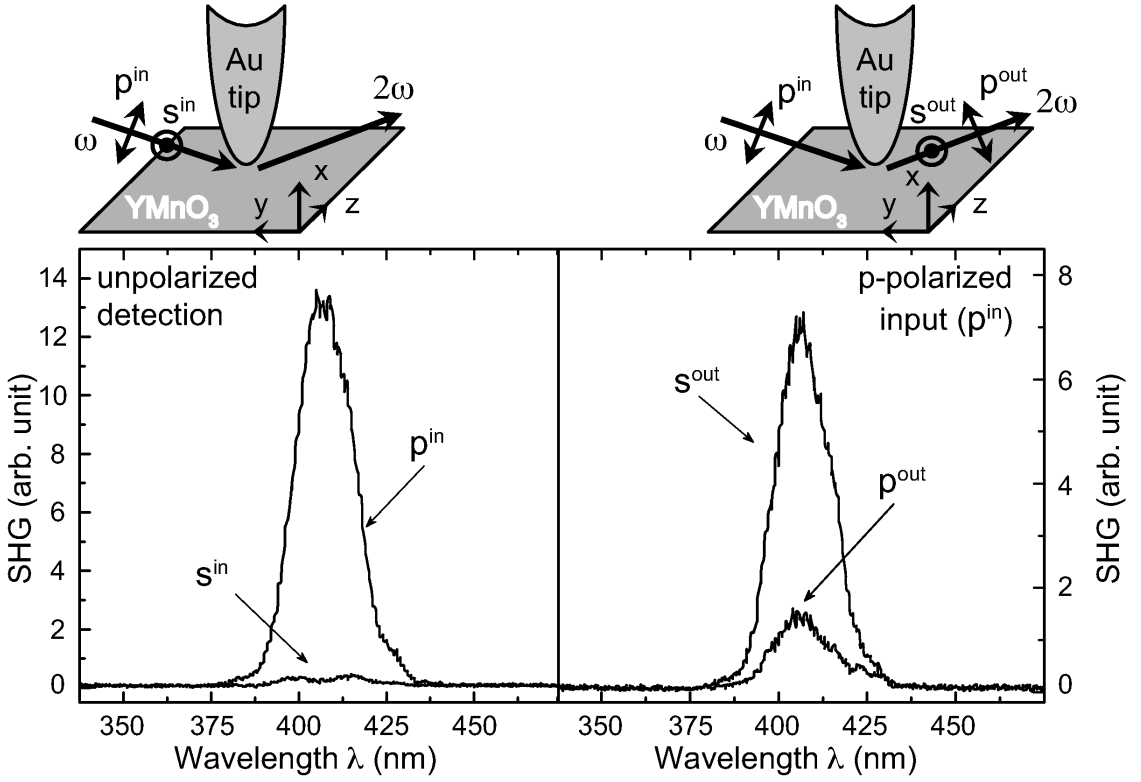

Figure 5.19: Polarization dependence of the near-field SH response. Left panel: spectrally resolved and unpolarized SH signal for p^{in} and s^{in} polarization geometries. Right panel: near-field SH spectra observed for p^{in} - p^{out} and p^{in} - p^{out} polarization configurations. Upper panels: corresponding schematics of the polarization geometries.

smaller than the one observed in the "tip in - tip out" experiment, consistent with the fact that when close to the surface (d < 200 nm) the tip also acts a scatterer of the far-field SH signal from the sample towards the detector.

Decoupling of the two SH emission mechanisms is possible via a polarization dependence measurement of the observed signal. Experimental results describing the polarization dependence of the spectrally resolved near-field SH response is presented in Fig. 5.19. For an unpolarized detection (left panel), the SH highest intensity is detected with the fundamental light p - polarized. According to Sect. 5.2, the SHG from the tip itself is observed for both fundamental and SH beams polarized along the tip axis (p^{in} - p^{out}). In contrast, the highest ferroelectric SH - having $\chi^{(2)}_{zxx}$ as source - is generated polarized along the z axis of the $YMnO_3$ sample (Sect. 5.4.5), thus perpendicular on the tip axis (p^{in} - s^{out}). The very small signal observed for s-polarized fundamental light is ferroelectric in origin, due to the $\chi^{(2)}_{zzz}$ tensor component.

The polarization analysis of the SH signal is performed for the p-polarized fundamental (right panel). The tip-generated SH shows up as expected for p-polarized output (strong $\chi^{(2)}_{s,\perp\perp\perp}$, Sect.5.2), where no ferroelectric SH is generated (see table 5.1). The output is clearly dominated by the s-polarized SHG (s^{out}), ferroelectric in origin ($\chi^{(2)}_{zxx}$). Here, the

tip generated SH is very small and can be neglected [47].

Thus, the latter polarization configuration (p^{in} - s^{out}), allows for the selection of the ferroelectric SH response form the strongest second order susceptibility tensor component $\chi^{(2)}_{zxx}$. The tip enhances the fundamental light field at its apex (p^{in}) and scatters the SH signal generated by the $YMnO_3$ sample.

Ferroelectric domain imaging

Throughout the data shown here, the SH signal is shown in counts per second (cps) and is normalized with respect to the laser power, so that the signal levels can be directly compared from one image to another. Unless specifically stated, the presented images are summed over both *trace* and *retrace* (see Ch. 2) scanning directions. The experimental arrangement is done such that the horizontal direction of all presented images is along the s-polarized direction of both incoming and scattered light beams.

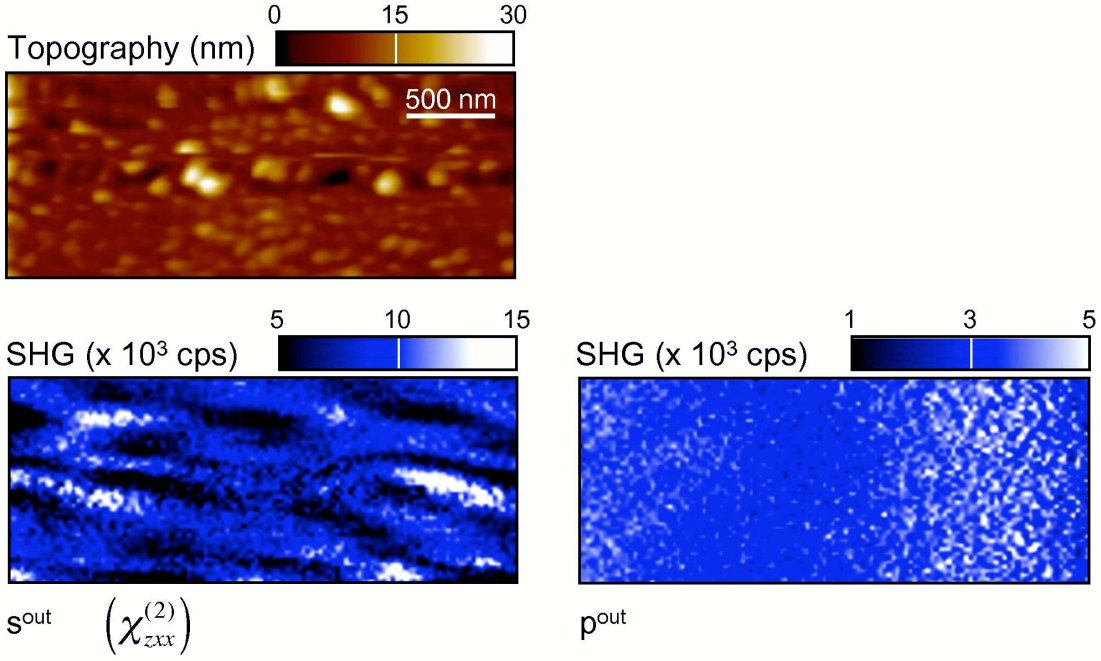

Figure 5.20: Shear-force topography of a 1 x 2.56 μm^2 region on the $YMnO_3$ sample (upper panel). The z axis of the $YMnO_3$ sample deviates from the horizontal direction of the image by about 10°. Near-field optical images for s^{out} (left panel) and p^{out} (right panel) polarization directions of the detected SH response. The fundamental light is polarized p^{in} and the optical signal is integrated for 30ms/pixel. Optical contrast denoting the ferroelectric domain structure of the sample surface is seen for the p^{in} - s^{out} configuration.

Shear-force topography and near-field SH images of the sample surface are shown in Fig 5.20. The sample is scanned over a 1 x 2.56 μm^2 area and the images comprise of 100 x 128 pixels. The surface topography displays a granular structure, with elements as high as 30 nm (upper panel). The optical images (lower panel) are acquired on the same

sample region in a consecutive manner, and the SH signal is integrated for 30 ms/pixel. The pump beam is p - polarized (p^{in}) and the nonlinear optical response is detected s^{out} and p^{out} (left and right image, respectively).

The s-polarized tip-scattered SH signal is much higher and displays a large imaging contrast, with no resemblance with the topographical features. In this configuration (*i.e.*, p^{in} - s^{out}), the SH response is ferroelectric, due to the selection of the dominating χ^2_{zxx} tensor component. The large spatial variation of the SH response is attributed to the presence of the 180° ferroelectric domains in $YMnO_3$.

The image contrast arises from a local interference process between the far-field SH signal and the near-field SHG on top of neighboring domains with antiparallel spontaneous polarizations (theoretical model discussed in Sect 5.4.7). The sample is rotated so that its z axis makes an angle of about 10° with the scanning direction (horizontal in the images). The domains are found to be anisotropically elongated mainly along the hexagonal z-axis taking a cigar-like shape.

In contrast the p^{out} configuration does not probe any nonzero tensor components ($\chi^2_{xxx} = \chi^2_{xyy} = 0$). Thus, the corresponding SH-signal does not exhibit the domain contrast (Fig. 1b, p^{out}). Despite pump and SH-polarization being parallel to the tip axis the signal is considerably weaker, being attributed solely to the generation of SH at the tip apex.

Fig. 5.21 shows the results of a similar experiment performed on a different sample region. The topography of the $YMnO_3$ sample is shown (left image in panel a) for a 3.2 x 3.2 μm^2 (128 x 128 pixel) surface area. The sample is oriented with its z axis along the horizontal of the image and the same granular structure of the surface elements is seen. Simultaneously, the near-field SH optical image is recorded (right image in panel a) with the signal integrated for 50 ms/pixel. Here, the polarization of the SH response is kept unpolarized while the incident field polarization state is switched from p^{in} to s^{in} during the scan (dashed line).

For the s^{in} case, the SH signal observed has relative low intensity, of ∼300 cps (the maximum of ∼500 cps are visible only for few pixels) and is spatially flat. Here, neither near-field enhancement nor SHG is expected from the tip. The obtained SH originates mainly from the rather small $\chi^{(2)}_{zzz}$ tensor component (see also Fig. 5.19 left panel). The lack of optical contrast demonstrates the need for near-field enhancement and selection of high-value components of the susceptibility tensor for ferroelectric domain structure imaging.

Indeed, with the incoming light polarized along the tip axis - and thus enhanced - the scattered SH signal is much higher (maximum ∼ 3000 cps) having its origin in both tip-generated SH and ferroelectric SHG ($\chi^{(2)}_{zxx}$). It has to be noted that the SHG intensity observed here is about five times lower than what is seen in Fig. 5.20, for different tips were used for the two experiments associated with different degrees of enhancement. The signature of the surface domains is clearly seen here. They are oriented along the ferroelectric z axis, akin to what is seen in Fig 5.20. The extension of the experimentally observed cigar-shaped domains along the hexagonal axis agrees with the theoretical descriptions which predicts 180° domain walls to lie parallel with the ferroelectric polarization in order to minimize the surface charge across the wall (see Sect. 5.4.1).

A very important observation is that for different sample orientation with respect to the

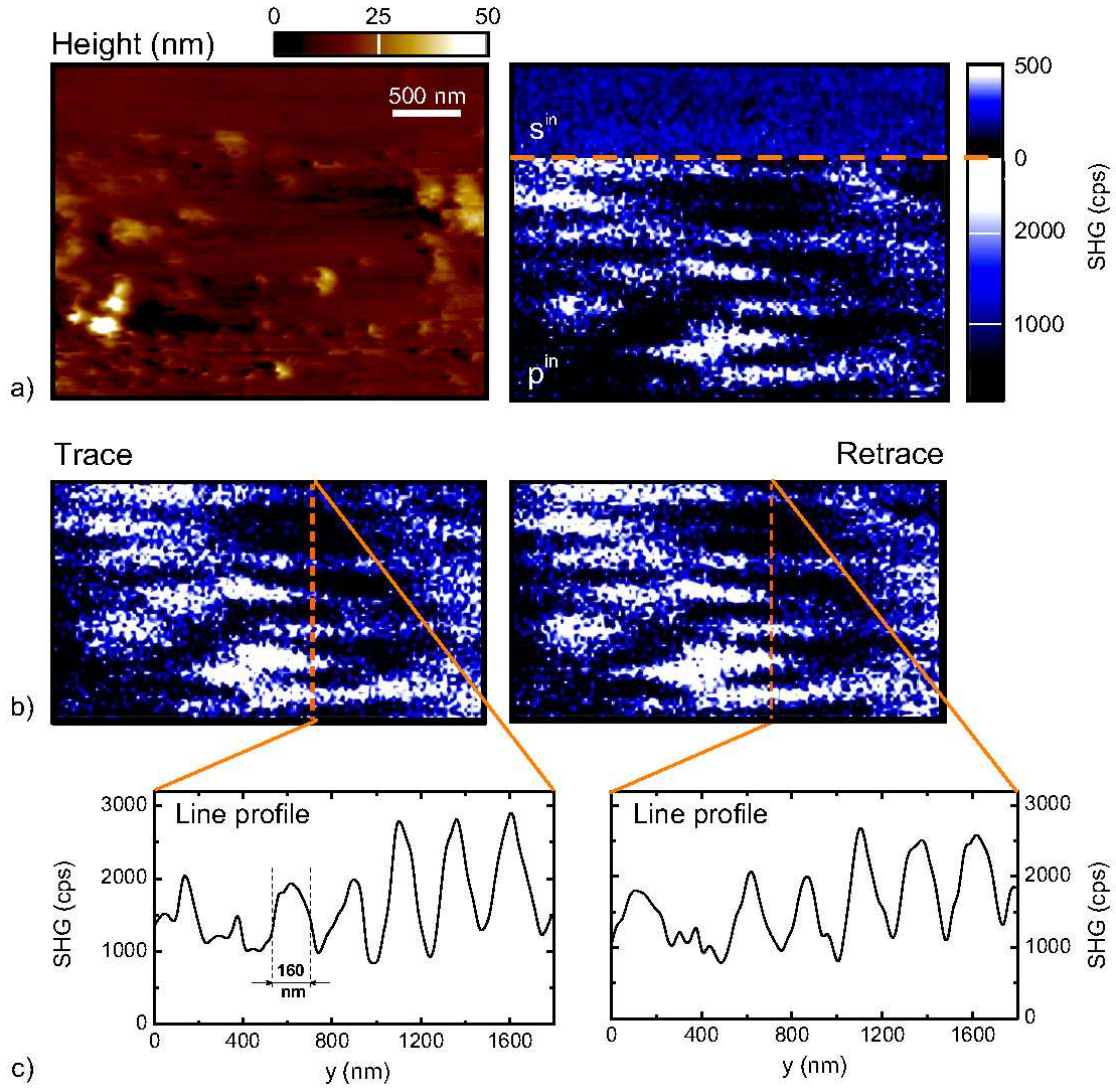

Figure 5.21: a) Shear-force topography of a 1.8 μm x 3.2 μm surface area (left) and simultaneously acquired s-SNOM SHG image of the same surface region (right), with the polarization of the pump light switched from s^{in} to p^{in} (dashed line). b) Trace and retrace SHG images of the s^{in} region, shown for comparison. c) Cross-section profile along y axis (orange dash lines) in the SHG images. The line profile is obtained as average along 5 consecutive scan lines. Spatial extension (160 nm) of one of the domains is shown.

propagation vectors of both incident and scattered light beams (Fig. 5.20 and Fig. 5.21), the observed optical features maintain their alignment along the ferroelectric axis of the crystal. This proves their sample-intrinsic provenience and rules out any artifact arising from possible far-field interference effects [351, 410].

The individual *trace* and *retrace* images are also shown in panel b of the figure together with cross section profiles (panel c) along the dashed lines. The overall signal level and image contrast are constant for both scanning directions and only small differences are noticeable in the cross sections. With $YMnO_3$ not a centrosymmetric material, the ob-

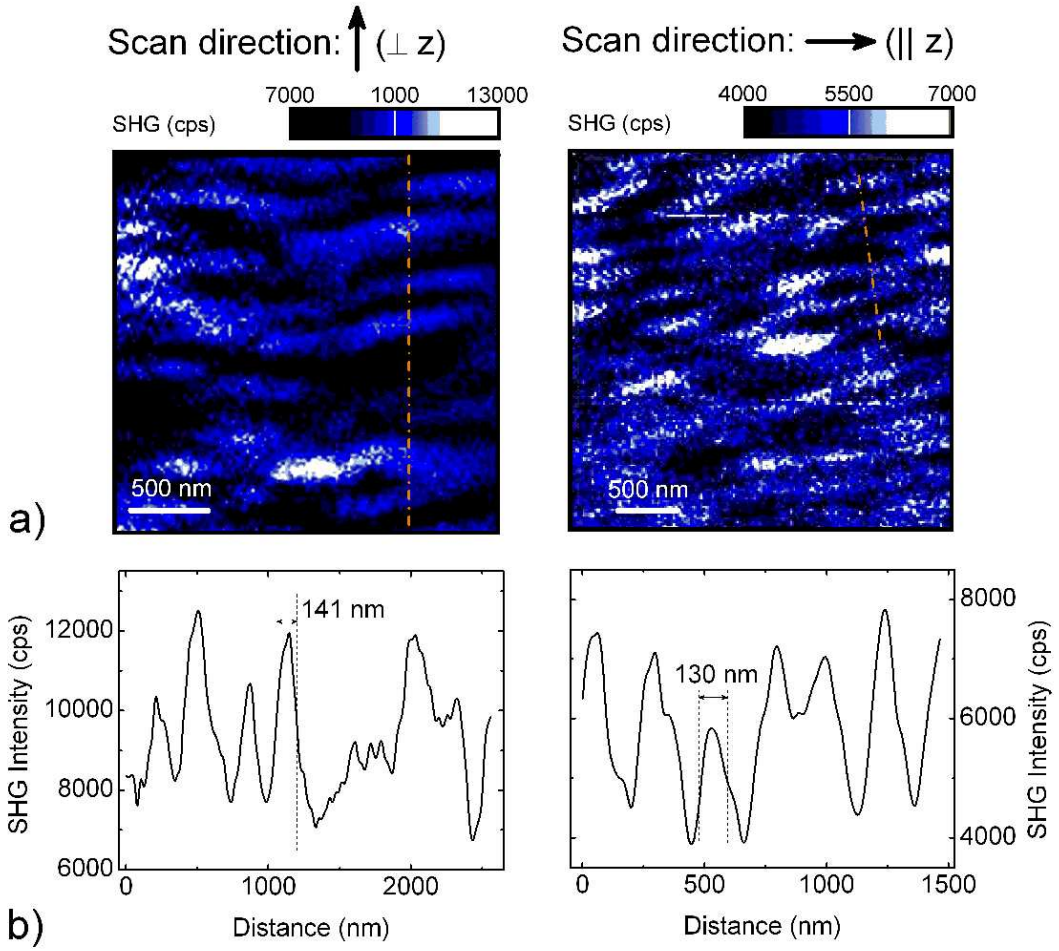

Figure 5.22: a) Near-field SH-imaging of ferroelectric domains of two different regions of the sample. The pump light is p-polarized, and the SHG is detected unpolarized for 40 ms/pixel.Left panel: 2.56 x 2.56 μm^2 image recorded with a scan direction perpendicular on z axis. Right panel: 3.2 x 3.2 μm^2 image recorded with a scan direction along z axis. b) Cross-section profiles (average along 5 consecutive scan lines) along dash lines in the 2D images are shown. Spatial extension (∼140 nm and ∼130 nm, respectively) of two of the observed domains is indicated.

served SH response is not surface specific. With the near-field probing a depth of few tens of nanometers underneath the surface, subsurface domains can as well contribute to the total intensity. The lack of information concerning the domain depth and stacking along the x axis, together with the domain walls much smaller than the achievable resolution (Sect. 5.4.1) and with the SH intensity resulting from a local interference between the responses of adjacent domains (Sect. 5.4.7), the experimental determination of the exact domain dimensions is not possible. Therefore, a domain wall is taken here to be at the position where the SH response is at the 50% level of the difference between the adjacent local maximum and minimum, respectively. The lateral dimension of one of the observed domains is indicated to be 160 nm. Along the z axis of the crystal, the domains are ex-

tending on a lengthscale of the order of 1 μm but the transition from one domain to the next seems not all the times so clear as for the orthogonal direction. This fact could be due to a possible artifact arising from the scanning direction ($\parallel z$), or is a natural and intrinsic property of the sample, where the domains do not always end abruptly, but rather reduce lateral dimensions and/or gradually "dive" towards the crystal bulk.

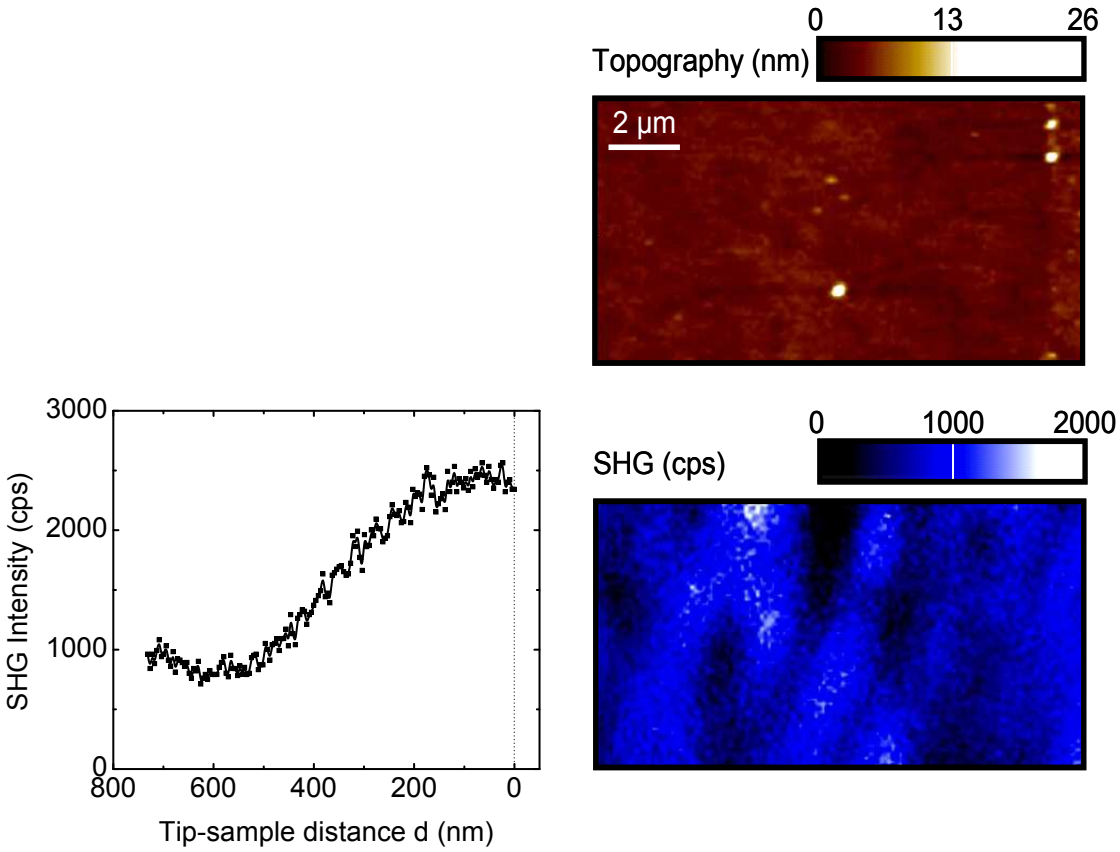

Figure 5.23: Tip scattered SHG imaging with no near-field contrast. Left: Tip sample distance dependence for a p^{in} - s^{out} polarization geometry showing a signal increase on the 500 nm lengthscale. Right: Shear-force topography (upper panel) and tip scattered SHG (lower panel) images. The scanned area is 12.8 x 6.4 μm^2, and optical signal integrated for 30 ms/pixel. The visible contrast in the optical image takes place on a $>1\mu$m lengthscale.

It is important to note that although it manifests itself with an accentuate modulation in intensity, the detected SH signal does not drop to zero. The non-zero far-field SH component acts as an offset and has an important role in the local interference model discussed below.

Fig. 5.22 shows the results of two experiments where two different sample regions were scanned along perpendicular and parallel directions on z axis (panel a, left and right image, respectively). The left image displays a 2.56 x 2.56 μm^2 area, and the right image is recorded on a 3.2 x 3.2 μm^2 area, and in both cases the optical signal is detected in a p^{in} - s^{out} geometry and integrated for 40 ms/pixel. Similar domains elongated along z are observed in both images, and thus independent of the scanning direction. Cross sectional

profiles - averaged for 5 consecutive experimental lines - along the dashed lines in the images are shown in panel b. The domain dimensions are on the same lengthscale as the ones presented above, with the two indicated in this figure being 141 nm and 130 nm, respectively.

With the degree of near-field enhancement highly dependent on the tip properties (*e.g.*, size, shape, surface roughness), not all the tips used in the experiments gave a near-field signature in the recorded SH response. Figure 5.23 presents one of these unfortunate cases. The left hand side panel shows the tip-sample distance dependence of the scattered SH signal for a p^{in} - s^{out} polarization configuration.The signal increases on a lengthscale of ∼500 nm, indicating the lack of near-field enhancement. The sample is scanned over 12.8 x 6.4 μm^2, and the shear-force topography is shown in the upper panel. Note the nonlinear color scale of the false-color image, chosen such that both low and high surface elements are visible. The high resolution visible in the topographic image demonstrates the sharpness of the tip. The simultaneously acquired SH image does not display the characteristic contrast due to the ferroelectric domain structure in $YMnO_3$. The spatial variation of the observed signal takes place on a >1 μm scale and is mainly oriented along the y crystallographic axis, and not along z as in the case of individual domains (see Fig. 5.22). It is given by a convolution between the focus dimensions and the number and size of the illuminated ferroelectric antiparallel domains.

5.4.7 Theoretical model and discussion

From the experimental results shown above and series of other images acquired for different positions on the sample we conclude that the strong optical contrast observed in the near-field SH images arises from the imaging of the ferroelectric domain structure of the $YMnO_3$ crystal. This is supported by the theoretical model detailed below.

$YMnO_3$ forms 180° ferroelectric domains where the spontaneous polarization has the same magnitude and only changes sign (*i.e.*, a $\Phi = \pi$ phase difference) in neighboring 'up' and 'down' domains. Without phase-sensitive detection, no optical contrast is expected between the domains due to identical SHG intensity. Therefore, the determination of the phase together with the amplitude is necessary for the domain visualization [411].

Several phase-sensitive methods were previously employed for SH domain imaging [412, 413, 414, 415]. They are usually based on the interference of the sample-generated SH light (signal wave) and a constant reference SH beam (reference wave). This way the phase of the signal wave is converted into a phase-dependent total SH intensity, which allows for the determination of the phase. In an elegant way, Fiebig *et al.* developed a technique where by achromatic beam imaging of the fundamental and both reference and sample-generated SH beams imaged 180° ferroelectric domains in electrically poled $YMnO_3$ and $HoMnO_3$ [415]. Kurimura *et al.* imaged domains in periodically poled $LiNbO_3$ and $LiTaO_3$ crystals interfering a signal wave with a uniform SH wave originating from a structure just underneath the system studied [414].

The above mentioned studies were performed in the far-field regime and thus were subject to the diffraction limit. With ferroelectric domains usually small compared with the

wavelength of light, a poling of large regions of the material was necessary for the domain visualization. This way, the information regarding the intrinsic domain size and orientation is usually lost.

Near-field SH methods to image ferroelectric domain structure were previously used. Bozhevolnyi *et al.* [347] imaged 180° domain walls in a periodically poled $LiNbO_3$ with a resolution of 150 nm. Without a phase-sensitive detection, the contrast there was due to the enhancement of the SH signal from neighboring domains above the domain wall. However, the contrast was observed only when the SH wave polarization was orthogonal to the domain wall, with no SH enhancement present for the parallel case. Levi *et al.* [416, 417] used a scattering SH SNOM method to map the inhomogeneous ferroelectric polarization in $Ba_xSr_{1-x}TiO_3$ thin films with a grainy structure and the achieved spatial resolution was as high as 30 Å. Phase-sensitive detection was obtained by the use of two incident laser beams resulting in interfering scattered SH signal. Dickson *et al.* [418] reported on near-field SH imaging of ferroelectric domains in PZT thin films. With no phase sensitive detection, the different domain orientation were only observed for different incident light polarizations, and their dimensions were found to be closely related to the grainy structure of the film.

Local interference

The above results can be explained via a *local interference* between the near-field tip-enhanced SH wave (signal wave) and the far-field SH wave generated in the focus region (reference wave). It is important to note that the simultaneous generation of the two interfering beams avoids difficulties associated with loss of coherence. A conceptual cartoon of the model is shown in Fig. 5.24.

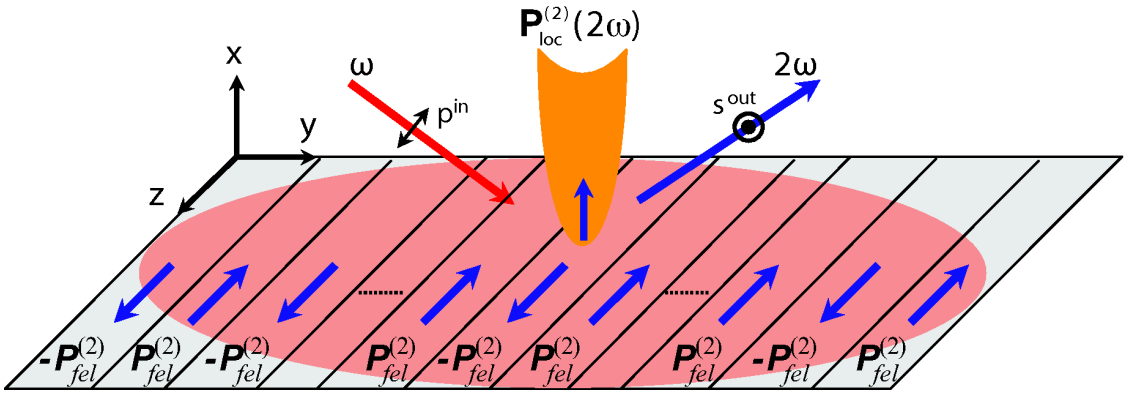

Figure 5.24: Cartoon of local interference model employed for the intensity contrast observed in the ferroelectric domain imaging. The localized and tip-enhanced SH signal from the tip apex region (signal wave) interferes with the far-field SH (reference wave). Depending on the direction of the spontaneous polarization vector of the domain just underneath the apex, it leads to an increase or decrease of the total detected signal.

With $YMnO_3$ a non-centrosymmetrical material, SH response is generated from the whole laser focus area (red region in figure). Even in the case of a homogeneous distribution of illuminated antiparallel domains, the far-field signal does not completely cancel, mainly

due to phase retardation influencing the interference process for laterally and vertically stacked domains [409]. For the considered polarization geometry (p^{in} - s^{out}), the large χ_{zxx} component of the second order nonlinear susceptibility tensor is selected and the SH response is s - polarized, as detailed above. For simplicity and without losing generality, we can consider all the ferroelectric domains present in the focus area as being equal in lateral dimensions, and each of them having a total induced polarization $\mathbf{P}^{(2)}_{fel}(2\omega)$. The latter is directly related to the ferroelectric polarization $\mathbf{P}_s$ and the proportionality is given by the domain dimensions.

With the focus diameter on the order of $\sim 2.5\ \mu$m, a large number of ferroelectric domains is expected to be probed. Therefore, the total induced polarization in the focus area $\mathbf{P}^{(2)}_{FF}(2\omega)$ is given by:

$$\mathbf{P}^{(2)}_{FF}(2\omega) = \sum_{i=1}^{N_1}(\mathbf{P}^{(2)}_{fel})_i(2\omega) + \sum_{j=1}^{N_2}(\mathbf{P}^{(2)}_{fel})_j(2\omega)e^{i\Phi} \tag{5.23}$$

where N_1 and N_2 are the total number of 'up' and 'down' domains illuminated, respectively. The angle $\Phi = \pi$ describes the phase shift of the spontaneous polarization for the antiparallel domains. Note that according to Eq. 5.23 the total far-field SH signal $I_{FF}(2\omega) \propto \left|\mathbf{P}^{(2)}_{FF}(2\omega)\right|^2$ would be different for each illuminated sample region. This can be seen in Fig. 5.23, where no near-field enhancement was observed and the detected SH response varies on a lengthscale of $> 1\mu$m.

On the other hand, the near-field component of the total SH signal is generated only in the tip-sample gap. With the incoming light polarized along its axis (p^{in}), the tip acts as effective enhancer for both incident and outgoing light. This spatial localization of the enhancement is comparable with the tip-apex radius (see Fig. 5.18), and therefore, when the tip is situated far away from the domain walls regions, the near-field signal originates mainly from the ferroelectric domain situated under the tip [i]. According to Eq. 5.1, the locally induced polarization $\mathbf{P}^{(2)}_{loc}(2\omega)$ can be expressed as:

$$\mathbf{P}^{(2)}_{loc}(2\omega) \propto L(2\omega)L(\omega)L(\omega)a\mathbf{P}^{(2)}_{fel}(2\omega) \tag{5.24}$$

with a a numerical factor with values between 0 and 1 introduced here to account for only the domain region situated under the tip. With the magnitude of the tip-enhancement being the same irrespective of the domain orientation, only a change in sign occurs for the antiparallel domains.

The local interference of the far-field ($\mathbf{P}^{(2)}_{FF}$) and near-field localized ($\mathbf{P}^{(2)}_{loc}$) terms lead to a total SH intensity I^{SH} described by:

$$I(2\omega) \propto \left|\mathbf{P}^{(2)}_{FF}(2\omega) \pm \mathbf{P}^{(2)}_{loc}(2\omega)\right|^2 \tag{5.25}$$

where the $\pm$ describes the change in orientation from the 'up' to the 'down' domains.

The result of this local interference process will be a modulation of the far-field signal by the

[i] Considering the p - polarized fundamental light, the tip itself generates SH light. But according to the symmetry selection rules discussed in Sect. 5.2, for an s - polarized detection, the contribution of the tip to the total observed signal is negligible.

near-field SHG component on the lengthscale of the domain dimension. If the tip probes a domain where the spontaneous polarization is oriented parallel with the far-field polarization described by Eq. 5.23, an increase in SH response is observed. In contrast, for the antiparallel case, the detected SH intensity will be below the far-field level. This describes conceptually the experimental findings presented in Sect. 5.4.6. It is very important to note that the degree of optical contrast will strongly depend on the relative magnitude of the far-field and near-field polarization components. and thus on the enhancement provided by the tip.

Spatial resolution

According to the simplified local interference model described above, the total SH response should remain constant (maximum of minimum) across one domain and abruptly change at the position of a domain wall to stay constant (minimum or maximum) on top of the neighboring antiparallel domain. Experimentally we found that the transition from the maximum to the minimum value of the signal occurs typically on a $\sim$ 50 nm lengthscale. With the ferroelectric domain walls predicted to extend only across few crystallographic unit cells, the change in signal - and correspondingly the lateral spatial resolution - is expected to be on the order of the tip apex radius r = (10 - 15) nm. This discrepancy can be accounted for by taking into account the interaction between the induced polarizations in neighboring domains.

In an intuitive manner, we can consider one domain consisting of a collection of identical electrical point-dipoles **P** discretely arranged with equal spacing in between. The total polarization of the domain would correspond to the $\mathbf{P}^{(2)}_{fel}(2\omega)$ used in the above discussion. A multiple domain pattern can be realized by placing individual domains near each other and the total electric field (as well as signal intensity) can be calculated in a spatially resolved manner. To reproduce the experimental conditions, the dipoles are considered to be aligned along the z axis and the direction of the polarization changes sign from one domain to the next. For symmetry reasons, it is sufficient to discuss the case of a single row of interacting dipoles centered along z = 0, at a wavelength λ = 400 nm. The domains are situated in the (y, z) plane and the total field is calculated in the (x, y) plane, that is orthogonal to the dipole direction. Here the tip is devoid of its physical characteristics, acting only as a point probe of the sample generated SH dipole field. The far-field polarization $\mathbf{P}^{(2)}_{FF}(2\omega)$ is considered to be constant.

Let us begin with a point dipole **P** located at the origin of the coordinates system. The total electric field $\mathbf{E}(\mathbf{r})$ generated by the dipole at an arbitrary observation point **r** is given by [419]:

$$\mathbf{E}(\mathbf{r}) = \frac{\mu_0\omega^2}{4\pi} \overleftrightarrow{G} \cdot\mathbf{P}, \mathbf{E}(\mathbf{r}) = \frac{\mu_0\omega^2}{4\pi} \overleftrightarrow{G} \cdot \mathbf{P}, \tag{5.26}$$

with μ_0 the vacuum permeability, $\Omega = 2\omega$ the angular frequency of the SH light and $\overleftrightarrow{G}$ the dyadic free-space Green function. The latter contains all the information about the field components created by the dipole pointing in an arbitrary direction and can be expressed as [420]:

$$\overleftrightarrow{G}(\mathbf{r}) = \left(\overleftrightarrow{U} + \frac{1}{k^2}\nabla\nabla\right) G(\mathbf{r}), \tag{5.27}$$

with $\overleftrightarrow{U}$ the unit dyadic, $k = \Omega/c = 2\pi/\lambda$ is the free-space wave number of the field and c the speed of light in vacuum. The function $G(\mathbf{r}) = exp(ikr)/r$ is the outgoing scalar free-space Green function which satisfies the inhomogeneous Helmholtz equation with a δ-function source term in the origin [120]. Eq. 5.27 becomes:

$$\overleftrightarrow{G}(\mathbf{r}) = \left[\left(\frac{1}{r} + \frac{i}{kr^2} - \frac{1}{k^2r^3}\right) \overleftrightarrow{U} + \left(-\frac{1}{r} - \frac{3i}{kr^2} + \frac{3}{k^2r^3}\right) \mathbf{nn}\right] e^{ikr} \tag{5.28}$$

where **n** a unit vector in the **r** direction [421].

The total field $\mathbf{E}(\mathbf{r})$ is composed from a propagating and an evanescent part, respectively. If in the far-field zone the field has only a propagating component, in the near-field region a rapidly decaying evanescent field adds. At the origin the propagating term is finite, while the evanescent one diverges.

In our experimental configuration, the tip is situated close to the source dipole ($\sim$ 10 nm, near-field region), and thus both field components must be considered. The following calculation is based on the total field of the dipole, and no decomposition is necessary. For a calculation of the evanescent and propagating fields, the reader is referred to Ref. [421, 422, 423]. In the (x, y) plane, $\mathbf{r} = (x, y, 0)$ and the unit vector $\mathbf{n}$ has the form $\mathbf{n} = (1, 1, 0)$. Being orthogonal onto the polarization direction, the second term in Eq. 5.28 is zero. Accordingly, the Dyadic becomes:

$$G(r) = \left[\left(\frac{1}{r} + \frac{i}{kr^2} - \frac{1}{k^2 r^3}\right)\right] e^{ikr}, \tag{5.29}$$

with $r = \sqrt{x^2 + y^2}$.

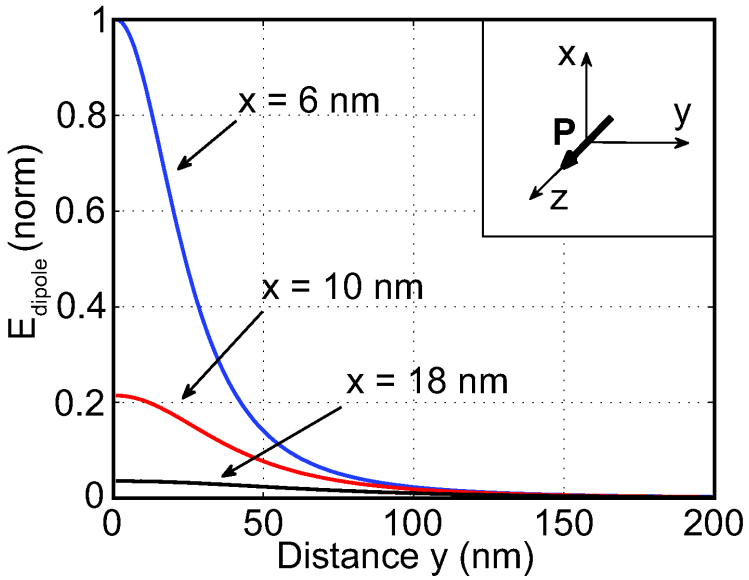

Figure 5.25: Electric field of a point dipole located in the origin and directed along z (inset). The magnitude of the field along the y axis is calculated for constant distances of 6 nm (blue), 10 nm (red) and 18 nm (black) from the dipole along axis x, respectively.

Fig. 5.25 shows the magnitude of the total dipole field in the (x,y) plane, for three discrete values of x: 6 nm (blue), 10 nm (red) and 18 nm (black). Upon increasing x, the field reduces drastically converging towards the propagating component. More important here is the decay of the field along the y axis. Looking at the case where x = 10 nm which is close to the experimental tip-sample separation, the field is still significant for a lateral distance y as large as 50 nm. This directly translates into an important interaction of the dipole with one situated within this range.

For a better visualization of the inter-dipole interaction, the model is expanded to a number of 400 dipoles arranged in 20 identical antiparallel domains. The spacing between adjacent is taken 5 nm and the calculation is performed according to the local interference

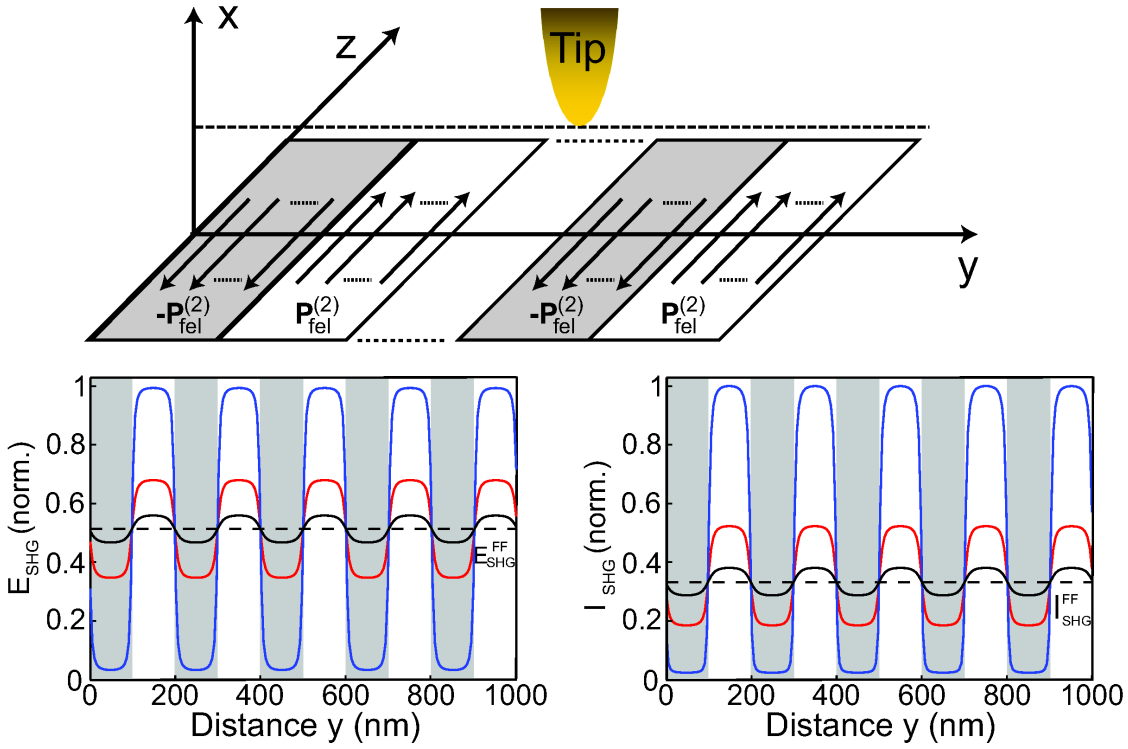

Figure 5.26: 200 interacting identical dipoles oriented along z axis and in the y = 0 plane and arranged in 10 antiparallel domains (gray and white areas, respectively). Each domain consists of 20 dipoles, with a dipole-dipole spacing of 5 nm. Calculation of the total electric field (panel a) and intensity (panel b) contrast according to the local interference model for different tip - sample separations: 6 nm (blue), 10 nm (red), 18 nm (black). The horizontal dashed line shows represents the constant far-field signal.

described above. Fig. 5.26 shows a schematics of the model geometry (upper panel) and the total electric field $|\mathbf{E}_{SHG}|$ and light intensity I_{SHG} (lower panel). Note that the results correspond to only the innermost 10 domains, to avoid asymmetries due to the boundary conditions.

The maximum signal contrast of I_{SHG} takes place in between the centers of adjacent domains. Upon approaching the domain wall region, the contrast decreases and the signal reaches the far-field level at the exact position of the wall. The lateral resolution decreases with increasing x, which is equivalent to an increase in the tip - sample separation. For the x = 10 nm distance, the signal changes from maximum to minimum on a $\sim$ 50 nm lengthscale. This demonstrates that the interaction between the dipoles strongly influences the maximum obtainable optical resolution for domain imaging.

For a more realistic description of the experimental conditions, a model where the real dimensions of the tip are considered is needed. This is because the spatial resolution will be given by the convolution of the ideal image (material properties) with the resolution function dependent on the probe geometry. Note also that here the dipoles are separated by a finite and rather large distance (5 nm) when compared with the real material properties.

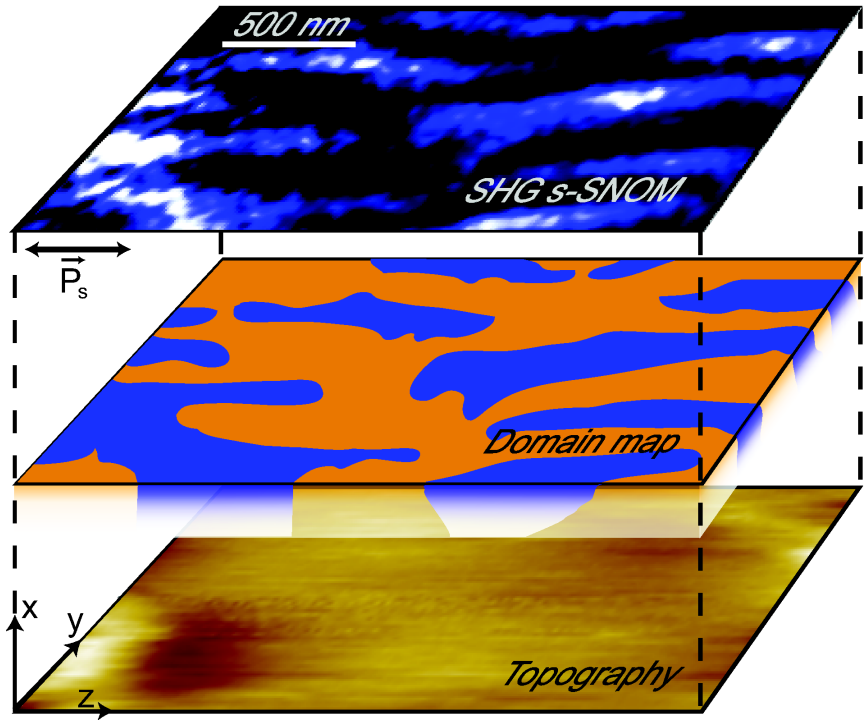

Figure 5.27: Near-field SH imaging of the 180° domains in $YMnO_3$ (upper panel), together with two colormap of the domain structure (middle panel) and corresponding shear-force topography (lower panel).

Furthermore, with the tip probing a sample depth of few tens of nanometers, it is possible that subsurface ferroelectric domains are influencing the observed SH signal. Nevertheless, the local interference model employed here correctly describes in a qualitative manner the experimental observations in terms of both imaging contrast mechanism and lateral spatial resolution.

The ferroelectric domains in $YMnO_3$ are observed experimentally to be anisotropically elongated along the hexagonal crystallographic axis z, with typical dimensions on the order of (100×1000) nm. The results presented here allow for a mapping of the surface intrinsic domain structure, as shown in Fig. 5.27 for one set of data. The blue and orange areas represent the antiparallel domains, with the walls being chosen at a ~ 50 % decrease of the maximum SH signal attributed to the domain central region.

This proves that nondestructive imaging with ultrahigh resolution based on ferroelectric contrast – not possible with linear optical response – can be achieved. It allows for the first time to address the important questions of the length scale of ferroelectric domain formation.

5.5 Conclusion

As partially asymmetric nanostructures, tapered metallic tips give the possibility to differentiate between *local* and *nonlocal* contributions to the nonlinear polarization, a long standing problem in the field of nonlinear optics. Furthermore, they provide near-field enhancement at the apex which allow for high spatial resolution nonlinear optical imaging. Average field enhancement factors of 8 - 25 were found for Au tips, while only a factor a 3 to 6 was derived for W as tip material.

The ferroelectric domain structure of single crystalline hexagonal $YMnO_3$ was investigated using near-field SH imaging. The strong optical contrast observed above antiparallel domains is based on a local interference process between the far-field and the near-field tip-enhanced components of the generated SH fields. Cigar-shaped domains elongated along the hexagonal crystallographic axis were found. Their typical dimensions are on the order of $\sim$(100 x 1000) nm^2 and the achieved lateral spatial resolution is estimated to about one tenth of the SH wavelength.

Although the investigation is restricted to the uniaxial manganite $YMnO_3$, the results are valid for any ferroelectric material with 180° domains, and could be generalized for multiaxial compounds.

6 Summary

In the present work a systematic understanding of the fundamental processes responsible for the field enhancement and plasmonic response of metallic tips is presented. Scattering-type near-field optical microscopy and spectroscopy (s-SNOM) is employed for linear, vibrational and nonlinear optical studies on the nanoscale. The main findings are:

Plasmonic light scattering from nanoscopic metallic tips

With the metallic tips responsible the field enhancement and confinement, a thorough understanding of their optical properties plays a major role in s-SNOM. Their identification and understanding proves to be crucial in the context of the near-field optical microscopy and spectroscopy. The tips are presented in the framework of optical nano-antennas and the fundamental mechanisms underlying the field enhancement at the apex are theoretically discussed, including the role of the plasmonic character of metallic tips, the tip-sample optical coupling and the local-field confinement. Dark-field optical spectroscopy based on frustrated total internal reflection at a dielectric interface is experimentally employed for the investigation of the spectral and polarization characteristics of elastic light scattering from individual tips. For Au as tip material, the scattering process is characterized by a strong plasmonic resonant behavior in the visible spectral range. In contrast, W tips show a weak and rather flat optical signal. Beside the tip material, the details of the spectral response depend sensitively on tip morphology and size as well as field polarization. The experimental results are found to agree with a theoretical model. Here the tip is modeled as a prolate hemispheroid treated in the electrostatic approximation and the relative polarizability is calculated as a function of the dielectric properties of the tip and its geometrical aspect ratio, as well as excitation excitation wavelength. The results presented underline the importance of the plasmonic character of the tip and provide selection criteria for suitable tips used in the experiments discussed in this study and in general for optical near-field studies.

Scanning probe Raman spectroscopy

An apertureless near-field optical microscope is developed and employed for tip-enhanced Raman spectroscopy (TERS). TERS arose as a promising alternative to optical far-field Raman microscopy and surface enhanced Raman spectroscopy, as it avoids some of the challenges inherent to the latter techniques. After discussing the fundamental principles of TERS and stressing the importance of the plasmonic resonant character of the metallic tips, criteria for the distinction of near-field signature from far-field artifacts are addressed. The experimental quantification of the Raman enhancement factor is described and compared with theoretical simulations. The TERS results from monolayer and submonolayer coverage of malachite green molecules adsorbed on flat Au samples are presented and en-

hancement factors as high as 10^9, corresponding to field enhancements of up to 130, are estimated. Notable spectral differences are found between far-field and the strong near-field tip-enhanced Raman responses obtained. Theoretical calculations of the normal Raman modes of malachite green molecules together with a number of control experiments rule out that molecular decomposition products or carboniferous species contribute to the observed signal. The differences are attributed to the gradient field Raman effect where the molecules are subjected to the strongly enhanced and localized field in the tip-sample gap. The high sensitivity achieved allows for the Raman detection down to the single molecule level. This is concluded from the ultra-low molecular coverage and the observed intensity and temporal fluctuations. The combination of sensitivity and spatial resolution of TERS with the intrinsic Raman selection rules and the unique symmetry properties of the scanning tip makes possible the spatially resolved vibrational mapping on the nanoscale. This can be applied, *e.g.*, for the determination of orientation in crystallographic nanostructures.

Nonlinear near-field optical microscopy

As partially asymmetric (∞mm) nanostructures with the mirror symmetry broken along their axis, tapered tips allow for distinct observation of local surface and bulk polarization contributions to the nonlinear polarization and their directional and polarization selection rules. The directional and polarization configurations are studied and the results are discussed in the context of the additional degrees of freedom offered by the tip geometry with its unique selection rules. Owing to its symmetry selectivity, SHG scattering allows for the experimental estimation of the local-field enhancement factor at the tip apex. Average enhancement factors of 8 to 25 are found for Au tips, and 3 to 6 for W as tip material. This field enhancement and its localization are employed later on for tip-enhanced second harmonic microscopy, and dielectric contrast imaging with high spatial resolution is proven. Furthermore, SHG is directly sensitive to ferroelectric ordering of materials due to the loss of inversion symmetry and in combination with scanning near-field microscopy gives access to the morphology of ferroelectric domains. This is demonstrated for single crystalline $YMnO_3$, an interesting material as intrinsic multiferroic. The surface topology of the nanoscopic ferroelectric 180° domains in $YMnO_3$ is resolved by phase-sensitive SHG imaging based on an implementation of a self-homodyne scheme in scattering-type scanning near-field microscopy (s-SNOM). Cigar-shaped domains ($\sim 100\times1000$ nm) oriented along the hexagonal crystallographic axis were found. The symmetry and phase selectivity of the technique allow to distinguish between domains of, in principle, arbitrary orientation and image the coexistence of ferroelectric and magnetic domains on the nanometer scale in multiferroics.

As demonstrated here, s-SNOM represents a versatile approach for spectroscopic imaging with ultrahigh spatial resolution and sensitivity combining optical methods with high resolution scanning probe techniques. It allows to address a wide variety of problems, ranging from plasmonic nanostructures, to molecules and quantum confined systems, and highly correlated materials, where the physical and chemical properties are determined by interactions on the nanometer length scale. Future developments in tip design and more efficient illumination and detection geometries and scanning probe implementation will permit for this technique to become a powerful nano-spectroscopic analysis tool. Furthermore,

the combination of s-SNOM with time-resolved optical methods would result in structural and dynamical characterization of individual nanostructures (*sensitivity*) chosen from an ensemble (*spatial resolution*) on the femtosecond time scale (*temporal resolution*).

Acknowledgments

In the first place I would like to thank Professor Dr. Thomas Elsaesser for giving me the possibility to work in his group, for the continuous support and research opportunities he provided.

Special thanks go to Professor Dr. Markus Raschke. The quest for high scientific standards in the exploratory research we performed and concepts like "multitasking" and "there is nothing we can't fix", led to many of the achievements I am proud of today. His close collaboration, continuous motivation and support were crucial in the completion of this project. To paraphrase him, "One's gotta do what one's gotta do!".

I acknowledge Prof. Dr. Oliver Benson who accepted to be part of my PhD defense committee.

I thank Dr. Manfred Fiebig, Dr. Jens Dreyer, Dr. Bas van Aken, Dr. Claus Ropers, Dr. Wolfgang Freyer, Dipl. Phys. Gesine Steudle and Dipl. Phys. Nicolas Behr for the fruitful scientific collaborations.

For numerous inspiring discussions and help throughout my time in Berlin I am grateful to Dr. Nils Huse, Prof. Dr. Cristoph Lienau, Dr. Michael Wörner, Prof. Dr. Klaus Reinmann, Dr. Eric Nibbering, Dr. Pancho Tzankov, Dr. Thomas Schultz, Dipl. Phys. Mathias Rang, Dipl. Phys. Markus Breusing, and all the other people part of the "C Bereich". I thank Frau Monika Tischer for helping with the tip etching.

I thank the Raschke group in Seattle: Alexandria Anderson, Samuel Berweger, Friedrich Kirchner, Andrew Jones, Rob Olmon for my whole american experience extending beyond Bagley Hall and also for careful proofreading of this work. Lady, to you my gratitude extends way more than a fathom.

Many thanks to Mushu, who supported me all this time, to Anca and Dani, and to all my friends from the Pribegia group in Berlin and from Gießen.

Aş vrea să mulţumesc familiei, şi mai ales părinţilor mei. Mi-aţi fost invăţători, aţi fost alături de mine şi aţi crezut in mine oriunde m-am aflat şi orice am făcut ca "fiu rătăcitor". Sper că sunteţi la fel de mândri de mine cum sunt eu mândru de voi. Săru'mâna.

Bibliography

[1] L. de Broglie. *Recherches sur la théorie des quanta.* PhD thesis, Paris, 1924.

[2] L. Rayleigh. Investigations in optics, with special reference to the spectroscopy. *Phil. Mag.*, 8:261, 403, 477, 1879.

[3] Ernst Abbe. Beitrage zur theorie des mikroskops und der mikroskopischen wahrnehmung. *Archiv f. Mikroskop. Anat.*, 9:413, 1873.

[4] Max Born and Emil Wolf. *Principles of Optics.* Cambridge University Press, seventh (expanded) edition, 1999. section 1.5.

[5] Stefan Hell and Ernst H. K. Stelzer. Fundamental improvement of resolution with a 4pi-confocal fluorescence microscope using two-photon excitation. *Opt. Commun.*, 93:277, 1992.

[6] M. Minsky. Memoir to inventing the confocal scanning microscope. *Scanning*, 10: 128, 1988.

[7] J.B. Pawley, editor. *Handbook of biological confocal microscopy.* Plenum Press, 1995.

[8] T. A. Klar, S. Jakobs, M. Dyba, A. Egner, and S. W. Hell. Fluorescence microscopy with diffraction resolution limit broken by stimulated emission. *Proc. Natl. Acad. Sci.*, 97:8206, 2000.

[9] Jean-Jacques Greffet and Remi Carminati. Image formation in near-field optics. *Progg. Surf. Sci.*, 56:133, 1997.

[10] Lukas Novotny and Bert Hecht. *Principles of Nano-Optics.* Cambridge University Press, 2006.

[11] S. Kawata, M. Ohtus, and M. Irie. *Nanooptics.* Springer Verlag, New York, 2002.

[12] S. Kawata. *Near-Field Optics and Surface Plasmon Polaritons.* Springer, Berlin, 2001.

[13] J.P. Fillard. *Near Field Optics and Nanoscopy.* World Scientific, Singapore, 1997.

[14] E.H. Synge. Suggested method for extending microscopic resolution into the ultra-microscopic region. *Phil. Mag.*, 6:356, 1928.

[15] Sir Isaac Newton. *Optiks.* Dover Publications Inc., New York, 1952.

[16] E.A. Ash and G. Nicholls. Super-resolution aperture scanning microscope. *Nature*, 237:510, 1972.

[17] G. Binnig, C. F. Quate, and Ch. Gerber. Atomic force microscope. *Phys. Rev. Lett.*, 56:930, 1986.

[18] A. Lewis, M. Isaacson, A. Muray, and A. Harootunian. Scanning optical spectral microscopy with 500åresolution. *Biophys.J.*, 41:405a, 1983.

[19] A. Lewis, M. Isaacson, A. Harootunian, and A. Muray. Development of a 500 åspatial resolution light microscope. light is efficiently transmitted through $\lambda/16$ diameter apertures. *Ultramicroscopy*, 13:227, 1984.

[20] D. W. Pohl, W. Denk, and M. Lanz. Optical stethoscopy: Image recording with resolution $\lambda/20$. *Appl. Phys. Lett.*, 44:651, 1984.

[21] E. Betzig, A. Lewis, A. Harootunian, M. Isaacson, and E. Kratschmer. Near field scanning optical microscopy (NSOM). development and biophysical applications. *Biophys. J.*, 49:269, 1986.

[22] L. Novotny and D. W. Pohl. *Photons and Local Probes*, chapter Light propagation in scanning near-field optical microscopy, page 21. Kluwer Academic, Dordrecht, 1995.

[23] M. Specht, J. D. Pedarnig, W. M. Heckl, and T. W. Hänsch. Scanning plasmon near-field microscopy. *Phys. Rev. Lett.*, 68:477, 1992.

[24] F. Zenhausern, M. P. O'Boyle, and H. K. Wickramasinghe. Apertureless near-field optical microscope. *Appl. Phys. Lett.*, 65:1623, 1994.

[25] Y. Inouye and S. Kawata. Near-field scanning optical microscope with a metallic probe tip. *Opt. Lett.*, 19:159, 1994.

[26] R. Bachelot, P. Gleyzes, and A. C. Boccara. Near-field optical microscope based on local perturbation of a diffraction spot. *Opt. Lett.*, 20:1924, 1995.

[27] A. Hartschuh, E. J. Sánchez, X. S. Xie, and L. Novotny. High-resolution near-field Raman microscopy of single-walled carbon nanotubes. *Phys. Rev. Lett.*, 90:095503, 2003.

[28] N. Anderson, P. Anger, A. Hartschuh, and L. Novotny. Subsurface Raman imaging with nanoscale resolution. *Nano Lett.*, 6(4):744–749, 2006. ISSN 1530-6984.

[29] Bruno Pettinger, Gennaro Picardi, Rolf Schuster, and Gerhard Ertl. Surface-enhanced and STM tip-enhanced Raman spectroscopy of cn ions at gold surfaces. *J. Electroan. Chem.*, 554:293, 2003.

[30] C. C. Neacsu, J. Dreyer, N. Behr, and M. B. Raschke. Scanning-probe Raman spectroscopy with single-molecule sensitivity. *Phys. Rev. B*, vol. 73:p. –406, 2006.

[31] Lukas Novotny, Randy X. Bian, and X. Sunney Xie. Theory of nanometric optical tweezers. *Phys. Rev. Lett*, 79:645, 1997.

[32] Gesine Anne Steudle. Modifikation der spontanen emmision nanoskopischer partikelpotential von optischen pinzetten für untersuchungen und andwendungen der quantenelektrodynamic. Master's thesis, Humboldt Universität zu Berlin, 2005.

[33] Julius Adams Stratton. *Electromagnetic Theory.* Mcgraw-Hill Book Company, Inc., 1941.

[34] D.B. Rutledge, D.P. Neikirk, and D.P. Kasilingan. *Infrared and Milimeter Waves*, volume 10. Academic, New York, 1983.

[35] J. Koglin, U. C. Fischer, and H. Fuchs. Material contrast in scanning near-field opticsl microscopy at 1-10 nm resolution. *Phys. Rev. B*, 55:7977, 1997.

[36] E. J. Sanchez, L. Novotny, and X. S. Xie. Near-field fluorescence microscopy on two-photon excitation with metal tips. *Phys. Rev. Lett.*, 82:4014, 1999.

[37] F. Keilmann, D. W. van der Weide, T. Eickelkamp, R. Merz, and D. Stöckle. Extreme sub-wavelength resolution with a scanning radio-frequency transmission microscope. *Opt. Commun.*, 129:15, 1996.

[38] B. Knoll and F. Keilmann. Near-field probing of vibrational absorption for chemical microscopy. *Nature*, 399:134, 1999.

[39] Bernhard Knoll and Fritz Keilmann. Enhanced dielectric contrast in scattering-type scanning near-field optical microscopy. *Opt. Commun.*, 182:321, 2000.

[40] M. B. Raschke, L. Molina, T. Elsaesser, D. H. Kim, W. Knoll, and K. Hinrichs. Apertureless near-field vibrational imaging of block-copolymer nanostructures with ultrahigh spatial resolution. *ChemPhysChem*, 6:2197, 2005.

[41] Anatoly V. Zayats, Thomas Kalkbrenner Vahid Sandoghdar, and Jürgen Mlynek. Second-harmonic generation from individual surface defects under local excitation. *Phys. Rev. B*, 61:4545, 2000.

[42] A. Bouhelier, M. Beversluis, A. Hartschuh, and L. Novotny. Near-field second-harmonic generation induced by local field enhancement. *Phys. Rev. Lett.*, 90:013903, 2003.

[43] C. C. Neacsu, B. B. van Aken, M. Fiebig, and M. Raschke. Tip-enhanced near-field second-harmonic imaging of the ferroelectric domain structure of $YMnO_3$. in preparation, 2008.

[44] Taro Ichimura, Norihiko Hayazawa, Mamoru Hashimoto, Yasushi Inouye, and Satoshi Kawata. Tip-enhanced coherent anti-stokes Raman scattering for vibrational nanoimaging. *Phys. Rev. Lett.*, 92:220801, 2004.

[45] N. Nilius, N. Ernst, and H.J. Freund. Tip influence on plasmon excitations in single gold particles in an stm. *Phys. Rev. B*, 65:115421, 2002.

[46] L. Aigouy, F. X. Andréani, A. C. Boccara, , J. C. Rivoal, J. A. Porto, R. Carminati, J.-J. Greffet, and R. Mégy. Near-field optical spectroscopy using an incoherent light source. *Appl. Phys. Lett.*, 76:397, 2000.

[47] C. C. Neacsu, G. A. Reider, and M. B. Raschke. Second-harmonic generation from nanoscopic metal tips: Symmetry selection rules for single asymmetric nanostructures. *Phys. Rev. B*, vol. 71:p. 201–402, 2005.

[48] G. Binnig. Atomic force microscope and method for imaging surfaces with atomic resolution. United States Patent 4724318, 1986.

[49] E. Betzig, P.L. Finn, and J. S. Weiner. Combined shear force and near-field scanning optical microscopy. *Appl. Phys. Lett.*, 60:2484, 1992.

[50] R. Toledo-Crow, P.C. Yang, Y. Chen, and M. Vaez-Iravani. Near-field differential scanning optical microscope with atomic force regulation. *Appl. Phys. Lett.*, 60:2957, 1992.

[51] Karrai K.and Grober R.D. Piezoelectric tip sample distance control for near field optical microscopes. *Applied Physics Letters*, 66:1842, 1995.

[52] J.P. Ibe, Jr. P.P. Bey, S.L. Brandow, R.A. Brizzolara, N.A. Burnham, D.P. Dilella, K.P. Lee, C.R.K. Marrian, and R.J. Colton. On the electrochemical etching of tips for scanning tunneling microscopy. *J. Vac. Sci. Technol. A*, 8:3570, 1990.

[53] D. A. Lapshin, V. S. Letokhov, G. T. Shubeita, S. K. Sekatskii, and G. Dietler. Direct measurement of the absolute value of the interaction force between the fiber probe and the sample in a scanning near-field optical microscope. *Appl. Phys. Lett.*, 81: 1503, 2002.

[54] Tomasz Kowalewski and Justin Legleiter. Imaging stability and average tip-sample force in tapping mode atomic force microscopy. *J. App. Phys.*, 99:064903, 2006.

[55] J. U. Schmidt, H. Bergander, and L. M. Eng. Experimental and theoretical analysis of shear force interaction in the non-contact regime with 100 pN force resolution. *Appl. Surf. Sci.*, 157:295, 2000.

[56] J. U. Schmidt, H. Bergander, and L. M. Eng. Shear force interaction in the viscous damping regime studied at 100 pn force resolution. *J. Appl. Phys.*, 87:3108, 2000.

[57] K. Karrai and I. Tiemann. Interfacial shear force microscopy. *Phys. Rev. B*, 62:13174, 2000.

[58] V. Emiliani, F. Intonti, Ch. Lineau, T. Elsaesser, R. Nötzel, and K.H. Ploog. Near-field optical imaging and spectroscopy of single GaAs quantum wires. *Phys. Stat. Sol. A*, 190:749, 2002.

[59] B. C. Stipe, H. J. Mamin, T. D. Stowe, T. W. Kenny, , and D. Rugar. Noncontact friction and force fluctuations between closely spaced bodies. *Phys. Rev. Lett.*, 87: 096801, 2001.

[60] M. J. Gregor, P. G. Blome, J. Schöfer, , and R. G. Ulbrich. Probe-surface interaction in near-field optical microscopy: The nonlinear bending force mechanism. *Appl. Phys. Lett*, 68:307, 1996.

[61] D. A. Lapshin, E. E. Kobylkin, and V. S. Letokhov. Shear force distance control in near-field optical microscopy: experimental evidence of the frictional probe-sample interaction. *Ultramicroscopy*, 83:17–23, 2000.

[62] R. L. Williamson, L. J. Brereton, M. Antognozzi, and M. J. Miles. Are artefacts in scanning near-field optical microscopy related to the misuse of shear force? *Ultramicroscopy*, 71:165, 1998.

[63] Stefan Hoppe, Georgios Ctistis, Jens J. Paggel, and Paul Fumagalli. Spectroscopy of the shear force interaction in scanning near-field optical microscopy. *Ultramicroscopy*, 102:221, 2005.

[64] M.P. Bernal, F. Marquis-Weible, P.Y. Boillat, and P. Lambelet. Theoretical and experimental study of the forces between different snom probes and chemically treated AFM cantilevers. *IEEE Proc.*, 88:1460, 2000.

[65] S. Davy, M. Spajer, , and D. Courjon. Influence of the water layer on the shear force damping in near-field microscopy. *Appl. Phys. Lett.*, 73:2594, 1998.

[66] C. Durkan and I. V. Shvets. Investigation of the physical mechanisms of shear-force imaging. *J. Appl. Phys.*, 80:5659, 1996.

[67] Takaharu Okajima and Shunsuke Hirotsu. Study of shear force between glass microprobe and mica surface under controlled humidity. *Appl. Phys. Lett.*, 71:545, 1997.

[68] Takaharu Okajima and Shunsuke Hirotsu. Study of probe-surface interaction in shear-force microscopy: Effects of humidity and lateral spring constant. *Opt. Rev.*, 5:303, 1998.

[69] R. Brunner, O. Marti, and O. Hollricher. Influence of environmental conditions on shear-force distance control in near-field optical microscopy. *J. Appl. Phys.*, 86:7100, 1999.

[70] P. K. Wei and W. S. Fann. The effect of humidity on probe-sample interactions in near-field scanning optical microscopy. *J. Appl. Phys.*, 87:2561, 2000.

[71] Fu Min Huang, Ferhat Culfaz, Frederic Festy, and David Richards. Effect of the surface water layer on the optical signal in apertureless scanning near field optical microscopy. *Nanotechnol.*, 18:015501, 2007.

[72] Jacob N. Israelachvili. *Intermolecular and surface forces.* Academic Press London, 2nd edition, 1991.

[73] Steve Granick. Motions and relaxations of confined liquids. *Science*, 253:1374, 1991.

[74] Hsuan-Wei Hu, George A. Carson, and Steve Granick. Relaxation time of confined liquids under shear. *Phys. Rev. Lett.*, 66:2758, 1991.

[75] P. J. James, M. Antognozzi, J. Tamayo, T. J. McMaster, J. M. Newton, and M. J. Miles. Interpretation of contrast in tapping mode AFM and shear force microscopy. A study of nafion. *Langmuir*, 17:349, 2001.

[76] D. Sarid. *Scanning Force Microscopy.* Oxford University Press, 1991.

[77] F. Froehlich and T.D. Milster. Mechanical resonance behavior of near-field optical microscope probes. *Appl. phys. Lett.*, 70:1500, 1997.

[78] K. Karrai and R. D. Grober. Piezo-electric tuning fork tip-sample distance control for near field optical microscopes. *Ultramicroscopy*, 61:197–205, 1995.

[79] Robert D. Grober, Jason Acimovic, Jim Schuck, Dan Hessman, Peter J. Kindlemann, Joao Hespanha, , A. Stephen Morse, Khaled Karrai, Ingo Tiemann, and Stephan Manus. Fundamental limits to force detection using quartz tuning forks. *Rev. Sci. Instr.*, 71:2776, 2000.

[80] T.R. Albrecht, P. Gruetter, D. Horne, and D. Rugar. Frequency modulation detection using high-Q cantilevers for enhanced force microscope sensitivity. *J. Appl. Phys.*, 69:668, 1991.

[81] J. F. Nye. *Physical Properties of crystals*. Oxford Press University, 1985.

[82] Paul Horowitz and Winfield Hill. *The Art of Electronics*. Cambridge University Press, 2nd edition, 1989. chapter 7.

[83] C. C. Neacsu, G. A. Steudle, and M. B. Raschke. Plasmonic light scattering from nanoscopic metal tips. *Appl. Phys. B*, vol. 80(no. 3):p. 295, 2005.

[84] R. Guckenberger, T. Hartmann, W. Wiegraebe, and W. Bauneister. *Scanning Tunneling Microsocpy II*. Springer, 1995.

[85] M. J. Vasile, D. A. Grigg, J. E. Griffith, E. A. Fitzgerald, and P. E. Russell. Scanning probe tips formed by focused ion beams. *Rev. Sci. Instr.*, 62:2167, 1991.

[86] A. J. Nam, A. Teren, T. A. Lusby, and A. J. Melmed. Benign making of sharp tips for STM and FIM: Pt, Ir, Au, Pd, and Rh. *J. Vac. Sci. technol. B*, 13:1556, 1995.

[87] M. Iwami, Y. Uehara, and S. Ushioda. Preparation of silver tips for scanning tunneling microscopy imaging. *Rev. Sci. Instr.*, 69:4010, 1998.

[88] M. Klein and G. Schwitzgebel. An improved lamellae drop-off technique for sharp tip preparation in scanning tunneling microscopy. *Rev. Sci. Instr.*, 68:3099, 1997.

[89] Bin Ren, Gennaro Picardi, and Bruno Pettinger. Preparation of gold tips suitable for tip-enhanced Raman spectroscopy and light emission by electrochemical etching. *Rev. Sci. Instr.*, 75:837, 2004.

[90] D. E. Spence, P. N. Kean, and W. Sibbet. 60-fsec pulse generation from a self-mode-locked Ti:sapphire laser. *Opt. Lett.*, 16:42, 1991.

[91] Bob Proctor, Erik Westwig, and Frank Wise. Characterization of a kerr-lens mode-locked ti:sapphire laser with positive group-velocity dispersion. *Opt. Lett.*, 18:1654, 1993.

[92] Claude Rulliere, editor. *Femtosecond laser pulses. Principles and experiments*. Springer Verlag, 1998.

[93] G. Tempea, B. Povazay, A. Assion, A. Isemann, W. Pervak, M. Kempeand A. Stingl, and W. Drexler. All-chirped-mirror pulse compressor for nonlinear microscopy. In *CLEO 2006*, 2006.

[94] A. M. Larson and A. T. Yeh. Ex vivo characterization of sub-10-fs pulses. *Opt. Lett.*, 31:1681, 2006.

[95] W.L. Stutzman and G.A. Thiele. *Antenna Theory and Design*. Wiley, 1998.

[96] Constantine A. Balanis. *Antenna theory*. Wiley-Interscience, 3 edition, 2005.

[97] H. Hertz. *Electric Waves*. Dover Publications, 1962.

[98] G. Marconi. Wireless telegraphic communication. Nobel Lecture, December 1909.

[99] Jean-Jacques Greffet. Nanoantennas for light emission. *Science*, 308:5728, 2005.

[100] P. Mühlschlegel, H.-J. Eisler, O. J. F. Martin, B. Hecht, and D. W. Pohl. Resonant optical antennas. *Science*, 308:1607, 2005.

[101] Gueroui Z and Libchaber A. Single-molecule measurements of gold-quenched quantum dots. *Phys. Rev. Lett.*, 93:166108, 2004.

[102] Gregory Schneider and Gero Decher. Distance-dependent fluorescence quenching on gold nanoparticles ensheathed with layer-by-layer assembled polyelectrolytes. *Nanolett.*, 6:530, 2006.

[103] C.F. Bohren and D.R. Huffman. *Absorption and scattering of light by small particles*. Wiley, New York, 1998.

[104] A. J. McAlister and E. A. Stern. Plasma resonance absorption in thin metal films. *Phys. Rev.*, 132:1599, 1963.

[105] Winfried Denk and Dieter W. Pohl. Near-field optics: Microscopy with nanometer-size fields. *J. Vac. Sci. Technol. B*, 9:510, 1991.

[106] Y. Wang, K. Kempa, B. Kimball, J. B. Carlson, G. Benham, W. Z. Li, T. Kempa, J. Rybczynski, A. Herczynski, and Z. F. Ren. Receiving and transmitting light-like radio waves: Antenna effect in arrays of aligned carbon nanotubes. *Appl. Phys. Lett.*, 85:2607, 2004.

[107] R.D. Grober, R.J. Schoelkopf, and D.E. Prober. High efficiency near-field electromagnetic probe having a bowtie antenna structure. United States Patent #5696372, 1997.

[108] C. Fumeaux, M.A. Gritz, I. Codreanu, W.L. Schaich, F.J. Gonzalez, and G.D. Boreman. Measurement of the resonant lengths of infrared dipole antennas. *Infrared Phys. and Technol.*, 41:271, 2000.

[109] G.D. Boreman, F.J. Gonzalez, M.A. Gritz, I. Codreanu, and C. Fumeaux. Area receiver with antenna-coupled infrared sensors. US Patent 6,459,084, 2002.

[110] C. Fumeaux, D. Baumann, and R. Vahldieck. Advanced FVTD simulation of dielectric resonator antennas and feed structures. *ACES Journal*, 19:155, 2004.

[111] F.J. Gonzalez and G.D. Boreman. Comparison of dipole, bowtie, spiral and log-periodic ir antennas. *Infrared Phys. Technol.*, 46:418, 2005.

[112] Arvind Sundaramurthy, P. James Schuck, Nicholas R. Conley, David P. Fromm, Gordon S. Kino, and W. E. Moerner. Toward nanometer-scale optical photolithography: Utilizing the near-field of bowtie optical nanoantennas. *Nanolett.*, 6:355, 2006.

[113] C.F. Middleton and G.D. Boreman. Technique for thermal isolation of antenna-coupled infrared microbolometers. *J. Vac. Sci. Technol. B*, 24:2356, 2006.

[114] V.A. Markel and T.F. George, editors. *Optics of Nanostructured Materials*. Wiley, New York, 2001.

[115] S. Kawata, editor. *Topics in Applied Optics*. Springer, Heidelberg, 2001.

[116] Kuiru Li, Mark I. Stockman, and David J. Bergman. Self-similar chain of metal nanospheres as an efficient nanolens. *Phys. Rev. Lett.*, 91:227402, 2003.

[117] Amanda J. Haes, W. Paige Hal, Lei Chang, William L. Klein, and Richard P. Van Duyne. A localized surface plasmon resonance biosensor: First steps toward an assay for alzheimer's disease. *Nanolett.*, 4:1029, 2004.

[118] F. Zenhausern, Y. Martin, and H. K. Wickramasinghe. Scanning interferometric apertureless microscopy: Optical imaging at 10 Angstrom resolution. *Science*, 269: 1083, 1995.

[119] P. K. Aravind and H. Metiu. The effects of the interaction between resonances in the electromagnetic response of a sphere-plane structure: applications to surface enhanced spectroscopy. *Surf. Sci.*, 124:506, 1983.

[120] John David Jackson. *Classical Electrodynamics*, volume I, Chapter II. John Wiley and Sons, New York, third edition, 1999.

[121] R. Hillenbrand and F. Keilmann. Complex optical constants on a subwavelength scale. *Phys. Rev. Lett.*, 85:3029, 2000.

[122] M. B. Raschke and Ch. Lienau. Apertureless near-field optical microscopy: Tip-sample coupling in elastic light scattering. *Appl. Phys. Lett.*, 83:5089, 2003.

[123] E.D. Palik, editor. *Handbook of Optical Constants of Solids*. Springer, Berlin, 2000.

[124] R. Hillenbrand, T. Taubner, and F. Keilmann. Phonon-enhanced light-matter interaction at the nanometre scale. *Nature*, 418:159, 2002.

[125] Mathias Rang. Diplomarbeit, Humboldt Universitäet zu Berlin, 2006.

[126] R. M. Roth, N. C. Panoiu, M. M. Adams, R. M. Osgood, C. C. Neacsu, and M. B. Raschke. Resonant-plasmon field enhancement from asymmetrically illuminated conical metallic-probe tips. *Opt. Expr.*, vol. 14:p. 2921, 2006.

[127] A. Downes, D. Salter, and A. Elfick. Finite element simulations of tip-enhanced raman and fluorescence spectroscopy. *J. Phys. Chem. B*, 110:6692, 2006.

[128] J. T. Krug II, E. J. Sànchez, and X. S. Xie. Design of near-field optical probes with optimal field enhancement by finite difference tipe domain electromagnetic simulation. *J. Chem. Phys.*, 116:10895, 2002.

[129] J. A. Porto, P. Johansson, S. P. Apell, and T. López-Ríos. Resonance shift effects in apertureless scanning near-field optical microscopy. *Phys. Rev. B*, 67:085409, 2003.

[130] James Clerk Maxwell. A dynamical theory of the electromagnetic field. *Phil.l Trans. of the R. Soc. of London*, 155:459, 1865.

[131] James C. Maxwell. *A Dynamical Theory of the Electromagnetic Field*. Wipf & Stock, 1996.

[132] F. Demming, J. Jersch, K. Dickmann, and P. I. Geshev. Calculation of the field enhancement on laser-illuminated scanning probe tips by the boundary element method. *Appl. Phys. B*, 66:593, 1998.

[133] Heinz Raether. *Surface plasmons on smooth and rough surfaces and on gratings*. Springer-Verlag, 1988.

[134] C. Ropers, C. C. Neacsu, T. Elsaesser, M. Albrecht, M. B. Raschke, and C. Lienau. Grating-coupling of surface plasmons onto metallic tips: A nanoconfined light source. *Nanolett*, vol. 7:p. 2784–2788, 2007. featured in: Nature Photonics, vol. 446, p. 500, 2007.

[135] Andrey K. Sarychev and Vladimir M. Shalaev. Electromagnetic field fluctuations and optical nonlinearities in metal-dielectric composites. *Phys. Rep.*, 335:275, 2000.

[136] T. W. Ebbesen, H. J. Lezec, H. F. Ghaemi, T. Thio, and P. A. Wolff. Extraordinary optical transmission through sub-wavelength hole arrays. *Nature*, 391:667, 1998.

[137] R. Müller, V. Malyarchuk, and C. Lienau. A three-dimensional theory on light induced near-field dynamics in a metal film with a periodic array of nanoholes. *Phys. Rev. B*, 68:205415, 2003.

[138] O. Sqalli, I. Utke, P. Hoffmann, and F. Marquis-Weible. Gold elliptical nanoantennas as probes for near field optical microscopy. *J. Appl. Phys.*, 92:1078, 2002.

[139] U. Kreibig and M. Vollmer. *Optical Properties of Metal Clusters*. Number 25 in Material sciences. Springer, Belrin, 1995.

[140] P. F. Liao, J. G. Bergman, D. S. Chemla, A. Wokaun, J. Melngailis, A. M. Hawryluk, and N. P. Economou. Surface-enhanced Raman scattering from microlithographic silver particle surfaces. *Chem.Phys. Lett.*, 82:355, 1981.

[141] A. Wokaun, J. P. Gordon, , and P. F. Liao. Radiation damping in surface-enhanced Raman scattering. *Phys. Rev. Lett*, 48:957, 1982.

[142] E.E. Hall. The penetration of totally reflected light into the rarer medium. *Phys. Rev.*, 15:73, 1902.

[143] H. Arzelies. Proprietes de l'onde e vanescente obtenue par reflexion totale. *Rev. Opt.*, 27:205, 1948.

[144] Paul Drude. *The Theory of Optics*. Dover Phoenix Editions. Dover Publications, New York, 2005.

[145] F. de Fornel, editor. *Evanescent waves.* Springer, Berlin, 2001.

[146] S. Zhu, A. W. Yu, D. Hawley, and R. Roy. Frustrated total internal reflection: A demonstration and review. *Am. J. Phys.*, 54:601, 1986.

[147] P. Leurgans and A. F. Turner. Frustrated total internal reflection interference filters. *J. Opt. Soc. Am.*, 37:983, 1947.

[148] L. Salomon, F. de Fornel, and J.P. Goudonnet. Sample-tip coupling coefficients of the photon-scanning tunneling microscope. *J. Opt. Soc. Am. A*, 8:2009, 1991.

[149] Jana Puls. Study of evanescent waves with a scattering tip. Master's thesis, Technische Fachhoch Schule Wildau, 2006.

[150] Leo Esaki. New phenomenon in narrow germanium p-n junctions. *Phys. Rev.*, 109: 603, 1958.

[151] J. C. Fisher and I. Giaever. Tunneling through thin insulating layers. *J. Appl. Phys.*, 32:172, 1961.

[152] B. D. Josephson. Possible new effects in superconductive tunnelling. *Phys. Rev.*, 1: 251, 1962.

[153] David Bohm. *Quantum Theory.* Prentice-Hall, 1951. p. 240.

[154] R.M. Eisberg and R. Resnick. *Quantum Physics.* Wiley, New York, 1974.

[155] E. Kretschmann. *Untersuchungen zur anregung und Streuung von Oberflaechenplasmaschwingungen an Silberschichten.* PhD thesis, University Hamburg, 1972.

[156] S. E. Sburlan, L. A. Blanco, and M. Nieto-Vesperinas. Plasmon excitation in sets of nanoscale cylinders and spheres. *Phys. Rev. B*, 73:035403, 2006.

[157] V.M.Shalaev. *Springer Tacts in Modern Physics.* Springer, Berlin, 2000.

[158] Joel Gersten and Abraham Nitzan. Electromagnetic theory of enhanced Raman scattering by molecules adsorbed on rough surfaces. *J. Chem. Phys.*, 73:3023, 1980.

[159] G.C. Schatz and R.P.V. Duyne. *Handbook of Vibrational Spectroscopy*, chapter Electromagnetic Mechanism of Surface-enhanced Spectroscopy, page 759. John Wiley and sons, Chichester, 2002.

[160] C. K. Chen, T. F. Heinz, D. Ricard, and Y. R. Shen. Surface-enhanced second-harmonic generation and Raman scattering. *Phys. Rev. B*, 27:1965, 1983.

[161] P. F. Liao and A. Wokaun. Lightning rod effect in surface enhanced Raman scattering. *J. Chem. Phys.*, 76:751, 1982.

[162] Yves C. Martin, Hendrik F. Hamann, and H. Kumar Wickramasinghe. Strength of the electric field in apertureless near-field optical microscopy. *J. Appl. Phys.*, 89:5774, 2001.

[163] Nils Calander and Magnus Willander. Theory of surface-plasmon resonance optical-field enhancement at prolate spheroids. *J. Appl. Phys.*, 92:4878, 2002.

[164] Peter Johansson. Light emission from a scanning tunneling microscope: Fully retarded calculation. *Phys. Rev. B*, 58:10823, 1998.

[165] T. Kalkbrenner, M. Ramstein, J. Mlynek, and V. Sandoghdar. A single gold particle as a probe for apertureless scanning near-field optical microscopy. *J. Microsc.*, 202: 72, 2001.

[166] J.M. Chalmers and P.R. Griffiths, editors. *Handbook of Vibrational Spectroscopy.* John Wiley and sons, Chichester, 2002.

[167] H. Kuzmany. *Solid-State Spectroscopy.* Springer, 1998.

[168] Edgar Bright Wilson, J. C. Decius, and Paul C. Cross. *Molecular Vibrations: The Theory of Infrared and Raman Vibrational Spectra.* Dover, 1980.

[169] P. J. Hendra and P. M. Stratton. Laser-Raman spectroscopy. *Chem. Rev.*, 69:325, 1968.

[170] P. J. Hendra and C. J. Vear. Laser Raman spectroscopy: A review. *The Analyst*, 95: 321, 1970.

[171] Peter P. Yu and Manuel Cardona. *Fundamentals of Semiconductors.* Springer, 3^{rd} edition, 2005.

[172] Ronald Tabaksblat, Robert J. Meier, and B. J. Kip. Confocal Raman microspectroscopy: Theory and application to thin polymer samples. *Appl. Spectr.*, 46:60, 1992.

[173] J.W. Strutt (Lord Rayleigh). On the theory of optical images, with special reference to the microscope. *Phil. Mag.*, 42:167, 1896.

[174] D. Courjon. *Near-Field Microscopy and Near-Field Optics.* Imperial Coll. Press, London, 2003.

[175] Lukas Novotny and Stephan J. Stranick. Near-field optical microscopy and spectroscopy with pointed probes. *Annu. Rev. Phys. Chem.*, 57:303, 2006.

[176] Gabor Keresztury. *Handbook of Vibrational Spectroscopy*, volume Vol. I, chapter Raman Spectroscopy: Theory, page 71. John Wiley and sons, Chichester, 2002.

[177] Adolf Smekal. Zur quantentheorie der dispersion. *Naturwissenschaften*, 11:873, 1923.

[178] C. V. Raman and K. S. Krishnan. A new type of secondary radiation. *Nature*, 121: 501, 1928.

[179] G. S. Landsberg and L. I. Mandelstam. Eine neue Erscheinung bei der Lichtzerstreuung in Krystallen. *Die Naturwissenschaften*, 16:557, 1928.

[180] G. Planczek. *Handbuch der Radiologie*, volume VI.2, chapter Rayleigh-Sreuung und Raman Effect, pages 205–374. Akademische Verlag, Leipzig, 1934.

[181] Ricardo Aroca. *Surface-enhanced vibrational spectroscopy.* John Wiley & sons, Ltd, 2006.

[182] A. L. Schawlow and C. H. Townes. Infrared and optical masers. *Phys. Rev.*, 112: 1940, 1958.

[183] Gerhard Herzberg. *Infrared and Raman Spectra of Polyatomic Molecules*. Van Nostrand, New York NY, 1945.

[184] Robert W. Boyd. *Nonlinear Optics*. Academic Press, second edition edition, 2003.

[185] E. J. Ayars and H. D. Hallen. Surface enhancement in near-field Raman spectroscopy. *Appl. Phys. Lett.*, 76:3911, 2000.

[186] B B Johnson and W L Peticolas. The resonant Raman effect. *Annu. Rev. Phys. Chem.*, 27:465, 1976.

[187] P.M. Champion and A.C. Albrecht. Resonance Raman scattering: The multimode problem and transform methods. *Annu. Rev. Phys. Chem.*, 33:353, 1982.

[188] W. Siebrand and M. Zgierski. *Excited States*, volume Vol. I, chapter Resonance Raman spectroscopy - a key to vibronic coupling, pages 1 – 36. Academic Press, New York, 1979.

[189] A.B. Myers and R.A. Mathies. *Biological applications of Raman spectroscopy*, volume Vol. I, chapter Resonance Raman intensities: a probe of excited state structure and dynamics, pages 1 – 58. WIley, New York, 1988.

[190] J. Behringer. Molecular spectroscopy. *Mol. Spectrosc.*, 2:100, 1974.

[191] J. Behringer. Molecular spectroscopy. *Mol. Spectrosc.*, 3:163, 1975.

[192] H. J. Bernstein and A. D. Buckingham. Resonance Raman spectra [and discussion]. *Phil. Trans. R. Soc. London A, Math. Phys. Sci.*, 293:287, 1979.

[193] Jeanne L. McHalle. *Handbook of Vibrational Spectroscopy*, volume Vol. I, chapter Resonance Raman Spectroscopy, pages 534 – 556. John Wiley and sons, Chichester, 2002.

[194] M. Fleischmann, P.J. Hendra, and A.J. McQuillan. Raman-spectra of pyridine adsorbed at a silver interface. *Chem. Phys. Lett*, 26:163, 1974.

[195] D.L. Jeanmaire and R.P. Van Duyne. Surface Raman spectroelectrochemistry. part i. heterocyclic, aromatic, and aliphatic amines adsorbed on the anodized silver electrode. *J. Electroanal. Chem.*, 84:1, 1977.

[196] M.G. Albrecht and J.A. Creighton. Anomalously intense Raman spectra of pyridine at a silver electrode. *J. Am. Chem. Soc.*, 99:5215, 1977.

[197] M. Moskovits. Surface roughness and the enhanced intensity of Raman scattering by molecules adsorbed on metals. *J. Chem. Phys.*, 69:4159, 1978.

[198] Joel I. Gersten. The effect of surface roughness on surface enhanced Raman scattering. *J. Chem. Phys.*, 72:5779, 1980.

[199] Joel I. Gersten. Rayleigh, Mie, and Raman scattering by molecules adsorbed on rough surfaces. *J. Chem. Phys.*, 72:5780, 1980.

[200] J.I. Gersten and A. Nitzan. Spectroscopic properties of molecules interacting with small dielectric particles. *J. Chem.Phys.*, 75:1139, 1980.

[201] S. L. McCall, P. M. Platzman, and P. A. Wolff. Surface enhanced Raman scattering. *Phys. Lett. A*, 77:381, 1980.

[202] Milton Kerker, Dau-Sing Wang, and H. Chew. Surface enhanced Raman scattering (sers) by molecules adsorbed at spherical particles: errata. *Appl. Opt.*, 19:4159, 1980.

[203] K. Kneipp, M. Moskovits, and H. Kneipp, editors. *Surface-Enhanced Raman Scattering: Physics and Applications*. Topics in Applied Physics 103. Springer, 2006.

[204] Martin Moskovits. Surface-enhanced spectroscopy. *Rev. Mod. Opt.*, 57:783, 1985.

[205] M. Moskovits. Surface selection rules. *J. Chem. Phys.*, 77:4408, 1982.

[206] Amir Weiss and Gilad Haran. Time-dependent single-molecule Raman scattering as a probe of surface dynamics. *J. Phys. Chem.*, 105:12348, 2001.

[207] A. M. Michaels, M. Nirmal, and L. E. Brus. Surface enhanced Raman spectroscopy of individual rhodamine 6g molecules on large ag nanocrystals. *J. Am. Chem. Soc.*, 121:9932, 1999.

[208] H. Xu, J. Aizpurua, M. Käll, and P. Apell. Electromagnetic contributions to single-molecule sensitivity in surface-enhanced Raman scattering. *Phys. Rev. E*, 62:4318, 2000.

[209] A. Otto, I. Mrozek, H. Grabhorn, and W. Akemann. Surface-enhanced Raman scattering. *J. Phys: Condens. Matter*, 4:1143, 1992.

[210] Katrin Kneipp, Yang Wang, Harald Kneipp, Lev T. Perelman, Irving Itzkan, Ramachandra R. Dasari, and Michael S. Feld. Single molecule detection using surface-enhanced Raman scattering (sers). *Phys. Rev. Lett.*, 78:1667, 1997.

[211] A. Otto. *Light Scattering in Solids IV*, chapter Surface enhanced Raman scattering: "classical" and "chemical" origins, pages 289–418. Topics in Applied Physics 54. Springer, Berlin, 1984.

[212] Peter Johansson, Hongxing Xu, and Mikael Käll. Surface-enhanced Raman scattering and fluorescence near metal nanoparticles. *Phys. Rev. B*, 72:035427, 2005.

[213] J. K. Sass, H. Neff ND M. Moskovits, and S. Holloway. Electric field gradient effects on the spectroscopy of adsorbed molecules. *J. Phys. Chem*, 85:621, 1981.

[214] E. J. Ayars, H. D. Hallen, and C. L. Jahncke. Electric field gradient effects in Raman spectroscopy. *Phys. Rev. Lett.*, 85:4180, 2000.

[215] V.M.Shalalev and A.K. Sarychev. Nonlinear optics of random metal-dielectric films. *Phys. Rev. B*, 57:13265, 1998.

[216] V. A. Markel, V. M. Shalaev, P. Zhang, W. Huynh, L. Tay, T. L. Haslett, , and M. Moskovits. Near-field optical spectroscopy of individual surface-plasmon modes in colloid clusters. *Phys. Rev. B*, 59:10903, 1999.

[217] A. M. Michaels, J. Jiang, and L. Brus. Ag nanocrystal junctions as the site for surface-enhanced Raman scattering of single rhodamine 6g molecules. *J. Phys. Chem. B*, 104: 11965, 2000.

[218] K. Kneipp, H. Kneipp, I. Itzkan, R. R. Dasari, and M. S. Feld. Ultrasensitive chemical analysis by Raman spectroscopy. *Chem. Rev.*, 99:2957, 1999.

[219] W. E. Moerner and Michel Orrit. Illuminating single molecules in condensed matter. *Science*, 293:1670, 1999.

[220] X. Sunney Xie and Robert C. Dunn. Probing single molecule dynamics. *Science*, 265:361, 1994.

[221] J. J. Macklin, J. K. Trautman, T. D. Harris, and L. E. Brus. Imaging and time-resolved spectroscopy of single molecules at an interface. *Science*, 272:5259, 19996.

[222] T. Basche, W.E. Moerner, M. Orrit, and U.P. Wild, editors. *Single-molecule optical detection, imaging and spectroscopy.* VCH, 1996.

[223] T. Ha, Th. Enderle, D. S. Chemla nad P. R. Selvin, and S. Weiss. Quantum jumps of single molecules at room temperature. *Chem. Phys. Lett.*, 271:1, 1997.

[224] Niek F. van Hulst, Joost-Anne Veerman, Maria F. Garcia-Parajo, and L. (Kobus) Kuipers. Analysis of individual (macro)molecules and proteins using near-field optics. *J. Chem. Phys.*, 112:7799, 2000.

[225] Shimon Weiss. Measuring conformational dynamics of biomolecules by single molecule fluorescence spectroscopy. *Nat. Struct. Biol.*, 7:724, 2000.

[226] Shuming Nie and Steven R. Emory. Probing single molecules and single nanoparticles by surface-enhanced Raman scattering. *Science*, 275:1102, 1997.

[227] Hongxing Xu, Erik J. Bjerneld, Mikael Käll, and Lars Börjesson. Spectroscopy of single hemoglobin molecules by surface enhanced Raman scattering. *Phys. Rev. Lett.*, 83:4357, 1999.

[228] Erik J. Bjerneld, Patrik Johansson, and Mikael Käll. Single molecule vibrational fine-structure of tyrosine adsorbed on ag nano-crystals. *Single. Mol.*, 1:239, 2000.

[229] K. Kneipp, A.S. Haka, H. Kneipp, K. Badizadegan, N. Yoshizawa, C. Boone, K.E. Shafer-Peltier, J.T. Motz, R.R. Dasari, and M.S. Feld. Surface-enhanced Raman spectroscopy in single living cells using gold nanoparticles. *Appl. Spectrosc.*, 56:150, 2002.

[230] A. M. Glass, P. F. Liao, J. G. Bergman, and D. H. Olson. Interaction of metal particles with adsorbed dye molecules: absorption and luminescence. *Opt. Lett.*, 5: 368, 1980.

[231] Max E. Lippitsch. Surface enhanced Raman spectra of biliverdine and pyrromethenone adsorbed to silver colloids. *Chem. Phys.Lett.*, 79:224, 1981.

[232] R.R. Chance, A. Prock, and R. Silbey. Molecular fluorescence and energy transfer near interfaces. *Adv. Chem. Phys.*, 37:1, 1978.

[233] G. Ritchie and E. Burstein. Luminescence of dye molecules adsorbed at a Ag surface. *Phys. Rev. B*, 24:4843, 1982.

[234] C.L. Haynes, C.R. Yonzon, X. Z., and R.P. Van Duyne. Surface-enhanced Raman sensors: early history and the development of sensors for quantitative biowarfare agent and glucose detection. *J. Raman Spectrosc.*, 36:471, 2005.

[235] P. K. Aravind, R. W. Rendel, and Horia Metiu. A new geometry for field enhancement in surface-enhanced spectroscopy. *Chem. Phys. Lett.*, 85:396, 1982.

[236] J. Wessel. Surface-enhanced optical microscopy. *J. Opt. Soc. Am. B*, 2:1538, 1985.

[237] U. Ch. Fischer and D. W. Pohl. Observation of single-particle plasmons by near-field optical spectroscopy. *Phys. Rev. Lett.*, 62:458, 1989.

[238] S. Kawata ad V. Shalaev, editor. *Tip enhancement*. Elsevier, 2007.

[239] K. Kneipp, M. Moskovits, and H. Kneipp, editors. *Surface-Enhanced Raman Scattering - Physics and Applications*. Topics in Applied Physics. Springer Berlin / Heidelberg, 2006.

[240] A. Rasmussen and V. Deckert. New dimension in nano-imaging: breaking through the diffraction limit with scanning near-field optical microscopy. *Anal. Bioanal. Chem.*, 381:165, 2005.

[241] Lukas Novotny. The history of near-field optics. *Progr. Opt.*, 50:137, 2007.

[242] D. Richards, R. G. Milner, F. Huang, and F. Festy. Tip-enhanced Raman microscopy: practicalities and limitations. *J. Raman Spectrosc.*, 34:663, 2003.

[243] Raoul M. Stöckle, Yung Doug Suh, Volker Deckert, and Renato Zenobi. Nanoscale chemical analysis by tip-enhanced Raman spectroscopy. *Chem. Phys. Lett.*, 318:131, 2000.

[244] Mark S. Anderson. Locally enhanced Raman spectroscopy with an atomic force microscope. *Appl. Phys. Lett.*, 76:3130, 2000.

[245] Norihiko Hayazawa, Yasushi Inouye, Zouheir Sekkat, and Satoshi Kawata. Metallized tip amplification of near-field Raman scattering. *Opt. Commun.*, 183:333, 2000.

[246] Norihiko Hayazawa, Yasushi Inouye, Zouheir Sekkata, and Satoshi Kawata. Near-field Raman scattering enhanced by a metallized tip. *Chem. Phys. Lett.*, 335:369, 2001.

[247] Norikiko Hayazawa, Yasushi Inouye, Zouheir Sekkat, and Satoshi Kawata. Near-field Raman imaging of organic molecules by an apertureless metallic probe scanning optical microscope. *J. Chem. Phys.*, 117:1296, 2002.

[248] Mark S. Anderson and William T. Pike. A Raman-atomic force microscope for apertureless-near-field spectroscopy and optical trapping. *Rev. Sci. Instrum.*, 73: 1198, 2002.

[249] A. Hartschuh, N. Anderson, and L. Novotny. Near-field Raman spectroscopy using a sharp metal tip. *J. Microscop.*, 210:234, 2002.

[250] H. Watanabe, Y. Ishida, N. Hayazawa, Y. Inouye, and S. Kawata. Tip-enhanced near-field raman analysis of tip-pressurized adenine molecule. *Phys. Rev. B*, 69:155418, 2004.

[251] Norihiko Hayazawa, Taro Ichimura, Mamoru Hashimoto, Yasushi Inouye, and Satoshi Kawata. Amplification of coherent anti-stokes Raman scattering by a metallic nanostructure for a high resolution vibration microscopy. *J. Appl. Phys.*, 95:2676, 2004.

[252] Bruno Pettinger, Bin Ren, Gennaro Picardi, Rolf Schuster, and Gerhard Ertl. Tip-enhanced Raman spectroscopy (ters) of malachite green isothiocyanate at au(111): bleaching behavior under the influence of high electromagnetic fields. *J. Raman. Spectr.*, 36:541, 2005.

[253] Neil Anderson, Achim Hartschuh, Steve Cronin, and Lukas Novotny. Nanoscale vibrational analysis of single-walled carbon nanotubes. *J. Am. Chem. Soc.*, 127:2533, 2005.

[254] K.F. Domke, D. Zhang, and B. Pettinger. Toward Raman fingerprints of single dye molecules at atomically smooth Au(111). *J. Am. Chem. Soc.*, 128:14721, 2006.

[255] P. Verma, K. Yamada, H. Watanabe, Y. Inouye, and S. Kawata. Near-field Raman scattering investigation of tip effects on C60 molecules. *Phys. Rev. B*, 73:145416, 2006.

[256] J. Steidtner and B. Pettinger. High-resolution microscope for tip-enhanced optical processes in ultrahigh vacuum. *Rev. Sci. Instr.*, 78:103104, 2007.

[257] Norihiko Hayazawa, Hiroyuki Watanabe, Yuika Saito, and Satoshi Kawata. Towards atomic site-selective sensitivity in tip-enhanced Raman spectroscopy. *J. Chem.Phys.*, 125:244706, 2006.

[258] Ute Neugebauer, Petra Roesch, Michael Schmitt, Juergen Popp, Carine Julien, Akiko Rasmussen, Christian Budich, and Volker Deckert. On the way to nanometer-sized information of the bacterial surface by tip-enhanced Raman spectroscopy. *ChemPhysChem*, 7:1428, 2006.

[259] W. Zhang, B. S. Yeo, T. Schmid, and R. Zenobi. Single molecule tip-enhanced Raman spectroscopy with silver tips. *J. Phys. Chem. C*, 111:1733, 2007.

[260] J. Jersch, F. Demming, L.J. Hildenhagen, and K. Dickmann. Field enhancement of optical radiation in the nearfield of scanning probe microscope tips. *Appl. Phys. A*, 66:29, 1998.

[261] Stefan Klein, Tobias Witting, Klaus Dickmann, Pavel Geshev, and Michael Hietschold. On the field enhancement at laser-illuminated scanning probe tips. *Single Mol.*, 3:281, 2002.

[262] D. L. Mills. Theory of STM-induced enhancement of dynamic dipole moments on crystal surfaces. *Phys. Rev. B*, 65:125419, 2002.

[263] Shiwei Wu and D. L. Mills. STM-induced enhancement of dynamic dipole moments on crystal surfaces: Theory of the lateral resolution. *Phys. Rev. B*, 65:205420, 2002.

[264] Miodrag Micic, Nicholas Klymyshyn, Yung Doug Suh, and H. Peter Lu. Finite element method simulation of the field distribution for AFM tip-enhanced surface-enhanced Raman scanning microscopy. *J. Phys. Chem.*, 107:1574, 2003.

[265] C. L. Jahncke, M. A. Paesler, and H. D. Hallen. Raman imaging with near-field scanning optical microscopy. *Appl. Phys. Lett.*, 67:2483, 1995.

[266] C. L. Jahncke, H. D. Hallen, and M. A. Paesler. Nano-Raman spectroscopy and imaging with a near-field scanning optical microscope. *J. Raman Spectrosc.*, 27:579, 1996.

[267] S. Webster, D. N. Batchelder, and D. A. Smith. Submicron resolution measurement of stress in silicon by near-field Raman spectroscopy. *Appl. Phys. Lett.*, 72:1478, 1998.

[268] M. De Serio, H. Mohapatra, R. Zenobi, and V. Deckert. Investigation of the liquid-liquid interface with high spatial resolution using near-field Raman spectroscopy. *Chem. Phys. Lett.*, 417:425, 2006.

[269] M. A. Bel, B. Crystall, G. Rumbles, G. Porter, and D. R. Klug. The influence of a solid/liquid interface on the fluorescence kinetics of the triphenylmethane dye malachite green. *Chem. Phys. Lett.*, 221:15, 19941.

[270] W. Freyer, C. C. Neacsu, and M. B. Raschke. Absorption, luminescence, and Raman spectroscopic properties of thin films of benzo-annelated metal-free porphyrazines. *J. Lumin.*, vol. 128:p. 661, 2008.

[271] C. Debus, <. A. Lieb, A. Drechsler, and A. J. Meixner. Probing highly confined optical field in the focal region of a high NA parbolic mirror with subwavelength spatial resolution. *J. Microsc.*, 210:203, 2002.

[272] P. Anger, A. Feltz, T. Berghaus, and A. J. Meixner. Near-field and confocal surface-enhanced resonance Raman spectroscopy at cryogenic temperatures. *J. Microsc.*, 209:162, 2003.

[273] L. Novotny, E. J. Sánchez, and X. S. Xie. Near-field optical imaging using metal tips illuminated by higher-order hermite-gaussian beams. *Ultramicroscopy*, 71:21, 1998.

[274] L. Novotny, M. R. Beversluis, K. S. Youngworth, and T. G. Brown. Longitudinal field modes probed by single molecules. *Phys. Rev. Lett.*, 86(23):5251–5254, Jun 2001. doi: 10.1103/PhysRevLett.86.5251.

[275] N. Behr and M.B. Raschke. Optical antenna properties of scanning probe tips: plasmonic light scattering, tip-sample coupling, and near-field enhancement. *J. Phys. Chem. C*, 112:3766, 2008.

[276] B. Pettinger, B. Ren, G. Picardi, R. Schuster, and G. Ertl. Nanoscale probing of adsorbed species by tip-enhanced Raman spectroscopy. *Phys. Rev. Lett.*, 92:096101, 2004.

[277] Horst B. Lueck, Douglas C. Daniel, and Jeanne L. McHale. Resonance Raman study of solvent effects on a series of triarylmethane dyes. *J. Raman Spectr.*, 24:363, 1993.

[278] Michael R. Beversluis, Alexandre Bouhelier, and Lukas Novotny. Continuum generation from single gold nanostructures through near-field mediated intraband transitions. *Phys. Rev. B*, 68:115433, 2003.

[279] M. J. Frisch and *et al.* Gaussian 03, Revision C.02, 2004. Gaussian, Inc., Wallingford, CT, 2004.

[280] J.A. Creighton. *Spectroscopy of Surfaces*, volume Vol 16 of *Advances in Spectroscopy*, chapter Selection Rules for Surface-enhanced Raman Spectroscopy, page 37. John Wiley & Sons, New York, 1988.

[281] R. C. Maher, L. F. Cohen, and P. Etchegoin. Single molecule photo-bleaching observed by surface enhanced resonant Raman scattering (SERRS). *Chem. Phys. Lett.*, 352:378, 2002.

[282] P.J. Moyer, J. Smith, L.M. Eng, and A. Meixner. Surface-enhanced Raman scattering spectroscopy of single carbon domains on individual Ag nanoparticles on a 25 ms time scale. *J. Am. Chem. Soc.*, 122:5409, 2000.

[283] Andrzej Kudelski and Bruno Pettinger. SERS on carbon chain segments: monitoring locally surface chemistry. *Chem. Phys. Lett*, 321:356, 2000.

[284] Genaaro Picardi. *Raman spectroscopy and light emission at metal surfaces enhanced by the optical near-field of a scanning tunneling tip.* PhD thesis, Freie Universität Berlin, 2003.

[285] K. G. Lee, H. W. Kihm, J. E. Kihm, W. J. Choi, H. Kim, C. Ropers, D. J. Park, Y. C. Yoon, S. B. Choi, D. H. Woo, J. Kim, B. Lee, Q. H. Park, C. Lienau, and D. S. Kim. Vector field microscopic imaging of light. *Nat. Photon.*, 1:53, 2006.

[286] H. Gersen, L. Novotny, L. Kuipers, and N. F. van Hulst. On the concept of imaging nanoscale vector fields. *Nat. Photon.*, 1:242, 2007.

[287] N. Lee, R. D. Hartschuh, D. Mehtani, A. Kisliuk, J. F. Maguire, M. Green, M. D. Foster, and A. P. Sokolov. High contrast scanning nano-Raman spectroscopy of silicon. *J. Raman Spectrosc.*, 38:789, 2007.

[288] Vladimir Poborchii, Tetsuya Tada, and Toshihiko Kanayama. Subwavelength-resolution raman microscopy of Si structures using metal-particle-topped AFM probes. *Jap. J. Appl. Phys.*, 44:202, 2005.

[289] Razvigor Ossikovski, Quang Nguyen, and Gennaro Picardi. Simple model for the polarization effects in tip-enhanced Raman spectroscopy. *Phys. Rev. B*, 75:045412, 2007. doi: 10.1103/PhysRevB.75.045412.

[290] Amanda J. Haes, Christy L. Haynes, Adam D. McFarland, George C. Schatz, Richard P. Van Duyne, and Shengli Zou. Plasmonic materials for surface-enhanced sensing and spectroscopy. *MRS Bulletin*, 30:368, 2005.

[291] A. D. McFarland, M. A. Young, J. A. Dieringer, and R. P. Van Duyne. Wavelength-scanned surface-enhanced Raman excitation spectroscopy. *J. Phys. Chem. B*, 109: 11279, 2005.

[292] R.G. Fowles. *Introduction to modern optics*. Holt, Rinehart & Winston, 2^{nd} edition, 1975.

[293] Frederic Festy, Anna Demming, and David Richards. Resonant excitation of tip plasmons for tip−enhanced raman snom. *Ultramicroscopy*, 100:437, 2004.

[294] S. C. Schneider, S. Grafstroem, and L. M. Eng. Scattering near-field optical microscopy of optically anisotropic systems. *Phys. Rev. B*, 71:115418, 2005.

[295] A. V. Goncharenko, M. M. Dvoynenko, Hung-Chih Chang, and Juen-Kai Wang. Electric field enhancement by a nanometer-scaled conical metal tip in the context of scattering-type near-field optical microscopy. *Appl. Phys. Lett.*, 88:104101, 2006.

[296] H. Metiu. Surface enhanced spectroscopy. *Progr. Surf. Sci.*, 17:153, 1984.

[297] A. Bouhelier, J. Renger, M. R. Beversluis, and L. Novotny. Plasmon-coupled tip-enhanced near-field optical microscopy. *J. Microsc.*, 210:220, 2003.

[298] S. Schneider, G. Brehm, and P. Freunscht. Comparison of surface-enhanced Raman and hyper-Raman spectra of the triphenylmethane dyes crystal violet and malachite green. *Phys. Stat. Sol. B*, 189:37, 1995.

[299] Gayle R. Erdheim, Ronald L Birke, and John R. Lombardi. Surface enhanced Raman spectrum of pyrazine. observation of forbidden lines at the electrode surface. *Chem. Phys. Lett.*, 69:495, 1980.

[300] Ralf Dornhaus, Marshall B. Long, Robert E. Benner, and Richard K. Chang. Time development of SERS from pyridine, pyrimidine, pyrazine, and cyanide adsorbed on ag electrodes during an oxidation-reduction cycle. *Surf. Sci.*, 93:240, 1980.

[301] M. Moskovits and Daniel P. Dilellla. Enhanced Raman spectra of ethylene and propylene adsorbed on silver. *Chem. Phys. Lett.*, 73:500, 1980.

[302] A. M. Polubotko. SERS phenomenon as a manifestation of quadrupole interaction of light with molecules. *Phys. Lett.*, 146:81, 1990.

[303] Daniel C. Harris and Michael D. Bertolucci. *Symmetry and Spectroscopy: An Introduction to Vibrational and Electronic Spectroscopy*. Dover Publications Inc., New York, 1989.

[304] Zhenjia Wang and Lewis J. Rothberg. Origins of blinking in single-molecule Raman spectroscopy. *J. Phys. Chem.*, 109:3387, 2005.

[305] Jay K. Trautman X. Sunney Xie. Optical studies of single molecules at room temperature. *Annu. Rev. Phys. Chem.*, 49:441, 1998.

[306] J.A. Dieringer, R.B. Lettan, K.A. Scheidt, and R.P Van Duyne. A frequency domain existence proof of single-molecule surface-enhanced Raman spectroscopy. *J. Am. Chem. Soc.*, 129:16249, 2007.

[307] M. Futamata, Y. Maruyama, and M. Ishikawa. Critical importance of the junction in touching Ag particles for single molecule sensitivity in SERS. *J. Molec. Struct.*, 735:75, 2005.

[308] E. C. Le Ru, P. G. Etchegoin, and M. Meyer. Enhancement factor distribution around a single sers hot-spot and its relation to single molecule detection. arXiv:Physics 0608139, August 2006. URL `http://arxiv.org/abs/physics/0608139`.

[309] Bretislav Friedrich and Dudley Herschbach. Alignment and trapping of molecules in intense laser fields. *Phys. Rev. Lett.*, 74:4623, 1995.

[310] K. F. Domke and B. Pettinger. Comment on ′Scanning-probe Raman spectroscopy with single-molecule sensitivity′. *Phys. Rev. B*, 75:236401, 2007.

[311] C. C. Neacsu, J. Dreyer, N. Behr, and M. B. Raschke. Reply to Comment on 'Scanning-probe Raman spectroscopy with single-molecule sensitivity'. *Phys. Rev. B*, vol. 75:p. 263–402, 2007.

[312] B. C. Stipe, M. A. Rezaei, and W. Ho. Single-molecule vibrational spectroscopy and microscopy. *Science*, 280:1732, 1998.

[313] X. H. Qiu, G. V. Nazin, and W. Ho. Vibrationally resolved fluorescence excited with submolecular precision. *Science*, 299:542, 2003.

[314] P. A. Franken, A. E. Hill, C. W. Peters, and G. Weinreich. Generation of optical harmonics. *Phys. Rev. Lett.*, 7:118, 1961.

[315] T. H. Maiman. Stimulated optical radiation in ruby. *Nature*, 187:493, 1960.

[316] J. A. Armstrong, N. Bloembergen, J. Ducuing, and P. S. Pershan. Interactions between light waves in a nonlinear dielectric. *Phys. Rev.*, 127:1918, 1962.

[317] Y.R. Shen. *The principles of nonlinear optics.* Wiley, New york, 1984.

[318] P.N. Butcher and D. Cotter. *The elements of nonlinear optics.* Cambridge University Press, 1990.

[319] T. F. Heinz, M. M. T. Loy, and W. A. Thompson. Study of Si(111) surfaces by optical second-harmonic generation: Reconstruction and surface phase transformation. *Phys. Rev. Lett.*, 54:63, 1985.

[320] A. V. Petukhov, Vera L. Brudny, W. Luis Mochán, Jesús A. Maytorena, Bernardo S. Mendoza, and Th. Rasing. Energy conservation and the manley-rowe relations in surface nonlinear-optical spectroscopy. *Phys. Rev. Lett*, 81:566, 1998.

[321] J. I. Dadap, J. Shan, K. B. Eisenthal, and T. F. Heinz. Second-harmonic Rayleigh scattering from a sphere of centrosymmetric material. *Phys. Rev. Lett.*, 83:4045, 1999.

[322] N. Yang, W. E. Angerer, and A. G. Yodh. Angle-resolved second-harmonic light scattering from colloidal particles. *Phys. Rev. Lett.*, 87:103902, 2001.

[323] Sylvie Roke, Mischa Bonn, and Andrei V. Petukhov. Nonlinear optical scattering: The concept of effective susceptibility. *Phys. Rev. B*, 70:115106, 2004.

[324] Jerry I. Dadap, Jie Shan, and Tony F. Heinz. Theory of optical second-harmonic generation from a sphere of centrosymmetric material: small-particle limit. *J. OPt. Soc. Am. B*, 21:1328, 2004.

[325] Vera L. Brudny, Bernardo S. Mendoza, and W. Luis Mochán. Second-harmonic generation from spherical particles. *Phys. Rev. B*, 62:11152, 2000.

[326] J. Nappa, I. Russier-Antoine, E. Benichou, Ch. Jonin, and P. F. Brevet. Second harmonic generation from small gold metallic particles: From the dipolar to the quadrupolar response. *J. Chem. Phys.*, 125:184712, 2006.

[327] J. Shan, J. I. Dadap, I. Stiopkin, G. A. Reider, and T. F. Heinz. Experimental study of optical second-harmonic scattering from spherical nanoparticles. *Phys. Rev. A*, 73: 023819, 2006.

[328] T. F. Heinz. *Nonlinear surface electromagnetic phenomena*, chapter Second-order nonlinear optical effects at surfaces and interfaces, pages 353–416. Elsevier, Amsterdam, 1991.

[329] J. E. Sipe, V. Mizrahi, and G. I. Stegeman. Fundamental difficulty in the use of second-harmonic generation as a strictly surface probe. *Phys. Rev. B*, 35:9091, 1987.

[330] B. Koopmans, F. van der Woude, and G. A. Sawatzky. Surface symmetry resolution of nonlinear optical techniques. *Phys. Rev. B*, 46:12780, 1992.

[331] G. A. Reider and T. F. Heinz. Second-order nonlinear optical effects at surfaces and interfaces: Recent advances. In P. Halevi, editor, *Photonic Probes of Interfaces*, page 413, Amsterdam, 1995. Elsevier.

[332] Sami Kujala, Brian K. Canfield, Martti Kauranen, Yuri Svirko, and Jari Turunen. Multipole interference in the second-harmonic optical radiation from gold nanoparticles. *Phys. Rev. Lett.*, 98:167403, 2007.

[333] S. Roke, W. G. Roeterdink, J. E. G. J. Wijnhoven, A. V. Petukhov, A. W. Kleyn, and M. Bonn. Vibrational Sum Frequency Generation from submicron suspensions. *Phys. Rev. Lett.*, 91:258302, 2004.

[334] S.A. Achmanov, A.S. Chirkin, K.N Drabovic, A.I. Kovrigin, R.V. Khokholov, and A.P. Sukhoruk. Nonstationary nonlinear optical effects and ultrashort light pulse formation. *IEEE J. Qunat. Electron.*, 4:598, 1968.

[335] M. Labardi, M. Allegrini, M. Zavelani-Rossi, D. Polli, G. Cerullo, S. De Silvestri, , and O. Svelto. Highly efficient second-harmonic nanosource for near-field optics and microscopy. *Opt. Lett.*, 29:62, 2004.

[336] Satoshi Takahashi and Anatoly V. Zayats. Near-field second-harmonic generation at a metal tip apex. *Appl. Phys. Lett.*, 80:3479, 2002.

[337] M. I. Stockman, D. J. Bergman, C. Anceau, S. Brasselet, and J. Zyss. Enhanced second-harmonic generation by metal surfaces with nanoscale roughness: Nanoscale dephasing, depolarization, and correlations. *Phys. Rev. Lett.*, 92:057402, 2004.

[338] Sergey I. Bozhevolnyi, Jonas Beermann, and Victor Coello. Direct observation of localized second-harmonic enhancement in random metal nanostructures. *Phys. Rev. Lett.*, 90:197403, 2003.

[339] A. V. Zayats and V. Sandoghdar. Apertureless scanning near-field second-harmonic microscopy. *Opt. Comm.*, 178:245, 2000.

[340] H. Wang, E. C. Y. Yan, E. Borguet, and K. B. Eisenthal. Second harmonic generation from the surface of centrosymmetric particles in bulk solution. *Chem. Phys. Lett.*, 259:15, 1996.

[341] John F. McGilp. Optical characterisation of semiconductor surfaces and interfaces. *Prog. Surf. Sci.*, 49:1, 1995.

[342] M. Floersheimer, M. Boesch, C. Brillert, M. Wierschem, and H. Fuchs. Second-harmonic microscopy - a quantitative probe for molecular surface order. *Adv. Mater.*, 9:1061, 1997.

[343] M. Floersheimer, H. Salmen, M. Boesch, C. Brillert, M. Wierschem, and H. Fuchs. Molecular surface orientation field of a Langmuir monolayer determined by second-harmonic microscopy. *Adv. Mater.*, 9:1056, 1997.

[344] M. Floersheimer, R. Paschotta, U. Kubitscheck, C. Brillert, D. Hofmann, L. Heuer, G. Schreiber, C. Verbeek, W. Sohler, and H. Fuchs. Second-harmonic imaging of ferroelectric domains in $LiNbO_3$ with micron resolution in lateral and axial directions. *Appl. Phys. B*, 67:593, 1998.

[345] S. Yamada and I.Y.S. Lee. Recent progress in analytical SHG spectroscopy. *Analyt. Sci.*, 6:1045, 1998.

[346] Igor I. Smolyaninov, Anatoly V. Zayats, and Christopher C. Davis. Near-field second harmonic generation from a rough metal surface. *Phys. Rev. B*, 56:9290, 1997.

[347] S.I. Bozhevolnyi, K. Pedersen, T. Skettrup, X. Zhang, and M. Belmonte. Far- and near-field second-harmonic imaging of ferroelectric domain walls. *Opt. Commun.*, 152:221, 1998.

[348] D. Jakubczyk, Y. Shen, M. Lal, C. Friend, K. S. Kim, J. Swiatkiewic, and P. N. Prasad. Near-fieldprobing of nanoscale nonlinear optical processes. *Opt. Lett.*, 24: 1151, 1999.

[349] Richard D. Schaller, Justin C. Johnson, Kevin R. Wilson, Lynn F. Lee, Louis H. Haber, and Richard J. Saykally. Nonlinear chemical imaging nanomicroscopy: From second and third harmonic generation to multiplex (broad-bandwidth) sum frequency generation near-field scanning optical microscopy. *J. Phys. Chem.*, 106:5143, 2002.

[350] Yoshimasa Kawata, Chris Xu, and Winfried Denk. Feasibility of molecular-resolution fluorescence near-field microscopy using multi-photon absorption and field enhancement near a sharp tip. *J. Appl. Phys.*, 85:1294, 1999.

[351] Mathias Rang. Kontrastmechanismen der streulicht-nahfeldmikroskopie im sichtbaren und infraroten spektralbereich. Master's thesis, Humboldt-Universität zu Berlin, 2006.

[352] Zhi-Yuan Li, Ben-Yuan Gu, and Guo-Zhen Yang. Strong localization of near-field second-harmonic generation for nonlinear mesoscopic surface structures. *Phys. Rev. B*, 59:12622, 1999.

[353] J.F. Scott. *Ferroelectric Memories*. Springer, Berlin, 2000.

[354] Hiroshi Ishiwara, Masanori Okuyama, and Yoshihiro Arimoto, editors. *Ferroelectric Random Access Memories: Fundamentals and Applications (Topics in Applied Physics)*. Springer, Berlin, 2004.

[355] Robert C. Miller. Optical harmonic generation in single crystal $BaTiO_3$. *Phys. Rev.*, 134:A1313, 1964.

[356] M.M. Fejer, G.A. Magel, D.H. Jundt, and R.L. Byer. Quasi-phase-matched second harmonic generation: tuning andtolerances. *IEEE J. Quantum ELectron.*, 28:2631, 1992.

[357] B. Matthias and A. von Hippel. Domain structure and dielectric response of barium titanate single crystals. *Phys. Rev.*, 73:1378, 1948.

[358] B. Zwicker and P. Scherrer. Electro-optical properties of the Rochelle-electric crystals KH_sPO_4 and KD_2PO_4. *Helv. Phys. Acta*, 17:346, 1944.

[359] E. Fatuzzo and W.J. Merz. *Ferroelectricity*. North-Holland, Amsterdam, 1967.

[360] M. E. Lines and A. M. Glass. *Principles and Applications of Ferroelectrics and Related Materials*. Oxford University Press, USA, 2001.

[361] L.M. Eng, M. Bammerlin, C. Loppacher, M. Guggisberg, R. Bennewitz, R. Luthi, E. Meyer, T. Huser, H. Heinzelmann, and H.J. Guntherodt. Ferroelectric domain characterisation and manipulation: a challenge for scanning probe microscopy. *Ferroel.*, 222:411, 1999.

[362] A. Gruverman. *Encyclopedia of nanoscience and nanotechnology*, volume 3. American Scientific Publishers, 2004.

[363] H. Birk, J. Glatz-Reichenbach, Li Jie, E. Schreck, and K. Dransfeld. The local piezoelectric activity of thin polymer films observed by scanning tunneling microscopy. *J. Vac. Sci. Technol. B*, 9:1162, 1991.

[364] P. Guthner and K. Dransfeld. Local poling of ferroelectric polymers by scanning force microscopy. *Appl. Phys. Lett.*, 61:1137, 1992.

[365] A. Gruverman, O. Auciello, and H. Tokumoto. Scanning force microscopy for the study of domain structure in ferroelectric thin films. *J. Vac. Sci. Technol. B*, 14:602, 1996.

[366] M. Alexe and A. Gruverman, editors. *Nanoscale Characterisation of Ferroelectric Materials*. NanoScience and Technology. Springer, 2004.

[367] M. Alexe, A. Gruverman, C. Harnagea, N. D. Zakharov, A. Pignolet, D. Hesse, and J. F. Scott. Switching properties of self-assembled ferroelectric memory cells. *Appl. Phys. Lett.*, 75:1158, 1999.

[368] A. L. Kholkin, S. V. Kalinin, A. Roelofs, and A. Gruverman. *Scanning Probe Microscopy: Electrical and Electromechanical Phenomena at the Nanoscale*, chapter Review of ferroelectric domain imaging by Piezoresponse Force Microscopy, page 173. Springer, 2006.

[369] G. Dolino. Direct observation of ferroelectric domains in TGS with second-harmonic light. *Appl. Phys. Lett.*, 22:123, 1973.

[370] Y. Uesu, S. Kurimura, and Y. Yamamoto. Optical 2^{nd} harmonic images of 90 degrees domain-structure in $BaTiO_3$, and periodically inverted antiparallel domains in $LiTaO_3$. *Appl. Phys. Lett.*, 66:2165, 1995.

[371] M. Floersheimer, M. Boesch, C. Brillert, M. Wierschem, and H. Fuchs. Second-harmonic imaging of surface order and symmetry. *Thins Solid Films*, 327:241, 1998.

[372] Ai-Fang Xie, Ben-Yuan Gu, Guo-Zhen Yang, and Ze-Bo Zhang. Image of near-field second-harmonic generation for inversely poled mesoscopic $LiNbO_3$ domains. *Phys. Rev. B*, 63:054104, 2001.

[373] B.A. Strukov and A.P. Levanyuk. *Ferroelectric Phenomena in Crystals. Physical Foundations*. Springer Berlin, 1998.

[374] H. L. Yakel, W. C. Koehler, E. F. Bertaut, and E. F. Forrat. On the crystal structure of the manganese(iii) trioxides of the heavy lanthanides and yttrium. *Acta Crystallogr.*, 16:957, 1963.

[375] C. Rao and J. Gopalakrishnan. *New directions in solid state chemistry*. Cambridge University Press, 1997.

[376] A. Yavari, M. Ortiz, and K. Bhattacharya. Anharmonic lattice statics analysis of 180 and 90 degree ferroelectric domain walls in $BaTiO_3$ and $PbTiO_3$. Preprint, 2007.

[377] M. DiDomenico and S. H. Wemple. Paraelectric-ferroelectric phase boundaries in semiconducting perovskite-type crystals. *Phys. Rev.*, 155:539, 1967.

[378] M. Dawber, K. M. Rabe, and J. F. Scott. Physics of thin-film ferroelectric oxides. *Rev. Mod. Phys.*, 77:1083, 2005.

[379] J. Grindlay. *An introduction to the phenomenological theory of ferroelectricity.* Pergamon Press, Oxford, First edition, 1970.

[380] V.A. Zhirnov. A contribution to the theory of domain walls in ferroelectrics. *Sov. Phys. JETP-USSR*, 8:822, 1959.

[381] L. I. Dontzova, N. A. Tikhomirova, and L. A. Shuvalov. Investigation of domain structure and switching processes in ferroelectrics by the liquid crystal method. *Ferroelectrics*, 97:87, 1989.

[382] J. Padilla, W. Zhong, and David Vanderbilt. First-principles investigation of 180° domain walls in $BaTiO_3$. *Phys. Rev. B.*, 53:R5969, 1996.

[383] M. Tanaka and G. Honjo. Electron optical studies of barium titanate single crystal films. *J. Phys. Soc. Jpn.*, 19:954, 1964.

[384] S.I. Yakunin, W. Shakmano, G.V. Spivak, and N.V. Vasileva. Microstructure of domains and domain boundaries of $BaTiO_3$ single crystalline films. *Fiz. Tverd. Tela*, 14:373, 1972.

[385] V.V. Shakmano, G.V. Spivak, N.V. Vasileva, S.I. Yakunin, and V.S. Melamed. Observinf repolarization of single-crystal films BaTiO3 with aid if stroboscope transmission electron-microscope. *Kristallografiya*, 17:351, 1972.

[386] E.V. Sinyakov, S.I. Yakunin, V.M. Duda, and E.F. Dudnik. Direct observation of 180 degrees domains in barium-titanate by means if a polarizing microscope. *Sov. Phys. Sol. Stat.*, 13:2149, 1972.

[387] Bas B. Van Aken, Thomas T.M. Palstra, Alessio Filippetti, and Nicola A. Spaldin. The origin of ferroelectricity in magnetoelectric $YMnO_3$. *Nat. Mat.*, 3:164, 2004.

[388] M. Fiebig. Revival of the magnetoelectric effect. *J. Phys. D: Appl. Phys.*, 38:R123, 2005.

[389] G. H. Jonker and J. H. van Santen. Ferromagnetic compounds of manganese with perovskite structure. *Physica*, 16:337, 1950.

[390] Ken ichi Chahara, Toshiyuki Ohno, Masahiro Kasai, and Yuzoo Kozono. Magnetoresistance in magnetic manganese oxide with intrinsic antiferromagnetic spin structure. *Appl. Phys. Lett.*, 63:1990, 1993.

[391] R. von Helmolt, J. Wecker, B. Holzapfel, L. Schultz, and K. Samwer. Giant negative magnetoresistance in perovskitelike $La_{2/3}Ba_{1/3}Mno_x$ ferromagnetic films. *Phys. Rev. Lett.*, 71:2331, 1993.

[392] S. Quezel-Ambrunaz. Magnetic structure of the perovskite-like compound $tbmno_3$. *Bull. Soc. Fr. Mineral. Cristallogr.*, B91:339, 1968.

[393] J. G. Bednorz and K. A. Mueller. Possible high t_c superconductivity in the ba-la-cu-o system. *Z. Phys. B: Cond. Matt.*, 64:189, 1986.

[394] S. Jin, T.H. Tiefel, M. McCormack, R.A. Fastnacht, R. Ramesh, and L.H. Chen. Thousandfold change in resistivity in magnetoresistive La−Ca−Mn−O films. *Science*, 64:413, 1994.

[395] B. B. van Aken. *Structural response to electronic transitions in hexagonal and orthomanganites*. PhD thesis, Rijksuniversiteit Groningen, 2001.

[396] P. Coeure, F. Guinet, J.C. Peuzin, G. Buisson, and E.F. Bertaut. Ferroelectric properties of hexagonal orthomanganites of Yttrium and rare earths. In V. Dvorak, editor, *Proceedings of the International Meeting on ferroelectricity, Prague, 1966*. institute of Physics of the Czechhoslovak Academy of Sciences, Prague, 1966.

[397] E. F. Bertaut, F. Forrat, and P. H. Fang. Are rare earth orthochromites ferroelectric? *C. R. Acad. Sci. (Paris)*, 256:1958, 1963.

[398] Nicola A. Hill. Why are there so few magnetic ferroelectrics? *J. Phys. Chem. B*, 104: 6694, 2000.

[399] Nicola A. Spaldin and Manfred Fiebig. The renaissance of magnetoelectric multiferroics. *Science*, 309:391, 2005.

[400] R. Ramesh and Nicola A. Spaldin. Multiferroics: progress and prospects in thin films. *Nat. Mater.*, 6:21, 2007.

[401] Thomas Lottermoser, Thomas Lonkai, Uwe Amann, Dietmar Hohlwein, Joerg Ihringer, and Manfred Fiebig. Magnetic phase control by an electric field. *Nature*, 430:541, 2004.

[402] Landolt-Boernstein, editor. *Numerical data and functional relationships*, volume Vol. 16a of *New Series*. Springer Verlag, Berlin, 1981.

[403] M. Fiebig, T. Lottermoser, D. Fröhlich, A. V. Goltsev, and R. V. Pisarev. Observation of coupled magnetic and electric domains. *Nature*, 419:818, 2002.

[404] D. Froehlich, St. Leute, V. V. Pavlov, and R. V. Pisarev. Nonlinear optical spectroscopy of the two-order-parameter compound $YMnO_3$. *Phys. Rev. Lett.*, 81:3239, 1998.

[405] N. Fujimura, T. Ishida, T. Yoshimura, and T. Ito. Epitaxially grown $YMnO_3$ film: New candidate for nonvolatile memory devices. *Appl. Phys. Lett.*, 69:1011, 1996.

[406] D. Sa, R. Valenti, and C. Gros. A generalized ginzburg-landau approach to second harmonic generation. *Eur. Phys. J. B*, 14:301, 2000.

[407] R.R. Briss. *Symmetry and Magnetism*. North-Holland, Amsterdam, 1966.

[408] Manfred Fiebig. Research group nonlinear magneto-optics - homepage. http://www.iskp.uni-bonn.de/gruppen/hikari/english/frame-mf.htm.

[409] M. Fiebig, D. Fröhlich, and Th. Lottermoser. Probing of ferroelectric surface and bulk domains in $RMnO_3$ (R=Y, Ho) by second harmonic generation. *Phys. Rev. B*, 66:144102, 2002.

[410] P. G. Gucciardi, G. Bachelier, M. Allegrini, M. Hong J. Ahn, S. Chang, W. Jhe, S.-C. Hong, and S. H. Baek. Artifacts identification in apertureless near-field optical microscopy. *J. Appl. Phys.*, 101:064303, 2007.

[411] R. Stolle, G. Marowsky, E. Schwarzberg, and G. Berkovic. Phase measurements in nonlinear optics. *Appl. Phys. Lett.*, 63:491, 1996.

[412] G. Dolino. Effects of domain shapes on second-harmonic scattering in triglycine sulfate. *Phys. Rev. B*, 6:4025, 1972.

[413] St. Leute, Th. Lottermoser, and D. Froehlich. Nonlinear spatially resolved phase spectroscopy. *Opt. Lett.*, 24:1520, 1999.

[414] S. Kurimura and Y. Uesu. Application of the second harmonic generation microscope to nondestructive observation of periodically poled ferroelectric domains in quasi-phase-matched wavelength converters. *J. Appl. Phys.*, 81:369, 1997.

[415] M. Fiebig, T. Lottermoser, D. Froehlich, and S. Kallenbach. Phase-resolved second-harmonic imaging with nonideal laser sources. *Opt. Lett.*, 29:41, 2004.

[416] Charles Hubert and Jeremy Levy. Nanometer-scale imaging of domains in ferroelectric thin films using apertureless near-field scanning optical microscopy. *Appl. Phys. Lett.*, 73:3229, 1998.

[417] J. Levy, C. Hubert, and A. Trivelli. Ferroelectric polarization imaging using apertureless near-field scanning optical microscopy. *J. Chem. Phys.*, 112:7848, 2000.

[418] W. Dickson, S. Takahashi, C. Morros, I. Boronat, R. M. Bowman, J. M. Gregg, and A. V. Zayats. Near-field second-harmonic imaging of thin ferroelectric films. *Phys. Rev. B*, 72:094110, 2005.

[419] M. Xiao, S. Bozhevolnyi, and O. Keller. Numerical study of configurational resonances in near-field optical microscopy with a mesoscopic metallic probe. *Appl. Phys. A*, 62: 115, 1996.

[420] C.T> Tai. *Dyadic Green's functions in electromagnetic theory.* Intext Educational Publishers, 1971.

[421] M. Xiao. On near-field scanning optical microscopy homogeneous and evanescent radiation. *J. Mod. Opt.*, 44:327, 1997.

[422] T. Setälä, M. Kaivola, and A. T. Friberg. Decomposition of the point-dipole field into homogeneous and evanescent parts. *Phys. Rev. E*, 59:1200, 1999.

[423] T. Setälä, M. Kaivola, and A.T. Friberg. Evanescent and propagating electromagnetic fields in scattering from point-dipole structures. *J. Opt. Soc. Am. A*, 18:678, 2001.

[424] M. Aeschlimann. *Encyclopedia of Nanoscience and Nanotechnology.* American Scientific Publishers, 2004.

[425] Martin Aeschlimann, Michael Bauer, Daniela Bayer, Tobias Brixner, F. Javier García de Abajo, Walter Pfeiffer, Martin Rohmer, Christian Spindler, and Felix Steeb. Adaptive subwavelength control of nano-optical fields. *Nature*, 446:301, 2007.

[426] A. Apostol and A. Dogariu. Light spectra in the near field of random media. *Opt. Lett.*, 29:920, 2004.

[427] Adela Apostol and Aristide Dogariu. First- and second-order statistics of optical near fields. *Opt. Lett.*, 29:235, 2004.

[428] A. Apostol and A. Dogariu. Spatial correlations in the near field of random media. *Phys. Rev. Lett.*, 91:093901, 2003.

[429] A. Apostol and A. Dogariu. Coherence properties near interfaces of random media. *Phys. Rev. E*, 67:055601, 2003.

[430] G. Arlt and J. H. Calderwood. Coercive and switching fields in ferroelectric ceramics. *Appl. Phys. Lett.*, 81:2605, 2002.

[431] G. Arlt, U. Bottger, and S. Witte. Emission of ghz shear waves by ferroelastic domain walls in ferroelectrics. *Appl. Phys. Lett.*, 63:602, 1993.

[432] F.R. Aussenegg, A. Leitner, and H. Gold. Optical second-harmonic generation of metal-island films. *Appl. Phys. A*, 60:97, 1995.

[433] P. Baierl, W. Kiefer, P. F. Williams, and D. L. Rousseau. Evidence for excited electronic state interference in resonance Raman scattering. *Chem. Phys. Lett.*, 50: 57, 1977.

[434] Anna Rita Bizzarri and Salvatore Cannistraro. Temporal fluctuations in the serrs spectra of single ironprotoporphyrin ix molecule. *Chem. Phys.*, 290:297, 2003.

[435] N. Bloembergen, R. K. Chang, S. S. Jha, and C. H. Lee. Optical second-harmonic generation in reflection from media with inversion symmetry. *Phys. Rev.*, 174:813, 1968.

[436] N. Bloembergen and P. S. Pershan. Light waves at the boundary of nonlinear media. *Phys. Rev.*, 128:606, 1962.

[437] J.C. Bose. On the determination of the wavelength of electric radiation by a diffraction grating. *Proc. Roy. Soc.*, 60:167, 1897.

[438] G. T. Boyd, Th. Rasing, J. R. R. Leite, and Y. R. Shen. Local-field enhancement on rough surfaces of metals, semimetals, and semiconductors with the use of optical second-harmonic generation. *Phys Rev. B*, 30:519, 1984.

[439] M. Breit, S. Malkmus, , and J. Feldmann. Near-field second harmonic generation by using uncoated silicon tips. *Appl. Phys. Lett.*, 90:093114, 2007.

[440] Carlos Bustamante, Zev Bryant, and Steven B. Smith. Ten years of tension: single-molecule dna mechanics. *Nature*, 424:423, 2003.

[441] Alan Campion and David R. Mullins. Normal Raman scattering from pyridine adsorbed on the low-index faces of silver. *Chem. Phys. Lett.*, 94:576, 1983.

[442] Brian K. Canfield, Hannu Husu, Janne Laukkanen, Benfeng Bai, Markku Kuittinen, Jari Turunen, and Martti Kauranen. Local field asymmetry drives second-harmonic generation in noncentrosymmetric nanodimers. *Nano Lett.*, 7:1251, 2007.

[443] G. Catalan, A. Schilling, J.F. Scott, and J.M. Gregg. Domains in three-dimensional ferroelectric nanostructures: theory and experiment. *J. Phys.: Condens. Mat.*, 19: 132201, 2007.

[444] A. Cavalleri, S. Wall, C. Simpson, E. Statz, D. W. Ward, K. A. Nelson, M. Rini, and R. W. Schoenlein. Tracking the motion of charges in a terahertz light field by femtosecond x-ray diffraction. *Nature*, 442:664, 2006. polaritons in ferroelectrics with terahertz.

[445] R. R. Chance, A. Prock, and R. Silbey. Lifetime of an excited molecule near a metal mirror: Energy transfer in the eu^{3+}/silver system. *J. Chem. Phys.*, 60:2184, 1974.

[446] Weibin Chen and Qiwen Zhan. Numerical study of an apertureless near field scanning optical microscope probe under radial polarization illumination. *Opt. Express*, 15: 4106, 2007.

[447] B. R. Cooper, H. Ehrenreich, and H. R. Philipp. Optical properties of noble metals. ii. *Phys. Rev.*, 138:A494, 1965.

[448] S. J. Cyvin, J. E. Rauch, and J. C. Decius. Theory of hyper-Raman effects (nonlinear inelastic light scattering): Selection rules and depolarization ratios for the second-order polarizability. *J. Chem. Phys.*, 43:4083, 1965.

[449] W. Dickson, S. Takahash, D. McHugh, R. Atkinson, R. Pollard, and A. V. Zayats. Near-field second-harmonic imaging of magnetic domains. *J. Appl. Phys.*, 97:033505, 2005.

[450] W. Dickson, S. Takahashi, R. Pollard, and A. V. Zayats. Near-field second-harmonic imaging of thin ferromagnetic films. *Appl. Phys. Lett.*, 85:6341, 2004.

[451] K.F. Domke, D. Zhang, and B. Pettinger. Enhanced Raman spectroscopy - single molecules or carbon? *J. Phys. Chem. C*, 111:8611, 2007.

[452] Chun-Gang Duan, Renat F. Sabirianov, Wai-Ning Mei, Sitaram S. Jaswal, and Evgeny Y. Tsymbal. Interface effect on ferroelectricity at the nanoscale. *Nanolett.*, 6:483, 2006.

[453] R.P. van Duyne, D.L. Jeanmaire, and D.F. Shriver. Mode-locked laser Raman spectroscopy. new technique for rejection of interfering background luminescence signals. *Anal. Chem.*, 64:213, 1974.

[454] J. G. Endriz. Surface waves and grating-tuned photocathodes. *Appl. Phys. Lett.*, 25: 261, 1974.

[455] M. Fee, S. Chu, and T. W. Hänsch. Scanning electromagnetic transmission line microscope with sub-wavelength resolution. *Opt. Commun.*, 69:219, 1989.

[456] D. Feili, B. Zimmermann, C. Neacsu, P. Bosselmann, K. H. Schartner, F. Folkmann, A. E. Livingston, E. Trabert, and P. H. Mokler. $2s^2\ ^1S_0 - 2s2p\ ^3P_1$ intercombination transition wavelengths in Be-like Ag^{43+}, Sn^{46+}, and Xe^{50+} ions. *Phys. Scripta*, 71 (1):48, 2005.

[457] A. Fert and P. Gruenberg. the discovery of giant magnetoresistance. Nobel prize in physics, 2007. pdf contains the scientific background.

[458] D.D. Fong, G.B. Stephenson, S.K. Streiffer, J.A. Eastman, O. Auciello, P.H. Fuoss, and C. Thompson. Ferroelectricity in ultrathin perovskite films. *Science*, 304:1650, 2004.

[459] D. D. Fong, A. M. Kolpak, J. A. Eastman, S. K. Streiffer, P. H. Fuoss, G. B. Stephenson, Carol Thompson, D. M. Kim, K. J. Choi, C. B. Eom, I. Grinberg, and A. M. Rappe. Stabilization of monodomain polarization in ultrathin pbtio$_3$ films. *Phys. Rev. Lett.*, 96:127601, 2006.

[460] Joel M. Friedman and Robin M. Hochstrasser. The use of fluorescence quenchers in resonance Raman spectroscopy. *Chem. Phys. Lett.*, 33:225, 1975.

[461] Huaxiang Fu and L. Bellaiche. Ferroelectricity in barium titanate quantum dots and wires. *Phys. Rev. Lett.*, 91:257601, 2003.

[462] M. Futamata and A. Bruckbauer. ATR-SNOM-Raman spectroscopy. *Chem. Phys. Lett.*, 341:425, 2001.

[463] M. Futamata and S. Masuda. Atr-snom Raman spectroscopy using surface plasmon polariton. *Anal. Sci.*, 17-supplement:i103, 2001.

[464] F. J. Garcia-Vidal and L. Martín-Moreno. Transmission and focusing of light in one-dimensional periodically nanostructured metals. *Phys. Rev. B*, 66:155412, 2002.

[465] P.I. Geshev, F. Demming, J. Jersch, and K. Dickmann. Calculation of the temperature distribution on laser-illuminated scanning probe tips. *Appl. Phys. B*, 70:91, 2000.

[466] Christian Girard and Alain Dereux. Near-field optics theories. *Rep. Progr. Phys.*, 59: 657, 1996.

[467] A. V. Goltsev, R. V. Pisarev, Th. Lottermoser, and M. Fiebig. Structure and interaction of antiferromagnetic domain walls in hexagonal ymno3. *Phys. Rev. Lett.*, 90: 177204, 2003.

[468] J.W. Goodman. *Introduction to Fourier Optics*. McGraw-Hill, 1968.

[469] V. Gopalan, K. Kitamura, and Y. Furukawa. Domain reversal and wall structure of 180° ferroelectric domains in litao$_3$ crystals. www.

[470] Victor V. Gozhenko, Leonid G. Grechko, and Keith W. Whites. Electrodynamics of spatial clusters of spheres: Substrate effects. *Phys. Rev. B*, 68:125422, 2003.

[471] A. Gruverman and A. Kholkin. Nanoscale ferroelectrics: processing, characterization and future trends. *Rep. Progr. Phys.*, 69:2443, 2006.

[472] P. Guyot-Sionnest, W. Chen, and Y. R. Shen. General considerations on optical second-harmonic generation from surfaces and interfaces. *Phys. Rev. B*, 33:8254, 1986.

[473] J.M. Harris, R.W. Chrisman, F.E. Lytle, and S.R. Tobias. Sub-nanosecond time-resolved rejection of fluorescence from Raman spectra. *Anal chem.*, 48:1937, 1976.

[474] Louis Harris, Joseph Kaminsky, and Roger G. Simard. The absorption spectrum of malachite green leucocyanide and the mechanism of the dark reaction after photolysis. *J. Am. Chem. Soc.*, 47:1151, 1935.

[475] N. Hayazawa, A. Tarun, Y. Inouye, and S. Kawata. near-field enhanced Raman spectroscopy using side illumination optics. *J. Appl. Phys.*, 92:6983, 2002.

[476] Bert Hecht, Hans-Jürgen Eisler, Dieter W. Pohl, and Olivier J.F. Martin. Nanostrukturen optische antennen. *Physik in unserer Zeit*, 306:209, 2005.

[477] T. F. Heinz and D. P. DiVincenzo. Comment on forbidden nature of multipolar contributions to second-harmonic generation in isotropic fluids. *Phys. Rev. A*, 42: 6249, 1990.

[478] Carsten Henkel and Vahid Sandoghdar. Single-molecule spectroscopy near structured dielectrics. *Opt. Commun.*, 158:250, 1998.

[479] David B. Hollis. Review of hyper-rayleigh and secondharmonic scattering in minerals and other inorganic solids. *Amer. Mineral.*, 73:701, 1988.

[480] M. Holt, Kh. Hassani, and M. Sutton. Microstructure of ferroelectric domains in batio$_3$ observed via x-ray microdiffraction. *Phys. Rev. Lett.*, 95:085504, 2005.

[481] D. Hornauer, H. Kapitza, and H. Raether. The dispersion realtion of surface plasmons on rough surfaces. *J. Phys. D: Appl. Phys.*, 7:L100, 1974.

[482] L.M. Huang, Z.Y. Chen, J.D. Wilson, S. Banerjee, R.D. Robinson, I.P. Herman, R. Laibowitz, and S. O'Brien. Barium titanate nanocrystals and nanocrystal thin films: Synthesis, ferroelectricity, and dielectric properties. *J. Appl. Phys.*, 100:034316, 2006.

[483] Charles Hubert, Jeremy Levy, Adrian C. Carter, Wontae Chang, Steven W. Kiechoefer, James S. Horwitz, and Douglas B. Chrisey. Confocal scanning optical microscopy of baxsr1 xtio3 thin films. *Appl. Phys. Lett.*, 71:3353, 1997.

[484] O. Hudak. Landau theory of 180 degrees domain walls in batio3 type ferroelectric particles: microcomposite materials. http://arxiv.org/abs/cond-mat/0504701, 2005.

[485] I.I.Smolyaninov, C.H.Lee, and C.C.Davis. Near-field second harmonic imaging of lead zirconate titanate piezoceramic. *J. Microscop.*, 194:426, 1999.

[486] Atif Imtiaz, Steven M. Anlage, John D. Barry, and John Melngailis. Nanometer-scale material contrast imaging with a near-field microwave microscope. *Appl. Phys. Lett.*, 90:143106, 2007.

[487] Patrick Irvin, Jeremy Levy, Ruyan Guo, and Amar Bhalla. Three-dimensional polarization imaging of (ba,sr)tio3:mgo composites. *Appl. Phys. Lett.*, 86:042903, 2005.

[488] J. Jersch, F. Demming, and K. Dickmann. Nanostructuring with laser radiation in the nearfield of a tip from a scanning force microscope. *Appl. Phys. A*, 64:29, 1996.

[489] J. Jersch, F. Demming, I. Fedotov, and K. Dickmann. Time-resolved current response of a nanosecond laser pulse illuminated stm tip. *Appl. Phys. A*, 68:637, 1999.

[490] Jun Kano, Yuhji Tsujimi, Keith Nelson, and Toshirou Yagi. Initial excitation process of ferroelectric b2 soft mode in kd2po4. *Ferroelectrics*, 308:17, 2004.

[491] Michael Kasha. Collisional perturbation of spin-orbital coupling and the mechanism of fluorescence quenching. a visual demonstration of the perturbation. *J. Chem. Phys.*, 20:71, 1962.

[492] Ole Keller. Towards a microscopic theory of spatial confinement of light. *Ultramicrosc.*, 71:1, 1998.

[493] Anne Myers Kelley, Xavier Michalet, and Shimon Weiss. Single-molecule spectroscopy comes of age. *Science*, 292:1671, 2001.

[494] S. H. Kim, S. H. Lee, T. H. Kim, T. Zyung, Y. H. Jeong, and M. S. Jang. Growth, ferroelectric properties, and phonon modes of $YMnO_3$ single crystal. *Cryst. Res. Technol.*, 35:19, 2000.

[495] T. Klar, M. Perner, S. Grosse, G. von Plessen, W. Spirkl, and J. Feldmann. Surface-plasmon resonances in single metallic nanoparticles. *Phys. Rev. Lett.*, 80:4249, 1998.

[496] Erwin Kretschmann. The determination of the optical constants of metals by excitation of surface plasmons. *Zeitschrift fuer Physik A Hadrons and Nuclei*, 241:313, 1971.

[497] John Lambe and S. L. McCarthy. Light emission from inelastic electron tunneling. *Phys. Rev. Lett.*, 37:923, 1976.

[498] B. Lamprecht, J.R. Krenn, A. Leitner, and F.R. Aussenegg. Particle-plasmon decay-time determination by measuring the optical near-field's autocorrelation: influence of inhomogeneous line broadening. *Appl. Phys. B*, 69:223, 1999.

[499] B. Lamprecht, A. Leitner, and F. R. Aussenegg. Shg studies of plasmon dephasing in nanoparticles. *Appl. Phys. B*, 68:419, 1999.

[500] W. N. Lawless. 180° domain-wall energies in $BaTiO_3$. *Phys. Rev.*, 175:619, 1968.

[501] J. Lenglet, A. Bourdon, J.-C. Bacri, , R. Perzynski, and G. Demouchy. Second-harmonic generation in magnetic colloids by orientation of the nanoparticles. *Phys. Rev. B*, 53:14941, 1996.

[502] Jong Kuk Lim, Kohei Imura, Tetsuhiko Nagahara, Seong Keun Kim, and Hiromi Okamoto. Imaging and dispersion relations of surface plasmon modes in silver nanorods by near-field spectroscopy. *Chem. Phys. Lett.*, 412:41, 2005.

[503] Jari Lindberg, Tero Setala, Matti Kaivola, , and Ari T. Friberg. Spatial coherence effects in light scattering from metallic nanocylinders. *JOpt. Soc. Am. A*, 23:1349, 2006.

[504] Zhaowei Liu, Hyesog Lee, Yi Xiong, Cheng Sun, and Xiang Zhang. Far-field optical hyperlens magnifying sub-diffraction-limited objects. *Science*, 315:1686, 2007.

[505] H. Peter Lu, Luying Xun, and X. Sunney Xie. Single-molecule enzymatic dynamics. *Science*, 282:1877, 1998.

[506] L. Luan, P.R. Sievert, and J.B. Ketterson. Near-field and far-field electric dipole radiation in the vicinity of a planar dielectric half space. *New J. Phys.*, 8:264, 2006.

[507] L. D. A. Lundeberg, G. P. Lousberg, D. L. Boiko, and E. Kapon. Spatial coherence measurements in arrays of coupled vertical cavity surface emitting lasers. *Appl. Phys. Lett.*, 90:021103, 2007.

[508] Hongzhou Ma, Won-Jeong Kim, James S. Horwitz, Stephen W. Kirchoefer, and Jeremy Levy. Lattice-scale domain wall dynamics in ferroelectrics. *Phys. Rev. Lett.*, 91:217601, 2003.

[509] Hongzhou Ma and Jeremy Levy. Ghz apertureless near-field scanning optical microscopy of ferroelectric nanodomain dynamics. *Nanolett.*, 6:341, 2006.

[510] R. C. Maher, L. F. Cohen, E. C. Le Ru, and P. G. Etchegoin. On the experimental estimation of surface enhanced Raman scattering (sers) cross sections by vibrational pumping. *J. Phys. Chem. B*, 110:19469, 2006.

[511] STEFAN A. MAIER, PIETER G. KIK, HARRY A. ATWATER, SHEFFER MELTZER, ELAD HAREL, BRUCE E. KOEL, and ARI A.G. REQUICHA. Local detection of electromagnetic energy transport below the diffraction limit in metal nanoparticle plasmon waveguides. *Nat. Mater.*, 2:229, 2003.

[512] L. M. Matarrese and K. M. Evenson. Improved coupling to infrared whisker diodes by use of antenna theory. *Appl. Phys. Lett.*, 17:8, 1970.

[513] I. D. Mayergoyz, Z. Zhang, and G. Miano. Analysis of dynamics of excitation and dephasing of plasmon resonance modes in nanoparticles. *Phys. Rev. Lett.*, 98:147401, 2007. theoretical study.

[514] Eric B. McDaniel and J. W. P. Hsu. Nanometer scale optical studies of twin domains and defects in lanthanum aluminate crystals. *J. Appl. Phys.*, 80:1085, 1996.

[515] Damien McHugh, Ron Atkinson, and Nikolai F. Kubrakov. Experimental characterization of the nonlinear optical and magneto-optical properties of interfaces. *J. Opt. Soc. Am. B*, 22:187, 2005.

[516] M.D. McMahon, D. Ferrara, C.T. Bowie, R. Lopez, and R.F. Haglund Jr. Second harmonic generation from resonantly excited arrays of gold nanoparticles. *Appl. Phys. B*, 87:259, 2007.

[517] O. Merchiers, F. Moreno, F. Gonzalez, J.M. Saiz, and G. Videen. Electromagnetic wave scattering from two interacting small spherical particles. Influence of their optical constants, ϵ and μ. *OPt. Commun.*, 269:1, 2006.

[518] B. Meyer and David Vanderbilt. Ab initio study of ferroelectric domain walls in pbtio3. *Phys. Rev. B*, 65:104111, 2002.

[519] A.B. Meyers, P. Tchenio, M.Z. Zgierski, and W.E. Moerner. Vibronic spectroscopy of individual molecules in solids. *J. Phys. Chem.*, 98:10377, 1994.

[520] A. A. Mikhailovsky, M. A. Petruska, M. I. Stockman, and V. I. Klimov. Broadband near-field interference spectroscopy of metal nanoparticles using a femtosecond white-light continuum. *Opt. Lett.*, 28:1686, 2003.

[521] S. Mori, Y. Horibe, and T. Katsufuji. Ferroelectric domains in $ymno_3$. *J. Kor. Phys. Soc.*, 46:37, 2005.

[522] A.N. Morozovska and E.A. Eliseev. Phenomenological description of domain recording in ferroelectric semiconductors by using atomic force microscopy. *Phys. Stat. Sol. B*, 242:R79, 2005.

[523] A.N. Morozovska and E.A. Eliseev. Phenomenological description of polarization switching in ferroelectric semiconductors with charged defects. *Phys. Stat. Sol. B*, 242:947, 2005.

[524] A.N. Morozovska and E.A. Eliseev. The study of screening phenomena under the nano-domain formation in ferroelectric semiconductors. *Phys. Stat. Sol. B*, 242:1996, 2005.

[525] Anna N. Morozovska, Eugene A. Eliseev, Svetlana L. Bravina, Sergei V. Kalinin-Decomposition of the point-dipole field into homogeneous, and evanescent parts. Resolution-function theory in piezoresponse force microscopy: Wall imaging, spectroscopy, and lateral resolution. *Phys. Rev. B*, 75:174109, 2007.

[526] M. Moskowits and D.P.DiLella. *Surface Enhanced Raman Scattering*, page 243. Plenum, New York, 1982.

[527] M. Mueller, E. Soergel, M.C. Wengler, and K. Buse. Light deflection from ferroelectric domain boundaries. *Appl. Phys. B*, 78:367, 2004.

[528] C. F. Mulhollandx, C. F. Bohren, and K. A. Fuller. Light scattering by agglomerates: Coupled electric and magnetic dipole method. *Langmuir*, 10:2533, 1994.

[529] Makiko Muto, Yukito Tanabe, Takako Iizuka-Sakano, and Eiichi Hanamura. Magnetoelectric and second-harmonic spectra in antiferromagnetic cr_2o_3. *Phys. Rev. B*, 57:9568, 1998.

[530] R. Hillenbrand N. Ocelic. Subwavelength-scale tailoring of surface phonon polaritons by focused ion-beam implantation. *Nat. Mat.*, 3:606, 2004.

[531] Ivan I. Naumov, L. Bellaiche, and Huaxiang Fu. Unusual phase transitions in ferroelectric nanodisks and nanorods. *Nature*, 432:737, 2004.

[532] N. Nilius, N. Ernst, and H.J. Freund. Photon emission spectroscopy of individual oxide-supported silver clusters in a scanning tunneling microscope. *Phys. Rev. Lett*, 84:3994, 2000.

[533] J. A. Osborn. Demagnetizing factors of the general ellipsoid. *Phys. Rev.*, 67:351, 1945.

[534] Andreas Otto. Excitation of nonradiative surface plasma waves in silver by the method of frustrated total reflection. *Zeitschrift fuer Physik A Hadrons and Nuclei*, 216:398, 1968.

[535] N. A. Pertsev and G. Arlt. Forced translational vibrations of 90° domain walls and the dielectric dispersion in ferroelectric ceramics. *J. Appl. Phys.*, 74:4105, 1993.

[536] N. A. Pertsev, G. Arlt, and A. G. Zembilgotov. Prediction of a giant dielectric anomaly in ultrathin polydomain ferroelectric epitaxial films. *Phys. Rev. Lett.*, 76: 1364, 1996.

[537] S. Prosandeev and L. Bellaiche. Initial excitation process of ferroelectric b2 soft mode in kd2po4. *Phys. Rev. Lett.*, 97:167601, 2006.

[538] M. S. Prosandeeva, S. A. Prosandeev, and L. Jastrabik. Diffuse first order phase transitions. *INtegr. Ferroel.*, 78:45, 2006.

[539] C.V. Raman. A new radiation. *Indian J. Phys.*, 2:387, 1928.

[540] R. C. Reddick, R. J. Warmack, and T. L. Ferrell. New form of scanning optical microscopy. *Phys. Rev. B*, 39:767, 1989.

[541] Bin Ren, Gennaro Picardi, Bruno Pettinger, Rolf Schuster, and Gerhard Ertl. Tip-enhanced Raman spectroscopy of bezenethiol adsorbed on au and pt single-crystal surfaces. *Angew. Chem.*, 44:139, 2005.

[542] U. Robels and G. Arlt. Domain wall clamping in ferroelectrics by orientation of defects. *J. Appl. Phys.*, 73:3454, 1993.

[543] Hema Roychowdhury and Emil Wolf. Effects of spatial coherence on near-field spectra. *OPt. Lett.*, 28:170, 2003.

[544] J. Rychen, T. Ihn, P. Studerus, A. Herrmann, K. Ensslin, H. J. Hug, P. J. A. van Schendel, and H. J. Gúntherodt. Operation characteristics of piezoelectric quartz tuning forks in high magnetic fields at liquid helium temperatures. *Rev. Sci. Instr.*, 71:1695, 2000.

[545] C. Sönnichsen, T. Franzl, T. Wilk, G. von Plessen, J. Feldmann, O. Wilson, and P. Mulvaney. Drastic reduction of plasmon damping in gold nanorods. *Phys. Rev. Lett.*, 88:077402, 2002.

[546] M. Safrankova, J. Fousek, and S.A. Kizaev. Domains in ferroelectric $ymno_3$. *Czech. J. Phys. B*, 17:560, 1967.

[547] M. Scharte, R. Porath, T. Ohms, M. Aeschlimann, B. Lamprecht, H. Ditlbacher, and F. R. Aussenegg. Lifetime and dephasing of plasmons in ag-nanoparticles. In A. Lewis, H.K. Wickramasingae, and K. Al-Shamery, editors, *Proc. of the SPIE*, volume 4456, page 14, 2001.

[548] M. Scharte, R. Porath, T. Ohms, J. R. Krenn, H. Ditlbacher, F. R. Aussenegg, A. Liebsch, and M. Aeschlimann. Do mie plasmons have a longer lifetime on resonance than off-resonance? *Appl. Phys. B*, 73:301, 2001.

[549] L. Schneider, Hl.J. Schmid, and W. Peukert. Influence of particle size and concentration on the second-harmonic signal generated at colloidal surfaces. *Appl. Phys. B*, 87:333, 2007.

[550] S. C. Schneider, S. Grafstroem, and L. M. Eng. Scattering near-field optical microscopy of optically anisotropic systems. *Phys. Rev. B*, 71:115418, 2005.

[551] P. J. Schuck, D. P. Fromm, A. Sundaramurthy, G. S. Kino, and W. E. Moerner. Improving the mismatch between light and nanoscale objects with gold bowtie nanoantennas. *Phys. Rev. Lett.*, 94:017402, 2005.

[552] A. K. Sheridan, A. W. Clark, A. Glidle, J. M. Cooper, and D. R. S. Cumming. Multiple plasmon resonances from gold nanostructures. *Appl. Phys. Lett.*, 90:143105, 2007.

[553] V. Ya. Shur, A. I. Lobov, A. G. Shur, S. Kurimura, Y. Nomura, K. Terabe, X. Y. Liu, and K. Kitamura. Rearrangement of ferroelectric domain structure induced by chemical etching. *Appl. Phys. Lett.*, 87:022905, 2005.

[554] V. V. Shvartsman, N. A. Pertsev, J. M. Herrero, C. Zaldo, and A. L. Kholkin. Nonlinear local piezoelectric deformation in ferroelectric thin films studied by scanning force microscopy. *J. Appl. Phys.*, 97:104105, 2005.

[555] Rajinder Singh. C. v. Raman and the discovery of the Raman effect. *Physics in Perspective*, 4:399, 2002.

[556] II Smolyaninov, AV Zayats, and CC Davis. Near-field second-harmonic imaging of ferromagnetic and ferroelectric materials. *Opt. Lett.*, 22:1592, 1997.

[557] Igor I. Smolyaninov. Dephasing of electrons in mesoscopic metal wires due to zero-point fluctuations of optically active localized plasmon modes. *Phys. Rev. B*, 71: 193404, 2005.

[558] Igor I. Smolyaninov, Chi H. Lee, and Christopher C. Davis. Near-field second harmonic imaging of lead zirconate titanate piezoceramic. *Appl. Phys. Lett.*, 74:1942, 1999.

[559] Carsten Soennichsen. *Plasmons in metal nanostructures.* PhD thesis, LUdwig-Maximilian Universitaet Muenchen, 2001.

[560] Uwe Stoebener. Active vibration isolation for highly sensitive measurement equipment. *Adaptonic Congress*, 2006.

[561] Patrick Stoller, Volker Jacobsen, and Vahid Sandoghdar. Measurement of the complex dielectric constant of a single gold nanoparticle. *Opt. Lett.*, 31:2474, 2006.

[562] R. M. Stöckle, Y. D. Suh, V. Deckert, and R. Zenobi. Nanoscale chemical analysis by tip-enhanced Raman spectroscopy. *Chem. Phys. Lett.*, 318:131, 2000.

[563] Yukito Tanabe, Makiko Muto, and Eiichi Hanamura. Theory of nonlinear optical susceptibilities of antiferromagnetic Cr_2O_3. *Solid State Commun.*, 102:643, 1997.

[564] M. Thomas, J.-J. Greffet, R. Carminati, and J. R. Arias-Gonzalez. Single-molecule spontaneous emission close to absorbing nanostructures. *Appl. Phys. Lett.*, 85:3863, 2004.

[565] T. Tybell, C. H. Ahn, and J.-M. Triscone. Control and imaging of ferroelectric domains over large areas with nanometer resolution in atomically smooth epitaxial pb(zr0.2ti0.8)o3 thin films. *Appl. Phys. Lett.*, 72:1454, 1998.

[566] Y. Uesu, S. Kurimura, and Y. Yamamoto. Non-destructive observations of the 180 degrees ferroelectric domain using the nonlinear optical (shg) microscope. *Ferroelectrics*, 191:1, 1997.

[567] M. Veres, M. Füle, S. Tóth, M. Koós, and I. Pócsik. Surface enhanced Raman scattering (sers) investigation of amorphous carbon. *Diam. Re. Mat.*, 13:1412, 2004.

[568] Feng Wang and Y. Ron Shen. General properties of local plasmons in metal nanostructures. *Phys. Rev. Lett.*, 97:206806, 2006.

[569] D.W. Ward, E.R. Statz, and K.A. Nelson. Fabrication of polaritonic structures in $LiNbO_3$ and $LiTaO_3$ using femtosecond laser machining. *Appl. Phys. A*, 86:49, 2007.

[570] D. R. Ward, N. K. Grady, C. S. Levin, N. J. Halas, Y. Wu, P. Nordlander, and D. Natelson. Electromigrated nanoscale gaps for surface-enhanced Raman spectroscopy. *Nano Lett.*, 2007.

[571] David W. Ward, Eric R. Statz, Keith A. Nelson, Ryan M. Roth, and Richard M. Osgood. Terahertz wave generation and propagation in thin-film lithium niobate produced by crystal ion slicing. *Appl. Phys. Lett.*, 86:022908, 2005.

[572] R.W. Wood. Optical properties of homogeneous and granular films of sodium and potassium. *Philos. Mag.*, 38:98, 1919.

[573] T. J. Yang, Venkatraman Gopalan, P. J. Swart, and U. Mohideen. Direct observation of pinning and bowing of a single ferroelectric domain wall. *Phys. Rev. Lett*, 82:4106, 1999.

[574] J. Zenneck. über die fortpflanzung ebener elektromagnetischer wellen längs einer ebenen leiterfläche und ihre beziehung zur drahtlosen telegraphie. *Annalen der Physik*, 328:846, 1907.

[575] W. Zhang, X. Cui, B.-S. Yeo, T. Schmid, and C. Zenobi. Nanoscale roughness on metal surfaces can increase tip-enhanced Raman scattering by an order of magnitude. *Nano Lett.*, 2007.

[576] Z.-Y. Zhang and Y.-P. Zhao. Tuning the optical absorption properties of ag nanorods by their topologic shapes: A discrete dipole approximation calculation. *Appl. Phys. Lett.*, 89:023110, 2006.

[577] W. Zhong, David Vanderbilt, and K. M. Rabe. First-principles theory of ferroelectric phase transitions for perovskites: The case of batio$_3$. *Phys. Rev. B*, 52:6301, 1995.

[578] W. Zhong, David Vanderbilt, and K. M. Rabe. Phase transitions in batio$_3$ from first principles. *Phys. Rev. Lett.*, 73:1861, 1994.

[579] L. Zhou, Y. P. Wang, Z. G. Liu, W. Q. Zou, and Y. W. Du. Structure and ferroelectric properties of ferroelectromagnetic ymno3 thin films prepared by pulsed laser depositon. *Phys. Stat. Sol. A*, 201:497, 2004.

[580] Yun Zhu and Shixun Zhou. An analytical expression for the dispersion relation of surface plasmons in a bounded and layered two-dimensional electron gas. *J. Phys. C: Solid State Phys.*, 20:L115, 1987.

[581] Y. Zou, R. Hutton, D. Feili, C. Neacsu, X. Ma, K.H. Schartner, and P.H. Mokler. Precision lifetime measurement of the $2p^2P_{3/2}$ level for Li-like Ni by beam-foil spectroscopy. *Nucl. Instr. and Meth. in Phys. Res. B*, 235:192, 2005.

[582] A. Zumbusch, G. R. Holtom, and X. Sunney Xie. Three-dimensional vibrational imaging by coherent anti-Stokes Raman scattering. *Phys. Rev. Lett.*, 82:4142, 1999.

[583] K. Kneipp, M. Moskovits, and H. Kneipp, editors. *Surface-Enhanced Raman Scattering Physics and Applications*. Topics in Applied Physics. Springer Berlin / Heidelberg, 2006.

[584] K. Kneipp, M. Moskovits, and H. Kneipp, editors. *Surface-Enhanced Raman Scattering - Physics and Applications*. Topics in Applied Physics. Springer Berlin / Heidelberg, 2006.

[585] C. C. Neacsu, S. Berweger, and M. B. Raschke. Tip-enhanced Raman imaging and spectroscopy: sensitivity, symmetry and selection rules. submitted, 2008.

[586] C. Ropers, C. C. Neacsu, M. B. Raschke, M. Albrecht, C. Lienau, and T. Elsaesser. Light confinement at ultrasharp metallic tips. submitted, 2008.

[587] L. Ciobotaru, P. Chiru, C. C. Neacsu, and G. Musa. PDP type barrier discharge ultraviolet radiation source. *J. Optoelectr. Adv. Mater.*, vol. 6(no. 1):p. 321, 2004.

[588] L. Ciobotaru, P. Chiru, C. C. Neacsu, A. Baltog, and G. Musa. The study of M-effect in Ne at the addition of different electronegative gases: O_2, H_2 and Cl_2. *Proc. ICPIG*, 2003.

[589] L. Ciobotaru, P. Chiru and. C. Neacsu, and G. Musa. PDP type discharge as an efficient excimer ultraviolet radiation source. *Proc. 16th ESCAMPIG and 5th ICRP Joint Conference*, vol. 1:p. 53, 2002.

Publications

1 Articles in conjunction with this work

[1] C. C. Neacsu, B. B. van Aken, M. Fiebig and M. Raschke, *Tip-enhanced near-field second-harmonic imaging of the ferroelectric domain structure of $YMnO_3$.*, 2008, in preparation

[2] C. C. Neacsu, S. Berweger and M. B. Raschke *Tip-enhanced near-field second-harmonic imaging of the ferroelectric domain structure of $YMnO_3$.*, 2008, submitted

[3] C. Ropers, C. C. Neacsu, M. B. Raschke, M. Albrecht, C. Lienau and T. Elsaesser *Light confinement at ultrasharp metallic tips.*, 2008, submitted

[4] C. C. Neacsu, J. Dreyer, N. Behr and M. B. Raschke *Reply to Comment on 'Scanning-probe Raman spectroscopy with single-molecule sensitivity'*, published in *Phys.Rev.B*, vol. 75, pages 263–402, 2007,

[5] C. Ropers, C. C. Neacsu, T. Elsaesser, M. Albrecht, M. B. Raschke and C. Lienau *Grating-coupling of surface plasmons onto metallic tips: A nanoconfined light source.'*, published in *Nanolett*, vol. 7, pages 2784–2788, 2007, featured in: Nature Photonics, vol. 446, p. 500, 2007

[6] C. C. Neacsu, J. Dreyer, N. Behr and M. B. Raschke *Scanning-probe Raman spectroscopy with single-molecule sensitivit'*, published in *Phys. Rev. B*, vol. 73, pages 406, 2006

[7] R. M. Roth, N. C. Panoiu, M. M. Adams, R. M. Osgood, C. C. Neacsu and M. B. Raschke *Resonant-plasmon field enhancement from asymmetrically illuminated conical metallic-probe tips*, published in *Opt. Expr.*, vol. 14, pages 2921, 2006

[8] C. C. Neacsu, G. A. Steudle and M. B. Raschke *Plasmonic light scattering from nanoscopic metal tips*, published in *Appl. Phys. B*, vol. 3, pages 295, 2005

[9] C. C. Neacsu, G. A. Reider and M. B. Raschke *Second-harmonic generation from nanoscopic metal tips: Symmetry selection rules for single asymmetric nanostructures*, published in *Phys. Rev. B*, vol. 71, pages 201–402, 2005

2 Other publications

[1] Y. Zou, R. Hutton, D. Feili, C. Neacsu, X. Ma, K.H. Schartner and P.H. Mokler, *Precision lifetime measurement of the $2p^2P_{3/2}$ level for Li-like Ni by beam-foil spectroscopy*, published in *J. Lumin.*, vol. 128, pages 661, 2008

[2] D. Feili, B. Zimmermann, C. Neacsu, P. Bosselmann, K. H. Schartner, F. Folkmann, A. E. Livingston, E. Trabert and P. H. Mokler, $2s^2\ ^1S_0 - 2s2p\ ^3P_1$ *intercombination transition wavelengths in Be-like Ag^{43+}, Sn^{46+}, and Xe^{50+} ions*, vol. 171 (1), pages 48, 2005

[3] W. Freyer, C. C. Neacsu and M. B. Raschke, *Absorption, luminescence, and Raman spectroscopic properties of thin films of benzo-annelated metal-free porphyrazines*, published in *Nucl. Instr. and Meth. in Phys. Res. B*, vol. 235, pages 192, 2005

[4] L. Ciobotaru, P. Chiru, C. C. Neacsu and G. Musa, *PDP type barrier discharge ultraviolet radiation source*, published in *J. Optoelectr. Adv. Mater.*, vol. 6 (no. 1), pages 321, 2004

[5] L. Ciobotaru, P. Chiru, C. C. Neacsu, A. Baltog and G. Musa, *The study of M-effect in Ne at the addition of different electronegative gases: O_2, H_2 and Cl_2*, published in *Proc. ICPIG*, 2003,

[6] L. Ciobotaru, P. Chiru,. C. Neacsu, G. Musa *PDP type discharge as an efficient excimer ultraviolet radiation source*, published in *J. Lumin.*, vol. 1, pages 53, 2002

List of Figures

List of Tables

Selbständigkeitserklärung

Ich erkläre, dass ich die vorliegende Arbeit selbständig und nur unter Verwendung der angegebenen Literatur und Hilfsmittel angefertigt habe.

Berlin, den 28.01.2008 Corneliu Catalin Neacsu